Ever more accurate effective-one-body waveforms for gravitational-wave astrophysics

Dissertation

zur Erlangung des akademischen Grades
doctor rerum naturalium
(Dr. rer. nat.)
im Fach Physik
Spezialisierung: Theoretische Physik

eingereicht an der
Mathematisch-Naturwissenschaftlichen Fakultät
der Humboldt-Universität zu Berlin

von

M. Sc. Lorenzo Pompili

Präsidentin der Humboldt-Universität zu Berlin:
Prof. Dr. Julia von Blumenthal

Dekan der Mathematisch-Naturwissenschaftlichen Fakultät:
Prof. Dr. Emil List-Kratochvil

Gutacher/innen:

1. Prof. Dr. Alessandra Buonanno
2. Prof. Dr. Sascha Husa
3. Dr. Geraint Pratten

Tag der mündlichen Prüfung: 23.09.2025

Abstract

With the recent adoption of the LISA mission by the European Space Agency and the anticipated operation of next-generation ground-based detectors in the 2030s, we are entering an exciting new phase in gravitational-wave astronomy. As we look forward to upcoming observing runs and future facilities, the accuracy of waveform models becomes critically important: successful detection, correct identification of sources, and precise inference of their astrophysical and cosmological properties all rely on a detailed understanding of the expected waveforms. This thesis focuses on the development of accurate and efficient models for the gravitational radiation emitted by coalescing binary black holes, with particular emphasis on the construction, calibration, and application of effective-one-body waveform models.

Central to this work is the development of the `SEOBNRv5HM` waveform model and the open-source `pySEOBNR` framework, which supports the development, calibration, and validation of the next generation of effective-one-body waveform models. The `SEOBNRv5HM` model improves upon previous generations by incorporating higher-order post-Newtonian results, information from second-order self-force calculations, additional subdominant modes, and calibration to a larger catalog of numerical-relativity simulations. It achieves significantly improved accuracy and higher computational efficiency compared to its predecessor. In parallel, we present progress toward incorporating post-Minkowskian results into the effective-one-body formalism, allowing us to inform the conservative dynamics of bound systems from scattering calculations. This culminates in the development of the `SEOBNR-PM` model.

The waveform models developed are applied to infer the source properties of binary black hole mergers, using both synthetic and real gravitational-wave data. To account for modeling uncertainties arising from numerical-relativity calibration, we introduce a novel probabilistic approach that marginalizes over waveform uncertainties, thereby improving the robustness of parameter inference.

Finally, we extend the `SEOBNRv5` models to explore potential deviations from general relativity. In the theory-specific direction, we construct inspiral-merger-ringdown waveforms in Einstein-scalar-Gauss-Bonnet gravity, an extension of general relativity predicting distinctive signatures in black hole coalescences. In the theory-agnostic direction, we extend the parameterized `pSEOBNR` framework to the spin-precessing binaries, focusing on black hole spectroscopy, which tests general relativity by analyzing the quasinormal modes of the remnant black holes.

Zusammenfassung

Mit der kürzlichen Annahme der LISA-Mission durch die Europäische Weltraumorganisation und dem bevorstehenden Betrieb der nächsten Generation erdgestützter Detektoren in den 2030er Jahren beginnt eine spannende neue Phase der Gravitationswellenastronomie. Angesichts bevorstehender Beobachtungskampagnen und zukünftiger Gravitationswellendetektoren wird die Präzision von Wellenformmodellen zunehmend entscheidend: Der erfolgreiche Nachweis, die korrekte Identifikation von Quellen sowie die genaue Bestimmung ihrer astrophysikalischen und kosmologischen Eigenschaften erfordern alle ein detailliertes Verständnis der erwarteten Signale. Diese Dissertation konzentriert sich auf die Entwicklung akkurater und effizienter Modelle für die Gravitationsstrahlung, die von verschmelzenden binären Schwarzen Löchern emittiert wird – mit besonderem Fokus auf die Konstruktion, die Kalibrierung und die Anwendung von sogenannten "effective-one-body" Wellenformmodellen.

Im Zentrum der Arbeit stehen die Entwicklung des `SEOBNRv5HM`-Wellenformmodells sowie des Open-Source-Frameworks `pySEOBNR`, das die Entwicklung, Kalibrierung und Validierung der nächsten Generation von effective-one-body Modellen unterstützt. `SEOBNRv5HM` verbessert frühere Generationen durch post-Newtonsche Resultate höherer Ordnung, Informationen aus der zweiten Ordnung der Gravitations-Strahlungsrückwirkung (self force), zusätzliche subdominante Moden sowie Kalibrierung anhand eines ausführlicheren Katalogs von Simulationen der numerischen Relativitätstheorie. Das Modell zeichnet sich auch durch eine deutlich gesteigerte Präzision und Recheneffizienz aus. Parallel dazu integrieren wir post-Minkowskische Resultate in den effective-one-body Formalismus, um die konservative Dynamik gebundener Systeme mittels Ergebnissen der Streutheorie zu verbessern. Dies kulminiert in dem `SEOBNR-PM`-Modell.

Die entwickelten Modelle werden zur Bestimmung der Eigenschaften von binären schwarzen Löchern eingesetzt, wobei sowohl synthetische als auch reale Gravitationswellendaten studiert werden. Um Unsicherheiten durch die Kalibrierung zu numerischer Relativität zu berücksichtigen, führen wir eine neue probabilistische Methode ein, bei der über Wellenformunsicherheiten marginalisiert wird und so die Robustheit der Parameterbestimmung verbessert wird. Abschließend erweitern wir die `SEOBNRv5`-Modelle, um potenzielle Abweichungen von der Allgemeinen Relativitätstheorie zu untersuchen. Theorie-spezifisch konstruieren wir Inspiral-Merger-Ringdown-Wellenformen in der Einstein-scalar-Gauss-Bonnet-Gravitation. Theorie-agnostisch erweitern wir das parametrisierte `pSEOBNR`-Framework auf präzessierende Binärsysteme, mit Fokus auf die Spektroskopie Schwarzer Löcher, bei der die Quasinormalmoden eines neu entstandenen schwarzen Lochs studiert werden.

List of Publications

This thesis is mainly based on the content of the following publications:

[1] Deyan P. Mihaylov, Serguei Ossokine, Alessandra Buonanno, Hector Estelles, **Lorenzo Pompili**, Michael Pürrer, Antoni Ramos-Buades "*pySEOBNR: a software package for the next generation of effective-one-body multipolar waveform models*"
SoftwareX 30 (2025), 102080, arXiv: 2303.18203

[2] **Lorenzo Pompili** et al. "*Laying the foundation of the effective-one-body waveform models SEOBNRv5: Improved accuracy and efficiency for spinning nonprecessing binary black holes*"
Phys.Rev.D 108 (2023) 12, 124035, arXiv: 2303.18039

[3] Alessandra Buonanno, Gustav Mogull, Raj Patil, **Lorenzo Pompili** "*Post-Minkowskian Theory Meets the Spinning Effective-One-Body Approach for Bound-Orbit Waveforms*"
Phys.Rev.Lett. 133 (2024) 21, 211402, arXiv: 2405.19181

[4] Félix-Louis Julié, **Lorenzo Pompili**, Alessandra Buonanno "*Inspiral-merger-ringdown waveforms in Einstein-scalar-Gauss-Bonnet gravity within the effective-one-body formalism*"
Phys.Rev.D 111 (2025) 2, 024016, arXiv: 2406.13654

[5] **Lorenzo Pompili**, Alessandra Buonanno, Michael Pürrer "*Accounting for Numerical-Relativity Calibration Uncertainty in Gravitational-Wave Modeling and Inference*"
Phys.Rev.D 112 (2025) 4, 044062, arXiv: 2410.16859

[6] **Lorenzo Pompili**, Elisa Maggio, Hector O. Silva, Alessandra Buonanno "*A parametrized spin-precessing inspiral-merger-ringdown waveform model for tests of general relativity*"
Phys.Rev.D 111 (2025) 12, 124040, arXiv: 2504.10130

An extended overview of my research contributions can be found in Section 1.4.

Declaration of Independent Work

I declare that I have completed the thesis independently using only the aids and tools specified. I have not applied for a doctor's degree in the doctoral subject elsewhere and do not hold a corresponding doctor's degree. I have taken due note of the Faculty of Mathematics and Natural Sciences PhD Regulations, published in the Official Gazette of Humboldt-Universität zu Berlin no. 42/2018 on 11/07/2018.

Contents

Notation

Throughout this thesis, we adopt natural units where $c = G = 1$, except in Chapter 1 where conventional units are used for clarity.

We consider a binary with masses m_1 and m_2, with $m_1 \geq m_2$, and define the following combinations of the masses:

$$\begin{aligned} M = m_1 + m_2, \qquad \mu = \frac{m_1 m_2}{M}, \qquad \nu = \frac{\mu}{M}, \\ \delta = \frac{m_1 - m_2}{M}, \qquad q = \frac{m_1}{m_2}, \qquad \mathcal{M}_c = \frac{(m_1 m_2)^{3/5}}{M^{1/5}}. \end{aligned} \tag{1}$$

Unless explicitly stated otherwise, we will refer to *detector-frame* (redshifted) masses $m_{1,2} = m^{\rm s}_{1,2}(1+z)$, where $m^{\rm s}_{1,2}$ are the source-frame masses, and z is the redshift of the source. For binaries with spins aligned or anti-aligned with the orbital angular momentum (aligned-spin or non-precessing binaries), where the spin magnitudes are S_1 and S_2, we define the dimensionless spins

$$\chi_{\rm i} = \frac{a_{\rm i}}{m_{\rm i}} = \frac{S_{\rm i}}{m_{\rm i}^2}, \tag{2}$$

where ${\rm i} = 1, 2$, and define the following spin combinations:

$$\begin{aligned} \chi_S = \frac{\chi_1 + \chi_2}{2}, \qquad \chi_A = \frac{\chi_1 - \chi_2}{2}, \\ a_\pm = M\chi_\pm = a_1 \pm a_2 = m_1\chi_1 \pm m_2\chi_2. \end{aligned} \tag{3}$$

The dimensionless spins $\chi_{\rm i}$ can take either positive or negative values, depending on whether they are aligned or anti-aligned with the orbital angular momentum. For binaries with generic spins (spin-precessing binaries), we also define the dimensionless spin vectors,

$$\boldsymbol{\chi}_{\rm i} = \frac{\boldsymbol{a}_{\rm i}}{m_{\rm i}} = \frac{\boldsymbol{S}_{\rm i}}{m_{\rm i}^2}, \tag{4}$$

the effective spin parameter $\chi_{\rm eff}$ [7, 8],

$$\chi_{\rm eff} = \frac{m_1\chi_1^{\parallel} + m_2\chi_2^{\parallel}}{m_1 + m_2}, \tag{5}$$

and the effective precessing-spin parameter $\chi_{\rm p}$ [9],

$$\chi_{\rm p} = \frac{1}{B_1 m_1^2} \max\left(B_1 m_1^2 \chi_1^{\perp}, B_2 m_2^2 \chi_2^{\perp}\right), \tag{6}$$

where $B_1 = 2 + 3m_2/(2m_1)$, $B_2 = 2 + 3m_1/(2m_2)$, and we have divided $\boldsymbol{\chi}_{\rm i}$ into its aligned-spin component ($\chi_{\rm i}^{\parallel}$) and in-plane component ($\chi_{\rm i}^{\perp}$).

The relative position and momentum vectors, in the binary's center-of-mass frame, are denoted $\boldsymbol{r}$ and $\boldsymbol{p}$, with

$$\boldsymbol{p}^2 = p_r^2 + \frac{L^2}{r^2}, \quad p_r = \boldsymbol{n}\cdot\boldsymbol{p}, \quad \boldsymbol{L} = \boldsymbol{r}\times\boldsymbol{p}, \tag{7}$$

where $\boldsymbol{n} = \boldsymbol{r}/r$, and $\boldsymbol{L}$ is the orbital angular momentum with magnitude L. When discussing aligned-spin binaries, we consider equatorial orbits, and use polar-coordinates phase-space variables (r, ϕ, p_r, p_ϕ), where the angular momentum reduces to $L = p_\phi$. We also often use $u = M/r$ instead of r. We will occasionally use dimensionless variables

$$\hat{r} = \frac{r}{M}, \quad \hat{p}_r = \frac{p_r}{\mu}, \quad \hat{p}_\phi = \frac{p_\phi}{M\mu}, \quad \hat{t} = \frac{t}{M}, \tag{8}$$

along with the Hamiltonian $\hat{H} = H/\mu$. The orbital frequency is denoted $\Omega = d\phi/dt$, and we define the dimensionless frequency parameter

$$x = v^2 = (M\Omega)^{2/3}. \tag{9}$$

ASD	Amplitude spectral density.
BBH	Binary black hole.
BH	Black hole.
BNS	Binary neutron star.
BS	Boson star.
CE	Cosmic Explorer.
EOB	Effective one body.
ESGB	Einstein-scalar-Gauss-Bonnet.
ET	Einstein Telescope.
FFT	Fast Fourier transform.
FTI	Flexible theory-independent.
GR	General relativity.
GSF	Gravitational self-force.
GW	Gravitational wave.
GWOSC	Gravitational-wave open science center.
GWTC	Gravitational-wave transient catalog.
IMR	Inspiral-merger-ringdown.
ISCO	Innermost stable circular orbit.
JSD	Jensen-Shannon divergence.
LO	Leading order.
LVK	LIGO-Virgo-KAGRA.
MCMC	Markov Chain Monte Carlo.
MDN	Mixture density network.
NLO	Next-to-leading order.
NNLO	Next-to-next-to-leading order.
NQC	Non-quasicircular correction.
NR	Numerical relativity.
NS	Neutron star.
NSBH	Neutron star-black hole.
ODE	Ordinary differential equation.
QNM	Quasinormal mode.
PA	Post-adiabatic.
PE	Parameter estimation.
PM	Post-Minkowskian.
PN	Post-Newtonian.
PSD	Power spectral density.
ROM	Reduced-order model.
RR	Radiation reaction.
SNR	Signal-to-noise ratio.
SO	Spin-orbit.
SS	Spin-spin.
SXS	Simulating eXtreme Spacetimes Collaboration.
TPL	Test-particle limit.
TT	Transverse-traceless gauge.
XG	Next-generation detector.

Table 1: Main acronyms used in this thesis.

1 Introduction

In this chapter, we present an overview of the fundamental concepts of general relativity (GR) and gravitational-wave (GW) theory. We also summarize the methods employed in GW data analysis and the techniques used to model GWs from binary black hole (BBH) coalescences, topics that will be explored in more detail in subsequent chapters.

1.1 Introduction to gravitational-wave theory

Gravitational waves are a prediction of GR, the theory of gravity and spacetime introduced by Albert Einstein in two seminal papers published in 1915 [10, 11]. In GR, spacetime is not a fixed, absolute background as in Newtonian physics; rather, it is a dynamic entity that is deformed by the presence of matter and energy. As John Wheeler succinctly put it, "Spacetime tells matter how to move; matter tells spacetime how to curve" [12]. Starting from its early experimental verifications, such as the bending of light observed during the 1919 solar eclipse [13] and the anomalous perihelion advance of Mercury [14], several GR predictions have been confirmed by multiple experiments over the years [15].

In GR, gravity is not a force transmitted between masses but an expression of spacetime curvature. This curvature is described using the metric tensor $g_{\mu\nu}$. Einstein's field equations relate this curvature to the mass-energy content of a system, as expressed by the energy-momentum tensor $T_{\mu\nu}$:

$$R_{\mu\nu} - \frac{1}{2} g_{\mu\nu} R = \frac{8\pi G}{c^4} T_{\mu\nu}. \tag{1.1}$$

Here, $R_{\mu\nu}$ and R are the Ricci tensor and scalar, respectively. They are functions of the metric tensor $g_{\mu\nu}$, and provide a measure of the curvature of spacetime. They are defined as

$$R_{\mu\nu} = R^{\alpha}_{\mu\alpha\nu}, \quad R = g^{\mu\nu} R_{\mu\nu}, \tag{1.2}$$

where

$$R^{\mu}_{\nu\rho\sigma} = \partial_\rho \Gamma^{\mu}_{\nu\sigma} - \partial_\sigma \Gamma^{\mu}_{\nu\rho} + \Gamma^{\mu}_{\alpha\rho} \Gamma^{\alpha}_{\nu\sigma} - \Gamma^{\mu}_{\alpha\sigma} \Gamma^{\alpha}_{\nu\rho} \tag{1.3}$$

is the Riemann tensor, and

$$\Gamma^{\rho}_{\mu\nu} = \frac{1}{2} g^{\rho\sigma} \left(\partial_\mu g_{\sigma\nu} + \partial g_{\sigma\mu} - \partial_\sigma g_{\mu\nu} \right) \tag{1.4}$$

are the Christoffel symbols. A solution to Einstein's field equations, namely a specific metric tensor $g_{\mu\nu}$, describes a spacetime geometry shaped by the distribution of mass and energy. The Einstein-Hilbert action, given by

$$S = \frac{c^4}{16\pi G} \int d^4x \, \sqrt{-g} \, R, \tag{1.5}$$

serves as the starting point for deriving these field equations via the principle of least action.

General relativity predicts a variety of phenomena that have no counterpart in Newtonian gravity (though Newtonian theory allowed for the early concept of "dark stars" [16]). Two such phenomena, directly relevant to this thesis, are BHs and GWs.

1.1.1 Black holes

The first exact and non-trivial solution to Einstein's field equations was found by Karl Schwarzschild [17] just one year after Einstein's first article on GR. This solution describes the spacetime geometry outside a spherically symmetric, non-rotating mass. In Schwarzschild coordinates (t, r, θ, ϕ), the metric is given by

$$ds^2 = g_{\mu\nu} dx^\mu dx^\nu = -\left(1 - \frac{R_s}{r}\right) c^2 dt^2 + \left(1 - \frac{R_s}{r}\right)^{-1} dr^2 + r^2 \left(d\theta^2 + \sin^2\theta \, d\phi^2\right), \tag{1.6}$$

where $R_s = 2GM/c^2$ is the Schwarzschild radius. This metric features a true curvature singularity at $r = 0$ and a coordinate singularity at $r = R_s$. If a spherically symmetric object of mass M is confined within a radius smaller than its Schwarzschild radius, then GR predicts that an event horizon forms at $r = R_s$. The event horizon is a null surface that causally separates regions of spacetime: outside the horizon, signals can reach distant observers along timelike or null paths, whereas inside, all causal trajectories are inevitably drawn toward the singularity at $r = 0$; no light or information can escape. This defines a Schwarzschild black hole (BH).

Subsequent generalizations of the Schwarzschild metric have advanced our understanding of BH solutions. Hans Reissner and Gunnar Nordström [18, 19] extended the solution to describe electrically charged, non-rotating BHs; Roy Kerr derived the solution for rotating BHs [20]; and Ezra Newman further generalized the solution to describe electrically charged, rotating BHs [21]. The so-called *no-hair* conjecture [22–25] posits that isolated BHs are remarkably simple objects that can be

completely characterized by just their mass, angular momentum, and electric charge, unlike regular stars, which require a host of parameters to describe their structure.[1] BHs are extraordinarily compact; for a BH, the ratio between its mass M and its radius $R \approx R_{\rm s}$ is given by $c^2/(2G)$, which is roughly 10^6 times the corresponding ratio for the Sun.

These solutions provide the theoretical foundation for our current understanding of astrophysical BHs, which have now been observed across a wide range of masses and environments. Several classes of astrophysical BHs have been identified: stellar-mass BHs, with masses approximately within $1M_\odot \lesssim M \lesssim 100M_\odot$ [42–49], intermediate-mass BHs spanning $100M_\odot \lesssim M \lesssim 10^5 M_\odot$ [50, 51], and massive ($10^5 M_\odot \lesssim M \lesssim 10^8 M_\odot$) to supermassive ($M \gtrsim 10^8 M_\odot$) BHs [52–57].

Stellar-mass BHs are thought to originate from the gravitational collapse of massive stars [58–60]. Although the formation mechanism of massive BHs is still debated, the prevailing theory suggests that they grow by accretion and mergers, starting from lighter *seed* BHs [61, 62]. These seeds are generally categorized as either *light seeds* ($\sim$10–100 $M_\odot$), thought to be the remnants of the universe's first, metal-poor (Population III) stars, or *heavy seeds* ($\sim 10^2$–10^5 $M_\odot$), which may form via the direct collapse of gas clouds in metal-poor, high-redshift environments. Intermediate-mass BHs are thought to form either as the direct remnants of early Population III stars, through runaway collisions in young, dense star clusters, or via the gradual, hierarchical merging of stellar-mass BHs and compact objects in older clusters. Additionally, some theories predict the existence of primordial BHs, which would have formed from the collapse of overdense regions in the early universe [63–66]; however, no conclusive observational evidence for them exists to date. For the purposes of this thesis, the focus is on stellar-mass BHs, key sources for ground-based GW detectors.

Historically, BHs were primarily inferred through indirect effects, such as the dynamical influence on the orbits of nearby bodies [52–55], gravitational lensing of background stars [67], and the electromagnetic radiation emitted from accretion disks surrounding them [42–44]. More recently, the Event Horizon Telescope Collaboration published in 2019 the first horizon-scale image of the supermassive BH at the center of the galaxy Messier 87 [56], based on the electromagnetic emission from its accretion flow. In 2022, a similar image was released for the BH at the center of our galaxy, SgrA* [57].

A major breakthrough in BH astrophysics came with the advent of GW astronomy. Since the first detection of GWs from a BBH merger in 2015 [45], the LIGO-Virgo-KAGRA (LVK) Collaboration has reported nearly 100 BBH events [46–49], with

[1] Interestingly, several theories of gravity beyond GR do not obey the no-hair conjecture, and instead predict *hairy* BHs with additional degrees of freedom [26–41], with potential observational signatures. We will revisit this topic in Sec. 4.2.

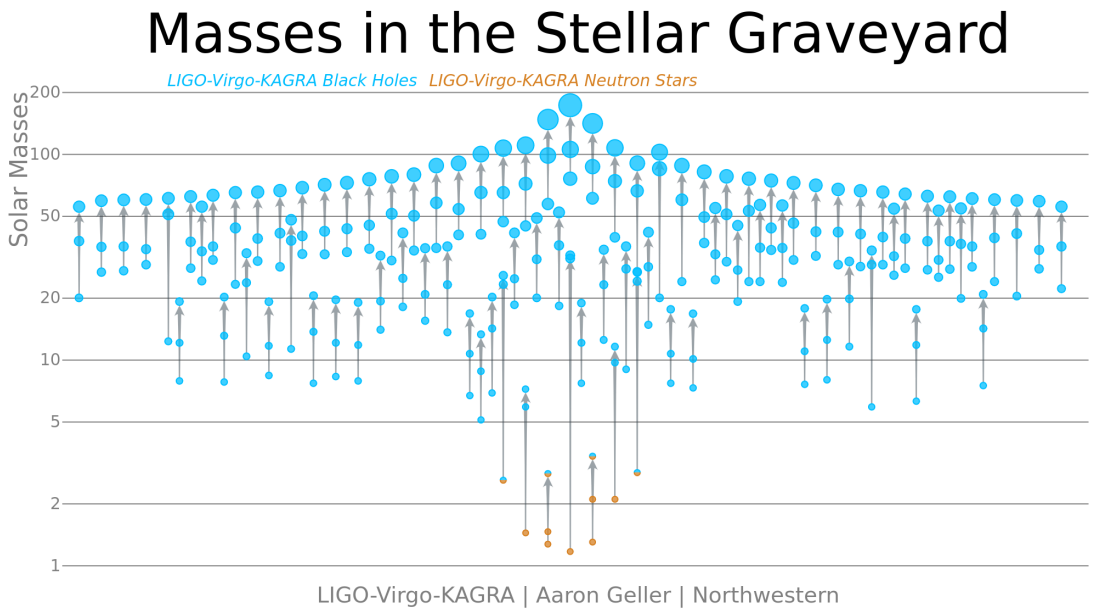

Figure 1.1: Summary of the gravitational-wave detections of stellar-mass black holes (blue) and neutron stars (orange), up to the third LIGO-Virgo-KAGRA observing run. Credit: [77]

component masses ranging from a few to about 100 solar masses. These findings have been complemented by independent analyses of public data [68–71] from the Advanced LIGO and Virgo detectors [72, 73]. Gravitational-wave observations have significantly advanced our understanding of the BH mass and spin distributions, providing constraints on population models [74] and testing the so-called mass gap hypotheses. The *lower mass gap* refers to the observed dearth of compact objects between the most massive neutron stars (NSs) (around 2 $M_\odot$) and the lightest BHs (around 5 $M_\odot$), while the *upper mass gap* is predicted by pair-instability supernova models [75]. In these models, stars with initial masses in the range 150-260 $M_\odot$ can undergo a collapse triggered by electron-positron pair production, leading to a runaway thermonuclear explosion that completely disrupts the star and leaves no remnant. This mechanism predicts a gap in the BH mass spectrum between roughly 50 and 150 $M_\odot$ [76]. Nonetheless, as shown in Fig. 1.1, the sources of several GW events have been measured with masses falling within these gaps, challenging the mass gap hypotheses and our current understanding of stellar evolution.

Stellar-mass BHs, like many other astrophysical objects, are often found in binary systems. The formation of BBHs is generally understood to proceed via two primary channels. The first is isolated binary evolution, in which two massive stars evolve together in a binary system. Over the course of their evolution, they undergo mass transfer episodes and potentially a common-envelope phase, eventually leading to the

formation of two BHs that remain gravitationally bound [78–82]. Binaries formed through this channel are typically characterized by nearly equal component masses, low orbital eccentricities (due to efficient circularization by gravitational radiation), and spin vectors aligned with the orbital angular momentum. The second major pathway is dynamical formation, which occurs in dense stellar environments such as globular clusters, nuclear star clusters, or young stellar clusters [83–87]. In this scenario, BHs form independently and later pair through multi-body interactions and gravitational capture. Dynamically formed BBHs are more likely to exhibit misaligned spins, higher mass ratios, and potentially significant eccentricities, especially if they merge soon after formation. These distinct features provide crucial observational signatures for disentangling the relative contributions of different formation channels to the BBH population [88–93].

1.1.2 Gravitational waves from compact binaries

The second GR prediction central to this thesis are GWs, perturbations of the gravitational field that propagate as waves far from the source, carrying energy and angular momentum. Einstein originally predicted their existence shortly after formulating GR [94, 95]. Einstein's derivation was originally received with skepticism [96, 97], and the physical reality of GWs remained a subject of debate for decades, until pivotal developments in the late 1950s. A major turning point occurred at the 1957 Chapel Hill Conference on the Role of Gravitation in Physics [96]. There, Felix Pirani introduced a novel approach to understanding GWs by analyzing the geodesic deviation equation, demonstrating that a passing GW would cause measurable oscillations in the separation of free-falling test particles. Building on this insight, Richard Feynman proposed the *sticky bead argument*, a thought experiment illustrating that GWs could do work by causing beads on a rod to move and generate heat through friction, thereby confirming that GWs carry energy. In 1959, a seminal paper by Bondi, Pirani, and Robinson [98] presented an exact plane wave solution with cylindrical symmetry and rigorously confirmed that these waves indeed carry energy and angular momentum. These theoretical foundations paved the way for Joseph Weber's pioneering experimental efforts at direct GW detection using resonant bar detectors [99].

The first observational evidence for GWs came from the precise measurements of radio pulse timings in a binary pulsar system by Hulse and Taylor [100]. Their observations revealed a gradual decay in the pulsar period, consistent with the loss of energy and angular momentum due to GW emission as predicted by GR. More recently, the LIGO Scientific Collaboration and the Virgo Collaboration detected, for the first time, a GW signal from a BBH merger using laser-interferometry techniques [45].

Following Ref. [101], we introduce the basic structure of the GW signal from

compact binaries by linearizing Einstein's field equations (1.1) around the Minkowski metric $\eta_{\mu\nu} = \mathrm{diag}(-1, 1, 1, 1)$ using the ansatz

$$g_{\mu\nu} = \eta_{\mu\nu} + h_{\mu\nu} + \mathcal{O}(h^2), \tag{1.7}$$

with $|h_{\mu\nu}| \ll 1$ being a small perturbation. This perturbation tensor will represent GWs propagating on a Minkowski background. The trace-reversed perturbation tensor $\bar{h}_{\mu\nu} = h_{\mu\nu} - \frac{1}{2}\eta_{\mu\nu}\eta^{\alpha\beta}h_{\alpha\beta}$ satisfies a simple wave equation if an appropriate coordinate system (gauge) is chosen in which

$$\partial_\mu \bar{h}^{\mu\nu} = 0, \tag{1.8}$$

commonly referred to as Lorenz gauge. With this choice of coordinates, the linearized Einstein equations are

$$\Box \bar{h}_{\mu\nu} = -\frac{16\pi G}{c^4} T_{\mu\nu} + \mathcal{O}(\bar{h}^2), \tag{1.9}$$

where $\Box = \eta^{\mu\nu}\partial_\mu\partial_\nu$ is the d'Alembertian operator in flat spacetime, and $T_{\mu\nu}$ is the stress-energy tensor associated with the source of GWs. The four conditions defining the Lorenz gauge reduce the 10 degrees of freedom of the symmetric tensor $h_{\mu\nu}$ to 6 in $\bar{h}_{\mu\nu}$, but do not yet fix the gauge completely.

Let us now consider GW propagation in the absence of a source term ($T_{\mu\nu} = 0$). A common choice to fix the remaining gauge freedom, which can only be imposed in vacuum away from the source, is the transverse-traceless (TT) gauge, defined by $h^{\mu 0} = 0$ and $h^i{}_i = 0$ ($i = 1, 2, 3$). In this gauge, we also can drop the distinction between $h_{\mu\nu}$ and its trace-reversed counterpart $\bar{h}_{\mu\nu}$. This gauge isolates the two physical polarization modes of a GW, commonly denoted "plus" (h_+) and "cross" ($h_\times$), which correspond to transverse shear deformations in orthogonal directions. A GW propagating in the z-direction has nonzero components h^{TT}_{ij} only in the transverse x-y plane,

$$h^{\mathrm{TT}}_{ij} = \begin{pmatrix} h_+ & h_\times & 0 \\ h_\times & -h_+ & 0 \\ 0 & 0 & 0 \end{pmatrix}_{ij}. \tag{1.10}$$

When this wave propagates through a ring of free-falling test masses in the x-y plane, it produces a characteristic stretching and squeezing effect, with the two polarization states causing distortions rotated by 45° relative to each other, as illustrated in Fig. 1.2.

Even though gravity itself does not have a local stress-energy tensor in GR (the gravitational field's energy cannot be localized in a coordinate-invariant way), in the weak-field limit one can define an effective energy density for GWs in the TT gauge. In particular, the power radiated as consequence of the GW emission can be computed

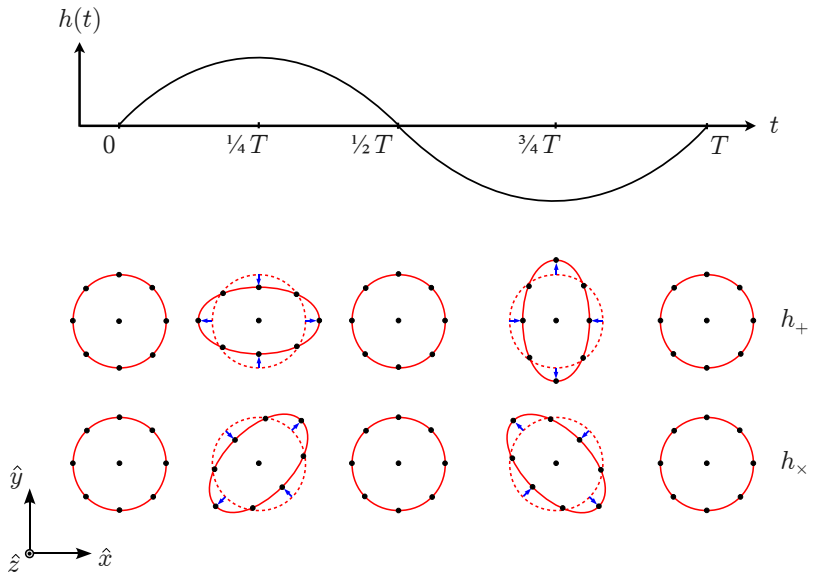

Figure 1.2: Displacement induced on a ring of free-falling test masses by a monochromatic gravitational wave with period T propagating in the z direction. Credit: [102]

as [101]

$$\frac{dE_{\rm GW}}{dt} = \frac{d_L^2 c^3}{32\pi G} \int d\Omega \left\langle \sum_{i,j} \dot{h}_{ij}^{\rm TT} \dot{h}_{ij}^{\rm TT} \right\rangle , \tag{1.11}$$

where dots denote time derivatives, d_L is the luminosity distance between the source and the observer, the integral is performed over the solid angle, and angle brackets denote an average computed over several characteristic periods of the GW.

Let us now consider how GWs are generated. The solution to the linearized Einstein equations (1.9) can be written using the Green's function method, as

$$\bar{h}_{\mu\nu}(t, \boldsymbol{x}) = \frac{4G}{c^4} \int d^3x' \frac{1}{|\boldsymbol{x} - \boldsymbol{x'}|} T_{\mu\nu} \left(t - \frac{|\boldsymbol{x} - \boldsymbol{x'}|}{c}, \boldsymbol{x'} \right) . \tag{1.12}$$

When the observer is located at a distance $d_L = |\boldsymbol{x}| \gg R$, where R is the typical size of the GW source, the term $|\boldsymbol{x} - \boldsymbol{x'}|$ can be approximated as d_L with an error of order $\sim R/d_L$. At leading order in R/d_L and v/c, and when using the TT-gauge, Eq. (1.12) reduces to [101]

$$\bar{h}_{ij}^{\rm TT} \simeq \frac{1}{d_L} \frac{2G}{c^4} \ddot{Q}_{ij}(t - d_L/c), \tag{1.13}$$

where $Q_{ij} = I_{ij} - \frac{1}{3}\delta_{ij}\delta^{kl} I_{kl}$ is the traceless part of the mass quadrupole moment, with $I_{ij} = \int \rho(\boldsymbol{x}) x_i x_j d^3x$ and $\rho = T^{00}/c^2$. Equation (1.13), commonly known as the *quadrupole formula*, shows that the leading-order GWs arise from the second time derivative of the source's mass quadrupole moment. Combining this result with

Eq. (1.11), one obtains the GW luminosity as

$$\frac{dE_{\rm GW}}{dt} = \frac{G}{5c^5} \left\langle \dddot{Q}_{ij} \dddot{Q}_{ij} \right\rangle . \tag{1.14}$$

Since Eq. (1.13) contains a second time-derivative of the quadrupole moment, axisymmetric mass distributions, for which the quadrupole moment is time-independent, do not emit gravitational radiation. Promising GW sources include non-axisymmetric systems, such as rotating NSs [103], supernova explosions [104], and compact binary systems.

As an illustrative example, let us consider a binary system in a circular orbit in the x-y plane, with masses $m_1 \geq m_2$, separation r, and orbital frequency ω. In the center-of-mass frame the positions of the masses are given by

$$\boldsymbol{x}_1 = \frac{m_2 r}{M}(\cos(\omega t), \sin(\omega t), 0), \quad \boldsymbol{x}_2 = -\frac{m_1}{m_2}\boldsymbol{x}_1, \tag{1.15}$$

where $M = m_1 + m_2$ is the total mass. Modeling the bodies as point masses, the mass density is

$$\rho(t, \boldsymbol{x}) = m_1 \delta \left[\boldsymbol{x} - \boldsymbol{x}_1(t)\right] + m_2 \delta \left[\boldsymbol{x} - \boldsymbol{x}_2(t)\right], \tag{1.16}$$

from which the mass quadrupole moment is obtained as

$$I^{ij}(t) = m_1 x_1^i(t) x_1^j(t) + m_2 x_2^i(t) x_2^j(t). \tag{1.17}$$

Using the quadrupole formula (1.13), the metric perturbation becomes

$$h_{ij}(t, d_L) = -\frac{4G}{rc^4}\frac{\mu M}{d_L} \begin{pmatrix} \cos(2\omega t') & \sin(2\omega t') & 0 \\ \sin(2\omega t') & -\cos(2\omega t') & 0 \\ 0 & 0 & 0 \end{pmatrix}, \tag{1.18}$$

where $t' = t - d_L/c$ denotes the retarded time, and we define the reduced mass, $\mu = (m_1 m_2)/M$. Equation (1.18) shows that binary systems emit GWs at twice their orbital frequency – an excellent approximation at leading order – with an amplitude proportional to M/d_L. The amplitude of gravitational radiation is also inversely proportional to the orbital separation r. Since physical objects have finite radii R and cannot orbit closer than roughly $r \gtrsim 2R$ without merging, the strongest sources of gravitational radiation are those with high compactness M/R, namely, binaries composed of BHs or NSs.

The GW luminosity, as given by Eq. (1.14), evaluates for a circular binary to

$$\frac{dE_{\rm GW}}{dt} = \frac{32}{5}\frac{G}{c^5}\mu^2 r^4 \omega^6. \tag{1.19}$$

The Newtonian orbital energy of the binary is $E = -GM\mu/(2r)$. As the system emits gravitational radiation, it loses orbital energy and undergoes an inspiral, characterized by a gradual increase in the orbital frequency and a corresponding decrease in the separation. Assuming the energy loss is adiabatic, we can use Kepler's third law, $r^3 = GM/\omega^2$, to eliminate r in favor of ω. By enforcing energy balance, we obtain the so-called *chirp* formula for the evolution of the orbital frequency:

$$\dot{\omega} = \left(\frac{96}{5}\right)\left(\frac{G\mathcal{M}_c}{c^3}\right)^{5/3}\omega^{11/3}, \tag{1.20}$$

where the chirp mass is defined as $\mathcal{M}_c = (\mu^3 M^2)^{1/5}$. This relation describes the evolution of the system as an inspiral: the orbital frequency increases (*chirps*), while the orbital separation shrinks in accordance with Kepler's law. Equation (1.20) can be integrated to obtain the GW frequency evolution

$$f_{\rm GW}(\tau) = \frac{1}{\pi}\left(\frac{5}{256}\frac{1}{\tau}\right)^{3/8}\left(\frac{G\mathcal{M}_c}{c^3}\right)^{-5/8} \simeq 18.2\ \text{Hz}\left(\frac{1s}{\tau}\right)^{3/8}\left(\frac{30M_\odot}{\mathcal{M}_c}\right)^{5/8}, \tag{1.21}$$

where $\tau = t_{\rm c} - t$ and t_c is the coalescence time. Inverting this equation, we can estimate the time to coalescence of a system emitting at a given GW frequency:

$$\tau = \frac{5c^5\left(f_{\rm GW}\pi\right)^{-8/3}}{256\left(G\mathcal{M}_c\right)^{5/3}} \simeq 3\ \text{s}\left(\frac{30M_\odot}{\mathcal{M}_c}\right)^{5/3}\left(\frac{10\ \text{Hz}}{f_{\rm GW}}\right)^{8/3}. \tag{1.22}$$

This evolution is the leading-order (*Newtonian*) term in a perturbative expansion in the velocity of the binary components. As the separation between the binary objects decreases and their velocities increase, entering the relativistic regime, this approximation becomes increasingly inaccurate. Higher-order corrections in this expansion are the subject of post-Newtonian (PN) theory [105–107] and provide a more accurate description of the binary inspiral at smaller separations.

The GW polarizations emitted by the binary system are given at leading PN order by [101]

$$\begin{aligned} h_+(\tau) &= \frac{1}{d_L}\left(\frac{G\mathcal{M}_c}{c^2}\right)^{5/4}\left(\frac{5}{c\tau}\right)^{1/4}\left(\frac{1+\cos^2\iota}{2}\right)\cos[\Phi(\tau)], \\ h_\times(\tau) &= \frac{1}{d_L}\left(\frac{G\mathcal{M}_c}{c^2}\right)^{5/4}\left(\frac{5}{c\tau}\right)^{1/4}\cos\iota\sin[\Phi(\tau)], \end{aligned} \tag{1.23}$$

where the GW phase $\Phi(\tau)$ is defined as

$$\Phi(\tau) = \int_0^\tau d\tau' 2\pi f_{\rm GW}\left(\tau'\right) = -2\left(\frac{5G\mathcal{M}_c}{c^3}\right)^{-5/8}\tau^{5/8} + \Phi_0, \tag{1.24}$$

with $\Phi_0 = \Phi(\tau = 0)$ an integration constant equal to the value of Φ at coalescence. Here, we have relaxed the assumption that the GW propagates along the z-axis. As a result, the waveform depends on the orientation of the binary relative to the observer. This dependence is encoded in the angles (ι, Φ_0) which describe the binary's inclination angle, with respect to the direction perpendicular to the orbital plane, and the azimuthal direction to the observer, respectively. As seen from Eq. (1.23), the GW signal is strongest when the source is viewed *face-on* ($\iota = 0$) or *face-off* ($\iota = \pi$), and weakest near an *edge-on* orientation ($\iota = \pi/2$).

For GW signals from compact binaries, the two polarizations are often combined and expanded in the basis of -2 spin-weighted spherical harmonics ${}_{-2}Y_{\ell m}$ [108, 109],

$$h = h_+ - ih_\times = \sum_{\ell=2}^{\infty} \sum_{m=-\ell}^{\ell} h_{\ell m}(t) {}_{-2}Y_{\ell m}(\iota, \varphi), \tag{1.25}$$

where $h_{\ell m}$ are the complex *modes* or *harmonics* of the gravitational radiation. This decomposition separates the dependence of the waveform on inclination and a phase angle, so that the modes $h_{\ell m}$ only depend on the remaining binary parameters. Rather than the phase at coalescence, the azimuthal angle is often defined as $\varphi = \pi/2 - \varphi_{\rm ref}$, where $\varphi_{\rm ref}$ is the phase at a reference frequency $f_{\rm ref}$ [110]. The $(\ell, m) = (2, 2)$ mode is typically dominant, while the others are referred to as subdominant or higher-order modes. As shown in Eq. (1.18), the leading-order GWs are emitted at twice the orbital frequency. More generally, during the early inspiral, the instantaneous frequency $f_{\ell m}$ of each mode $h_{\ell m}$ is related to the orbital frequency of the binary $f_{\rm orb}$ by $f_{\ell m} \simeq m f_{\rm orb}$ [106].

The multipolar structure of the waveform depends on both the intrinsic properties of the binary and its orientation relative to the observer. For equal-mass, nonspinning binaries, symmetry under rotations ($\varphi \to \varphi + \pi$) requires that only modes with even m are non-zero [106], with the $(2, 2)$ mode being the dominant. As the mass ratio becomes more unequal, the $(3, 3)$ mode and subsequent modes with $\ell = m$ gain increasing importance [106, 111–113]. In systems with high mass ratios and large negative spin on the primary BH, or with comparable masses but large spin differences, the $(2, 1)$ mode can also contribute appreciably [113–115]. Source orientation also affects the observed higher-mode content: due to the angular structure of the spin-weighted spherical harmonics, face-on/off configurations primarily exhibit even-m modes – especially the $(2, 2)$ mode – while systems viewed edge-on have enhanced contributions from higher modes with odd m [113]. Incorporating higher-order modes in waveform models helps break parameter degeneracies, particularly between inclination and luminosity distance, and leads to more precise estimates of source properties [116–120].

Spin effects

Black-hole spins in merging binaries also imprint distinctive signatures in the orbital dynamics and waveforms. If the BH spins are aligned (parallel or anti-parallel) with the orbital angular momentum, the orbital plane remains fixed, and the GW emission is a simple chirp with steadily increasing frequency and amplitude until merger, qualitatively similar to that of non-spinning binaries. In the aligned-spin case, the dominant spin dependence of the waveform is encoded in the effective spin parameter $\chi_{\rm eff}$ (5) [7, 8]. For binaries with positive $\chi_{\rm eff}$ the spin-orbit coupling delays the onset of the plunge compared to the non-spinning case (*hang-up* effect), while binaries with negative $\chi_{\rm eff}$ merge at larger separation and lower frequency [121].

By contrast, a misalignment between the spins and the orbital angular momentum induces relativistic spin-orbit precession [122, 123]: the orbital angular momentum and spin vectors precess around the nearly conserved total angular momentum $\boldsymbol{J}$ (with $\boldsymbol{J} = \boldsymbol{L} + \boldsymbol{S}_1 + \boldsymbol{S}_2$), resulting in a more complex waveform characterized by pronounced amplitude and phase modulations. These modulations occur on a precession timescale $T_{\rm prec}$, associated to the change in the direction of the orbital plane, which is typically larger than the orbital timescale $T_{\rm orb}$, and smaller than the radiation-reaction (RR) timescale $T_{\rm RR}$, which characterizes the secular shrinking of the orbit due to GW emission [122, 124, 125]. In configurations where $\boldsymbol{J} \simeq 0$, the system can undergo *transitional precession* [122], a regime in which the directions of the spin and orbital angular momentum vectors drastically change during the evolution. Such cases are expected to be rare among LVK detections due to the fine-tuned parameters required.

In an inertial frame, the strong amplitude and phase modulations induced by spin precession can significantly complicate waveform modeling. However, precessional effects can be minimized in a non-inertial reference frame that tracks the precession of the orbital plane (*co-precessing* frame) [126–130]. In this frame, the GW signal from a spin-precessing binary resembles that of an aligned-spin system, greatly simplifying its modeling. The transformation from the inertial to the co-precessing frame is described by a set of three Euler angles $\{\alpha(t), \beta(t), \gamma(t)\}$, which parametrize the time-dependent orientation of the orbital plane. A widely used approximation for modeling precessing binaries, motivated by this intuition, is the *twisting-up* approach [126, 130–139]. In this method, an aligned-spin (or approximately aligned-spin) waveform in the co-precessing frame, $h^{\rm CP}_{\ell m}$, is *twisted* using the Euler angles to approximately account for the effects of precession:

$$h_{\ell m} = \sum_{m=-\ell}^{\ell} h^{\rm CP}_{\ell m'} e^{-im\alpha(t)} e^{-im'\gamma(t)} d^{\ell}_{mm'}(\beta(t)), \tag{1.26}$$

where $d^{\ell}_{mm'}$ are the real-valued Wigner d matrices. Different definitions of the co-

precessing frame are possible. The Euler angles can be extracted from numerical simulations by tracking the direction of dominant GW emission, which approximately corresponds to that of the orbital angular momentum [127]. Alternatively, they can be computed from PN evolutions of the orbital angular momentum and spin vectors [123, 140–144]. In particular, the relativistic angular momentum $\boldsymbol{L} = \boldsymbol{r} \times \boldsymbol{p}$ is generally *not* perpendicular to the orbital plane defined by the Newtonian angular momentum $\boldsymbol{L}_N = \mu \boldsymbol{r} \times \dot{\boldsymbol{r}}$, due to relativistic corrections from the spin-orbit coupling and higher-spin effects [123].

The behavior of the waveform modes under parity transformations is important for understanding how spin precession affects the waveform structure. Under parity, the modes transforms as [145]

$$h_{\ell m}(t, \phi) = (-1)^{\ell+m} h^*_{\ell,-m}(t, \phi + \pi), \tag{1.27}$$

where we explicitly indicate the dependence on the orbital phase ϕ. In the co-precessing frame the orbital phase dependence can be factored out of the modes,

$$h^{\rm CP}_{\ell m}(t, \phi) = \hat{h}_{\ell m}(t, \phi) e^{-im\phi} \tag{1.28}$$

which substituting in Eq. (1.27) gives

$$h^{\rm CP}_{\ell m}(t, \phi) = (-1)^{\ell+m} \hat{h}^*_{\ell,-m}(t, \phi + \pi) e^{im(\phi+\pi)} = (-1)^{\ell} \hat{h}^*_{\ell,-m}(t, \phi + \pi) e^{im\phi}. \tag{1.29}$$

If $\hat{h}_{\ell,-m}$ is independent of in-plane spin projections, then it is invariant under $\phi \to \phi + \pi$ and Eq. (1.29) implies a reflection symmetry across the orbital plane [145, 146]:

$$h_{\ell m}(t, \phi) = (-1)^{\ell} h^*_{\ell -m}(t, \phi). \tag{1.30}$$

This symmetry is respected by non-precessing binaries, while for spin-precessing systems it is broken even in the co-precessing frame by the presence of in-plane spin effects [146]. As a result, the modes in the co-precessing frame can be decomposed in contributions that transforms symmetrically and anti-symmetrically under orbital-plane reflection:

$$h^{\rm sym}_{\ell m} = \frac{h^{\rm CP}_{\ell m} + (-1)^{\ell} h^{\rm CP}_{\ell,-m}}{2}, \qquad h^{\rm asym}_{\ell m} = \frac{h^{\rm CP}_{\ell m} - (-1)^{\ell} h^{\rm CP}_{\ell,-m}}{2}. \tag{1.31}$$

The antisymmetric contributions lead to an imbalance in the GW energy emitted above and below the orbital plane. This asymmetry plays a key role in determining the net linear momentum carried by the GWs and can result in substantial recoil (or *kick*) velocities imparted to the remnant BH after merger [146–149].

Eccentric orbits

So far, we have considered binaries in quasi-circular orbits. However, binary systems may follow eccentric or even unbound trajectories. In the bound case, the orbit is additionally characterized by its eccentricity e and a radial phase angle (or *anomaly* – the fraction of the orbital period that has elapsed since the last periastron passage), both of which are time-dependent quantities typically specified at a given reference frequency [150, 151].

Eccentricity modifies the gravitational waveform by increasing the power radiated near periastron (small separation, high velocity), and reducing it near apoastron (large separation, low velocity) resulting in amplitude and frequency modulations. The net effect is an overall increase in the radiated energy, which accelerates the orbital evolution [106]. Gravitational radiation also circularizes the orbit over time, a process that is typically very efficient [152]. As a result, most binaries are expected to have negligible eccentricity by the time they enter the sensitive frequency band of ground-based GW detectors – unless they were dynamically formed [87, 153, 154]. Unbound systems – such as hyperbolic encounters – emit GWs during a single close passage, producing a burst-like signal with no inspiral. While such events are expected to be rare, their detection would provide valuable insights into dynamical interactions in dense astrophysical environments [155].

1.2 Fundamental concepts in gravitational-wave astronomy

The first direct detection of a GW signal by the LIGO and Virgo Collaborations on September 14, 2015 marked a turning point in GW astronomy, transforming it from a theoretical pursuit into an experimental science. This landmark event, named GW150914 [45], was the culmination of decades of research in interferometric detector technology [72], sophisticated data analysis methods [156], and theoretical modeling of compact binary mergers [97]. The signal was captured by the two Advanced LIGO interferometers located in Hanford, Washington, and Livingston, Louisiana, which recorded the final moments of the merger of two BHs about $30M_\odot$ each. Separated by about 10 milliseconds in light travel time, both detectors observed a near-identical waveform, confirming the astrophysical origin of the signal. As the GW passed through the detectors, it caused a minute, oscillatory stretching and compression of spacetime, producing a time-varying differential displacement $\delta L(t)$ between the test masses suspended at the ends of each $L = 4$ km interferometer arm. This distortion induced

a measurable signal in the detector:

$$h(t) \propto \frac{\delta L(t)}{L}, \tag{1.32}$$

known as the GW *strain*. Although the merger of two stellar-mass BHs can release energy equivalent to several solar masses within less than a second, momentarily outshining all stars in the observable universe, the strain observed on Earth is incredibly small, typically $h \lesssim 10^{-21}$. This extreme weakness can be understood from the smallness of the coupling constant G/c^4, and the $1/d_L$ scaling of the GW amplitude with luminosity distance (hundreds of megaparsec for GW150914) in Eq. (1.13).

Detecting such tiny distortions poses immense experimental challenges, as the GW signal is easily masked by various sources of noise that disturb the interferometers [156]. At low frequencies (below ∼20 Hz), seismic noise dominates. It arises not only from natural sources like earthquakes, ocean waves, and storms, but also from human activity such as nearby car traffic. To mitigate this, the test masses are suspended using multi-stage pendulum systems and isolated via both passive and active vibration suppression techniques. At high frequencies (above ∼1 kHz), the sensitivity is limited by quantum shot noise, stemming from the uncertainty in photon arrival times at the interferometer output. Increasing the laser power helps reduce this uncertainty, but it introduces radiation pressure noise, an effect where fluctuating photon momentum exerts force on the mirrors, primarily affecting lower frequencies. *Squeezed light* reduces quantum uncertainties in specific quadratures, correlating shot noise and radiation pressure noise, and enables detectors to surpass the standard quantum limit within targeted frequency bands [157, 158]. The most sensitive region of the detector, around 100 Hz, is limited by thermal noise in the reflective mirror coatings, driven by residual thermal vibrations and laser heating.

Detecting signals from noisy data

Given the sensitivity of current detectors, astrophysical GW signals are often buried in the instrumental noise. Therefore, the first step in claiming a detection is to assess the presence of the GW signal within the noisy data stream. In the case of signals from compact binary coalescences, this is typically done through the matched filtering technique. The measured strain at the detector, $d(t)$, is a superposition between background noise $n(t)$ and the true GW signal,

$$d(t) = h(t) + n(t), \tag{1.33}$$

where $h(t)$ is the detector response to a GW signal. To accurately reconstruct $h(t)$, the detector must be carefully calibrated [159, 160]. Calibration involves determining the transfer function that maps the raw interferometer output to the physical strain. Uncertainties in the calibration, which affect the amplitude and phase of the recovered signal, are quantified and incorporated into the data analysis [161]. The noise $n(t)$ is commonly assumed to be a stationary, Gaussian random process on short timescales.

Given a theoretical prediction for the gravitational waveform, the detector response can be expressed as:

$$h(t) = F_+(\alpha, \delta, \psi)\; h_+(t; \iota, \varphi, d_L, \mathbf{\Lambda}, t_\mathrm{c}) + F_\times(\alpha, \delta, \psi)\; h_\times(t; \iota, \varphi, d_L, \mathbf{\Lambda}, t_\mathrm{c})\,, \tag{1.34}$$

where $F_{+,\times}$ are the antenna pattern functions [162]. They depend on the source location in the sky, given by right ascension α and declination δ, and on the polarization angle ψ, which specifies the orientation of the GW polarization axes relative to a fixed coordinate system. For a Michelson interferometer, the antenna pattern functions take the form [162]

$$\begin{aligned} F_+(\alpha, \delta, \psi) &= \frac{1}{2}\left(1 + \cos^2\alpha\right)\cos 2\delta \cos 2\psi - \cos\alpha \sin 2\delta \sin 2\psi, \\ F_\times(\alpha, \delta, \psi) &= \frac{1}{2}\left(1 + \cos^2\alpha\right)\cos 2\delta \sin 2\psi + \cos\alpha \sin 2\delta \cos 2\psi. \end{aligned} \tag{1.35}$$

Equations (1.35) assume that the wavelength of the GW is much longer than the detector arm length. This long-wavelength approximation holds for current ground-based detectors with arm lengths of about 4 km, but planned next-generation detectors, with arms an order of magnitude longer, will need to account for frequency-dependent effects [163]. The two GW polarizations h_+ and $h_\times$ depend on the intrinsic parameters of the binary $\mathbf{\Lambda}$ (e.g., component masses and spins for quasi-circular BBH systems), the orientation of the binary relative to the observer (ι, φ), the luminosity distance d_L, and the coalescence time t_c. The total mass M sets the overall timescale of the system and can be scaled out; it determines the physical frequency of the GW signal but not its intrinsic shape in dimensionless units.

Gravitational-wave searches usually rely on matched filtering, which involves comparing the data stream against a *template bank* of waveforms corresponding to different source parameters. A high level of agreement between the data and a template indicates the presence of a GW signal, as quantified by the matched filter signal-to-noise ratio (SNR) [156, 164]:

$$\mathrm{SNR} = \frac{(d \mid h)}{\sqrt{(h \mid h)}}. \tag{1.36}$$

Here, we have introduced the noise-weighted inner product between two signals $h_1(t)$ and $h_2(t)$ with Fourier transforms $\tilde{h}_1(f)$ and $\tilde{h}_2(f)$, given by [162]

$$(h_1 \mid h_2) = 4\,\mathrm{Re}\int_{f_{\mathrm{low}}}^{f_{\mathrm{high}}} \frac{\tilde{h}_1(f)\tilde{h}_2^*(f)}{S_n(f)}\mathrm{d}f, \tag{1.37}$$

where the * superscript indicates complex conjugation, and the one-sided power spectral density (PSD) of noise, $S_n(f)$, represents the variance associated with the noise distribution,

$$\langle \tilde{n}^*(f)\tilde{n}\,(f')\rangle = \delta\,(f - f')\,\frac{1}{2}S_n(f). \tag{1.38}$$

The PSD can be estimated from a long segment of data with no GW signal (*off-source*) [165], or directly from stretch of data containing a signal (*on-source*) using Bayesian methods that jointly model the GW signal and the noise [166]. The square root of the PSD defines the amplitude spectral density (ASD), which is commonly used to visualize detector sensitivity as a function of frequency.

The optimal SNR is obtained when the template waveform exactly matches the GW signal in the data:

$$\mathrm{SNR}_{\mathrm{opt}} = \sqrt{(h \mid h)}. \tag{1.39}$$

Another interpretation is that $\tilde{h}(f)/S_n(f)$ defines the optimal filter, known as the matched or Wiener filter, for extracting the signal from the noise [101, 167].

The size and density of a template bank are designed to ensure adequate coverage of the parameter space while balancing computational efficiency. Templates are placed such that the SNR loss due to finite template spacing remains below an acceptable threshold, typically ensuring that no more than approximately 10% of potential signals are lost due to discretization effects [168, 169].

A simplistic detection criterion involves filtering the data stream with a bank of predicted waveforms and identifying candidate events when the SNR exceeds a predefined threshold, based on the statistical properties of known instrumental noise. However, high SNR alone is not sufficient to claim a confident detection. To reduce the false-alarm rate and increase confidence, detections must be coincident and consistent across multiple detectors. A genuine GW signal should appear in all operating detectors with consistent arrival times and waveform parameters, accounting for detector locations and orientations. To further distinguish real signals from transient noise artifacts (*glitches*), additional signal-consistency tests are employed. One commonly used diagnostic is the χ^2 test [170], which checks whether the observed signal morphology matches that of the template across different frequency bands. In parallel, unmodeled searches – which do not rely on specific waveform templates – are also used [171, 172]. These approaches, often based on wavelet transforms or other

time-frequency methods, scan the data for coherent excess power across detectors. While less sensitive than matched filtering for well-modeled signals, unmodeled searches are more robust to unexpected or poorly understood sources.

After identifying a candidate GW signal in the data, targeted parameter estimation (PE) analyses are performed to determine the properties of its source. Since each GW measurement represents a unique, non-repeatable event, a Bayesian inference framework is more suitable than frequentist methods. The goal of Bayesian PE is to infer the posterior probability distribution $p(\boldsymbol{\lambda}|d)$ for the source parameters $\boldsymbol{\lambda}$ given the observed data d [173, 174]. This requires prior assumptions $\pi(\boldsymbol{\lambda})$, and a model for the likelihood $\mathcal{L}(d|\boldsymbol{\lambda})$, which quantifies the probability of observing the data d given a particular set of parameters $\boldsymbol{\lambda}$, and is derived from theoretical predictions of gravitational waveforms (see also Sec. 3.1). Accurate waveform models are especially crucial in PE. While a detection may still be possible with an imperfect waveform model, inaccuracies in the model can introduce systematic biases in the inferred source properties [175, 176]. Because the likelihood is rarely tractable analytically, stochastic sampling techniques are typically required. For example, Markov Chain Monte Carlo (MCMC) [177] or nested sampling [178] algorithms can generate posterior samples that approximate the target distribution. For a single event, PE analyses typically involve millions to hundreds of millions of waveform evaluations [179], making computational efficiency, in addition to accuracy, a key requirement for waveform models.

To date, approximately 90 GW events have been reported by the LVK Collaboration [46–49], consisting primarily of BBH mergers, along with a smaller number of binary neutron star (BNS) [180, 181] and neutron star-black hole (NSBH) mergers [182, 183]. The event GW170817 [180] was particularly significant as it was the first to be observed both in GWs and across the electromagnetic spectrum [184], marking the advent of multi-messenger astronomy with GWs.

At the time of writing, over 200 additional candidate events from the fourth observing run have been announced [185]. These candidates are released publicly within minutes of detection, along with their sky localization, to enable prompt electromagnetic follow-up when necessary. Their statistical significance and source properties will be assessed in detail and published in the upcoming fourth gravitational-wave transient catalog (GWTC-4).

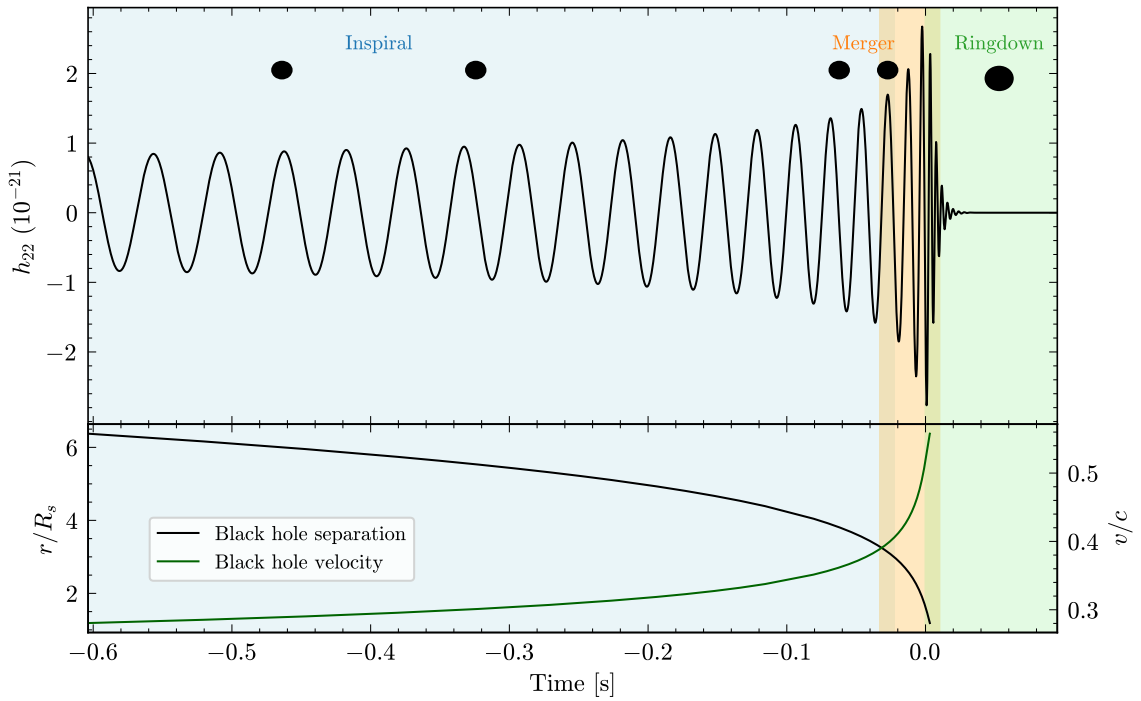

Figure 1.3: Inspiral, merger, and ringdown of a binary black hole waveform compatible with GW150914, generated using the `SEOBNRv5HM` model [2].

1.3 Gravitational waveform models for binary black hole mergers

Gravitational-wave detection and PE methods rely on predictions of gravitational waveforms. In the following section, we describe in more detail the morphology of BBH signals, the techniques used to develop state-of-the art waveform models for these systems, and their application in current GW astronomy.

1.3.1 Anatomy of the gravitational waveforms: inspiral, merger, and ringdown

Gravitational waves from BBH coalescences exhibit a characteristic inspiral-merger-ringdown (IMR) structure, as shown in Fig. 1.3. The inspiral phase is the long, chirping signal produced as the two compact objects orbit each other and gradually spiral inward under GW emission. During this phase, the waveform is a nearly sinusoidal oscillation of increasing frequency and amplitude, well-described by weak-field, slow-motion approximations such as the PN expansion.

As the binary's separation shrinks and the orbital velocity approaches relativistic

speeds, the system enters the merger phase. The PN approximation is typically valid only for orbital separations much larger than the innermost stable circular orbit (ISCO), the smallest radius at which stable orbital motion can exist. A simple approximation of the transition frequency can be obtained by considering a test particle orbiting a Schwarzschild BH of mass M. In this case the ISCO is located at $r = 6GM/c^2 = 3R_s$, and it corresponds to a GW frequency given by:

$$f_{\rm ISCO} = \frac{1}{6\sqrt{6}\pi}\frac{c^3}{GM} \simeq 440 \text{ Hz} \left(\frac{10M_\odot}{M}\right). \tag{1.40}$$

As the system approaches this limit, the orbital velocity increases sharply and strong-field effects dominate, marking the end of the inspiral and the onset of merger. Here, the BHs rapidly coalesce, generating a short-lived, intense burst of gravitational radiation near the waveform's peak amplitude. Finally, after the merger, the newly formed BH settles down to a stationary Kerr state by emitting damped oscillatory GWs named *quasinormal modes* (QNMs), in the so-called *ringdown* stage. The ringdown waveform is a sum of exponentially decaying sinusoids whose frequency and decay times are determined solely by the remnant's mass and spin, independent of the prior merger dynamics. At even later times, GW tails have been predicted [186, 187], but they remain negligible for the sensitivity of current detectors.

Different techniques are applicable to modeling each stage of the coalescence. In the early inspiral (weak-field regime), one can employ analytical perturbative schemes to obtain approximate solutions to Einstein's equations. The most common is the PN expansion [105–107], which assumes slow-motion and weak-field, expanding the equations of motion and radiation in powers of (v/c). State-of-the-art PN calculations have reached high orders: 4PN order in the conservative dynamics [188–192] (with partial results at 5PN and above [193–195]), 4.5PN in the energy flux, and 4PN in the $(2, 2)$ mode waveform beyond the leading quadrupole term [196, 197], for nonspinning binaries on circular orbits. The PN expansion accurately describes the early inspiral regime and is crucial for generating approximate waveforms for this phase of the signal. However, the accuracy of the PN approximation degrades as the orbit becomes more relativistic near merger.

An alternative weak-field expansion is the post-Minkowskian (PM) approximation [198–205], which expands the two-body problem in powers of the gravitational coupling G (perturbation about flat Minkowski spacetime), without assuming $v \ll c$. The PM approach is particularly interesting since an $(n + 1)$ PM-order Hamiltonian includes all information up to the nPN order, and additional weak-field/high-velocity information from infinitely higher PN orders, making it suitable for systems with high velocities or large eccentricities at fixed periastron distances [206]. Post-Minkowskian

calculations have gained renewed interest thanks to connections with quantum-field-theory–based methods, developed over the last several decades to address precision-collider physics. Significant progress has been made on high-order PM computations using both scattering amplitudes [207–209] and worldline methods [210–214], reaching the nonspinning (conservative) 4PM order [208, 210] (plus partial contributions at 5PM [215]) and spinning 5PM order [212, 216–222]. However, the use of PM computations to inform waveform models for bound-orbit binaries has been limited until recently [3, 223]. We will return to this topic in Sec. 2.3.

A third analytic approach is the gravitational self-force (GSF) formalism [224–234], relevant in the extreme mass-ratio regime, in which one body is much less massive than the other. Self-force theory treats the small object as a perturbation of the spacetime of the large object, usually a massive BH, expanding Einstein's equations in powers of the mass ratio $\epsilon = m_2/m_1$ (with $\epsilon \ll 1$). The spacetime metric is written as the background metric of the primary (e.g., a Kerr BH) plus perturbations due to the smaller secondary; these perturbations include the GWs emitted and also exert a self-force on the smaller object, driving its inspiral. Recent calculations produced waveforms for nonspinning compact binaries undergoing quasicircular inspirals at second order in the self-force expansion (2GSF) [233, 234]. Gravitational self-force waveforms and orbital dynamics are very accurate for binaries with large mass ratios, making them especially crucial for modeling extreme mass-ratio inspirals detectable by space-based GW detectors such as LISA. Although GSF is formally an expansion in a small mass ratio, its results can inform the comparable-mass regime as well. In fact, studies have found that certain GSF-derived quantities remain surprisingly accurate even for comparable masses [233, 234].

Overall, the PN, PM and GSF approximations each tackle the two-body problem from different perturbative limits, and their cross-over can be leveraged to improve waveform models, as well as to derive new analytical results [193, 235]. However, by themselves they cannot capture the full IMR signal for arbitrary masses - their realm is the weak-field inspiral (PN, PM) or extreme mass ratio limit (GSF).

After the merger of two BHs, the remnant BH rapidly settles into a stationary Kerr configuration through a phase known as the ringdown. At sufficiently late times, the GW signal is well described by a superposition of exponentially damped sinusoids, corresponding to the BH's QNMs [236–240], with complex amplitudes $A_{\ell mn}$:

$$h_{\ell m}(t) \simeq \sum_{n=0}^{\infty} A_{\ell mn} e^{-i\sigma_{\ell mn} t}. \tag{1.41}$$

The (complex) QNM frequencies $\sigma_{\ell mn}$ are the natural oscillations of a perturbed BH, determined by solving the linearized Einstein equations around the Schwarzschild

or Kerr metric, subject to outgoing-wave conditions at spatial infinity and ingoing conditions at the horizon [241]. The resulting perturbation equations are known as the Regge-Wheeler and Zerilli equations [242, 243], for Schwarzschild BHs, and the Teukolsky equation [237], for Kerr BHs. Solutions to the Teukolsky equation are naturally expressed in terms of spin-weighted *spheroidal* harmonics related to the Kerr background, rather than the spin-weighted *spherical* harmonics used in Eq. (1.25), so the parameters $\sigma_{\ell mn}$ and $A_{\ell mn}$ are related to the Kerr QNM frequencies and amplitudes by a transformation between the two bases [244].

Astrophysical BHs are expected to carry no electric charge because of neutralization from surrounding material, which happens on a time scale much shorter than the one probed by GW observations [245, 246]. For electrically neutral BHs in GR, the QNM frequencies are determined uniquely by the mass and spin of the remnant object, making the ringdown stage a promising ground for testing the no-hair conjecture. Notably, the measurement of at least two QNMs allows to test the consistency between the estimates of mass and spin of the remnant object across multiple frequencies, an idea known as BH spectroscopy [247–251]. On the other hand, the complex amplitudes $A_{\ell mn}$ depend on the previous merger dynamics, and are usually determined from NR simulations. We will revisit this topic in Chapter 4.

1.3.2 Numerical relativity and surrogate models

As the binary approaches merger, its dynamics enter a highly nonlinear regime where perturbative approximations break down, requiring to solve the full Einstein's field equations numerically. *Numerical relativity* (NR) is employed to solve Einstein's equations on a computer grid (typically in a 3+1 dimensional spacetime decomposition), capturing the complex behavior during the late inspiral, merger, and ringdown phases. After decades of development, NR achieved a major breakthrough in the mid-2000s when the first stable BBH merger simulations were produced [252–254]. In these simulations, two BHs were evolved through few orbits, then seen to plunge and merge, and the code extracted the gravitational waveform emitted during the entire process.

Although computationally expensive, NR is indispensable for producing accurate waveforms in the strong-field regime, and is considered the ground-truth for GW physics of mergers, as it solves Einstein's equations with the main approximation being numerical discretization. Numerical-relativity waveforms include all non-perturbative effects, making them indispensable for validating and calibrating semi-analytical models. However, NR comes with significant challenges. Simulating a binary coalescence requires supercomputer-level resources, careful handling of BH singularities or NS matter, and maintaining high accuracy over many orbital cycles. A single high-precision NR simulation may take weeks to months of run-time. Moreover, the parameter

space (mass ratio, spins, orbital eccentricity) is vast, and a dense coverage with NR simulations is unfeasible.

Current NR efforts have produced catalogs of BBH simulations [255–259], covering mass ratios roughly from $q = 1$ up to about $q = 20$ and a wide range of spin configurations, including systems with misaligned spins. Most NR simulations to date have focused on binaries in quasi-circular orbits, but recent efforts have been invested in simulating binaries in eccentric orbits [150,257,260–264], as well as dynamical captures and scattering configurations [265–270]. High mass ratios, $q \gtrsim 20$, are challenging for NR to handle due to resolution requirements arising from the disparate length scales involved [271]. Likewise, long-duration inspirals – such as those to be observed by future GW detectors – are out of reach because evolving thousands of orbits is computationally unfeasible. These limitations mean NR alone cannot provide a dense coverage of waveforms for direct use in GW data analysis.

Despite these challenges, NR has been crucial to GW astronomy. The first GW event, GW150914, was analyzed using waveform models calibrated against NR simulations, and NR results directly confirmed that the signal was consistent with GR's predictions for a BBH merger [45, 272]. Moreover, NR waveforms continue to serve as the training data for building fast surrogate models, and for calibrating and validating semi-analytic waveform models (`IMRPhenom` and EOB, introduced in the next section).

For data analysis applications, such as GW searches and PE, we require fast, continuous models of the GW signal that cover the entire IMR stages and can be generated in fractions of a second. For comparable-mass binaries, neither pure PN/PM approximations (valid only in the inspiral) nor NR only (too expensive and sparse in coverage) meet these needs. Therefore, several classes of waveform models have been developed to bridge this gap, combining analytical approximation methods with calibration to numerical results. These models aim to reproduce the full IMR waveform accurately while being fast to evaluate and valid across a broad range of binary parameters. In general, they are constructed by incorporating PN and other perturbative results for the early inspiral, NR information for the nonlinear merger-ringdown, and often some phenomenological ansatz or resummation technique to smoothly connect the pieces. Below we provide an overview of the main modeling approaches: NR surrogates, phenomenological models, and effective-one-body (EOB) models.

Numerical-relativity surrogate models

Numerical-relativity surrogates [135, 273–282] are data-driven interpolated models built directly from NR waveform datasets. The core idea is to perform a set of NR

simulations at selected points in the parameter space, and then construct an efficient representation that can produce waveforms for arbitrary parameter values within that range without rerunning NR. This is typically achieved by decomposing the training waveforms (either in time or frequency domain) into a suitable orthonormal basis, and then fitting the coefficients of that basis as smooth functions of the binary parameters. The result is a model that is fast to evaluate and highly faithful, as it directly interpolates NR data.

One key limitation of NR surrogates is that NR waveforms are often short in duration. A typical NR simulation might cover the last ~ 20 orbits before merger, which corresponds to a starting frequency of approximately 20-30 Hz for systems in the LVK mass range ($M \sim 60M_\odot$). To extend the waveform to lower frequencies and model the full inspiral, some surrogate models *hybridize* the NR simulations with PN or EOB waveforms at early times [276, 281, 282], allowing the surrogate to cover the entire frequency band of ground-based detectors. The other restriction of NR surrogates is that they are limited to regions of parameter space where enough NR waveforms are available, though surrogate models can sometimes extrapolate beyond their training region (e.g., to slightly higher mass ratios or spins) with reasonable success. Numerical-relativity surrogates have demonstrated excellent accuracy within their training domains, often outperforming semi-analytical models in regions where NR data exist, as they interpolate between full NR solutions. For instance, `NRSur7dq4` was shown to be an order of magnitude more accurate than earlier semi-analytical models [135], with errors comparable to the numerical error of the underlying NR simulations.

The current state-of-the-art NR surrogate model is `NRSur7dq4` [135], which models spin-precessing binaries up to mass ratio 4 and spin magnitudes up to 0.8. The length of the training NR data restricts its use to binaries with total masses $\gtrsim 60M_\odot$ for a starting frequency of 20 Hz. Surrogate models for BBHs with aligned-spins are available up to higher mass ratios. State-of-the art models include `NRHybSur3dq8` [276], valid for binaries up to mass ratio 8 and recently extended to include GW memory effects [282], and `NRHybSur2dq15` [281], which models single-spin binaries up to $q = 15$. Both models are hybridized with PN/EOB waveforms in the early inspiral. A first surrogate model for eccentric BBHs is `NRSur2dq1Ecc` [279], which covers nonspinning, equal-mass systems with initial eccentricities up to 0.2. In addition to waveform models, NR surrogates have also been developed to predict remnant properties such as the final BH mass, spin, and kick velocity [135, 279, 283], and ringdown amplitudes [284–286].

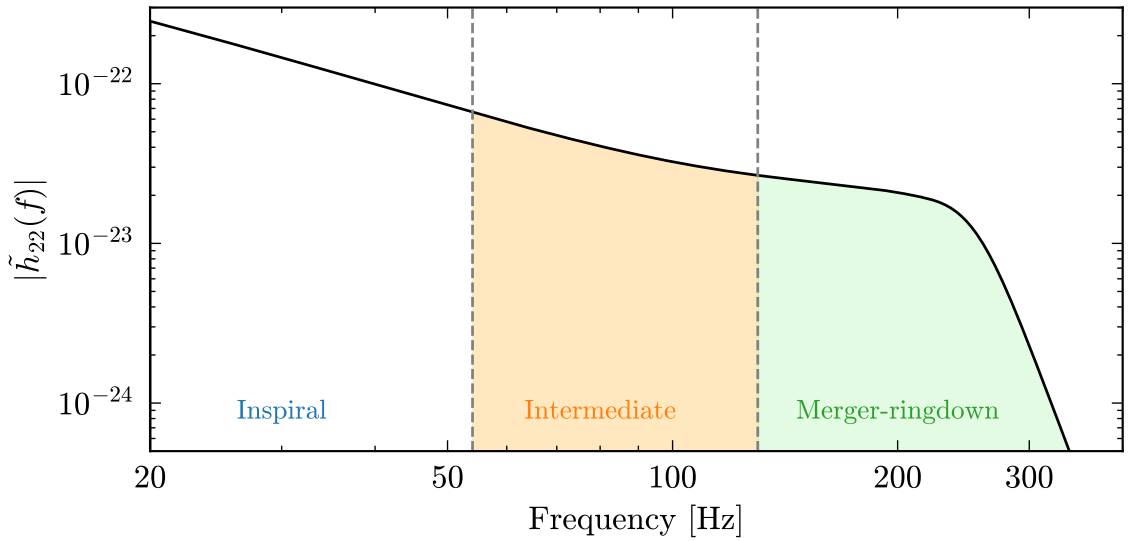

Figure 1.4: Absolute value of the frequency-domain amplitude for a binary black hole waveform compatible with GW150914, generated using the `IMRPhenomD` model [291].

1.3.3 Phenomenological waveform models

Inspiral-merger-ringdown phenomenological models, commonly referred to as `IMRPhenom` [8, 131, 136, 137, 287–303], take a different approach. They assume an analytic ansatz for the waveform's functional form (either in the frequency domain or in the time domain), and calibrate the parameters of this ansatz to NR simulations. The ansatz is designed to be flexible enough to represent the main features of the IMR signal, but is not directly derived from first-principles dynamics (hence *phenomenological*). For example, an `IMRPhenom` model might represent the frequency-domain GW amplitude as a piecewise function: a PN-like series in the low-frequency inspiral regime, a polynomial through the intermediate region, and a Lorentzian for the high-frequency ringdown phase. The coefficients in these functional forms are determined by fitting to a set of hybrid PN/EOB and NR waveforms. As an example, Fig. 1.4 illustrates the frequency-domain structure of an `IMRPhenomD` waveform, highlighting the inspiral, intermediate, and merger-ringdown regions.

By fitting to a large catalog of NR simulations and EOB waveforms, `IMRPhenom` models capture the effective dependencies of the waveform on physical parameters. The final product is a closed-form frequency-domain or time-domain waveform model that can be generated in milliseconds, making it highly efficient for data analysis applications. `IMRPhenom` models have been extensively used for PE within the LVK Collaboration. Their accuracy depends on the density and quality of the NR/EOB waveforms used for calibration and on the flexibility of the chosen functional forms.

Modern IMRPhenom models, such as those in the the IMRPhenomX and IMRPhenomT families, achieve excellent agreement with NR within their calibration regions, with typical mismatches on the order of 10^{-4} to 10^{-2} for comparable-mass binaries. However, like any fit, the model may incur systematic errors if one ventures to extreme corners of parameter space not covered by the calibration data. The phenomenological approach is also less directly tied to first-principles physics compared to EOB models; it does not explicitly impose theoretical constraints except those implicit in the NR data. This may complicate accurately modeling more complex waveform morphologies, such as those arising from spin precession and eccentricity, for which finding closed-form expressions is more difficult.

Early phenomenological models were developed for nonspinning binary systems [304]. Later versions – IMRPhenomB [289], IMRPhenomC [8], and IMRPhenomD [290, 291] – incorporated aligned-spin effects. The *twisting-up* technique was first applied to build the spin-precessing model IMRPhenomP from IMRPhenomC [131], and later applied to IMRPhenomD to produce IMRPhenomPv2 [305] and IMRPhenomPv3 [293]. Higher-order modes were incorporated into IMRPhenomHM [292] by extending IMRPhenomD, albeit without direct calibration to NR simulations; a spin-precessing extension of this model, IMRPhenomPv3HM [294], was later developed. More recently, a new generation of IMRPhenom waveform models has offered significant improvements in accuracy. These include IMRPhenomXAS [296] for the dominant harmonic of aligned-spin binaries, IMRPhenomXHM [297] including higher modes calibrated to NR simulations, and its spin-precessing extension IMRPhenomXPHM [137]. Recent advancements in the IMRPhenomXPHM model have included explicit calibration to spin-precessing NR simulations, leading to the development of the IMRPhenomXO4a model [300, 301, 306], and improvements in modeling spin-precession dynamics via the numerical integration of the PN spin-precession equations [302]. In parallel, a time-domain phenomenological model, IMRPhenomTPHM [136, 298, 299], has been developed to overcome limitations of the stationary-phase approximation in frequency-domain models, offering more accurate modeling of spin-precessing binaries. Within the IMRPhenomT family, recent efforts have focused on extending the model to eccentric BBH systems with aligned spins [303], and including GW memory effects [307].

1.3.4 Effective-one-body waveform models

The EOB approach [308–312] is a semi-analytical framework developed to provide a unified description of the motion and radiation of coalescing compact binaries throughout their entire evolution – including the late inspiral, merger, and ringdown – by leveraging available information about the two-body problem, particularly (but not exclusively) from PN theory. The key strategies to achieve this goal are essentially

two:

- The use of various resummation techniques, which involve replacing PN results – expressed as polynomials in powers of v/c – with suitable non-polynomial functions. These resummations are designed to capture expected non-perturbative features of the exact solution and reproduce the original PN-expanded expressions when re-expanded.
- The calibration of several free parameters – either analytically unknown higher-order terms or coefficients specifically added in the EOB description – to the non-perturbative data provided by NR simulations.

The EOB approach, even in its early forms, could produce complete IMR waveforms for comparable-mass binaries [309], something PN or perturbation theory alone could not do. In fact, the EOB approach successfully predicted qualitative features of the merger dynamics, such as the simplicity of the merger signal and the sharp frequency rise at plunge, later confirmed by NR [313]. An EOB waveform model consists of three main ingredients:

- The Hamiltonian, which describes the conservative binary dynamics.
- The RR force, which accounts for the energy and angular momentum losses due to GW emission.
- The IMR waveform modes, built upon improved PN resummations for the inspiral part, and functional forms calibrated to NR waveforms for the merger-ringdown signal.

A cornerstone of the EOB approach is the mapping of the real two-body dynamics to that of an effective particle, either a test mass or a test spin, moving in a deformed Schwarzschild or Kerr background. The deformation is parametrized by the symmetric mass ratio $\nu = \mu/M$, with $0 \leq \nu \leq 1/4$. More specifically, the real (or EOB) Hamiltonian, $H_{\rm EOB}$, is related to the effective Hamiltonian, $H_{\rm eff}$, by [308]

$$H_{\rm EOB} = M\sqrt{1 + 2\nu\left(\frac{H_{\rm eff}}{\mu} - 1\right)}. \tag{1.42}$$

This energy map provides a compact resummation of PN information within the EOB Hamiltonian using relatively few terms. Through this mapping, EOB models naturally incorporate the test-mass limit, while also including all available PN information for comparable-mass systems. Crucially, by incorporating perturbative results in a resummed form, EOB models remain more accurate than a straightforward PN series in the strong-field regime, close to merger, where the PN approximation breaks down.

In the center-of-mass frame, the EOB equations of motion are:

$$\frac{d\boldsymbol{r}}{dt} = \frac{\partial H_{\rm EOB}}{\partial \boldsymbol{p}}\,, \qquad \frac{d\boldsymbol{p}}{dt} = -\frac{\partial H_{\rm EOB}}{\partial \boldsymbol{r}} + \boldsymbol{\mathcal{F}}\,, \qquad \frac{d\boldsymbol{S}_{1,2}}{dt} = \frac{\partial H_{\rm EOB}}{\partial \boldsymbol{S}_{1,2}} \times \boldsymbol{S}_{1,2}, \tag{1.43}$$

where $\boldsymbol{r}$ and $\boldsymbol{p}$ are the canonical variables corresponding to the relative position and momentum, $\boldsymbol{S}_i$ $(i = 1, 2)$ are the spins of the two objects, and $\boldsymbol{\mathcal{F}}$ is the RR force, which accounts for the energy and angular-momentum losses in the system due to the emission of GWs. In the nonspinning limit, where the coordinates reduce to (r, ϕ, p_r, p_ϕ), the effective Hamiltonian reads [308, 310]

$$H_{\rm eff} = \sqrt{A(r)\left[\mu^2 + A(r)\bar{D}(r)\,p_r^2 + \frac{p_\phi^2}{r^2} + Q(r, p_r)\right]}\,, \tag{1.44}$$

where $A(r)$ and $D(r)$ are effective metric potentials that reduce to their Schwarzschild values in the test-mass limit and are modified by PN corrections depending on the symmetric mass ratio ν. The potential $Q(r, p_r)$ is a non-geodesic correction introduced at 3PN order [310] to preserve the mapping (1.42), and it vanishes in the test-mass limit. These potentials are fully known up to 4PN order, with partial results available at 5PN and beyond [144, 314]. Unknown higher-order PN contributions – particularly to $A(r)$ – can be calibrated to NR simulations to improve accuracy in the strong-field regime.

In the original EOB formulation [309], the RR force was modeled using a Padé resummation of the PN-expanded energy flux at 2.5PN order, following the approach of Ref. [315]. Later developments expressed the quasi-circular RR force as a sum of factorized and resummed waveform modes [316–319], which are also used to construct the inspiral-plunge waveform. To further improve accuracy during the plunge phase – where radial motion becomes dominant – numerically tuned non-quasicircular (NQC) corrections are also applied to the waveform modes [112, 316, 320].

As the binary approaches merger, the inspiral-plunge waveform is smoothly matched to a merger-ringdown waveform, at a suitable matching time $t = t_{\rm match}$, typically near the peak of the EOB orbital frequency [309]. Early EOB models represented the ringdown signal as a superposition of QNMs of the remnant BH [112, 114, 132, 133, 309, 311, 313, 321–325]. More recently, a factorized waveform ansatz with NR-informed fits of the amplitude and phase has become standard [326].

Figure 1.5 provides an illustration of the EOB dynamics and waveform for an aligned-spin binary with mass ratio $q = 4.67$ and dimensionless spins $\chi_1 = -0.5$, $\chi_2 = 0.8$, computed using the `SEOBNR-PM` model (see Sec. 2.3). The figure shows the time evolution of the dynamical variables and the dominant $(\ell, m) = (2, 2)$ mode of the gravitational waveform. From top left, the panels show, using dimensionless EOB

variables (8): the radial separation r, orbital phase ϕ, radial momentum p_r, angular momentum p_ϕ, the real part of the $(2,2)$ mode, and its instantaneous frequency. The waveform is constructed by smoothly matching the inspiral-plunge signal to a ringdown model at the matching time $t = t_{\rm match}$, which corresponds to $t = 0$ and is marked by a vertical dashed line; the dotted line indicates the crossing of the ISCO radius. The red dashed curve in the frequency panel shows $2M\Omega$, which closely tracks the $(2,2)$-mode GW frequency $M\omega_{22}$ almost until merger.

Modern EOB models have been extended to capture a wide range of physical effects, including spins (both aligned and generic orientations) [132–134, 138, 139, 311, 312, 323, 325, 327–338], higher-order modes [2, 112, 113, 339, 340], orbital eccentricity [341–347], and tidal effects in NSBH and BNS systems [348–356]. The analytical nature of the EOB framework also makes it uniquely capable of integrating inputs from approximation schemes beyond PN theory, including PM and GSF results [3, 206, 223, 266, 357–366]. Its flexibility has also enabled the introduction of parametrized deviations from GR, allowing EOB models to be used for theory-agnostic tests of gravity [6, 367–370]. In addition, the EOB formalism has been successfully extended to specific modified theories of gravity, including scalar-tensor theories and Einstein-scalar-Gauss-Bonnet gravity [371–375].

EOB waveforms are natively expressed in the time domain, which provides a direct connection between the source dynamics and gravitational radiation, and naturally accommodates time-dependent effects such as spin precession and orbital eccentricity. By modeling both the orbital dynamics and gravitational radiation, EOB models can also be validated through comparisons with NR using gauge-invariant quantities like the binding energy and fluxes [358, 362, 376–378], periastron advance [379, 380], and scattering angles [206, 265–270, 365]. However, this also makes EOB models computationally more expensive than frequency-domain `IMRPhenom` waveform models. To mitigate this, techniques such as the post-adiabatic (PA) approximation [381–383] have been employed to accelerate the integration of the EOB dynamics. Reduced-order modeling and surrogate techniques, similar to those used to build NR surrogates, can also be applied to speed-up EOB waveform generation [2, 384–389].

There is considerable freedom in modeling and resumming the EOB Hamiltonian, RR force, and GW modes. Variations in these elements – along with differences in gauge choices, deformations of the EOB potentials, treatment of spin effects, and calibration strategies against NR – have led to the development of two main EOB families: `SEOBNR` and `TEOBResumS` (see, e.g., Refs. [138, 332, 336, 338, 340, 346, 347]). This thesis focuses on developments within the `SEOBNR` family. The `SEOBNR` models follow the naming convention `SEOBNRvnEPHM`, which indicates that the version `vn` of the EOB model is calibrated to NR simulations (NR), includes spin (S) and precessional

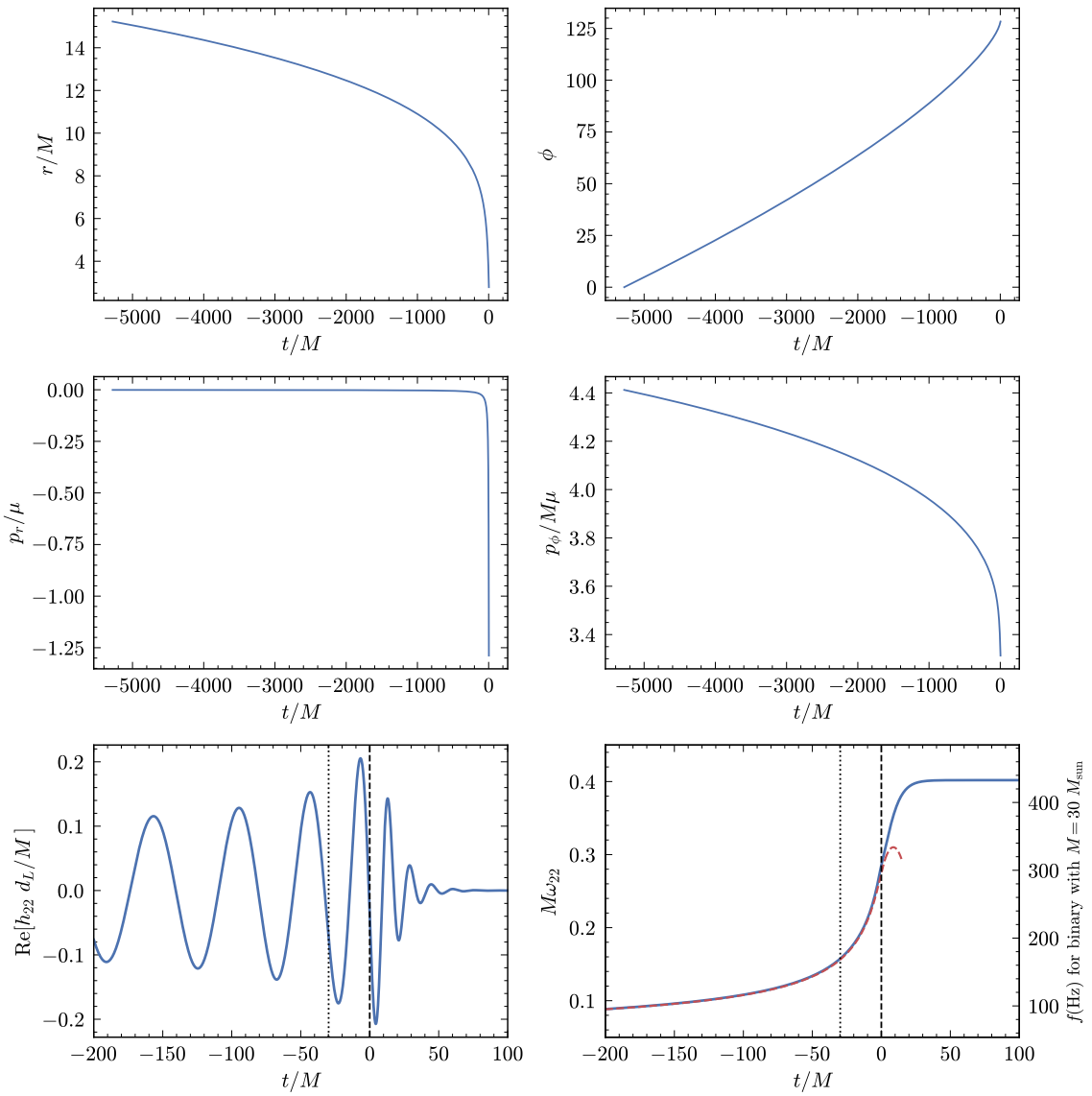

Figure 1.5: Effective-one-body (EOB) dynamics and waveform for an aligned-spin binary black hole with parameters $q = 4.67$, $\chi_1 = -0.5$, $\chi_2 = 0.8$ computed using the `SEOBNR-PM` model (see Sec. 2.3). Starting from the top left, panels show: radial separation, orbital phase, radial momentum, angular momentum, real part of the $(2, 2)$-mode waveform, $(2, 2)$-mode frequency. The vertical dashed line at $t = 0$ denotes the time $t_{\rm match}$ at which the ringdown waveform is attached; the vertical dotted line corresponds to the ISCO radius. The red dashed curve shows twice the orbital frequency, $2M\Omega$, which closely tracks the $(2, 2)$-mode frequency almost until merger. We use dimensionless EOB variables (8).

(P) effects, eccentricity (E), and higher modes (HM).

The first NR-calibrated EOB model, `EOBNRv1`, was introduced in Ref. [321], following earlier comparisons to nonspinning NR waveforms [313]. The second generation included `SEOBNRv0` [328], which incorporated spin effects calibrated to NR simulations of equal-mass, aligned-spin binaries. Higher modes were first modeled in the nonspinning `EOBNRv2HM` model [112], using the improved factorized waveform resummation [316, 318, 319]. The third-generation of `SEOBNR` models introduced major improvements in modeling spin effects in the two-body dynamics and waveforms. Notably, an EOB Hamiltonian for a test spin in a deformed Kerr spacetime was derived in Refs. [329, 330, 390]; to ensure a peak in the orbital frequency for aligned-spin binaries, it used a logarithmic resummation of the EOB potentials. This generation introduced the aligned-spin model `SEOBNRv1` [323], as well as the first precessing-spin model, `SEOBNRv2P` [132], which used the *twisting-up* prescription to describe spin precession. With access to a larger and more accurate set of NR waveforms, and additional analytic input from PN theory, the model was upgraded to `SEOBNRv2` [325], and its precessing-spin counterpart, `SEOBNRv3P` [133]. The fourth generation of `SEOBNR` models, beginning with `SEOBNRv4` [335], introduced a more accurate and computationally efficient calibration to NR waveforms and adopted an improved phenomenological description of the merger-ringdown phase [326]. This generation was extended to include higher-order modes calibrated to NR (`SEOBNRv4HM`) [113], generic spin orientations (`SEOBNRv4PHM`) [134], and eccentric or hyperbolic orbits for aligned-spin systems (`SEOBNRv4EHM`) [344]. Several key advancements introduced in the fifth generation, `SEOBNRv5`, are presented and discussed in this thesis.

The `SEOBNR` waveforms have been a central component of LVK data analysis. They have been used in GW searches since the early LIGO science runs [391–393], and alongside the `IMRPhenom` family they are one of the two standard waveform model families used for PE and tests of GR [49, 251]. These models are particularly crucial in regions of parameter space where NR simulations or NR surrogates are not yet available, such as long-duration inspirals, binaries with high mass ratios, and eccentric systems.

1.3.5 Challenges in gravitational waveform modeling

GW astronomy has rapidly advanced since the first detection of GWs from a BBH merger in 2015 [45]. Approximately ten events were observed during the initial and second observing runs [46] and about one hundred were reported in the third observing run [47–49, 68, 69] of the LIGO-Virgo detectors [72, 73]. The fourth observing run, which also includes the KAGRA interferometer in Japan [394], has started in May

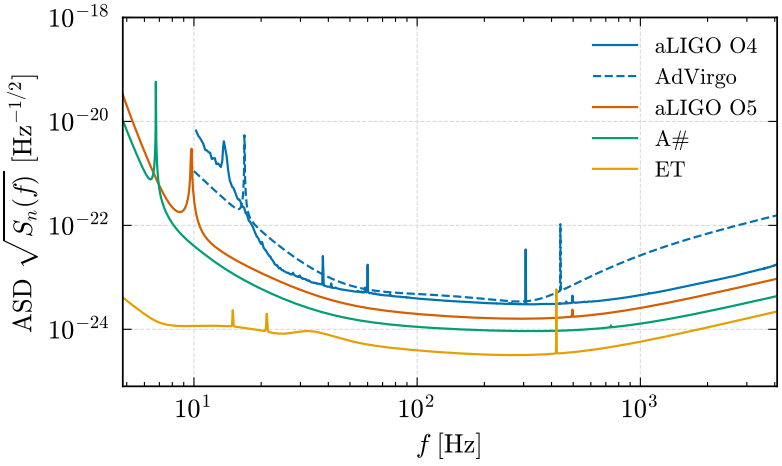

Figure 1.6: The amplitude-spectral-density curves for several ground-based detectors referenced in this thesis. The curves labeled by aLIGO O4 and AdVirgo denote the sensitivity of the LIGO detectors during the fourth observing run, and the design sensitivity of the Virgo detector, respectively [395, 398]. The aLIGO O5 and A# curves refer to the design (A+) and upgraded sensitivity of the LIGO detectors, respectively [399, 400].

2023 and is expected to end in October 2025. By its conclusion, it is anticipated that more than 300 GW events will have been observed [395]. Current GW detectors are projected to reach their design sensitivity within the next few years during the fifth observing run (O5) and will continue to operate until the end of the decade. Following this period, significant upgrades are anticipated, in preparation for the transition to next-generation (XG) observatories. The next generation of ground-based detectors, including the Einstein Telescope (ET) [396] in Europe, and the Cosmic Explorer (CE) [397] in the US, is planned for the 2030s. These facilities aim to achieve a tenfold increase in strain sensitivity and extend the low-frequency range down to ~ 1 Hz, enabling the detection of events at cosmological distances, potentially back to the era of the first stars and BHs. A summary of the sensitivity curves of current and future ground-based detectors is shown in Fig. 1.6.

In the millihertz regime ($\sim 10^{-4} - 10^{-1}$Hz), space-based observatories will play a crucial role. The LISA mission, scheduled for launch in 2035 [401], will consist of three spacecrafts in a triangular formation with $\sim 10^6$ km arms in a heliocentric orbit. LISA will probe a wide variety of sources inaccessible from the ground, including the mergers of massive BHs in galactic cores and extreme mass-ratio inspirals. Unlike ground-based observations that last only seconds, LISA signals can persist for months or years, providing exquisitely detailed information about the binary parameters. Additional space-based missions such as TianQin [402] and Taiji [403] have also been

proposed to operate on similar timescales.

With these developments, the field is entering an era of high-precision GW astronomy. The anticipated improvements in detector sensitivity will not only increase the number of detectable events by orders of magnitude [404], but also enable observations with SNRs up to two orders of magnitude higher than what is currently achievable [405], and potentially unveil new classes of weaker sources. These major advancements will provide unprecedented opportunities to advance our understanding of astrophysics, cosmology, gravity, and fundamental physics.

Several studies have highlighted the scientific potential of XG ground-based detectors [396, 397, 405–408]. A global network of XG detectors will be capable of detecting nearly all stellar-origin BBH mergers and most BNS mergers across the observable Universe, with potentially $\mathcal{O}(10^5)$ detections per year [405]. This dramatic increase in detection rate will enable unprecedented population studies, offering new insights into the formation channels, mass and spin distributions, and evolutionary pathways of compact binaries [409]. In addition, XG detectors may uncover previously undetected populations, including high-redshift sources and intermediate-mass BHs [410, 411]. Thousands of BNS mergers with electromagnetic counterparts, as well as especially informative *golden* BBH events [412], will serve as standard sirens, and have the potential to resolve the current tension in Hubble constant measurements [413]. Next-generation detectors will also probe the fundamental physics of dense matter: measurements of tidal deformability in BNS inspirals, and possibly high-frequency post-merger oscillations, will place stringent constraints on the NS equation of state [414–416].

The space-based LISA mission will complement ground-based efforts by detecting mergers of massive BHs up to redshifts $z \gtrsim 10$, tracing the formation, growth, and merger history of massive BHs and their host galaxies across cosmic time. These events will be observed with SNR up to $\mathcal{O}(10^3)$, making them ideal candidates for precision tests of the no-hair conjecture [417, 418]. Extreme mass ratio inspirals will complete $\mathcal{O}(10^5)$ cycles in the LISA band, allowing for exquisite measurements of their parameters and detailed mapping of the spacetime geometry around Kerr black holes [419]. Moreover, LISA will be sensitive to subtle environmental effects – accretion disks, dark matter spikes, and clouds of ultra-light scalar fields – providing new insights into the astrophysical environments of compact binaries and potentially revealing signatures of dark matter [420–422]. Multiband observations combining data from LISA and XG ground-based detectors will offer unprecedented insight into the full dynamical evolution of compact binary systems, enabling continuous tracking from early inspiral in the milli-Hertz band to merger and ringdown in the kilo-Hertz [423–425], and allowing for unique tests of GR [426, 427]. With precise sky

localization and early warnings days before merger, it will also be possible to coordinate electromagnetic follow-up campaigns to search for any counterpart associated to these signals.

Waveform accuracy challenges

To fully realize the scientific potential of next-generation detectors, improvements in detector technology must go hand in hand with the development of ever more accurate predictions for the GW signals. Waveform models are *approximate* representations of the true GW signals and include various simplifications. These approximations are often motivated by the high computational cost of NR simulations, the decision to neglect certain physical effects considered subdominant for current analysis, or the lack of known analytical results. While statistical uncertainties, caused by detector noise, are reflected in the width of posterior distributions, systematic errors primarily introduce a *bias*, shifting the recovered parameter values away from their true values [175,176]. Such biases can significantly impact the interpretation of source properties. As detector sensitivity improves, statistical uncertainties – which scale inversely with the SNR – decrease, whereas systematic errors remain largely independent of SNR. This means that systematic uncertainties can become the dominant source of error in high-SNR detections. Accurate modeling of GW signals from binary systems is therefore essential to fully exploit the discovery potential of increasingly sensitive detectors. As our observational capabilities continue to improve, understanding and mitigating the impact of waveform modeling errors on PE becomes ever more critical to avoid drawing incorrect conclusions from the data.

Current waveform models have been sufficiently accurate to analyze most GW signals detected to date [428, 429], with only a few exceptions where different models recovered noticeably different parameters [49, 430, 431]. However, recent studies [139, 429, 432–436] have shown that state-of-the-art waveform models could exhibit systematic biases when applied to future LVK runs and next-generation detectors. These biases can become particularly significant for systems with high spin magnitudes and significant asymmetries in spins and masses, corresponding to less common, but particularly interesting binary systems at the edge of the astrophysical distributions. Even NR simulations, the benchmark for generating highly accurate waveforms, are expected to fall short of the required accuracy [437,438]. Crucially, waveform systematics have the potential to compromise key scientific goals of upcoming GW observatories, potentially leading to incorrect astrophysical interpretations [435].

Gravitational-wave observations also offer an unprecedented testing ground for fundamental physics. By comparing detected waveforms with theoretical predictions from GR, we can perform stringent tests of gravity in the dynamical strong-field

regime. To date, observations have shown no significant deviations from Einstein's theory, and placed robust constraints on alternative theories [250, 251, 439–441]. As measurement precision continues to improve with better detectors and a growing number of signals, even minute discrepancies, if present, might be discerned, carrying profound implications for our understanding of gravity. It is therefore crucial to distinguish between genuine deviations from GR and errors arising from imperfect modeling, which can mimic apparent violations of GR [369, 418, 442–445]. This further motivates the development of accurate waveform models for performing reliable tests of gravity.

In addition to accuracy, it is essential that waveform models incorporate all relevant physical effects. As the number of detected events increases, so does the likelihood of observing subtle features that may appear only in specific subpopulations. For example, many waveform models have historically neglected orbital eccentricity, based on the assumption that GW emission circularizes binaries before they enter the sensitive band of ground-based detectors [152]. However, certain formation channels may preserve a measurable level of eccentricity at detection [154], and its measurement carries crucial astrophysical information. In addition, neglecting such effects in the waveform model can lead to significant systematic biases in PE [263, 446–449].

Waveform accuracy is often quantified in terms of the *mismatch* (or *unfaithfulness*), $\mathcal{M}$, defined as 1 minus the overlap $\mathcal{O}$ between the normalized waveforms, maximized over a relative time and phase shift, that is:

$$\mathcal{M} = 1 - \max_{\varphi, t_c} \frac{(h_1 \mid h_2)}{\sqrt{(h_1 \mid h_1)\,(h_2 \mid h_2)}} = 1 - \mathcal{O}. \tag{1.45}$$

The mismatch between two waveforms can be used to estimate at which SNR they could be distinguishable, given the detector sensitivity. This is usually formulated in terms of an indistinguishability criterion [175, 429, 450–454], which states that if two waveforms satisfy the condition

$$\mathcal{M} < \frac{D}{2\ \mathrm{SNR}^2}, \tag{1.46}$$

for a given PSD and SNR, then these waveforms are considered indistinguishable, and the differences in the recovered parameters are expected to be smaller than statistical errors. The prefactor D can be estimated as the number of intrinsic parameters in the model [453], or it can be tuned by considering synthetic injections at increasing SNR [429]. This criterion is typically applied by computing the mismatch between a waveform model and NR simulations, or between two waveform models.

While easy to evaluate, indistinguishability criteria are often overly conservative.

The criterion is only sufficient, but not necessary, and if it is violated, biases can, but need not arise. To assess actual biases, injection studies are commonly employed. In these studies, a waveform – often from a NR simulation – is injected into simulated detector noise and analyzed using a different model through Bayesian inference. Such studies have shown that even when indistinguishability criteria suggest the possibility of biases, key source parameters may still be recovered without significant deviations [429]. However, injection studies can be computationally expensive, particularly at high SNR.

As a more efficient alternative, the linear signal approximation offers a useful compromise. Assuming that the waveform varies approximately linearly with model parameters near the true signal, one can use the Fisher information matrix to estimate statistical uncertainties [455, 456],

$$\Gamma_{ij} = \left(\frac{\partial h}{\partial \boldsymbol{\lambda}^i} \middle| \frac{\partial h}{\partial \boldsymbol{\lambda}^j} \right), \qquad \Delta \boldsymbol{\lambda}^i = \sqrt{\Gamma^{-1}_{ii}}, \tag{1.47}$$

and combine it with an estimate of the systematic bias from the maximum likelihood point [175, 176]

$$\delta \boldsymbol{\lambda}^i = (\Gamma^{-1})^{ij} \left\langle \partial_j h \mid \delta h \right\rangle, \tag{1.48}$$

where $\partial_j h = \partial h / \partial \boldsymbol{\lambda}^j$ and $\delta h = s - h$, with s denoting the true signal. With careful alignment between waveform models [435], this approach provides a computationally efficient way to estimate biases with reasonable accuracy.

Computational challenges

While waveforms from the `SEOBNR` family have been widely used for GW data analysis, they are often computationally expensive, particularly with PE methods that rely on nested sampling or MCMC techniques. This computational burden has motivated the development of several strategies to accelerate inference.

One approach is the construction of surrogate or reduced-order models (ROMs), which approximate the original waveforms at a fraction of the computational cost [384–389]. While effective, building such models can be complex and time-consuming, potentially slowing the integration of new physical effects or improvements into the underlying `SEOBNR` models. Achieving a balance between accuracy, computational efficiency, and parameter-space coverage remains a significant challenge, as there is usually a trade-off among these goals. While current surrogate models are generally adequate for existing detectors, they fall short of meeting the more stringent accuracy requirements anticipated for future observatories. To date, most surrogate models have targeted individual physical effects – such as spin precession, eccentricity, or

tidal effects – in isolation. Building more realistic models that incorporate multiple effects simultaneously remains an open challenge, due to the increased dimensionality and variability of the training data. Crucially, model complexity should not come at the cost of increased runtime; however more complex models often require a larger number of basis functions, leading to higher memory usage and evaluation time. Machine learning–based methods have shown promising results in addressing some of these limitations [389, 457–459], but they have yet to reach the level of maturity and robustness needed to replace traditional techniques in production-level analyses.

Similar approaches can be applied to accelerate likelihood evaluations by exploiting sparse representations in the frequency domain, taking advantage of the chirping morphology of GW signals [460]. One such method is likelihood heterodyning (or relative binning) [461–464], which improves efficiency by dividing the data by a reference waveform, resulting in a smoother residual that can be represented with fewer frequency points. Multibanding [465, 466] leverages the varying frequency resolution needed at different stages of the signal's evolution to reduce computational cost. Reduced order quadratures [467, 468] accelerate inner product evaluations by constructing an optimized integration rule tailored to a reduced basis. However, these methods often rely on the ability to evaluate waveforms at arbitrary frequencies, which is generally not feasible for time-domain waveform models, which typically require generating a dense frequency grid via fast Fourier transform (FFT). Moreover, further development is needed to extend these techniques to more complex scenarios involving nontrivial time- or frequency-evolutions, such as systems with orbital eccentricity, or analyses incorporating detailed detector models that account for the Earth's motion and a frequency-dependent response [469].

Another strategy focuses on improving the sampling methods themselves. Inference frameworks such as `parallel Bilby` [470] and `RIFT` [471] have been designed to reduce wall-time by leveraging parallelization and alternative likelihood evaluation schemes. More recently, machine learning has emerged as a promising solution: `DINGO` [472–474], a neural posterior estimation framework, has demonstrated the ability to accelerate PE using `SEOBNR` waveforms [448,474]. Other promising directions involve hybrid approaches that combine automatically-differentiable and GPU-accelerated waveform models with gradient-based MCMC sampling, enhanced through normalizing flows [475].

Despite these advancements, challenging events – particularly those involving long-duration signals, high SNRs, or complex waveform morphologies such as spin precession and eccentricity – remain computationally demanding. Current techniques require further extension or optimization to handle these cases efficiently, especially given the increased number of signals expected with future detectors. Data analysis for

the LISA mission will prove especially challenging, as it requires a global fit approach to simultaneously model the multitude of overlapping GW signals expected in its data stream – such as galactic binaries, massive BH mergers, and extreme mass ratio inspirals – alongside instrumental noise within a unified framework [476–478].

These challenges highlight the growing need for a modern, flexible framework for waveform development, that supports rapid prototyping, calibration to NR, and integration of analytical results from different perturbative techniques. Crucially, such a framework should be implemented in a modern programming language to take full advantage of emerging computational techniques. In particular, GPU-accelerated batched waveform evaluation, automatic differentiation, and machine learning offer promising avenues to significantly reduce computational costs and enable scalable, high-fidelity inference, especially in anticipation of the large volume of detections expected in upcoming observing runs and the rich physical information encoded in long, high-SNR signals.

1.4 Research overview

This thesis focuses on the development of accurate and efficient models for the gravitational radiation emitted by coalescing compact binaries, with particular emphasis on the construction, calibration, and application of EOB waveform models for BBH mergers. This thesis is structured as follows:

- Chapter 2 presents my research on the development of gravitational waveform models for BBH mergers. It is based on Refs. [1–3].
- Chapter 3 describes my research on the application of these waveform models to the PE of GW signals from BBH mergers. It is based on Refs. [2, 5].
- Chapter 4 focuses on my research on testing GR using GW observations from BBH mergers. It is based on Refs. [4, 6].

I briefly summarize my contribution to each of these publications:

- The works presented in Refs. [1,2] are part of a series of publications [1,2,139,144, 364] describing the development of the `SEOBNRv5` family of waveform models. I contributed to all development stages of the models, from theoretical formulation to implementation, with a leading role in developing the aligned-spin model `SEOBNRv5HM` [2], which serves as the foundation for all subsequent extensions, and calibrating it against NR data. Specifically, in Ref. [2], I performed all calibration and validation between the `SEOBNRv5HM` model and NR waveforms, generated all the figures, and wrote the original draft of the manuscript. I also contributed to the development of the open-source software framework `pySEOBNR`, introduced in

Ref. [1], which was used for implementing and validating the SEOBNRv5 models. I contributed significantly to the development and validation of the code and reviewed and edited the original draft of the associated publication. I also contributed to the other publications in the series, though they are not described in detail in this thesis. In Ref. [144], which presents the theoretical foundations of the models, my main contributions were the derivation of the aligned-spin Hamiltonian and testing of several resummation and gauge choices. In Ref. [364], which discusses the calibration of the SEOBNRv5HM fluxes and waveform modes to 2GSF results, I implemented the GSF corrections in pySEOBNR and generated all results and figures presented in Sec. V and Appendix A. SEOBNRv5PHM, the extension of SEOBNRv5HM to precessing-spin binaries, is presented in Ref. [139], where I was primarily involved in the implementation and validation of the model. More recently, Ref. [479] presented a model for antisymmetric multipoles within the SEOBNRv5PHM model. I contributed background expertise on the SEOBNRv5 model family, and provided technical assistance with the development and implementation of the model. Additionally, I have been actively involved in the internal review process of the SEOBNRv5 models within the LVK Collaboration, contributing to their reliable integration into LVK data analysis pipelines, and serving as the primary contact person for the models. The SEOBNRv5 waveform models are currently being employed by the LVK Collaboration during its fourth observing run for parameter inference, matched-filter template banks, and tests of GR. I have actively contributed to several of these analyses, applying and validating the models on real GW data.

- Ref. [3] presents the development of the SEOBNR-PM waveform model. I contributed to the implementation of the model, performed the majority of the comparisons between SEOBNR-PM and NR waveforms, and generated all the figures included in the manuscript. All authors contributed to writing and editing the final version of the paper.
- Ref. [5] presents a novel probabilistic approach to marginalize over waveform uncertainties in PE. I developed the method and the final implementation of the code, building on a preliminary prototype provided by Michael Pürrer. I also generated all results and figures presented in the manuscript, and wrote the original draft of the paper.
- Ref. [4] presents the construction of an IMR waveform model in Einstein-scalar-Gauss-Bonnet gravity, an extension of GR predicting distinctive signatures in BH coalescences. This work was jointly led by myself and Félix-Louis Julié. I developed the code implementation of the model and generated all results and

figures included in the manuscript. Félix-Louis Julié contributed the analytical foundations, deriving expressions for the scalar energy flux and the factorized corrections to the waveform modes. The original draft of the paper was co-written by both of us.

- Ref. [6] presents the extension of the parametrized `pSEOBNR` framework for tests of GR to the spin-precessing `SEOBNRv5PHM` model. I led the code implementation of the model, generated all figures included in the manuscript, and produced the majority of the results, except for a subset of PE runs performed by collaborators. I also wrote the original draft of the paper. Additionally, I contributed to the internal review process of the `pSEOBNRv5PHM` model within the LVK Collaboration, and performed analyses of several events from the fourth LVK observing run.

Besides the works discussed above, I am also a co-author on several other publications not included in this thesis, including articles published by the LVK Collaborations.

- Ref. [418] presets a BH spectroscopy study for massive BH binaries with LISA using the `pSEOBNR` framework, for aligned-spin binaries. I developed the code implementation of the model, provided input on the interpretation the results, and contributed to writing Sec. II, Sec. V, and Appendix A.
- Ref. [435] presents a systematic assessment of waveform inaccuracies across the full parameter space of stellar-mass BBHs for next-generation ground-based detectors. I contributed to the methods for estimating biases discussed in Sec. III, contributed to discussions on the interpretation and presentation of the results, and reviewed and edited the original draft of the manuscript.
- Ref. [345] presents `SEOBNRv5EHM`, an extension of the `SEOBNRv5HM` model to eccentric BBH systems. I contributed background expertise on the `SEOBNRv5` model family, provided technical assistance with the development and implementation of the waveform model, and gave feedback on the manuscript.
- Ref. [264] presents an exploration of the impact of eccentricity and mean anomaly in NR simulations. I wrote and produced all figures and results in Sec. 3.3, "Effective-one-body estimates of the final mass and spin", and contributed to discussions on the interpretation and presentation of results in other sections.
- Ref. [444] presents a review of possible causes of false GR violations in GW observations. I co-authored with Alessandra Buonanno the original draft of Sec. 3.2.2, "Sub-optimal calibration and agreement with NR waveforms", and contributed to other sections.
- Ref. [249] presents a comprehensive review of BH ringdown physics, including QNMs predictions in GR and beyond, ringdown modeling, current observational

status, and future prospects. I co-authored with Simone Albanesi the original draft of Sec. 5.2, "Time-dependent amplitudes: phenomenological models", and contributed to other sections.

- I contributed to the section on EOB waveforms in the LISA Waveform White Paper [480], and to the sections on EOB waveforms and on BBH waveforms in the Einstein Telescope Blue Book [396].
- I performed some of the PE analyses using the `SEOBNRv5PHM` waveform model for GW230529 [183], a NSBH merger detected by the LVK Collaboration during its fourth observing run. This event is notable for involving a compact object within the *lower mass gap* between the heaviest known NSs and the lightest BHs.
- I contributed to the PE analyses for the upcoming LVK GWTC-4 catalog, scheduled for publication in August 2025. During the fourth LVK observing run (O4), I served multiple times on the PE Rota, coordinating preliminary PE analyses for significant events. As a member of the O4a production PE team, I have been responsible for reviewing final PE results prior to their public release in GWTC-4. In addition, the `SEOBNRv5PHM` waveform model has been used for the measuring the parameters for all BBH signals reported in the catalog. Finally, the `SEOBNRv5_ROM` model has been employed to construct the matched-filter template banks used by the `pyCBC` pipeline for offline searches.
- I contributed to the tests of GR paper accompanying GWTC-4, scheduled for publication in August 2025. There, I served as the liaison between the TGR and PE working groups, acting as the primary point of contact for PE-related matters and ensuring that developments in PE methods were integrated into TGR analysis pipelines. I also served as an analyst for the `pSEOBNR` parametrized ringdown test featured in the paper, and performed analyses of several events from the fourth LVK observing run. In addition, the `SEOBNRv5HM_ROM` model I developed is employed in the flexible theory-independent (FTI) inspiral test of GR.
- I identified and corrected a bug affecting the joint posterior results of the `pSEOBNR` analysis in the tests of GR paper accompanying GWTC-3 [251].

Within the LVK Collaboration, I also contributed to the internal reviews of the `IMRPhenomXPNR` waveform model and of `gwsignal`, a new waveform interface in `LALSimulation` that enables the generation of waveforms from models not implemented directly in `LALSimulation`, including those written in `C` or `Python`. As part of these tasks, I performed line-by-line code reviews, conducted sanity checks, and ensured

that all tests were carried out in accordance with the LVK Collaboration guidelines.

Additionally, I contributed to early activities of the Waveform Coordinating Unit within the LISA Distributed Data Processing Center, providing support for the `SEOBNRv5PHM` model and the `pySEOBNR` code, to be used in the upcoming LISA Data Challenge (`Mojito`).

2 Improved gravitational waveform models for binary black hole mergers

2.1 pySEOBNR: a software package for the next generation of SEOBNR models

This section provides an overview of the pySEOBNR package [1], which has been used to obtain most of the results presented throughout this thesis. We outline the motivation for developing pySEOBNR, and describe its key features, the required inputs and configurable options, and explain how the core submodules interact with each other. For a comprehensive reference of the package's full functionality, we refer the reader to the official documentation [481].

2.1.1 Motivation for developing pySEOBNR

The next generation of GW detectors, including ground-based facilities such as ET and CE, as well as space-based missions like LISA, will achieve unprecedented sensitivity. This dramatic improvement in sensitivity introduces several key challenges for GW data analysis, notably the need for waveform models that are faster, more accurate, and physically more complete than those currently available. The correct interpretation of the anticipated high-SNR detections, and the identification of subtle astrophysical effects, requires highly accurate waveform models that incorporate all relevant physical features. Furthermore, for ground-based detectors, each new observing run is expected to yield an exponential increase in the number of detected events, while both LISA and ground-based observatories will observe signals of significantly longer duration, spanning many more GW cycles. These challenges make it computationally prohibitive to apply highly accurate, physically complete GW models across the entire parameter space using conventional techniques.

Addressing these challenges requires not only advances in theoretical modeling, but also the development of modern computational infrastructure capable of rapidly integrating new theoretical results and enabling efficient calibration to NR data. Existing frameworks for waveform generation and development, such as `LALSuite` [482], although successful for current detectors, are based on outdated programming standards, such as the `C99` language, and have become increasingly difficult to maintain and extend. Adopting more modern programming languages can streamline the development of more efficient models, and facilitate integration with modern computational tools, such as machine learning techniques and GPU acceleration, which will be essential for meeting the computational demands of next-generation observatories. This motivates the need for flexible, maintainable software frameworks explicitly designed to address these requirements.

To this end, this thesis importantly contributed to `pySEOBNR`, a newly developed `Python` package designed to support the development, calibration, and validation of the next generation of EOB waveform models, particularly within the `SEOBNR` family. We have chosen `Python` [483] as the primary programming language, due to its rich scientific ecosystem, maintainability and wide adoption in the GW community [473,484–486]. Performance-critical components of the code are implemented in `Cython` [487], a compiled extension of `Python`, to achieve better computational efficiency while maintaining flexibility. Analytical results, which form the foundation of the `SEOBNR` family of models, are provided via `Mathematica` [488] notebooks, which are efficiently parsed, simplified and integrated into `pySEOBNR`.

The package depends on a number of well-established and regularly maintained packages under open-software licenses: `numpy` [489], `scipy` [490], `Cython` [487], `GSL` [491], `pygsl` [492], as well as `lal` and `lalsimulation` [482]. Optional dependencies include `wolframclient` [493] and `bilby` [486], used for the extensions that support the development and calibration of new waveform models. `pySEOBNR` is distributed under the GNU General Public License [494]. Version control is managed using `git` [495], which supports efficient collaborative development, issue tracking, and versioned releases. Stable versions of `pySEOBNR` are published through the `Python` Package Index (PyPI) and can be installed via `pip install pyseobnr`; the package is also distributed via `conda`.

Most of the results presented throughout this thesis have been obtained using `pySEOBNR`, demonstrating its practical utility and flexibility in developing accurate and efficient GW models, as well as for applications in PE and tests of GR. Currently, `pySEOBNR` supports several state-of-the-art waveform models, including the aligned-spin `SEOBNRv5HM` model [2], described in Sec. 2.2 of this thesis, and the precessing-spin `SEOBNRv5PHM` model [139], which were the first models to be developed within

this framework. Additional publicly available models include a waveform model for BBHs in eccentric orbits, SEOBNRv5EHM [345], and a parametrized extension of the SEOBNRv5PHM model, named pSEOBNRv5PHM, designed for testing GR [6]. The latter will be discussed in Sec. 4.3. All of these models have undergone internal review within the LVK Collaboration before public release, including line-by-line code review, comprehensive validation, and extensive testing to ensure their reliability for realistic data analysis applications. Additional developments presented in this thesis have also been implemented within pySEOBNR, but currently remain private within the Albert Einstein Institute as they have not yet undergone internal review by the LVK Collaboration. These include the PM-based waveform model SEOBNR-PM [3] described in Sec. 2.3, the waveform model for BBHs in Einstein-scalar-Gauss-Bonnet gravity [4] described in Sec. 4.2, and the method for marginalizing over waveform uncertainties [5] described in Sec. 3.3.

Importantly, pySEOBNR interfaces with state-of-the-art GW data analysis software packages, such as bilby [179, 486], DINGO [473], pyCBC [484], and RIFT [471]. Its interface with bilby has been widely used for PE and tests of GR analyses during the LVK Collaboration's fourth observing run, including the analysis of the recently reported event GW230529 [183], as well as the upcoming GWTC-4 catalog and the associated tests of GR paper.

2.1.2 Description of the software package

pySEOBNR has been developed with two primary objectives. The first is to provide a user-friendly interface for generating state-of-the-art waveform models suitable for GW data analysis. The second objective is to offer a flexible and extensible framework for the development and validation of new EOB waveform models. To this end, pySEOBNR includes several development tools, such as symbolic parsing of Mathematica expressions and automatic code generation for incorporating analytical results, a calibration pipeline for tuning EOB models to NR simulations, and utilities for testing and validating waveform performance.

The design of pySEOBNR is highly modular to facilitate extensibility, development, and long-term maintainability. The codebase is organized into a set of well-defined submodules, each serving a distinct purpose. Comprehensive documentation accompanies all components of the package. In addition, pre-commit hooks and continuous integration pipelines are used to enforce code formatting standards and ensure correctness through unit and regression tests.

Figure 2.1 illustrates the overall architecture of the pySEOBNR package. The bottom panels represent the primary steps for generating aligned- and precessing-spin waveforms. Above them, intermediate layers detail the computational steps involved

in this process. The top panels highlight the development infrastructure, including tools for parsing analytical input from `Mathematica` and a calibration pipeline to NR and GSF data. The diagram also distinguishes between steps performed during model development (dashed arrows), and those executed during waveform generation (solid arrows). In physical terms, waveform generation begins by numerically integrating the EOB Hamiltonian system with a dissipative RR force that accounts for GW energy loss, to solve for the binary's dynamics (1.43). Spherical-harmonic modes of the emitted waveform are computed in an inertial reference frame, incorporating free parameters calibrated against NR data. Finally, the two GW polarizations are computed from the waveform modes (1.25).

The GenerateWaveform class

The core functionality of `pySEOBNR` is organized around the `GenerateWaveform` class, which provides a unified interface for generating gravitational waveforms. The user can specify input parameters when creating an instance of this class, and obtain waveform outputs and derived quantities through the class's instance methods.

Input parameters are provided as a `Python` dictionary, which allows for easy customization and extensibility. These parameters specify the physical properties of the binary system, such as component masses, spins, eccentricity, and orbital orientation, as well as model-specific options related to waveform generation. Only a minimal subset of parameters (the masses m_1, m_2 of the primary and secondary binary components) are strictly required, but the class supports a number of optional input parameters, most of which have sensible default values appropriate for standard use cases, including:

- `distance`: The luminosity distance d_L to the GW source, expressed in megaparsecs (Mpc). The default value is 100, reflecting the typical scale of extragalactic sources.
- `inclination`: The inclination angle ι between the line of sight and the orbital angular momentum, in radians. By default, the binary is assumed to be viewed face-on ($\iota = 0$).
- `phi_ref`: The orbital phase at the reference frequency, in radians. The default value is 0.
- `f22_start`: The starting gravitational-wave frequency (in Hz) for waveform generation. By default, it is set to 20 Hz.
- `f_ref`: The reference frequency (in Hz) at which time-dependent quantities such as component spins, eccentricity, or orbital phase are defined. By default, it is

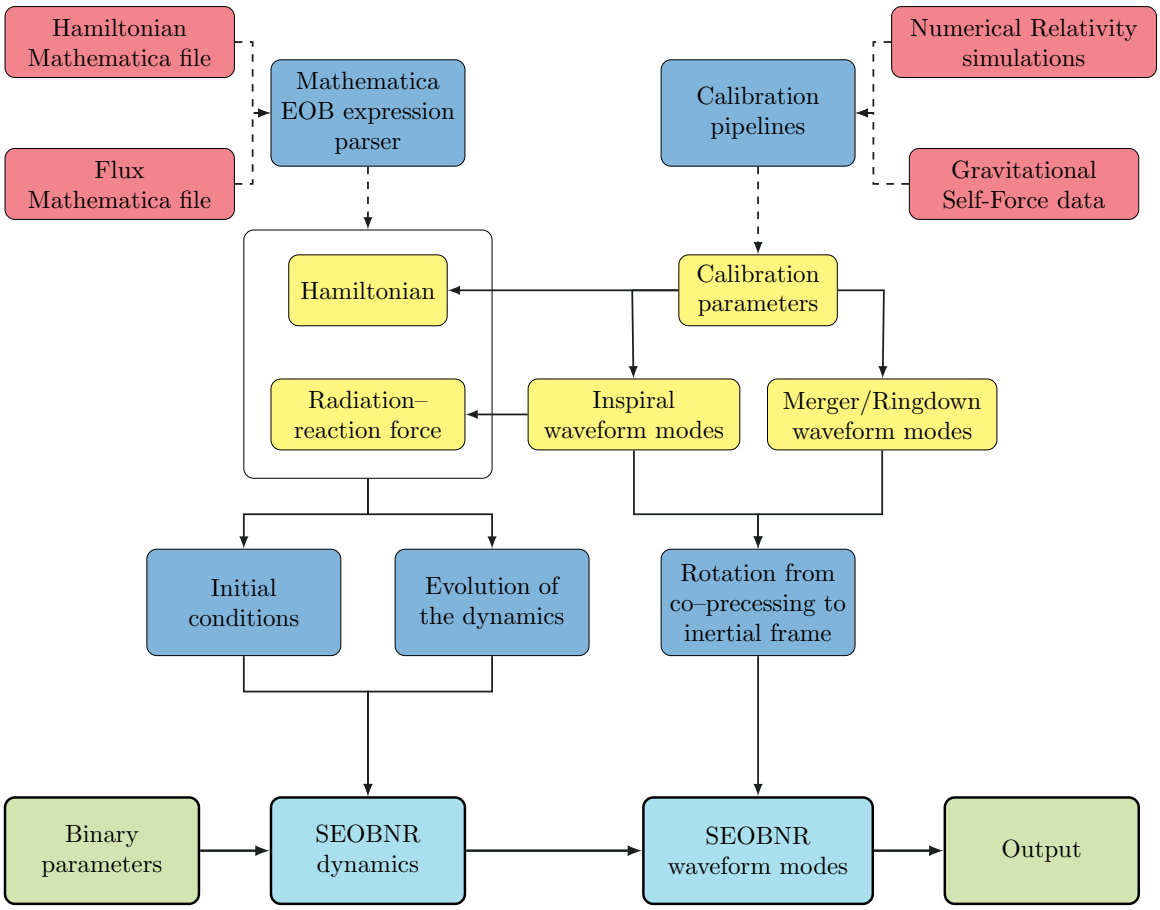

Figure 2.1: Diagram illustrating the structure and interaction of the various `pySEOBNR` submodules. The bottom row shows the primary sequence of operations involved in generating a time-domain gravitational waveform. Boxes shaded in red represent model ingredients that are prepared and provided externally, such as `Mathematica` files containing analytical expressions or NR simulations. Dark blue boxes indicate internal submodules of `pySEOBNR` responsible for specific tasks in the waveform generation process. Yellow boxes denote components of the code that are either automatically or manually generated from the external inputs (red boxes). Solid arrows indicate the flow of information and interactions between submodules during waveform generation. Dashed arrows represent steps performed offline during the development and calibration of a new waveform model, such as incorporating new theoretical inputs or fitting model parameters to NR data.

set equal to `f22_start`.

- `deltaT`: The waveform time resolution (in seconds). The default value is 1/2048 s.
- `f_max`: The maximum frequency (in Hz) of the waveform. If not provided, it is inferred from `deltaT` as the Nyquist frequency (1024 Hz by default).
- `deltaF`: The frequency spacing (in Hz) for Fourier-domain outputs. The default value is 0.125 Hz.
- `mode_array`: Specifies which waveform modes are computed and returned, in the coprecessing frame. Only positive-m modes need to be listed; for example, `[(3, 2)]` includes both the $(3, 2)$ and $(3, -2)$ modes. By default, all modes with $\ell \leq 4$ are selected. The $(5, 5)$ mode is also available but not selected by default.
- `approximant`: Specifies the waveform model used. Currently supported models are `SEOBNRv5HM` (default), `SEOBNRv5PHM`, and `SEOBNRv5EHM`.
- `conditioning`: Determines the tapering method applied to the waveform. A value of `1` applies a taper equivalent to that used for `SEOBNRv4PHM` via `SimInspiralFD()` in `LALSuite` [482]. The default value, `2`, adds extra time at the beginning of the waveform for tapering using the standard `SimInspiralFD()` procedure.
- `postadiabatic`: Controls whether the PA approximation is used during the binary inspiral. By default, this option is set to `True`.

Automatic validation of input parameters is performed during initialization. This includes checking that all required parameters are provided, and ensuring that optional parameters fall within acceptable ranges. Once the `GenerateWaveform` class has been initialized, waveforms can be generated using its instance methods. The class has been designed for compatibility with standard GW data analysis tools such as `LALSuite` [482]. To this end, `pySEOBNR` reuses standard `LALSuite` data types and closely mirrors the interfaces of primary API functions such as `SimInspiralChooseTDWaveform()` and its frequency-domain counterpart, provided via the `lalsimulation` sub-package. The waveform generator offers several output formats, accessible through dedicated methods:

- *Time-domain modes*: Generated using the `generate_td_modes()` method. This returns an array representing the time axis and a dictionary containing the requested waveform modes, as specified by the `mode_array` input parameter.
- *Time-domain polarizations*: Generated using the `generate_td_polarizations()` method. This returns two `REAL8TimeSeries` objects representing the plus and

cross polarizations.

- *Frequency-domain polarizations*: Generated using the `generate_fd_polarizations()` method. This returns the Fourier transforms of the plus and cross polarizations as `COMPLEX16FrequencySeries` objects.

All outputs are provided in SI units, and the data types `REAL8TimeSeries` and `COMPLEX16FrequencySeries` follow `LALSuite` conventions [482]. The available waveform generator routines are summarized in Table 2.1.

Method	LALSuite Counterpart	Output
`generate_td_modes()`	`SimInspiralChooseTDModes()`	`times` `hlm_dict`
`generate_td_polarizations()`	`SimInspiralChooseTDWaveform()`	`hp` `hc`
`generate_fd_polarizations()`	`SimInspiralChooseFDWaveform()`	`hptilde` `hctilde`

Table 2.1: Instance methods of the `GenerateWaveform` class and their `LALSuite` counterparts. The returned outputs include waveform modes or polarizations in either time or frequency domains.

Generating an aligned-spin gravitational waveform

Finally, we show how to use `pySEOBNR` to generate a gravitational waveform for a BBH system with aligned spins, using the `SEOBNRv5HM` model. As shown in Listing 2.1, we employ the `GenerateWaveform` class just introduced. We consider a binary with total mass $M = 80M_{\odot}$, a starting frequency of 20 Hz, and a sampling rate of 1024 Hz. The dimensionless spin magnitudes of the primary and secondary components are 0.8 and 0.3, respectively. The binary is placed at a luminosity distance of 100 Mpc and observed at an inclination angle of $\pi/3$. Once the class instance is initialized, we invoke the `generate_td_polarizations()` method to compute the time-domain the plus and cross polarizations. For this binary configuration, generating waveform polarizations requires around 113 ms. The resulting waveform polarizations are shown in Fig. 2.2.

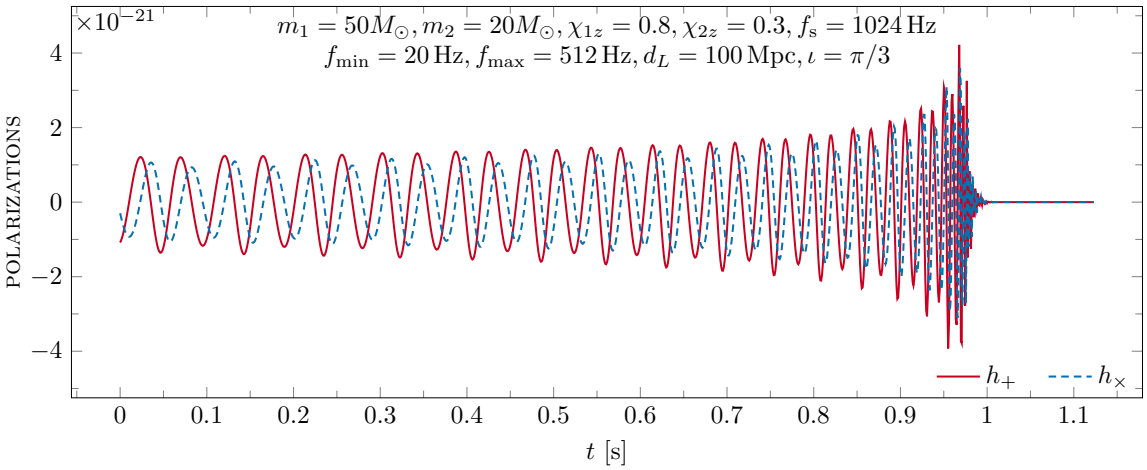

Figure 2.2: Time-domain gravitational-wave polarizations $h_+(t)$ and $h_\times(t)$ generated using the `generate_td_polarizations()` method of the `pySEOBNR` package. The binary parameters used for waveform generation are indicated in the figure.

```
from pyseobnr.generate_waveform import GenerateWaveform

m1, m2 = 50.0, 20.0
s1x, s1y, s1z = 0.0, 0.0, 0.8
s2x, s2y, s2z = 0.0, 0.0, 0.3
f_min, f_max = 20.0, 512.0
distance = 100.0
inclination = 1.047
phi_ref = 0.0
approximant = "SEOBNRv5HM"

params_dict = {
        "mass1": m1, "mass2": m2,
        "spin1x": s1x, "spin1y": s1y, "spin1z": s1z,
        "spin2x": s2x, "spin2y": s2y, "spin2z": s2z,
        "f22_start": f_min, "f_max": f_max,
        "phi_ref": phi_ref,
        "distance": distance,
        "inclination": inclination,
        "approximant": approximant,
}

waveform_gen = GenerateWaveform(params_dict)
hp, hc = waveform_gen.generate_td_polarizations()
```

Listing 2.1: Generating aligned-spin waveform polarizations in time-domain.

2.2 Construction and validation of the effective-one-body waveform model SEOBNRv5HM

With an increasing number of detections and the observation of higher SNR signals, the fourth observing run of the LVK Collaboration is expected to uncover GW events in previously unexplored regions of parameter space, including high-spin and large-mass-ratio systems. In these regions of parameter space, state-of-the-art waveform models often disagree [134, 137, 299, 335, 496], as they are mostly calibrated to NR simulations with both moderate spins and comparable mass ratios. As a result, modeling errors may become comparable to statistical uncertainties. Improving the accuracy of EOB models requires incorporating strong-field information from NR simulations, alongside the latest analytical insights from PN, PM, and GSF theory.

Within the SEOBNR family of EOB models, we present SEOBNRv5HM, a new IMR multipolar waveform model for quasi-circular, spinning, nonprecessing BBHs [2]. SEOBNRv5HM is developed in the pySEOBNR code [1], described in Sec. 2.1. The model includes the latest PN results for the three main components of the EOB dynamics and gravitational radiation: the Hamiltonian [144, 333, 334], the RR force, and waveform modes [497]. Furthermore, it incorporates information from 2GSF [233, 234, 364] in the modes and RR force. Compared to its predecessor SEOBNRv4HM [113], SEOBNRv5HM adds the $(3, 2)$ and $(4, 3)$ modes, modeling their mode-mixing during merger and ringdown, alongside the previously included $(2, 2)$, $(3, 3)$, $(2, 1)$, $(4, 4)$, and $(5, 5)$ modes. SEOBNRv5HM is calibrated to 442 NR waveforms - significantly more than the 140 used in SEOBNRv4 [335] - mostly produced with the pseudo-Spectral Einstein code (SpEC) of the Simulating eXtreme Spacetimes (SXS) Collaboration [135, 256, 273, 274, 276, 281, 335, 498–507], along with one Einstein Toolkit simulation [508], and 13 waveforms from BH perturbation theory at extreme mass ratio ($q = 10^3$) [114, 115]. Importantly, this expands coverage to mass ratios between 10 and 20, a region of parameter space where no simulations were available when SEOBNRv4 was developed.

We assess the accuracy of the model by computing mismatches against NR simulations, and by comparing dynamical quantities such as the binding energy. SEOBNRv5HM is computationally efficient, with significantly faster evaluation times than SEOBNRv4HM, thanks to its high-performance implementation in pySEOBNR. We also present frequency-domain ROMs, SEOBNRv5_ROM and SEOBNRv5HM_ROM. These ROMs approximate their respective time-domain counterparts, SEOBNRv5 and SEOBNRv5HM, and further accelerate waveform generation by roughly an order of magnitude.

SEOBNRv5HM [2] serves as the cornerstone of the SEOBNRv5 family of waveform models, providing a foundation for several generalizations that target more complex physical scenarios, all of which reduce to SEOBNRv5HM in the appropriate limit:

- `SEOBNRv5PHM`: Precessing-spin BBHs in quasi-circular orbits [139, 479],
- `SEOBNRv5EHM`: Aligned-spin BBHs in eccentric orbits [345],
- `pSEOBNRv5PHM`: Parametrized extension of `SEOBNRv5PHM` for testing GR [6],
- `SEOBNRv5PHM_ESGB`: Extension of `SEOBNRv5PHM` to BBHs in Einstein-scalar-Gauss-Bonnet gravity [4],
- `SEOBNRv5THM` and `SEOBNRv5_ROM_NRTidalv3`: Aligned-spin BNSs in quasi-circular orbits [356, 509].

As in previous EOB families [335], we use the name `SEOBNRv5` to refer both to the entire family and, when context makes it clear, to the base model `SEOBNRv5HM` with only the dominant $(2, 2)$ mode. The `SEOBNR-PM` [3] and `SEOBNR-GSF` [366] models are also based on `SEOBNRv5`; they share its multipolar waveform and RR force, but introduce modifications to the EOB Hamiltonian and NR calibration.

2.2.1 Hamiltonian and equations of motion

In the EOB formalism [308–312], the two-body Hamiltonian in the center-of-mass frame is mapped, through canonical transformations, to the effective Hamiltonian $H_{\rm eff}$ of a test mass in a deformed BH spacetime, the deformation parameter being the symmetric mass-ratio ν (1.42). The generic-spin Hamiltonian used in `SEOBNRv5` is based on that of a *test mass* in a deformed Kerr background [144,311,327,328,331–334]. In contrast, the `SEOBNRv4` [113, 134, 335] Hamiltonian was based on the one of a *test spin* in a deformed Kerr background [330, 390, 510].

The `SEOBNRv5` Hamiltonian includes most of the 5PN nonspinning contributions, together with spin-orbit (SO) information up to the next-to-next-to-leading order (NNLO), spin-spin (SS) information to NNLO, as well as cubic- and quartic-in-spin terms at leading order (LO). This corresponds to all currently available PN information up to 4PN for generic spin orientations. Full derivations and expressions are presented in Ref. [144]. Here, we summarize the aligned-spin Hamiltonian and its nonspinning limit, with particular attention to the role of NR calibration parameters.

Nonspinning effective Hamiltonian

The effective Hamiltonian for nonspinning (noS) binaries is given by

$$H_{\rm eff}^{\rm noS} = \sqrt{p_{r_*}^2 + A_{\rm noS}(r)\left[\mu^2 + \frac{p_\phi^2}{r^2} + Q_{\rm noS}(r, p_{r_*})\right]}, \tag{2.1}$$

where we use the tortoise-coordinate momentum p_{r_*} to improve the stability of the equations of motion close to merger – p_r diverges when approaching the zero of $A_{\rm noS}(r)$, while p_{r_*} is finite [316, 328]. For nonspinning binaries, r_* is defined by

$$\frac{dr_*}{dr} = \frac{1}{\xi(r)}, \qquad \xi(r) = A_{\rm noS}(r)\sqrt{\bar{D}_{\rm noS}(r)}, \tag{2.2}$$

with the conjugate momentum p_{r_*} given by $p_{r_*} = p_r\,\xi(r)$. For the potentials $A_{\rm noS}(r)$ and $\bar{D}_{\rm noS}(r)$, we use the 5PN results of Refs. [193, 194], which are complete except for two quadratic-in-ν coefficients. For the $Q_{\rm noS}(r)$ potential, we use the full 5.5PN expansion [194, 195], which is also expanded in eccentricity to $\mathcal{O}(p_r^8)$. The 5PN Taylor-expanded $A_{\rm noS}$-potential is given by

$$\begin{aligned} A^{\rm Tay}_{\rm noS}(u) &= 1 - 2u + 2\nu u^3 + \nu\left(\frac{94}{3} - \frac{41\pi^2}{32}\right)u^4 \\ &+ \left[\nu\left(\frac{2275\pi^2}{512} - \frac{4237}{60} + \frac{128\gamma_E}{5} + \frac{256\ln 2}{5}\right) + \left(\frac{41\pi^2}{32} - \frac{221}{6}\right)\nu^2 + \frac{64}{5}\nu\ln u\right]u^5 \\ &+ \left[\nu a_6 + \left(-\frac{144\nu^2}{5} - \frac{7004\nu}{105}\right)\ln u\right]u^6, \end{aligned} \tag{2.3}$$

where $u = M/r$, and we replace the coefficient of u^6, except for the part proportional to $\ln(u)$, by the parameter a_6, which is calibrated to NR simulations. Expressions for $\bar{D}_{\rm noS}(r)$ and $Q_{\rm noS}(r)$ can be found in Refs. [2, 144].

Aligned-spin effective Hamiltonian

For aligned-spin binaries, the effective Hamiltonian reduces to the equatorial Kerr Hamiltonian in the test-particle limit (TPL), with the Kerr spin a mapped to the binary's spins via $a = a_1 + a_2 = a_+$. To incorporate 4PN spin effects for arbitrary mass ratios, we adopt the ansatz [144]:

$$\begin{aligned} H^{\rm align}_{\rm eff} = H_{\rm odd} + H_{\rm even} &= \frac{Mp_\phi\left(g_{a_+}a_+ + g_{a_-}\delta a_-\right) + {\rm SO}_{\rm calib} + G^{\rm align}_{a^3}}{r^3 + a_+^2(r+2M)} \\ &+ \left[A^{\rm align}\left(\mu^2 + p^2 + B^{\rm align}_{np}p_r^2 + B^{{\rm Kerr\,eq}}_{npa}\frac{p_\phi^2 a_+^2}{r^2} + Q^{\rm align}\right)\right]^{1/2}, \end{aligned} \tag{2.4}$$

where the first term on the right-hand side collects the odd-in-spin contributions, while the second term (square root) includes the even-in-spin contributions.

The SO sector depends on gyro-gravitomagnetic functions g_{a_+} and g_{a_-}. These functions are sometimes chosen to be in a gauge where they depend only on $1/r$ and p_r^2 [327, 331], though Refs. [329, 330] made different choices. In building the SEOBNRv5

model, we find better agreement with NR when using a gauge in which $g_{a_+}(r)$ and $g_{a_-}(r)$ depend instead on $1/r$ and p_ϕ^2/r^2. The 4.5PN SO coupling was derived in Refs. [235, 511–513]; however, when calibrating to NR simulations, we find that using a calibration term at 5.5PN has a small effect on the dynamics. Thus, we only include the 3.5PN SO information, and a 4.5PN SO calibration term of the form

$$\mathrm{SO}_{\mathrm{calib}} = \nu d_{\mathrm{SO}} \frac{M^4}{r^3} p_\phi a_+. \tag{2.5}$$

The $G_{a^3}^{\mathrm{align}}(r)$ term captures cubic-in-spin (S^3) effects. The nonspinning and SS contributions are included in $A^{\mathrm{align}}(r)$, $B_{np}^{\mathrm{align}}(r)$ and $Q^{\mathrm{align}}(r)$, with no S^4 corrections needed since the Kerr Hamiltonian reproduces all even-in-spin leading PN orders for binary BHs [514]. Explicit expressions for the functions in the Hamiltonian are provided in Refs. [2, 144].

For spinning binaries, we adopt a generalized tortoise-coordinate transformation

$$\xi(r) = \frac{\sqrt{\bar{D}_{\mathrm{noS}}}\left(A_{\mathrm{noS}} + a_+^2/r^2\right)}{1 + a_+^2/r^2}, \tag{2.6}$$

which reduces to the Kerr value $(dr/dr_*) = (r^2 - 2Mr + a_+^2)/(r^2 + a_+^2)$ in the $\nu \to 0$ limit,

Equations of motion and radiation-reaction force

The equations of motion for aligned-spin binaries on quasi-circular orbits, in terms of p_{r_*}, read [112]

$$\begin{aligned} \dot{r} &= \xi \frac{\partial H}{\partial p_{r_*}}, \qquad & \dot{p}_{r_*} &= -\xi \frac{\partial H}{\partial r} + \frac{p_{r_*}}{p_\phi} \mathcal{F}_\phi, \\ \dot{\phi} &= \frac{\partial H}{\partial p_\phi}, & \dot{p}_\phi &= \mathcal{F}_\phi, \end{aligned} \tag{2.7}$$

where the dot indicates a derivative with respect to t. The RR force $\mathcal{F}_\phi$ is computed by summing the factorized GW modes $h_{\ell m}^{\mathrm{F}}$ [316–319] (defined in Sec. 2.2.2) as

$$\mathcal{F}_\phi = -\frac{\Omega}{8\pi} \sum_{\ell=2}^{8} \sum_{m=1}^{\ell} m^2 \left| d_L h_{\ell m}^{\mathrm{F}} \right|^2, \tag{2.8}$$

where Ω is the orbital frequency, and d_L is the luminosity distance of the binary to the observer. We adopt quasi-circular adiabatic initial conditions [312], and numerically integrate Eqs. (2.7) to evolve the binary dynamics.

To accelerate waveform generation, especially for long signals, `SEOBNRv5` also

supports the PA approximation [324, 381–383], which computes the orbital dynamics on a sparse radial grid. In the PA approximation, the binary dynamics is expanded perturbatively around the adiabatic inspiral, where the system follows a sequence of circular orbits with vanishing radial momentum. At leading order radiation reaction is neglected, so that $p_{r_*} = 0$, and the circular angular momentum $j_0(r)$ is determined by imposing

$$\left.\frac{\partial H}{\partial r}\right|_{p_{r_*}=0,\, p_\phi = j_0(r)} = 0\,. \tag{2.9}$$

at fixed r. Corrections due to radiation reaction are then incorporated iteratively. At each step the PA scheme provides higher-order updates to (p_{r_*}, p_ϕ) from the Hamiltonian equations of motion (2.7). In practice, one introduces a bookkeeping parameter ϵ and expands the radiation reaction and momenta as power series, with odd (even) powers contributing to p_{r_*} (p_ϕ). Following Refs. [381, 382], we derive explicit algebraic equations for the momenta, which we solve iteratively up to eighth PA order on a sparse radial grid $r \in [r_{\rm max}, r_{\rm min}]$. Once $(p_{r_*}(r), p_\phi(r))$ are known up to the desired PA order, the time and orbital phase follow from

$$t(r) = \int_{r_{\rm max}}^{r} dr \left(\frac{\partial H}{\partial p_{r_*}}\right)^{-1}, \qquad \phi(r) = \int_{r_{\rm max}}^{r} dr \left(\frac{\partial H}{\partial p_\phi}\right)\left(\frac{\partial H}{\partial p_{r_*}}\right)^{-1}. \tag{2.10}$$

The PA approximation bypasses need for ODE integrations and reproduces the full EOB dynamics to high accuracy when carried to sufficiently high order.

2.2.2 The SEOBNRv5HM multipolar waveform modes

In this section, we describe the construction of the multipolar, spinning, nonprecessing waveform modes $h_{\ell m}$ in the SEOBNRv5HM model. In the EOB framework, the -2 spin-weighted spherical harmonic modes defined in Eq. (1.25) are decomposed into inspiral-plunge and merger-ringdown modes. SEOBNRv5HM models the dominant (2,2) and the largest subdominant modes [113]: (3,3), (2,1), (4,4), (3,2), (5,5) and (4,3). For aligned-spin binaries, reflection symmetry implies $h_{\ell m} = (-1)^\ell h^*_{\ell -m}$, so we focus on (ℓ, m) modes with $m > 0$.

Each mode is decomposed as:

$$h_{\ell m}(t) = \begin{cases} h_{\ell m}^{\text{insp-plunge}}\,(t), & t < t_{\rm match}^{\ell m} \\ h_{\ell m}^{\text{merger-RD}}\,(t), & t > t_{\rm match}^{\ell m} \end{cases}, \tag{2.11}$$

with the matching time $t^{\ell m}_{\rm match}$ defined as

$$t^{\ell m}_{\rm match} = \begin{cases} t^{22}_{\rm peak}\,, & (\ell,m) = (2,2),(3,3),(2,1),(4,4),(3,2),(4,3) \\ t^{22}_{\rm peak} - 10M, & (\ell,m) = (5,5), \end{cases} \tag{2.12}$$

where $t^{22}_{\rm peak}$ is the peak time of the $(2,2)$-mode amplitude. The choice of a different attachment point for the $(5,5)$ mode is motivated by the fact that at late times the error in some of the NR waveforms is too large to accurately extract the quantities needed to build merger-ringdown waveform [113]. For the same reason, since typically $t^{\ell m}_{\rm peak} - t^{22}_{\rm peak} > 0$ [112, 114] the merger-ringdown attachment for all other modes is done at the peak of the $(2,2)$ mode, rather than at each mode's peak time as in other EOB models [112, 340].

Inspiral-plunge $h_{\ell m}$ modes

The inspiral-plunge EOB waveform modes are written as

$$h^{\rm insp\text{-}plunge}_{\ell m} = h^{\rm F}_{\ell m} N_{\ell m}\,, \tag{2.13}$$

where $h^{\rm F}_{\ell m}$ is a factorized, resummed version of the PN-expanded GW modes for aligned-spin binaries in circular orbits [316–319], while $N_{\ell m}$ is the numerically-tuned NQC correction [112, 316, 320], aimed at capturing radial effects during the plunge.

The factorized inspiral modes are written as:

$$h^{\rm F}_{\ell m} = h^{\rm N}_{\ell m} \hat{S}_{\rm eff} T_{\ell m} f_{\ell m} e^{i\delta_{\ell m}}. \tag{2.14}$$

The first factor $h^{\rm N}_{\ell m}$ is the mode at leading PN order (Newtonian). Its explicit expression can be found in Refs. [318, 319] for all (ℓ, m). The second factor $\hat{S}_{\rm eff}$ takes inspiration from the Regge-Wheeler-Zerilli equation sourced by a test mass μ, on circular orbits in a Schwarzschild background of mass M [318]. Depending on the parity of $\ell + m$, it is either identified with the effective energy $E_{\rm eff}$, or with the orbital angular momentum p_ϕ, both expressed as functions of $v = (M\Omega)^{1/3}$. The factor $T_{\ell m}$ resums an infinite number of leading logarithms entering the tail contributions [515]. The remaining factor is expressed as an amplitude $f_{\ell m}$ and a phase $\delta_{\ell m}$, which are computed such that the expansion of $h^{\rm F}_{\ell m}$ agrees with the PN-expanded modes. For m even, or for nonspinning binaries, $f_{\ell m}$ is further resummed as [318] $f_{\ell m} = (\rho_{\ell m})^\ell$ to reduce the magnitude of the 1PN coefficient, which grows linearly with ℓ. The $f_{\ell m}$ and $\rho_{\ell m}$ functions are expressed as expansions in $x = (M\Omega)^{2/3}$. In the phase terms $\delta_{\ell m}$, x can be replaced by $y = (H_{\rm EOB}\Omega)^{2/3}$ to gather relativistic corrections sourced by the binary's Arnowitt-Deser-Misner mass [318].

For m odd, the spins deserve a particular treatment to ensure a well-defined equal-mass limit. Indeed, the procedure above yields spin contributions to $\delta_{\ell m}$ and $\rho_{\ell m}$ inversely proportional to $\delta = \frac{m_1 - m_2}{M}$, making $h^{\rm F}_{\ell m}$ ill-defined in the equal-mass case. This issue traces back to $h_{\ell m}$ being zero when $\delta = 0$ at Newtonian order, while some of its spin contributions, entering at subleading PN orders, are not. Following Refs. [113, 319, 323, 325], we redefine the amplitude and phase as follows:

$$f_{\ell m} = \begin{cases} (\rho_{\ell m})^\ell, & m \text{ even}, \\ (\rho^{\rm noS}_{\ell m})^\ell + f^{\rm S}_{\ell m}, & m \text{ odd}, \end{cases} \tag{2.15}$$

$$\delta_{\ell m} = \begin{cases} \delta_{\ell m}, & m \text{ even}, \\ \delta^{\rm noS}_{\ell m}, & m \text{ odd}, \end{cases} \tag{2.16}$$

where $\rho^{\rm noS}_{\ell m}$ and $\delta^{\rm noS}_{\ell m}$ are inferred from the nonspinning limit of $f_{\ell m}$ and $\delta_{\ell m}$, while the additive constant $f^{\rm S}_{\ell m}$ reabsorbs their spin contributions, by expanding the complex exponential in Eq. (2.14). With these definitions, Eq. (2.14) has a well-defined equal-mass limit, as the terms inversely proportional to δ only enter $f_{\ell m}$ (and not $\rho_{\ell m}$ or $\delta_{\ell m}$), which is multiplied by $h^{\rm N}_{\ell m} \propto \delta$.

The explicit expressions for $\rho_{\ell m}$, $f_{\ell m}$ and $\delta_{\ell m}$ used in the SEOBNRv5HM model are given in Appendix B of Ref. [2]. Compared to the SEOBNRv4HM model, several improvements and corrections have been made:

- We correct the $\mathcal{O}(v^5 \delta \chi_A \nu)$ coefficient in ρ_{22}, whose value is 19/42, but was mistakenly replaced in the SEOBNRv4 code by 196/42.
- We correct the expressions for the (2,1) mode. As noted in Ref. [497], the $\mathcal{O}(v^6 \chi^2 \nu^2)$ terms in the $(2,1)$ mode in the SEOBNRv4HM model [113] are not correct, as well as the $\mathcal{O}(\nu v^5)$ nonspinning part of δ_{21}, whose coefficient had the value $-493/42$ [112, 318] instead of $-25/2$, due to an error in the (2,1) mode in Ref. [516], which was later corrected in an erratum.
- We include in ρ_{22} the next-to-leading order (NLO) spin-squared contribution at 3PN and the LO spin-cubed part at 3.5PN [Eq. (4.11a) of Ref. [497]].
- We include all known spin contributions to the (3,2) and (4,3) amplitudes [Eqs. (B2a) and (B5b) of Ref. [497]].
- We consistently include the high-order PN terms from Appendix A of Ref. [113] not only in the waveform modes but also in the RR force.

The remaining $N_{\ell m}$ factor in the inspiral-plunge modes (2.13) is the NQC correction

and reads

$$N_{\ell m} = \left[1 + \frac{\hat{p}_{r_*}^2}{(r\Omega)^2}\left(a_1^{h_{\ell m}} + \frac{a_2^{h_{\ell m}}}{\hat{r}} + \frac{a_3^{h_{\ell m}}}{\hat{r}^{3/2}}\right)\right] \times \exp\left[i\left(b_1^{h_{\ell m}}\frac{\hat{p}_{r_*}}{r\Omega} + b_2^{h_{\ell m}}\frac{\hat{p}_{r_*}^3}{r\Omega}\right)\right], \quad (2.17)$$

where $\hat{r} = r/M$ and $\hat{p}_{r_*} = p_{r_*}/\mu$. The NQC corrections ensures that the EOB modes amplitude and frequency match NR *input values*, given by fitting formulas, at the attachment time $t^{\ell m}_{\rm match}$. Specifically, the 5 constants ($a_1^{h_{\ell m}}$, $a_2^{h_{\ell m}}$, $a_3^{h_{\ell m}}$, $b_1^{h_{\ell m}}$, $b_2^{h_{\ell m}}$) are determined by requiring that the amplitude of the EOB modes $\left|h^{\rm insp\text{-}plunge}_{\ell m}\left(t^{\ell m}_{\rm match}\right)\right|$ and its first two derivatives, and the frequency of the EOB modes $\omega^{\rm insp\text{-}plunge}_{\ell m}\left(t^{\ell m}_{\rm match}\right)$ and its first derivative, are the same as those of the NR modes at $t = t^{\ell m}_{\rm match}$ [325, 335]. We point out that the NQC corrections are not included in the `SEOBNRv5HM` radiation-reaction force (2.8).

In the `SEOBNRv5` model, the input values are enforced at $t = t^{\ell m}_{\rm match}$, given in Eq. (2.12) as a function of the (2,2)-mode peak time $t^{22}_{\rm peak}$. We define

$$t^{22}_{\rm peak} = t_{\rm ISCO} + \Delta t_{\rm NR}\,, \quad (2.18)$$

where $t_{\rm ISCO}$ is the time at which the orbital separation reaches the geodesic ISCO radius $r_{\rm ISCO}$ of a Kerr spacetime with the mass and spin of the remnant, computed with NR fitting formulas [517, 518]. The parameter $\Delta t_{\rm NR}$ is a calibration coefficient, determined by comparing against NR simulations.

By contrast, in the `SEOBNRv4` model, the merger time was defined as

$$t^{22}_{\rm peak} = t^{\Omega}_{\rm peak} + \Delta t^{22}_{\rm peak}\,, \quad (2.19)$$

with $t^{\Omega}_{\rm peak}$ being the time when the orbital frequency peaks, and $\Delta t^{22}_{\rm peak}$ encodes the time delay between the peak of the orbital frequency and the $(2,2)$-mode amplitude peak observed in the test-mass limit [114, 115].

The definition adopted in `SEOBNRv5` is more robust, as it avoids relying on late-time dynamical features such as the existence of a well-defined orbital-frequency peak, which may not be present for all binary configurations when the Hamiltonian and modes are not the same as the ones used in the `SEOBNRv4` model. In particular, the `SEOBNRv4` model relied on a log-resummation of the A-potential [329, 330] to ensure the presence of a peak in the orbital frequency for aligned-spin binaries. This guarantee no longer holds in `SEOBNRv5`, where a Padé-resummed A-potential is used instead (see discussion below).

Another notable improvement in the `SEOBNRv5HM` waveforms is the addition of 2GSF calibration coefficients in the nonspinning GW mode amplitudes and RR force [364].

In that work, the amplitude factors $\rho_{\ell m}$ are expanded in the symmetric mass ratio as

$$\rho_{\ell m} = \rho^{(0)}_{\ell m} + \nu \rho^{(1)}_{\ell m} + \mathcal{O}\left(\nu^2\right), \tag{2.20}$$

and the terms $\rho^{(1),\mathrm{EOB}}_{\ell m}$ are augmented with corrections $\Delta\rho^{(1)}_{\ell m}$, expressed as polynomial in v^2 starting at the lowest order in v^2 not already included. The corrections $\Delta\rho^{(1)}_{\ell m}$ are determined by fitting to the numerical $\rho^{(1),\mathrm{GSF}}_{\ell m}$ results, and are then added directly to the full (not ν-expanded) $\rho_{\ell m}$ coefficients.

Merger-ringdown $h_{\ell m}$ modes

The merger-ringdown modes use a phenomenological ansatz [326], calibrated NR simulations and TPL waveforms. For the modes $(2,2)$, $(3,3)$, $(2,1)$, $(4,4)$, $(5,5)$, which show monotonic amplitude and frequency evolution, we adopt the same ansatz as Refs. [113, 335]:

$$h^{\text{merger-RD}}_{\ell m}(t) = \nu \tilde{A}_{\ell m}(t) e^{i\tilde{\phi}_{\ell m}(t)} e^{-i\sigma_{\ell m 0}\left(t - t^{\ell m}_{\text{match}}\right)}, \tag{2.21}$$

where $\sigma_{\ell m 0} = \sigma^{\mathrm{R}}_{\ell m} - i\sigma^{\mathrm{I}}_{\ell m}$ is the complex frequency of the least-damped QNM of the remnant BH, computed using the `qnm` package [519], with final BH mass and spin obtained from NR fits [517, 518].

The amplitude and phase functions $\tilde{A}_{\ell m}$ and $\tilde{\phi}_{\ell m}$ take the form [113, 335]:

$$\tilde{A}_{\ell m}(t) = c^{\ell m}_{1,c} \tanh\left[c^{\ell m}_{1,f}\left(t - t^{\ell m}_{\text{match}}\right) + c^{\ell m}_{2,f}\right] + c^{\ell m}_{2,c}, \tag{2.22}$$

$$\tilde{\phi}_{\ell m}(t) = \phi^{\ell m}_{\text{match}} - d^{\ell m}_{1,c} \log\left[\frac{1 + d^{\ell m}_{2,f} e^{-d^{\ell m}_{1,f}\left(t - t^{\ell m}_{\text{match}}\right)}}{1 + d^{\ell m}_{2,f}}\right], \tag{2.23}$$

where $\phi^{\ell m}_{\text{match}}$ is the phase of the inspiral-plunge mode (ℓ, m) at $t = t^{\ell m}_{\text{match}}$. The coefficients $d^{\ell m}_{1,c}$ and $c^{\ell m}_{i,c}$ $(i = 1, 2)$ are constrained by requiring $\mathcal{C}^1$-continuity for the amplitude and phase of $h_{\ell m}(t)$ at $t = t^{\ell m}_{\text{match}}$. The remaining free coefficients $c^{\ell m}_{i,f}$ and $d^{\ell m}_{i,f}$ $(i = 1, 2)$ are obtained by least-squares fits to a large set of 442 NR waveforms and BH perturbation-theory waveforms. We then interpolate these values across the parameter space using polynomials in fits in ν and χ, selected via a recursive feature elimination algorithm [520] with third- or fourth-order polynomial features, depending on the quantity. A similar fitting strategy is used for most input values, except for odd-m mode amplitudes and their derivatives, which vanish in the equal-mass and equal-spin limit and are better captured using custom nonlinear ansätze that enforce this symmetry.

Mode mixing in the (3,2) and (4,3) merger-ringdown $h_{\ell m}$ modes

The $(3,2)$ and $(4,3)$ merger-ringdown modes show post-merger oscillations [313, 521], due to the mismatch between the *spherical* harmonic basis used in waveform extraction and the *spheroidal* harmonics employed in BH perturbation theory. As a result, the standard ansätze of Eqs. (2.21), (2.23) cannot be directly applied.

Equation (1.25) can be formulated in terms of -2 spin-weighted spheroidal harmonics ${}_{-2}S_{\ell mn}$ as [522]:

$$h(t;\iota,\varphi) = \sum_{\ell\geq 2}\sum_{|m|\leq\ell}\sum_{n\geq 0} {}_{-2}S_{\ell mn}(\iota,\varphi)\ {}^{S}h_{\ell mn}(t), \tag{2.24}$$

where the superscript S denotes that the ${}^{S}h_{\ell mn}$ modes are expanded in the spheroidal-harmonics basis. The spheroidal-harmonic modes ${}^{S}h_{\ell mn}$ relate to the spherical-harmonic modes $h_{\ell m}$ via the transformation:

$$h_{\ell m}(t) = \sum_{\ell'\geq|m|}\sum_{n\geq 0} {}^{S}h_{\ell' mn}(t)\,\mu^{*}_{m\ell\ell' n}, \tag{2.25}$$

where the *mode-mixing* coefficients $\mu_{m\ell\ell' n}$ are obtained from fits in Ref. [244], and the star denotes the usual complex conjugation. Neglecting overtones ($n > 0$) and higher ℓ' contributions, which decay rapidly and are subdominant, we approximate Eq. (2.25) as [523]:

$$h_{\ell m}(t) \simeq \sum_{\ell'\leq\ell} {}^{S}h_{\ell' m0}(t)\,\mu^{*}_{m\ell\ell' 0}. \tag{2.26}$$

Applying this to the modes of interest:

$$h_{22}(t) \simeq \mu^{*}_{2220}\,{}^{S}h_{220}(t), \tag{2.27a}$$
$$h_{33}(t) \simeq \mu^{*}_{3330}\,{}^{S}h_{330}(t), \tag{2.27b}$$
$$h_{32}(t) \simeq \mu^{*}_{2320}\,{}^{S}h_{220}(t) + \mu^{*}_{2330}\,{}^{S}h_{320}(t), \tag{2.27c}$$
$$h_{43}(t) \simeq \mu^{*}_{3430}\,{}^{S}h_{330}(t) + \mu^{*}_{3440}\,{}^{S}h_{430}(t). \tag{2.27d}$$

From these equations, we can solve for the spheroidal ${}^{S}h_{\ell m0}$ modes to obtain

$${}^{S}h_{320}(t) \simeq \frac{h_{32}(t)\mu^{*}_{2220} - h_{22}(t)\mu^{*}_{2320}}{\mu^{*}_{2330}\mu^{*}_{2220}}, \tag{2.28a}$$
$${}^{S}h_{430}(t) \simeq \frac{h_{43}(t)\mu^{*}_{3440} - h_{33}(t)\mu^{*}_{3430}}{\mu^{*}_{3330}\mu^{*}_{3440}}. \tag{2.28b}$$

Figure 2.3 illustrates the effectiveness of this decomposition for the NR waveform `SXS:BBH:2138`. The h_{32} and h_{43} modes shows oscillations in their amplitude and

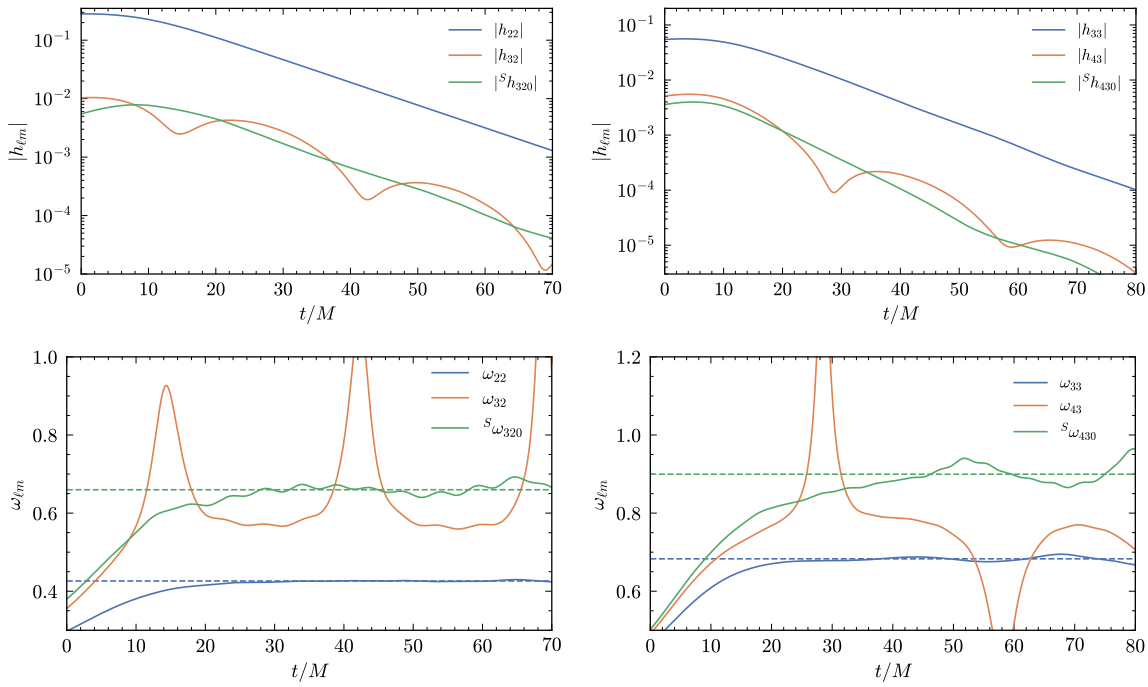

Figure 2.3: Mode-mixing in the NR simulation SXS:BBH:2138 ($q = 3.0, \chi_1 = -0.6, \chi_2 = 0.4$). *Upper panel*: Amplitude of the modes $|h_{\ell m}|$ and of $|{}^S h_{\ell m0}|$. We denote with $t = 0$ the time of the peak of the $(2, 2)$-mode amplitude. *Lower panel*: Frequencies of the modes $h_{\ell m}$ and of ${}^S h_{\ell m0}$. The ringdown frequencies of the spheroidal ${}^S h_{320}$ and ${}^S h_{430}$ modes are well approximated by the (3,2,0) and (4,3,0) QNM frequencies (dashed horizontal lines) after the mode-mixing removal.

frequency, while the "unmixed" spheroidal modes ${}^S h_{320}$ and ${}^S h_{430}$ exhibit smooth amplitude and frequency evolution, well approximating the corresponding (3,2,0) and (4,3,0) QNM frequencies at late times. We then model the spheroidal ${}^S h_{\ell m0}$ modes using the ansatz of Eq.(2.21), substituting $\phi^{\rm match}_{\ell m}$ with ${}^S\phi^{\rm match}_{\ell m0}$ and applying analogous replacements for amplitude and frequency in the matching conditions. Once ${}^S h_{320}$ and ${}^S h_{430}$ are modeled, the spherical $(3, 2)$ and $(4, 3)$ modes are reconstructed via Eqs. (2.28a) and (2.28b), combining them with the $(2, 2)$ and $(3, 3)$ modes.

2.2.3 Calibration to numerical-relativity waveforms

The inspiral-plunge modes described in Sec. 2.2.2 depend on the binary parameters $\mathbf{\Lambda} = (q, \chi_1, \chi_2)$, and a set of calibration parameters $\boldsymbol{\theta}$, to be determined as a function of $\mathbf{\Lambda}$ in order to maximize the agreement between the waveform model and NR simulations. In SEOBNRv5, we employ the following calibration parameters:

- $\boldsymbol{a_6}$: A linear-in-ν 5PN coefficient entering the nonspinning $A_{\rm noS}(u)$ potential [Eq. (2.3)].

- $\boldsymbol{d_{\rm SO}}$: A 4.5PN SO coefficient entering the odd-in-spin part of the Hamiltonian [Eqs. (2.4) and (2.5)].
- $\boldsymbol{\Delta t_{\rm NR}}$: A time shift between the Kerr ISCO and the peak of the $(2,2)$-mode amplitude [Eq.(2.18)].

The resummation of EOB potentials plays a key role in determining the model's flexibility to reduce differences with NR waveforms. In the `SEOBNRv5` model we apply:

- A (1,5) Padé resummation of the Taylor-expanded potential $A^{\rm Tay}_{\rm noS}(u)$ [Eq. (2.3)], while treating $\ln u$ as a constant.
- A (2,3) Padé resummation of the 5PN Talyor-expanded $\bar{D}^{\rm Tay}_{\rm noS}(u)$.

The Padé resummation of $A_{\rm noS}$ was originally introduced in Ref. [310] to guarantee the presence of an ISCO in the EOB dynamics at 3PN order for any mass ratio. It has since been used in several `SEOBNR` [112,112,321,328] and `TEOBResumS` [138,317,327,336,340] models. A (2,3) Padé resummation of $\bar{D}_{\rm noS}(u)$ has been recently explored in Ref. [524], albeit with different modeling choices for $A_{\rm noS}$ and $Q_{\rm noS}$.

In contrast, `SEOBNRv4` used a log-resummation of the A-potential, designed to enforce a peak in the orbital frequency for aligned-spin binaries, which was needed to attach the merger-ringdown at a time offset $\Delta t^{22}_{\rm peak}$ as given in Eq. (2.19). In `SEOBNRv5`, the attachment is based on $\Delta t^{22}_{\rm NR}$ relative to the Kerr ISCO, removing the reliance on the presence a peak in the orbital frequency. This enables us to use resummation choices that may not necessarily exhibit a light ring, but lead to improved agreement with NR. Similarly, the different resummation of the generic-spin Hamiltonian in `SEOBNRv5`, based on that of a test mass in a deformed Kerr background [144,311,333,334], instead of on the one of a test spin [330,390,510] in as in `SEOBNRv4`, is a crucial factor in achieving high faithfulness compared to NR simulations. Notably, this change allows us to reach higher accuracy with just one spin-dependent calibration parameter in the Hamiltonian ($d_{\rm SO}$), surpassing what could be obtained by tuning three such parameters in `SEOBNRv4`.

Numerical relativity dataset

We calibrate `SEOBNRv5HM` to 442 NR waveforms, all produced with the `SpEC` code of the SXS Collaboration [135,256,273,274,276,281,335,498–507], except for a simulation with mass ratio and dimensionless spins ($q=8,\ \chi_1=0.85,\ \chi_2=0.85$) produced with the `Einstein Toolkit` code [113,508]. We also include 13 waveforms computed by solving the Teukolsky equation in the framework of BH perturbation theory [114,115], with mass ratio $q=10^3$ and dimensionless spins $-0.99\leq\chi\leq 0.99$.

Figure 2.4 illustrates the NR and BH-perturbation-theory waveform coverage in

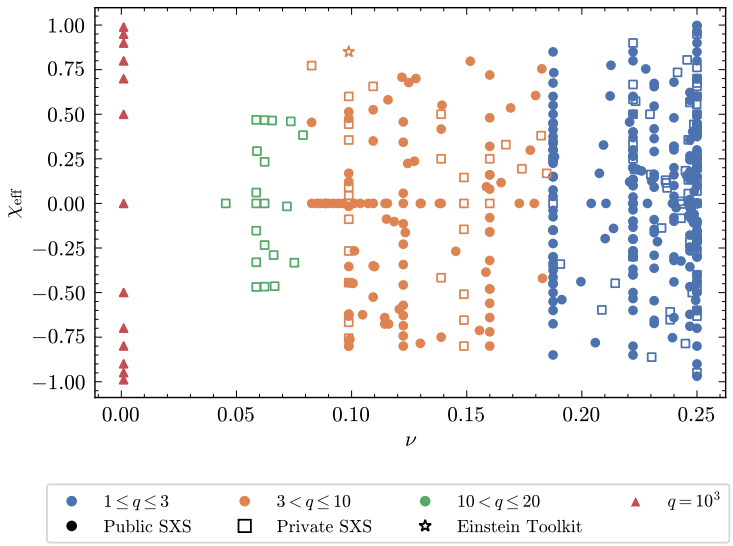

Figure 2.4: NR and BH-perturbation-theory waveforms used to calibrate SEOBNRv5HM, projected on the binary's parameters ν and $\chi_{\rm eff} = (\chi_1 m_1 + \chi_2 m_2)/M$. We highlight four regions as explained in the text, and use different markers to distinguish between 327 simulations from the public SXS catalog [256], 114 private SXS waveforms, one Einstein Toolkit simulation, and 13 Teukolsky-code waveforms.

the $(\nu, \chi_{\rm eff})$ plane, grouped by mass-ratio regions. For $1 \le q \le 3$, the dataset includes many configurations with spins on both BHs, reaching $\chi_{1,2} = 0.998$ for $q = 1$ and $\chi_{1,2} = 0.85$ for $q = 3$, similar to the coverage in SEOBNRv4HM. In the $3 < q \le 10$ range, we include significantly more configurations – with $-0.9 \le \chi_1 \le 0.85$ – than in SEOBNRv4HM. For $10 < q \le 20$, we have waveforms with spins only on the primary (up to $\chi_1 = 0.5$), and is a region where SEOBNRv4HM was previously uncalibrated. The final group consists of 13 Teukolsky-based waveforms at $q = 10^3$, with $-0.99 \le \chi \le 0.99$.

Calibration requirements

To calibrate the waveform model to NR, we first need to define a metric for waveform agreement. We use the mismatch (or unfaithfulness), defined in Eq. (1.45), computed using the zero-detuned high-power design PSD of Advanced LIGO [525]. In Eq. (1.37), we set $f_{\rm high} = 2048$ Hz and choose $f_{\rm low} = 1.35 f_{\rm start}$, where $f_{\rm start}$ is the frequency-domain peak of the NR waveform. The 1.35 factor helps exclude artifacts from the Fourier transform, especially important when comparing time-domain waveforms to frequency-domain models.

Given binary parameters:

$$\mathbf{\Lambda} = \{q, \chi_1, \chi_2\}, \tag{2.29}$$

and calibration parameters

$$\boldsymbol{\theta} = \{a_6, d_{\rm SO}, \Delta t_{\rm NR}\}, \tag{2.30}$$

we consider mismatch between $h_{\rm EOB}$ and $h_{\rm NR}$, for the same physical parameters $\boldsymbol{\Lambda}$, and as a function of the calibration parameters $\boldsymbol{\theta}$:

$$\mathcal{M}(\boldsymbol{\theta}) = 1 - \langle h_{\rm EOB}(\boldsymbol{\Lambda};\boldsymbol{\theta}) \mid h_{\rm NR}(\boldsymbol{\Lambda})\rangle \,. \tag{2.31}$$

Our calibration goal for `SEOBNRv5` is to find values of the calibration parameters $\boldsymbol{\theta}(\boldsymbol{\Lambda})$ to achieve $\mathcal{M} < 10^{-3}$ (99.9% faithfulness) for the dominant $(2,2)$ mode, an improvement over the 1% target in `SEOBNRv4`. Reaching this level of accuracy is challenging, but comparable to other state-of-the-art aligned-spin models [296, 298, 336], and it is motivated by the growing sensitivity of current and next-generation detectors [429]. Achieving $\mathcal{M} < 10^{-4}$ would require additional calibration parameters and careful treatment of NR uncertainties (estimated, for example, by comparing different resolutions or extrapolation orders of the same simulation), which are often at this level. As in `SEOBNRv4`, we also require that the merger time difference $\delta t_{\rm merger}$ (measured from the peak of the $(2,2)$ mode after low-frequency alignment) remains below $5M$, since the mismatch alone is not very sensitive to time offsets.

Nested-sampling analysis

Given the dimensionality of the problem and the large number of NR simulations available, we develop a computationally efficient and flexible calibration pipeline that improves upon the one used in `SEOBNRv4` [335]. That model employed MCMC to obtain a posterior distribution of the calibration parameters for each NR simulation; this is particularly beneficial as it provides insight on the correlations between calibration parameters. For our problem, we find better performance using nested sampling [178], implemented via the `nessai` sampler [526] through the `bilby` package [486].

We define the likelihood as:

$$\mathcal{L}(h^{\rm NR}|\boldsymbol{\theta}) \propto \exp\left[-\frac{1}{2}\left(\frac{\mathcal{M}_{\rm max}(\boldsymbol{\theta})}{\sigma_{\mathcal{M}}}\right)^2 - \frac{1}{2}\left(\frac{\delta t_{\rm merger}(\boldsymbol{\theta})}{\sigma_t}\right)^2\right], \tag{2.32}$$

where $\mathcal{M}_{\rm max}(\boldsymbol{\theta})$ is the maximum mismatch between EOB and NR waveforms over the total mass range $10M \leq M_\odot \leq 200M$, $\sigma_{\mathcal{M}}$ is chosen to be 10^{-3}, and σ_t is chosen to be $5M$, consistent with our calibration requirements. We calibrate `SEOBNRv5` to 442 NR waveforms, 441 from the `SXS` catalog and one from the `Einstein Toolkit`. We use uniform priors: $a_6 \in [-500, 500]$, $d_{\rm SO} \in [-500, 500]$, and $\Delta t^{22}_{\rm NR} \in [-100, 40]$.

For each NR simulation, the posterior $p(\boldsymbol{\theta}|h^{\rm NR})$ encodes the optimal values for the

calibration parameters and their correlations. To construct smooth functions $\boldsymbol{\theta}(\boldsymbol{\Lambda})$, we extract one mode from each posterior, based on continuity in parameter space. We then discard samples exceeding the mismatch or merger-time requirements. If this removes over 50% of the samples, we keep half of the original samples with the best likelihood values instead. We do this since, for a few of the most challenging NR simulations, like SXS:BBH:1124 ($q = 1$, $\chi_1 = \chi_2 = 0.998$), we do not find values of the calibration parameters that satisfy both requirements on $\mathcal{M}_{\rm max}$ and $\delta t_{\rm merger}$.

Following the strategy used in SEOBNRv4, we calibrate SEOBNRv5 hierarchically, starting with nonspinning (noS) simulations, then extending to aligned-spin systems. For the nonspinning calibration, we sample over 18 configurations (reserving the remaining 21 for validation), using the parameters

$$\boldsymbol{\theta}_{\rm noS} = \{a_6, \Delta t_{\rm NR,noS}\}. \tag{2.33}$$

Once the fits for $a_6(\nu)$ and $\Delta t_{\rm NR,noS}(\nu)$ are obtained, we fix them and proceed to calibrate against the 403 aligned-spin waveforms using

$$\boldsymbol{\theta}_{\rm S} = \{d_{\rm SO}, \Delta t_{\rm NR,S}\}, \tag{2.34}$$

with the total time shift expressed as

$$\Delta t_{\rm NR} = \Delta t_{\rm NR,noS} + \Delta t_{\rm NR,S}, \tag{2.35}$$

and where $\Delta t_{\rm NR,S}$ vanishes in the nonspinning limit.

Calibration-parameter fits and extrapolation

We now describe how we fit the calibration parameters $\boldsymbol{\theta} = \{a_6, \Delta t_{\rm NR}, d_{\rm SO}\}$ as functions of the binary parameters $\boldsymbol{\Lambda} = \{q, \chi_1, \chi_2\}$, using the calibration posteriors and incorporating information from the $\nu \to 0$ limit.

For a_6, we constrain its value in the test-mass limit by matching the ISCO frequency shift to GSF results [359, 527, 528], obtaining

$$a_6|_{\nu\to 0} \simeq 39.0967. \tag{2.36}$$

For $\Delta t_{\rm NR}$, we estimate the test-mass values, for different spin magnitudes, by imposing that the difference between the peak of the (2,2) mode and the peak of the orbital frequency in the EOB test-mass–limit waveforms matches the one measured in the Teukolsky-code waveforms [115]. We then convert the corresponding value to the difference between the ISCO and the peak of the (2,2)-mode amplitude.

The nonspinning parameters $\boldsymbol{\theta}_{\rm noS} = \{a_6, \Delta t_{\rm NR,noS}\}$ are simple to fit directly using least-squares regression on the maximum-likelihood points of the calibration posteriors, supplemented with their test-mass limits. We use a quartic polynomial in ν for a_6, and for $\Delta t_{\rm NR,noS}$ we adopt the ansatz

$$\Delta t_{\rm NR,noS} = (a_0 + a_1\,\nu + a_2\,\nu^2 + a_3\,\nu^3)\,\nu^{-1/5+a_4\,\nu}, \tag{2.37}$$

where the $\nu^{-1/5}$ factor ensures the expected test-mass scaling for $(t^{22}_{\rm peak} - t_{\rm ISCO})$ [309], and provides a better extrapolation of the fit in the $\nu \to 0$ limit.

For the aligned-spin parameters $\boldsymbol{\theta}_{\rm S} = \{d_{\rm SO}, \Delta t_{\rm NR,S}\}$, we improve on the method from `SEOBNRv4` [335]. Rather than fitting the mean of each posterior, we fit their medians, as this provides better agreement with NR. We express the fits in terms of $(\nu, a+, a_-)$ instead of (ν, χ), where $\chi = \chi_S + \chi_A\delta/(1-2\nu)$, as this provides a better result, also when using a subset of NR simulations for the fit, or when comparing to independent sets of `NRHybSur3dq8` [276] waveforms not used in the calibration. We rescale $\Delta t_{\rm NR,S}$ by $\nu^{1/5}$ to ensure the correct test-mass scaling. We parametrize $d_{\rm SO}$ by a cubic polynomial in (ν, a_+, a_-) and $\Delta t_{\rm NR,S}\nu^{1/5}$ by a cubic polynomials in (ν, a_+, a_-) with an additional a_+^4 feature. The polynomial coefficients are obtained by minimizing

$$\chi^2_{\rm s} = \sum_{n\in\mathcal{S}_{\rm s}} \frac{w}{2}\left(\boldsymbol{\theta}_{\rm S} - \langle\boldsymbol{\theta}_{\rm S}\rangle_{(n)}\right)\left(C^{-1}_{\rm S}\right)_{(n)}\left(\boldsymbol{\theta}_{\rm S} - \langle\boldsymbol{\theta}_{\rm S}\rangle_{(n)}\right)^{\rm T} + \chi^2_{\rm TPL}, \tag{2.38}$$

where $\langle\boldsymbol{\theta}_{\rm S}\rangle_{(n)}$ are the medians, and $C_{{\rm S}(n)}$ the covariance matrices of the calibration posteriors, with n labeling each of the 442 NR simulations. The term $\chi^2_{\rm TPL}$ penalizes deviations from the test-mass values of $\Delta t_{\rm NR,S}$:

$$\chi^2_{\rm TPL} = \sum_{\chi_i\neq 0} \frac{\left(\Delta t_{\rm NR,S} - \Delta t^{22,\rm TPL}_{{\rm ISCO},\chi_{\rm i}}\right)^2}{\sigma^2_{\rm TPL}}, \tag{2.39}$$

in which $\Delta t^{22,\rm TPL}_{{\rm ISCO},\chi_{\rm i}}$ are the estimated test-mass values of $\Delta t^{22}_{\rm ISCO,S}$, and we take $\sigma_{\rm TPL} = 5M$. The weighting function

$$w = \chi_1^2 + \chi_2^2 + \frac{|\chi|}{2\nu}\,, \tag{2.40}$$

accounts for the uneven NR coverage across the BBH parameter space. Final fit expressions are provided in Eqs.(78) – (81) of Ref. [2].

To ensure a robust behavior of the fits between the last calibration points and extreme-mass-ratio limit, we perform exhaustive checks of the sanity of the waveform model across a broad range of the parameter space ($q \in [1, 100]$, covering the full spin

range). The tests include visual inspections of the waveforms, assessing stability in response to perturbations of the intrinsic parameters, verifying the monotonicity of the amplitude and frequency of the $(2,2)$ mode up its peak and confirming that the higher modes consistently maintain amplitudes smaller than the $(2,2)$ mode, up to the merger.

2.2.4 Validation of the SEOBNRv5HM model

To assess the accuracy improvements introduced in the SEOBNRv5HM model, we compare it against the NR simulations described in Sec. 2.2.3, as well as against other state-of-the-art aligned-spin waveform models. We assess performance using faithfulness calculations, as well as comparisons of the binding energy against NR.

Faithfulness for multipolar waveforms

The strain in the detector caused by a passing GW in Eq. (1.34) can be expressed in terms of an effective polarization angle $\kappa(\alpha,\delta,\psi)$ as

$$h(t) = \mathcal{A}(\alpha,\delta)(h_+\cos\kappa + h_\times \sin\kappa), \tag{2.41}$$

where the dependences of κ, h_+ and $h_\times$ have been removed to ease the notation, and the definition of the coefficient $\mathcal{A}(\alpha,\delta)$ can be found in Refs. [113, 134].

To quantify agreement between two multipolar waveforms – the signal h_s and template h_t – we define the faithfulness [113, 134, 297]:

$$\mathcal{F}(M_\mathrm{s},\iota_\mathrm{s},\varphi_\mathrm{s},\kappa_\mathrm{s}) = \max_{t_c,\varphi_t,\kappa_t}\left[\frac{\langle h_s|h_t\rangle}{\sqrt{\langle h_s|h_s\rangle\langle h_t|h_t\rangle}}\bigg|_{\iota_\mathrm{s}=\iota_t}\right]. \tag{2.42}$$

The maximization is performed over coalescence time t_c, reference phase φ_t, and effective polarization angle κ_t (the latter analytically, following [529]), and we set the inclination angle $\iota_s = \iota_t$. To reduce the dimensionality of the faithfulness function, it is useful to define the sky-and-polarization-averaged faithfulness [133, 134] as

$$\overline{\mathcal{F}}\,(M_\mathrm{s},\iota_\mathrm{s}) = \frac{1}{8\pi^2}\int_0^{2\pi} d\kappa_\mathrm{s}\int_0^{2\pi} d\varphi_\mathrm{s}\mathcal{F}\,(M_\mathrm{s},\iota_\mathrm{s},\varphi_\mathrm{s},\kappa_\mathrm{s})\,, \tag{2.43}$$

as well as the SNR-weighted variant [113, 134]:

$$\overline{\mathcal{F}}_\mathrm{SNR}\,(M_\mathrm{s},\iota_\mathrm{s}) = \sqrt[3]{\frac{\int_0^{2\pi} d\kappa_\mathrm{s}\int_0^{2\pi} d\varphi_\mathrm{s}\mathcal{F}^3\,(M_\mathrm{s},\iota_\mathrm{s},\varphi_\mathrm{s},\kappa_\mathrm{s})\,\mathrm{SNR}^3\,(\iota_\mathrm{s},\varphi_\mathrm{s},\kappa_\mathrm{s})}{\int_0^{2\pi} d\kappa_\mathrm{s}\int_0^{2\pi} d\varphi_\mathrm{s}\,\mathrm{SNR}^3\,(\iota_\mathrm{s},\varphi_\mathrm{s},\kappa_\mathrm{s})}}, \tag{2.44}$$

where $\mathrm{SNR}\,(\iota_\mathrm{s}, \varphi_\mathrm{s}, \kappa_\mathrm{s}) = \sqrt{(h_\mathrm{s}, h_\mathrm{s})}$. The weighting by the SNR in Eq. (2.44) accounts for the different loudness of the signal as function of the phase and effective polarization angle, at a fixed distance. The corresponding sky-and-polarization averaged, SNR-weighted unfaithfulness is

$$\overline{\mathcal{M}}_\mathrm{SNR} = 1 - \overline{\mathcal{F}}_\mathrm{SNR}. \tag{2.45}$$

Accuracy of `SEOBNRv5` (2,2) mode

We begin by considering (2,2)-mode only mismatches. In this case, the mismatch is independent of inclination and reduces to the definition given by Eq. (1.45). Figure 2.5 shows the (2,2)-mode mismatch as a function of total mass (10 – 300) $M_\odot$ for the 442 NR simulations described in Sec. 2.2.3, comparing several state-of-the-art aligned-spin waveform models: `SEOBNRv5`, its predecessor `SEOBNRv4` [335], `TEOBResumS-GIOTTO` [336, 339, 340, 530], and the Fourier-domain phenomenological model `IMRPhenomXAS` [296]. Colored lines highlight cases with the worst maximum mismatch for each model. As expected, the largest mismatches arise for systems with high mass ratios and large spins, regions with limited NR calibration coverage. Notably, `SEOBNRv5` exhibits no mismatches above 0.3% and achieves systematically lower unfaithfulness than other models, particularly compared to `SEOBNRv4` and `TEOBResumS-GIOTTO`. The top two panels of Fig. 2.5 show that `SEOBNRv5` improves unfaithfulness by nearly an order of magnitude over `SEOBNRv4`.

The top panel of Fig. 2.6 shows histograms of the maximum (2,2)-mode mismatch over the same range of total masses. We also include an estimate of the NR error, computed as the mismatch between the highest and second-highest resolution waveforms; differences due to extrapolation order are typically an order of magnitude smaller and are omitted here. Vertical dashed lines mark to the medians. Among all models, `IMRPhenomXAS` yields the lowest median unfaithfulness (1.31×10^{-4}), though it has two outliers above 0.3%. `SEOBNRv5` follows closely with median mismatch 1.99×10^{-4}, and a long tail extending to mismatches as low as 10^{-5}. `TEOBResumS-GIOTTO` performs slightly worse, with a median of 5.12×10^{-4}, while `SEOBNRv4` is the least faithful, with a median of 1.44×10^{-3} – nearly an order of magnitude above `SEOBNRv5`. Table 2.2 summarizes these results, including the fraction of cases below 10^{-3} and 10^{-4}. The median NR error, $\sim 2 \times 10^{-5}$, is about an order of magnitude smaller than the modeling error of `SEOBNRv5`. However, in a few cases they are comparable, indicating that improving NR accuracy would be critical for reducing modeling errors by another order of magnitude. The right panel of Fig. 2.6 provides a complementary summary of the unfaithfulness calculation, by showing the distribution of the maximum (blue), median (orange) and minimum (green) mismatch over the same range of total masses for the different models.

Approximant	SEOBNRv4	SEOBNRv5	IMRPhenomXAS	TEOBResumS
median $\max_M \mathcal{M}$	1.44×10^{-3}	1.99×10^{-4}	1.31×10^{-4}	5.12×10^{-4}
% $\max_M \mathcal{M} < 10^{-3}$	38%	90%	97%	76%
% $\max_M \mathcal{M} < 10^{-4}$	1%	27%	29%	1%

Table 2.2: Summary of the (2,2)-mode mismatch over a range of total masses between 10 and 300 $M_\odot$, between different aligned-spin approximants and the 442 NR simulations used in this work. We show the median of the maximum mismatch across total mass, and the fraction of cases with unfaithfulness below 10^{-3} and 10^{-4}.

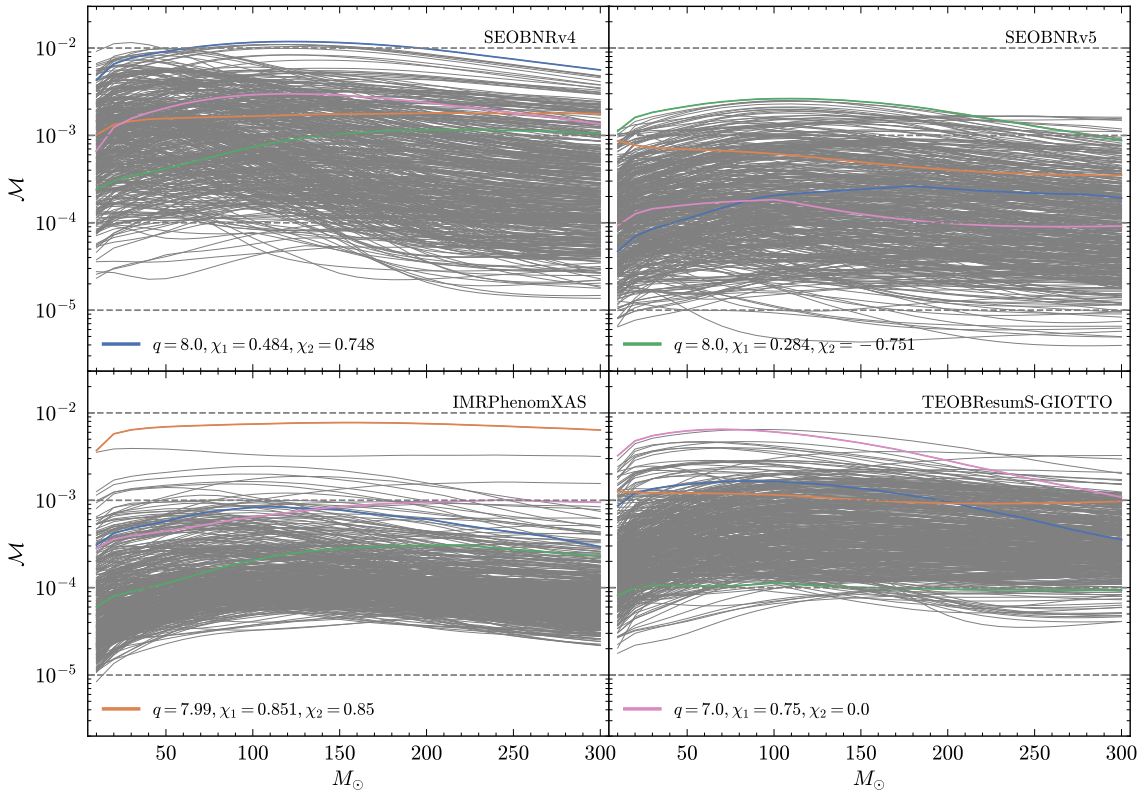

Figure 2.5: (2,2)-mode mismatch as a function of total mass (10 – 300) $M_\odot$, between different aligned-spin approximants and the 442 NR simulations used in this work. Colored lines highlight cases with the worst maximum mismatch for each model. SEOBNRv5 shows no mismatches above 0.3% and significantly lower unfaithfulness overall, particularly relative to SEOBNRv4 and TEOBResumS-GIOTTO.

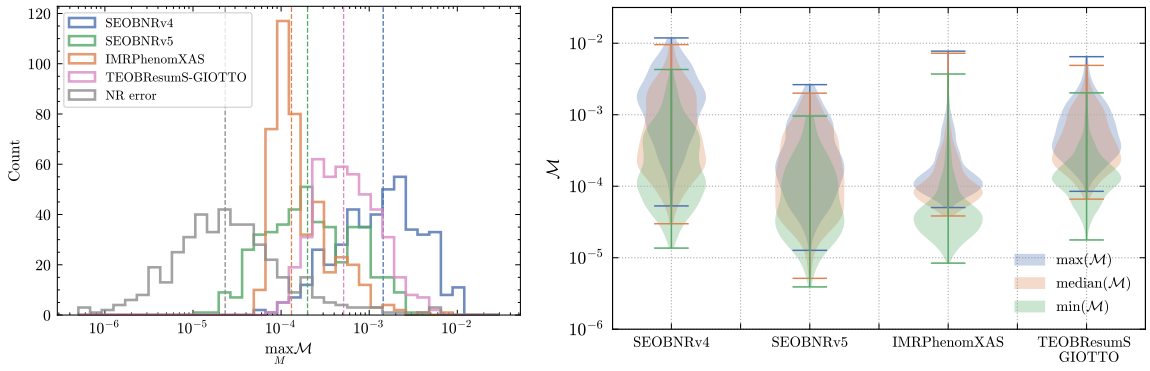

Figure 2.6: *Left panel*: Histogram of the maximum (2,2)-mode mismatch over a range of total masses between 10 and 300 $M_\odot$, between different aligned-spin approximants and the 442 NR simulations used in this work. The NR error is estimated by computing the mismatch between NR simulations with the highest and second-highest resolutions. The vertical dashed lines show the medians. *Right panel:* Distribution of the maximum (blue), median (orange) and minimum (green) mismatch over the same range of total masses for the different models.

Approximately 10% of the configurations give mismatches above 0.1% for `SEOBNRv5`, primarily corresponding to high-spin systems, both for large mass-ratios and for $q \simeq 1$ where spin magnitudes can reach values up to 0.998. These cases could be improved in future upgrades by incorporating full 5PN spin contributions to the conservative dynamics [235,511–513,531–536], as well as complete 3.5PN spin terms in the waveform modes [497, 537], or by introducing additional spin-dependent calibration parameters beyond $d_{\rm SO}$.

Accuracy of the `SEOBNRv5HM` modes

We now consider mismatches for the full polarizations, including higher-order modes. Figure 2.7 shows the sky-and-polarization averaged, SNR-weighted mismatch, for inclination $\iota = \pi/3$, across total masses between 20 and 300 $M_\odot$, comparing the 441 `SXS` NR simulations to various multipolar aligned-spin approximants: `SEOBNRv4HM` [113], `SEOBNRv5HM`, `TEOBResumS-GIOTTO` [336, 339, 340, 530] and `IMRPhenomXHM` [297]. Each model includes its full available mode content: $(\ell, |m|) = (2,2), (2,1), (3,3), (4,4), (5,5)$ for `SEOBNRv4HM`, $(\ell, |m|) = (2,2), (2,1), (3,3), (3,2), (4,4), (4,3), (5,5)$ for `SEOBNRv5HM`, $(\ell, |m|) = (2,2), (2,1), (3,3), (3,2), (4,4)$ for `IMRPhenomXHM` and $(\ell, |m|) = (2,2)$,-$(2,1), (3,3), (3,2), (3,1), (4,4), (4,3), (4,2)$ for `TEOBResumS-GIOTTO`. We exclude the `Einstein Toolkit` simulation here, as it only provides the (2,2) mode.

As in earlier comparisons, we highlight the configurations with the worst mismatch for each model. These outliers occur near the boundaries of the NR parameter space,

Approximant	SEOBNRv4HM	SEOBNRv5HM	IMRPhenomXHM	TEOBResumS
median $\max_M \overline{\mathcal{M}}_{\rm SNR}$	3.11×10^{-3}	1.01×10^{-3}	2.50×10^{-3}	4.59×10^{-3}
% $\max_M \overline{\mathcal{M}}_{\rm SNR} < 10^{-2}$	88%	98%	86%	74%
% $\max_M \overline{\mathcal{M}}_{\rm SNR} < 10^{-3}$	5%	49%	23%	0%

Table 2.3: Summary of the sky-and-polarization averaged, SNR-weighted mismatch, for inclination $\iota = \pi/3$, over a range of total masses between 20 and 300 $M_\odot$, between different aligned-spin multipolar approximants and the 441 SXS NR simulations used in this work. We show the median of the maximum mismatch across total mass, and the fraction of cases with unfaithfulness below 10^{-2} and 10^{-3}.

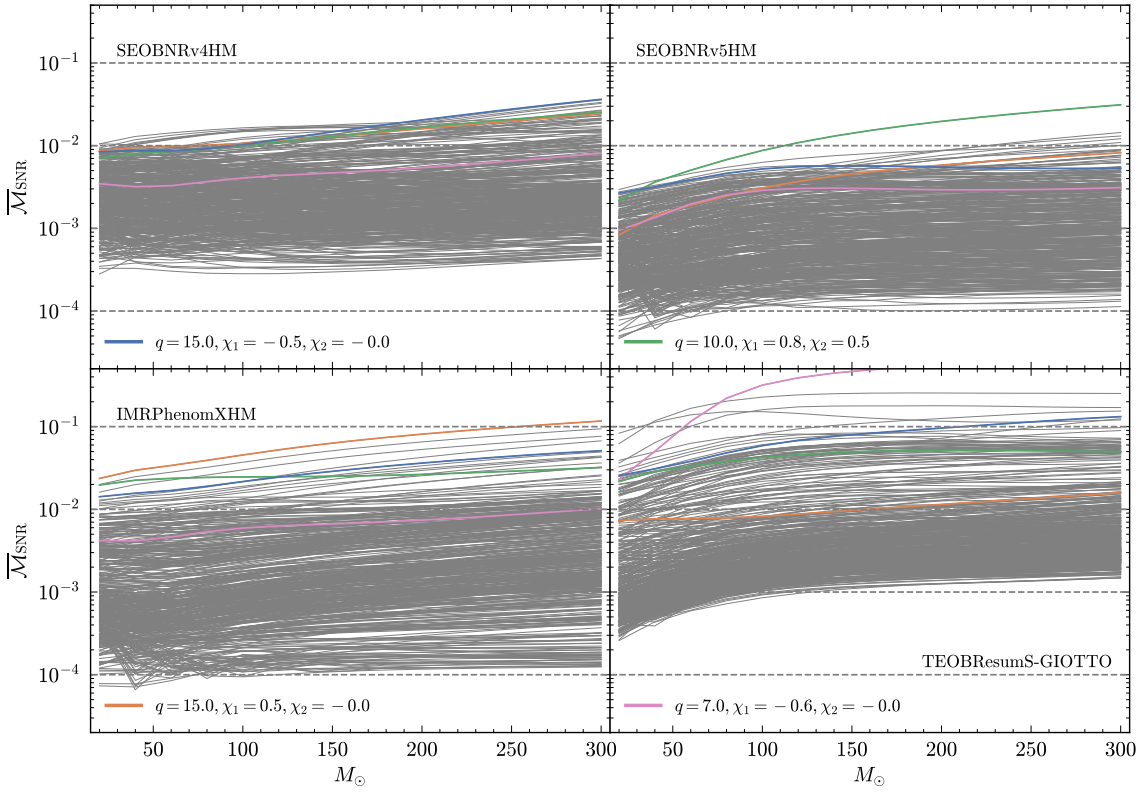

Figure 2.7: The sky-and-polarization averaged, SNR-weighted mismatch, for inclination $\iota = \pi/3$, as a function of total mass (20 – 300 $M_\odot$), between different aligned-spin multipolar approximants and the 441 SXS NR simulations used in this work. The colored lines highlight cases with the worst maximum mismatch for each model.

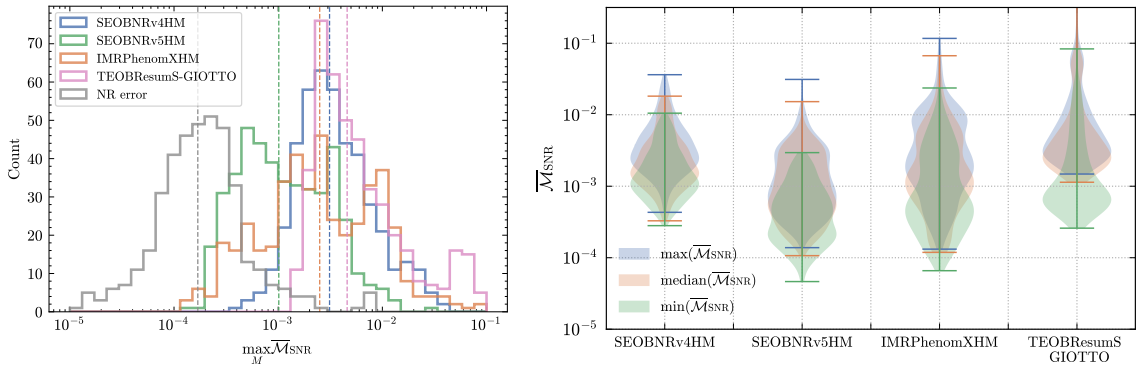

Figure 2.8: *Left panel:* Histogram of the maximum sky-and-polarization averaged, SNR-weighted mismatch, for inclination $\iota = \pi/3$, over a range of total masses between 20 and 300 $M_\odot$, between different aligned-spin multipolar approximants and the 441 `SXS` NR simulations used in this work. The NR error is estimated by computing the mismatch between NR simulations with the highest and second-highest resolutions. The vertical dashed lines show the medians. *Right panel:* Distribution of the maximum (blue), median (orange) and minimum (green) mismatch over the same range of total masses for the different models.

typically at large mass ratios with non-zero spins, where higher modes contribute substantially to the waveform, also due to the significant inclination $\iota = \pi/3$. All models show larger mismatches than in the (2,2)-only case, as expected due to the limited alignment freedom (the phase φ in Eq. (1.25) is shared across all modes), but also because the higher modes are available at lower PN order than the dominant one, and their modeling close to merger is complicated by numerical noise in NR simulations.

Focusing on the upper panels, we observe a clear improvement from `SEOBNRv4HM` to `SEOBNRv5HM`, with many more cases falling in the 10^{-4} – 10^{-3} range, and only a few outliers exceeding 1% mismatch at high total mass. The improvement at low total mass, where the inspiral dominates, is especially notable: `SEOBNRv5HM` stays below 0.3% against all simulations. However, the rise in mismatch at high masses (not seen in the (2,2)-only case) suggests limitations in the merger-ringdown modeling of higher modes, a common issue among models. Another contributing factor is the absence of some subdominant modes, which can significantly affect the ringdown signal for high-q, at a high inclination.

Turning to the lower panels, `IMRPhenomXHM` performs well in many cases, with a significant fraction of mismatches in the 10^{-4} – 10^{-3} range. However, it shows large mismatches, exceeding 10%, for high mass-ratio spinning binaries, where higher modes are critical. This is expected, since `IMRPhenomXHM` was not calibrated to the recently produced $q = 15$ `SXS` simulations [281], but instead to private $q = 18$ `BAM` waveforms

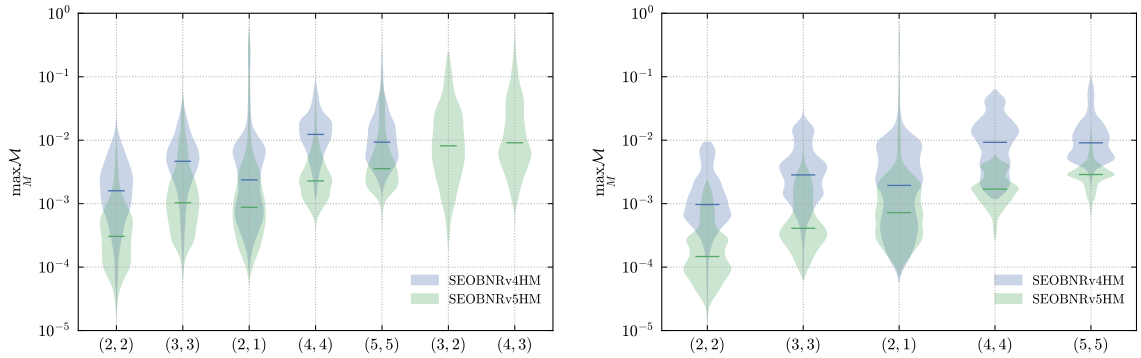

Figure 2.9: *Left panel*: Mode-by-mode mismatches between SEOBNRv4HM, SEOBNRv5HM and NRHybSur3dq8, for 5000 random configurations with $q \in [1, 8], |\chi_i| \leq 0.9$. *Right panel*: Mode-by-mode mismatches between SEOBNRv4HM, SEOBNRv5HM and NRHybSur2dq15, for 5000 random configurations with $q \in [1, 15], |\chi_1| \leq 0.6, \chi_2 = 0$. For each mode we show the maximum mismatch over a range of total masses between 10 and 300 $M_\odot$. The horizontal lines show the medians

with different spin configurations, which were not used in SEOBNRv5HM calibration. TEOBResumS-GIOTTO generally yields mismatches between 10^{-3} and 10^{-2}, but also exhibits several outliers with mismatches up to 10%, possibly due to instabilities in some higher-modes close to merger.

Figure 2.8 summarizes the comparison of Fig. 2.7. The left panel shows histograms of the maximum mismatch across total mass, with vertical lines marking the medians, alongside an estimate of NR error from different numerical resolution. As in the (2,2)-mode only case, the NR error is roughly one order of magnitude smaller than the SEOBNRv5HM modeling error, with median mismatch $\sim 1 \times 10^{-4}$. Among the models compared, SEOBNRv5HM achieves the lowest overall unfaithfulness, with a median of 1.01×10^{-3} and only 7 cases exceeding 1%, as summarized in Table 2.3. The violin plots in the right panel provide a further comparison by showing the distribution of the maximum (blue), median (orange) and minimum (green) mismatch for each approximant.

To further validate SEOBNRv5HM, we compare it against the multipolar aligned-spin surrogate model NRHybSur3dq8 [276]. This model was trained for binaries with mass-ratios $1 - 8$ and spin magnitudes up to 0.8, and provides waveforms with errors comparable to the NR accuracy in its training region. Since NRHybSur3dq8 was not used in constructing SEOBNRv5HM, this serves as an important cross-validation of our NR calibration. For these comparisons, we use a dimensionless initial orbital frequency of $M\Omega_0 = 0.015$.

The left panel of Fig. 2.9 compares SEOBNRv4HM and SEOBNRv5HM against NRHyb-

Sur3dq8, showing a distribution of the maximum mode-by-mode mismatches between them. We use 5000 random configurations with $q \in [1, 8]$, $|\chi_i| \leq 0.9$, allowing some extrapolation outside of the surrogate's training region. The (2,2) mode mismatch for SEOBNRv5HM has a median of $\sim 3 \times 10^{-4}$, consistent with results against NR and only slightly higher due to the inclusion of more challenging high-q, high-spin systems. Maximum mismatches remain below 1% within the surrogate's training region, and only marginally exceed it when extending to $|\chi_i| = 0.9$, confirming good extrapolation behavior of the SEOBNRv5HM fits. Compared to SEOBNRv4HM, SEOBNRv5HM shows fewer cases above 0.01 mismatch, and much lower median unfaithfulness. Higher-mode mismatches are generally larger, as expected due to increased modeling difficulty (both for EOB models and for NRHybSur3dq8) and larger NR noise. Still, SEOBNRv5HM outperforms SEOBNRv4HM across all modes, thanks to improved calibration and a better merger-ringdown model. The (2,1) mode shows a tail of higher mismatches for both models: as also discussed in Ref. [113] those are cases with a minimum in the amplitude close to merger, which can be especially difficult to model given that the current merger-ringdown ansatz assumes a monotonic post-merger amplitude evolution. Nonetheless, these are configurations where the (2,1) mode is highly suppressed, and contribute little to the full polarizations. The (3,2) and (4,3) modes, absent in SEOBNRv4HM, are included in the comparison with SEOBNRv5HM; as expected, they show the largest mismatches due to their small amplitude and approximate treatment of mode mixing.

The right panel of Fig. 2.9 shows a similar comparison against NRHybSur2dq15 [281], limited to the modes modeled by the surrogate. This model was trained for binaries with mass-ratios $1 - 15$, primary spin up to 0.5 and no secondary spin. We consider 5000 random configurations with $q \in [1, 15]$, $|\chi_1| \leq 0.6$, $\chi_2 = 0$, allowing again some extrapolation outside of the surrogate's training region. We see a similarly large improvement for all the modes comparing SEOBNRv5HM to SEOBNRv4HM, and the (2,2) mode result, with maximum value 2.3×10^{-3} and median 1.5×10^{-4}, confirms the robustness and accuracy of the SEOBNRv5HM calibration across a broad parameter range.

In the upper panel of Fig. 2.10 we show the sky-and-polarization averaged, SNR-weighted mismatch, for inclination $\iota = \pi/3$, between SEOBNRv5HM and NRHybSur3dq8, for 2000 random configurations with $q \in [1, 8]$, $|\chi_i| \leq 0.8$. The color scale shows the maximum mismatch as a function of the mass-ratio q and the primary spin χ_1. As expected, the unfaithfulness grows with mass ratio and spin, reaching values up to 0.04. This trend is also amplified by the fact that we start all the waveforms at the same frequency, and for higher q the number of cycles in band grows as $\sim 1/\nu$. The lower panel of Fig. 2.10 shows similar comparison between SEOBNRv5HM and IMRPhenomXHM,

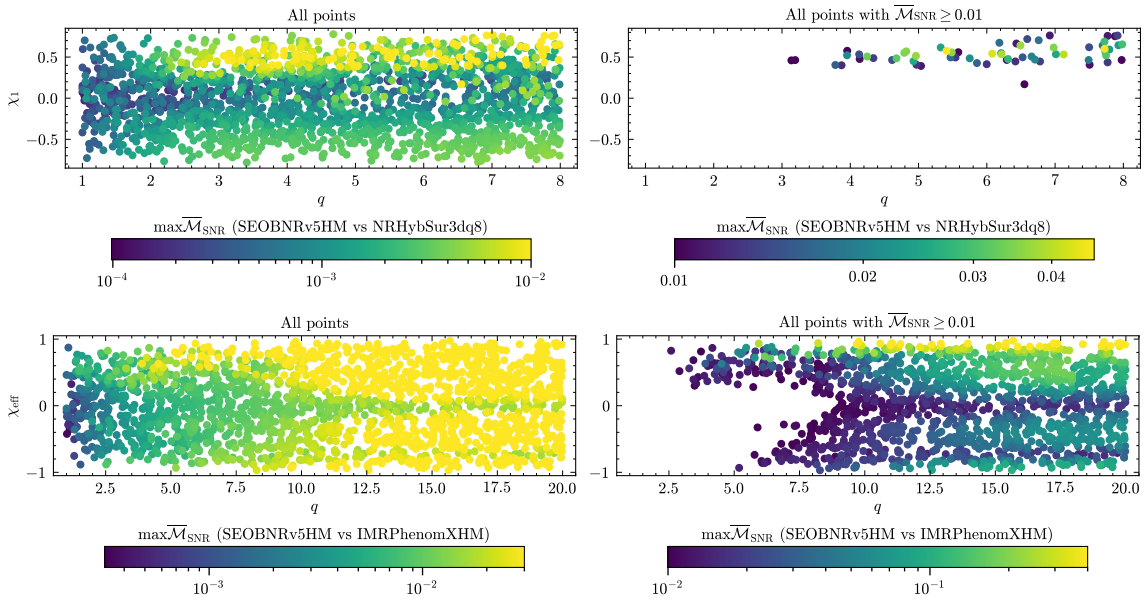

Figure 2.10: *Upper panel*: Sky-and-polarization averaged, SNR-weighted mismatch, for inclination $\iota = \pi/3$, between `SEOBNRv5HM` and `NRHybSur3dq8`, for 2000 random configurations with $q \in [1, 8], |\chi_i| \leq 0.8$. The color scale shows the maximum mismatch over a range of total masses between 20 and 300 $M_\odot$, as a function of the mass-ratio q and the primary spin χ_1. *Lower panel*: Same quantity, but comparing `SEOBNRv5HM` and `IMRPhenomXHM`, for 2000 random configurations with $q \in [1, 20], |\chi_i| \leq 0.99$, as a function of the mass-ratio q and the effective spin $\chi_{\rm eff}$.

for 2000 random configurations with $q \in [1, 20]$, $|\chi_i| \leq 0.99$ in order to examine the behavior of the models outside of the region in which they were calibrated to NR. As in the previous comparsion, the unfaithfulness grows with mass-ratio and spin, and can reach very large values for $q \simeq 20$ and high $\chi_{\rm eff}$. This confirms that waveform systematics are important, even for aligned-spin systems observed by current detectors, in the region where waveform models are not calibrated to NR simulations.

Accuracy of the `SEOBNRv5` binding energy

The performance of waveform models is typically assessed by computing their unfaithfulness against NR waveforms, as the waveform itself is the relevant quantity used in data analysis. In EOB models, however, the knowledge of the binary's dynamics allows us to complement the waveform comparison with other dynamical quantities. Since the calibration of the model to NR is based on the waveforms, seeing an improvement in different dynamical quantities is an important check of the physical robustness of the model. In particular, we examine the binding energy [376–378]. The NR binding energy data used here was obtained in Ref. [378], while the EOB binding energy is computed by evaluating $E_{\rm EOB} = (H_{\rm EOB} - M)/\mu$ along the EOB dynamics. The

EOB orbital frequency is obtained as $\Omega_{\rm EOB} = \partial H_{\rm EOB}/\partial p_\phi$, to be consistent with the gauge-invariant definition used for NR [378].

The upper panel of Fig. 2.11 shows the fractional difference between the NR binding energy for nonspinning configurations, and that of `SEOBNRv4` and `SEOBNRv5`, for different mass-ratios. The gray region is an estimate of the NR error obtained from the $q = 1$ data. Both EOB models agree well with NR throughout most of the inspiral, and stay within the NR uncertainty until around 3 GW cycles before merger. The `SEOBNRv5` model shows, however, a much better agreement in the late-inspiral, between 3 and 1 cycles before merger, and remains within the error until $v \simeq 0.45$ for all mass-ratios. As highlighted in Ref. [364], this improvement is largely due to the calibration to 2GSF results.

We now examine aligned-spin cases, focusing on different spin contributions to the binding energy. These can be isolated combining results from equal-mass NR simulations with various spin configurations, following Refs. [334, 378, 538]:

$$E_{\rm SO} = -\frac{1}{6}(-0.6, 0) + \frac{8}{3}(0.3, 0) - 2(0, 0) - \frac{1}{2}(0.6, 0), \tag{2.46a}$$

$$E_{\rm S^2} = \frac{3}{2}(-0.6, 0) - 2(0, 0) + \frac{3}{2}(0.6, 0) - (0.6, -0.6), \tag{2.46b}$$

where the numbers in brackets correspond to the dimensionless spins (χ_1, χ_2) of the BHs.

We begin by considering the spin-orbit effects. In the bottom-left panel of Fig. 2.11 we compare the NR data to `SEOBNRv4` and `SEOBNRv5`. In both cases, we consider calibrated and uncalibrated models (where calibration parameters in the Hamiltonian are set to zero). `SEOBNRv5` has better agreement with NR compared to `SEOBNRv4`, and remains within the NR error almost until merger. Moreover, the calibrated `SEOBNRv5` model performs better than the uncalibrated model during the entire inspiral, whereas in `SEOBNRv4` the NR-calibration degrades the agreement after $v \simeq 0.45$. The results for the spin-spin term are shown in the bottom-right panel of Fig. 2.11: again, `SEOBNRv5` outperforms `SEOBNRv4`, and has differences compatible with the NR uncertainty almost up to merger. An interesting difference is that NR-calibration improves `SEOBNRv5`'s performance, while it degrades agreement in `SEOBNRv4`. This shows that the calibration of the model, which focuses on producing accurate waveforms, is not guaranteed to provide a better description of the conservative dynamics in the strong-field regime. A possible reason for this difference might be the additional presence of a spin-spin calibration parameter $d_{\rm SS}$ in `SEOBNRv4`, breaking the symmetry underlying the extraction of the terms used here [378]. It is also possible that, due to degeneracies between changes in the dissipative and conservative dynamics, the less accurate flux of `SEOBNRv4` is compensated by the calibration of the Hamiltonian, and results in an

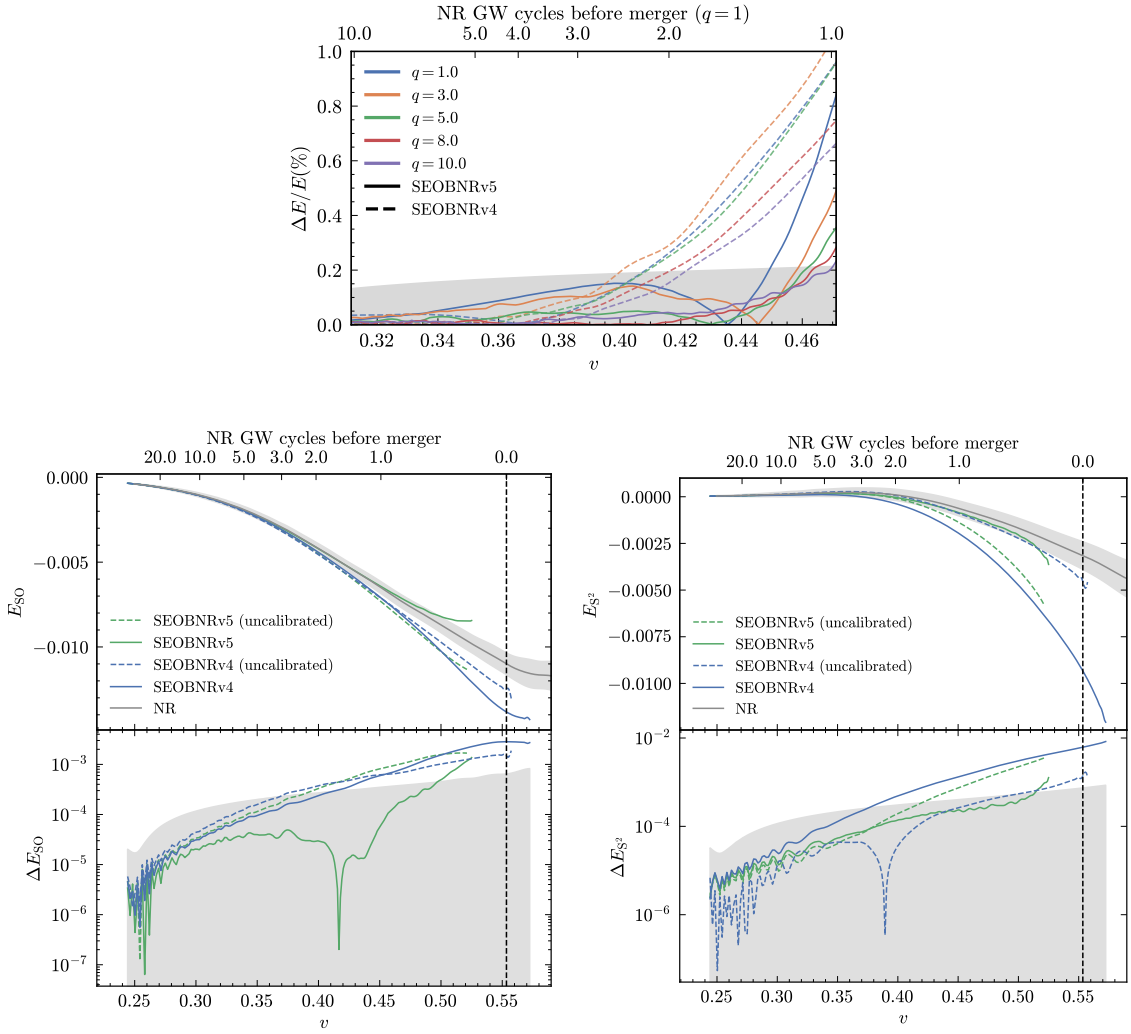

Figure 2.11: *Upper panel*: Fractional difference between the EOB and NR nonspinning binding energy as a function of $v = (M\Omega)^{1/3}$, for SEOBNRv5 and SEOBNRv4. The gray region represents an estimate of the NR error. Notice the improvement in the agreement of SEOBNRv5 compared to SEOBNRv4, especially between 3 and 1 cycles before merger. *Lower panels*: Spin-orbit (bottom-left panel) and spin-squared (bottom-right panel) contribution to the binding energy, for an equal-mass BBH, as a function of v for SEOBNRv4 (blue), SEOBNRv5 (green) and NR (gray). The uncalibrated models are obtained by setting to zero the calibration parameters entering the Hamiltonian. The dashed vertical line represents the merger of the NR configuration (the one at the lowest velocity among those used), with the number of GW cycles (top axis) referring to the same simulation. while the EOB curves terminate at EOB merger. The shaded regions represent the NR error. SEOBNRv5 has a better agreement with NR compared to SEOBNRv4, and remains within the NR error almost until merger.

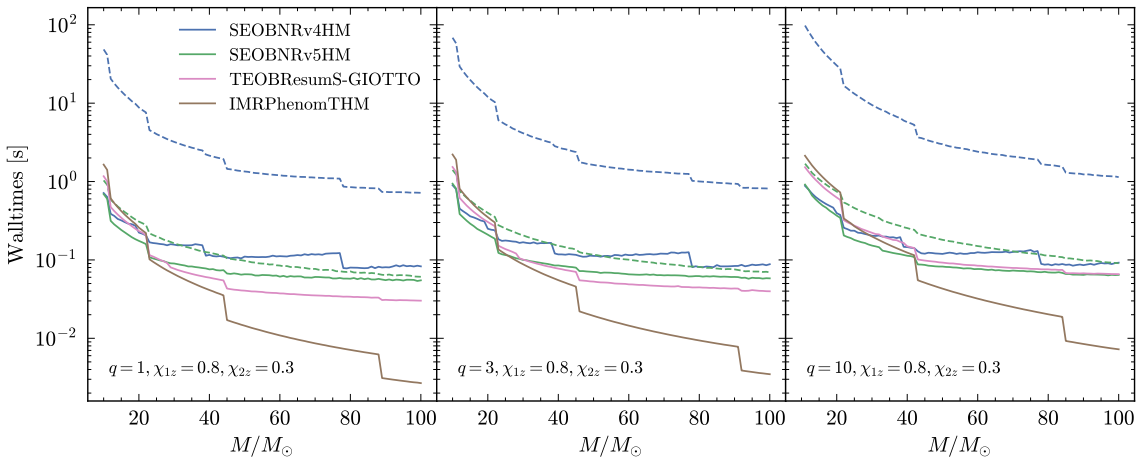

Figure 2.12: Walltimes for `SEOBNRv5HM` and `SEOBNRv4HM`, with PA approximation (solid lines) and without (dashed lines), `TEOBResumS-GIOTTO` and `IMRPhenomTHM`, starting from $f_{\rm start} = 10$ Hz, as a function of the total mass M. `SEOBNRv5HM` outperforms `SEOBNRv4HM`, particularly for low total mass systems, both with and without the PA approximation, and shows walltimes close to `TEOBResumS-GIOTTO`. `IMRPhenomTHM` is the fastest model for low total masses due to its use of closed-form expressions, with the gap narrowing for lower total masses.

overall worse agreement of the conservative dynamics with NR.

2.2.5 Computational performance

As described in Sec. 2.1, the `SEOBNRv5HM` model is implemented in `pySEOBNR`, a `Python` package designed for flexible, efficient waveform modeling within the `SEOBNR` framework [1]. We benchmark the computational efficiency of `SEOBNRv5HM` against other state-of-the-art time-domain aligned-spin models with higher modes: `SEOBNRv4HM`, both with and without the PA approximation, `TEOBResumS-GIOTTO`, which also employs the PA approximation, and `IMRPhenomTHM`.

Figure 2.12 shows the walltime for generating a waveform in the time domain, including interpolation onto a uniform time grid, for total masses between 10 and $100M_\odot$, at starting frequency of 10 Hz. We consider three mass ratios $q = 1, 3, 10$ and spins $\chi_1 = 0.8$, $\chi_2 = 0.3$. All models include modes up to $\ell = 4$ and use default settings. We choose the sampling rate such that the Nyquist criterion is satisfied for the $\ell = 4$ multipoles. Compared to `SEOBNRv4HM` without PA (dashed lines), `SEOBNRv5HM` achieves a major speedup, of up to a factor of 50 for low-mass systems, and about $\sim 10\times$ at higher masses. When comparing the PA versions (solid lines), `SEOBNRv5HM` remains consistently faster despite modeling two additional modes, achieving up to 70% lower runtimes at low total masses. A key improvement in

the implementation of the PA appriximantion is the use of analytical expressions for the momenta, whereas SEOBNRv4HM computes them numerically. It's important to note that the performance difference between the PA and non-PA versions of SEOBNRv4HM is not solely due to the PA approximation: SEOBNRv4HM_PA also benefits from optimizations such as analytical Hamiltonian derivatives. These improvements are incorporated into SEOBNRv5HM regardless of the use of PA, which explains why the performance gap between its PA and non-PA versions is smaller, roughly $\sim 2\times$ at low mass and 10–40% at $M \sim 100, M_\odot$. Relative to TEOBResumS-GIOTTO, which also uses the PA approximation, SEOBNRv5HM is more efficient at low masses, though TEOBResumS is faster at high masses, by factors of about $\sim 3\times$ for $q = 1$ and $\sim 1.5\times$ for $q = 10$. Finally, IMRPhenomTHM remains the fastest at high total mass, outperforming EOB models by an order of magnitude due to its use of closed-form expressions instead of integrating ordinary differential equations (ODEs). The gap between the models narrows as the total mass decreases, as the mode interpolation on a uniform time grid, needed for the FFT, becomes the dominant cost for long inspirals (excluding SEOBNRv4HM without PA approximation, where ODE integration remains by far the main cost factor).

2.2.6 Frequency domain reduced order model

The need to numerically integrate a system of ODEs to evolve the binary's dynamics is a key computational bottleneck in generating EOB waveforms for data analysis. To overcome this, surrogate or ROM techniques [384–389] have been applied to accelerate waveform evaluation. We present here SEOBNRv5HM_ROM, a frequency-domain ROM of SEOBNRv5HM. Although SEOBNRv5HM is sufficiently fast for many GW data analysis applications, using a ROM can lead to further increase in efficiency. In particular, SEOBNRv5HM_ROM can be evaluated on arbitrary, un-equispaced frequency grids, which allows to take advantage of likelihood acceleration techniques such as heterodyning [462, 463] and multibanding [465, 466]. Additionally, several applications benefit from a waveform model natively in the frequency domain. For instance, SEOBNRv5HM_ROM is currently used during the O4 LVK observing run as the baseline waveform model for the FTI test of GR [370], while its dominant-mode version, SEOBNRv5_ROM, has been employed in constructing matched-filter template banks for offline searches by the PyCBC pipeline.

The construction follows the method of SEOBNRv4HM_ROM [385–387], which involves modeling the frequency-domain phase of a carrier signal (based on the time-domain orbital phase) and the coorbital waveform modes, from which the carrier phasing has been factored out. The coorbital modes exhibit nearly constant phase during the inspiral, avoiding zero crossings that would otherwise complicate interpolation, especially

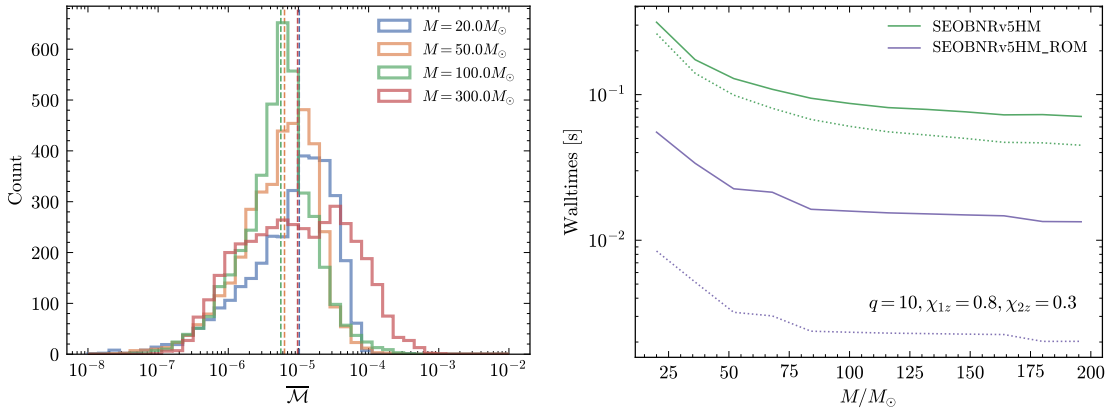

Figure 2.13: *Left panel:* Mismatch of `SEOBNRv5HM_ROM` against `SEOBNRv5HM` for different values of the total mass, for 4000 random configurations. Dashed vertical lines indicate the median values. *Right panel:* Walltime comparison between `SEOBNRv5HM` and `SEOBNRv5HM_ROM` as a function of total mass M, using a starting frequency of $f_{\rm start} = 10$ Hz. For `SEOBNRv5HM`, the cost includes time-to-frequency-domain conversion. Solid lines correspond to waveforms with higher modes; dotted lines show results for the (2,2) mode only.

in the subdominant modes. As for `SEOBNRv4HM_ROM`, the `SEOBNRv5HM_ROM` model combines a higher resolution high-frequency ROM, starting from 20 Hz for binaries with total mass of $50M_\odot$, and a lower resolution low-frequency ROM, starting from 20 Hz for binaries with total mass of $5M_\odot$, and can be extended to arbitrarily low frequencies by hybridizing it with multipolar PN waveforms (`TaylorF2`). `SEOBNRv5HM_ROM` can be generated for mass-ratios between 1 and 100, dimensionless spins between $[-0.998, 0.998]$, and includes the same modes $(\ell, |m|) = (2,2), (3,3), (2,1), (4,4), (5,5), (3,2), (4,3)$ as the baseline time-domian model. In the `SEOBNRv4HM_ROM` construction it was found beneficial to build the high-frequency ROM by combining 4 patches covering different regions of the $(q,\ \chi_1,\ \chi_2)$ parameter space. For `SEOBNR5HM_ROM` we achieve a satisfactory performance by using a single patch, despite the larger parameter space (`SEOBNRv4HM_ROM` is only valid up to $q \leq 50$). This simplifies the model construction, and avoids possible issues due to a non-smooth transition between different patches.

To validate `SEOBNRv5HM_ROM`, we show in the left panel of Fig. 2.13 its unfaithfulness against `SEOBNRv5HM`, for 4000 configurations with mass-ratios between 1 and 100 and dimensionless spins in $[-0.998, 0.998]$, across different total masses. To ease comparison with Ref. [387], we use a mismatch $\overline{\mathcal{M}}$ averaged over (ι, φ, κ) as defined in Eq. (4.8) of that work. We find excellent agreement, with median values $\lesssim 10^{-5}$, indicating that the modeling error introduced in the construction of the ROM is negligible compared to the inaccuracy of the `SEOBNRv5HM` waveforms against NR simulations. The right panel of Figure 2.13 shows the speedup of the ROM with respect to `SEOBNRv5HM`,

by comparing their walltimes for generating a frequency-domain waveform with the parameters ($q = 10,\ \chi_1 = 0.8,\ \chi_2 = 0.3$), as a function of the total mass M. Solid lines indicate results including higher modes, while dotted lines refer to the (2,2)-mode only. For SEOBNRv5HM we employ the PA approximation. We use a starting frequency $f_{\rm start} = 10$ Hz, a sampling rate $1/4096$ s, and frequency resolution $1/T$ where T is the waveform duration. The ROM achieves a speedup of $\sim 20-30\ \times$ in the (2,2)-only case, and $\sim 5-6\ \times$ when including higher modes. The ROM's runtime scales approximately with the number of modes, with the full multipolar SEOBNRv5HM_ROM being about 7 times more expensive to generate than its (2,2)-only counterpart.

2.3 Construction and validation of the effective-one-body waveform model SEOBNR-PM

The SEOBNRv5HM model discussed in the previous section relies primarily on resummations of the PN expansion. Recent progress in PM theory [360, 539–549] and GSF theory [233, 234] has sparked growing interest in exploring and developing waveform models that combine information from various perturbative methods in innovative ways, in order to address the waveform accuracy challenge.

The PM approach is especially promising, since an $(n+1)$ PM-order Hamiltonian – i.e., $\mathcal{O}(G^{n+1})$ – includes all information up to nPN order (where $v^2/c^2 \sim GM/(rc^2)$), as well as weak-field, high-velocity contributions from infinitely many higher-order PN terms. This makes PM theory particularly well suited for modeling systems with high velocities or large eccentricities at fixed periastron distances [206]. Notably, recent progress has leveraged advanced quantum-field-theory techniques, adapted from collider physics, which have enabled high-order PM calculations using both scattering amplitudes [207–209] and worldline methods [210–214].

In this section, we present the first PM-informed aligned-spin EOB waveform model, SEOBNR-PM [3], which covers the full inspiral, merger, and ringdown stages. This model, building on Refs. [2, 144, 365], incorporates the latest results from PM theory into the EOB Hamiltonian, and it is mildly calibrated to NR simulations. The SEOB-PM Hamiltonian (so named as it does not include NR calibration terms) includes the conservative, nonspinning 4PM contributions [208, 210] and spinning terms up to 5PM order [212, 216–222]. It also includes the known nonspinning 4PN terms [188–192], which account for tail effects from unbound to bound orbits up to that order. We adopt a physical PM counting scheme, in which spin orders contribute in addition to loop orders (see Table II in Ref. [365]). The SEOBNR-PM model has been developed in the pySEOBNR code [1], described in Sec. 2.1.

2.3.1 Post-Minkowskian–informed effective-one-body Hamiltonian

The SEOBNR-PM model uses the RR force $\mathcal{F}_\phi$ from the SEOBNRv5 model (2.8), which is computed by summing over factorized PN waveform modes [316–319], augmented with GSF corrections [364]. These modes are further improved with NQC corrections [112, 316, 320] to model the plunge phase. For the merger-ringdown part of the EOB waveform, the model adopts a phenomenological ansatz [2, 326] based on input from numerical NR and BH perturbation theory, as implemented in SEOBNRv5 (see Sec. 2.2.2). The transition to the merger-ringdown stage is set to occur at the peak of the $(2,2)$-

mode amplitude, $t^{22}_{\rm peak}$, which is calibrated to NR data via the $\Delta t_{\rm NR}$ parameter (2.18).

The key novel feature of SEOBNR-PM is its effective Hamiltonian, similar to that recently introduced in the SEOB-PM scattering model [365]:

$$H_{\rm eff} = \frac{M p_\phi (g_{a_+} a_+ + g_{a_-}\delta a_-)}{r^3 + a_+^2(r+2M)} + \sqrt{A\left(\mu^2 + \frac{p_\phi^2}{r^2} + (1+B^{\rm Kerr}_{\rm np})p_r^2 + B^{\rm Kerr}_{\rm npa}\frac{p_\phi^2 a_+^2}{r^2}\right)}, \tag{2.47}$$

where $B^{\rm Kerr}_{\rm np} = \chi_+^2 u^2 - 2u$, $B^{\rm Kerr}_{\rm npa} = -(1+2u)/[r^2 + a_+^2(1+2u)]$, and $u = M/r$ is a dimensionless PM counting parameter. In the $\nu \to 0$ limit, $H_{\rm eff}$ reduces to the Hamiltonian of a test-mass μ in a Kerr spacetime with mass M and spin a_+. This Hamiltonian is derived by computing the scattering angle and matching it to known PM results, using only the conservative contributions, which contain even powers of the center-of-mass momentum $p_\infty = \mu\sqrt{\gamma^2-1}$, where $\gamma = E_{\rm eff}/\mu > 1$ for scattering orbits.

Following Ref. [365], the ν-corrections with respect to the tets-mass limit are incorporated into the A-potential and the gyro-gravitomagnetic factors:

$$A = \frac{1 - 2u + \chi_+^2 u^2 + \Delta A}{1 + \chi_+^2 u^2(2u+1)}, \qquad\qquad g_{a_\pm} = \frac{\Delta g_{a_\pm}}{u^2}. \tag{2.48}$$

These encode even- and odd-in-spin corrections, respectively, and are PM expanded up to 5PM order (u^5), except in the nonspinning case where the full 5PM term is not known:

$$\Delta A = \sum_{n=2}^{5} u^n \Delta A^{(n)} + \Delta A^{\rm 4PN}, \qquad\qquad \Delta g_{a_\pm} = \sum_{n=2}^{5} u^n \Delta g^{(n)}_{a_\pm}. \tag{2.49}$$

The γ-dependent coefficients $\Delta A^{(n)}$ and $\Delta g^{(n)}_{a_\pm}$ are series expanded in even powers of the spins, up to a highest quartic order at 5PM,

$$\Delta A^{(n)} = \sum_{s=0}^{(n-1)/2} \sum_{i=0}^{2s} \alpha^{(n)}_{(2s-i,i)} \delta^{\sigma(i)} \chi_+^{2s-i} \chi_-^{i}, \tag{2.50}$$

where $\sigma(i) = 0, 1$ if i is even or odd, respectively. Similarly, for the gyro-gravitomagnetic factors, we have

$$\Delta g^{(n)}_{a_+} = \sum_{s=0}^{(n-2)/2} \sum_{i=0}^{s} \alpha^{(n)}_{(2(s-i)+1,2i)} \chi_+^{2(s-i)} \chi_-^{2i}, \quad \Delta g^{(n)}_{a_-} = \sum_{s=0}^{(n-2)/2} \sum_{i=0}^{s} \alpha^{(n)}_{(2(s-i),2i+1)} \chi_+^{2(s-i)} \chi_-^{2i}. \tag{2.51}$$

The dimensionless parameters $\alpha^{(n)}_{(i,j)}$ are functions of $\gamma = E_{\rm eff}/\mu$ and the symmetric mass ratio ν. The nonspinning coefficients are provided in the Supplemental Material

of Ref. [3], while the complete expressions for the spinning case are available in the ancillary files of the corresponding `arXiv` submission. Since $\gamma = E_{\rm eff}/\mu = H_{\rm eff}/\mu$, the Hamiltonian (2.47) is self-dependent. To produce an expression that depends only on the canonical variables (r,p_r,p_ϕ), we interpret $\gamma = H_{\rm Kerr}/\mu$ within these deformations, and add any necessary corrections to ensure the full Hamiltonian $H_{\rm EOB}$ is correct up to the desired PM order. This method has been previously applied in the nonspinning case [206, 361, 362], and is described in detail in the Supplemental Material of Ref. [3].

A subtlety in the construction of the Hamiltonian is the inclusion of tail effects, which depend on the full past history of the binary and distinguish between bound and unbound orbits. In the scattering Hamiltonian of Ref. [365], these appear as terms like $\log(\gamma^2-1)$, which become complex for bound systems. To avoid this, we replace them with $\log(u)$, ensuring the Hamiltonian remains real. We also include a 4PN correction $\Delta A^{\rm 4PN}$ in Eq. (2.49), which ensures the correct bound-orbit dynamics at 4PN order in the nonspinning case

$$\Delta A^{\rm 4PN} = u^4(\gamma^2-1)c_1 + u^5(c_2 + c_3 \log u), \tag{2.52}$$

with coefficients c_i provided in the Supplemental Material of Ref. [3].

2.3.2 Comparing the `SEOB-PM` binding energy to numerical relativity

EOB models provide access to the binary's dynamics, enabling validation against NR through gauge-invariant dynamical quantities like the binding energy [206,358,376–378] and periastron advance [379, 380]. Since the key new feature of `SEOBNR-PM` is its PM-informed `SEOB-PM` Hamiltonian, the binding energy is a particularly relevant quantity to compare with NR data.

Previous comparisons in the nonspinning sector [206, 362] have focused on the binding energy computed for circular orbits, neglecting radiation reaction. We instead compute the (dimensionless) binding energy by evaluating $\mathcal{E} = (H_{\rm EOB} - M)/\mu$ along inspiral trajectories, and compare with NR–binding-energy data from Ref. [378]. The upper panel of Fig. 2.14 shows the EOB and NR nonspinning binding energies as a function of the quasi-circular velocity parameter $v = (M\Omega)^{1/3}$, for both `SEOBNRv5` (with a calibrated a_6 parameter in the A-potential) and `SEOB-PM`, evaluated along circular orbits and inspirals. Both models show excellent agreement with NR during most of the inspiral, with errors within the NR uncertainty (represented by the gray region) until around 1 GW cycle before merger. Notably, the uncalibrated `SEOB-PM` maintains agreement within NR error up to slightly higher velocities for higher mass ratios, and shows much better agreement than in the circular-orbit approximation [206, 362].

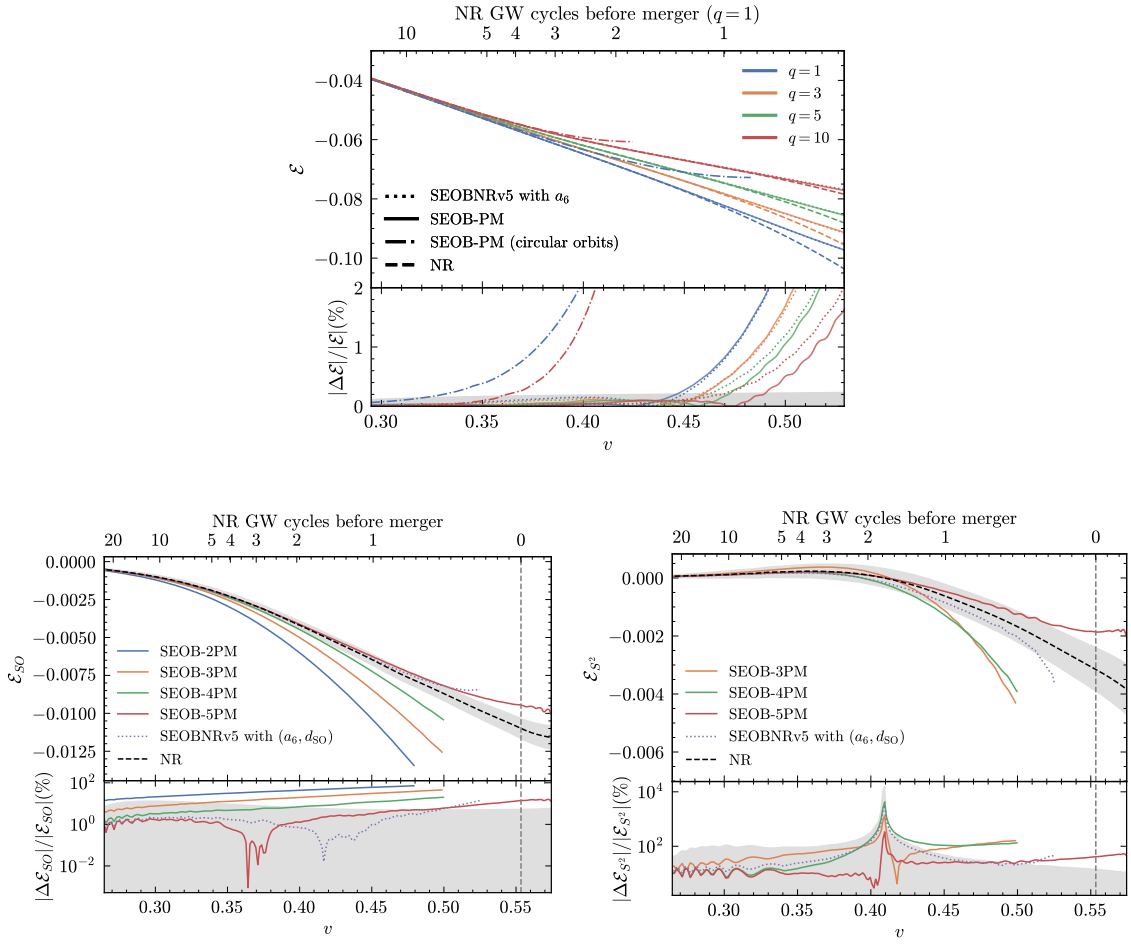

Figure 2.14: *Upper panel*: nonspinning binding energy as a function of the quasi-circular velocity $v = (M\Omega)^{1/3}$, for the (calibrated) `SEOBNRv5` with a_6 and (uncalibrated) `SEOB-PM` Hamiltonians (both along a circular orbit [206, 362] and inspiral) across different mass ratios $q = m_1/m_2$. The shaded region is an estimate of the NR uncertainty [378]. The lower panel shows the fractional difference. *Lower panels*: Spin-orbit (bottom-left panel) and spin-squared (bottom-right panel) contributions to the binding energy, for an equal-mass BBH, as a function of v, for the (calibrated) `SEOBNRv5` with (a_6,$d_{\rm SO}$) and (uncalibrated) `SEOB-PM` Hamiltonians at different PM orders. The vertical line represents the merger of the NR configuration (the one at the lowest velocity among those used), with the number of GW cycles (top axis) referring to the same simulation. The shaded regions are estimates of the NR uncertainty [378]. The lower panels show the fractional difference. The feature in the lower-right panel around $v \sim 0.4$ is due to a zero-crossing.

As in Sec. 2.2.4, we also extract different spin contributions to the binding energy by combining results from equal-mass NR simulations with various spin configurations [378, 538] (see Eqs. (2.46a) and (2.46b)). The lower panels of Fig. 2.14 show the spin-orbit and spin-squared contributions to the binding energy for an equal-mass BBH , comparing the (uncalibrated) `SEOB-PM` at different PM orders with NR results, and with the calibrated `SEOBNRv5` model (including a_6 and $d_{\rm SO}$ calibration parameters). Despite not being calibrated to NR, `SEOB-PM` shows excellent agreement with the NR results, with a clear convergence toward the NR prediction as more PM orders are included. Its accuracy is slightly better than `SEOBNRv5`, even though the latter uses a Hamiltonian calibrated in the nonspinning (a_6) and spin-orbit ($d_{\rm SO}$) sector.

2.3.3 Calibration to numerical relativity and waveform-model performance

As discussed in Sec. 2.2.3, the accuracy of EOB waveforms can be improved by calibration to NR simulations. For the inspiral-plunge stage, this is typically done by introducing higher-order (still unknown) PN terms in the Hamiltonian, whose coefficients are tuned to NR, and fitting the time of merger to NR data.

The `SEOBNRv5` model employs three calibration parameters: $(\Delta t_{\rm NR}, a_6, d_{\rm SO})$. The parameter $\Delta t_{\rm NR}$ determines the merger time, and is defined by $t^{22}_{\rm peak} = t_{\rm ISCO} + \Delta t_{\rm NR}$ (2.18). The parameter a_6 is a 5PN correction to the A-potential (2.3) and $d_{\rm SO}$ is a 4.5PN correction in the gyro-gravitomagnetic coefficients (2.5) (see Sec. 2.2.3). For the `SEOBNR-PM` model, we do not calibrate high-order PN terms in the Hamiltonian (2.47); instead, we calibrate only the merger time through $\Delta t_{\rm NR}$. In future work, we plan to investigate NR calibration strategies tailored specifically to the structure of the PM-based Hamiltonian.

We calibrate `SEOBNR-PM` using the `pySEOBNR` code [1], and follow the procedure used for the `SEOBNRv5` model, which determines the optimal calibration parameters by minimizing a combination of the waveform mismatch and the difference in merger time between EOB and NR waveforms with the same physical parameters (q, χ_1, χ_2). We calibrate $\Delta t_{\rm NR}$ using the same set of 441 aligned-spin BBH simulations from the SXS Collaboration used for `SEOBNRv5`, shown in Fig. 2.4. The best-fit $\Delta t_{\rm NR}$ values are then interpolated over the (q, χ_1, χ_2) parameter space.

To assess the accuracy of the waveform model, we compute its mismatch against the set of 441 SXS NR simulations, and compare its performance to the `SEOBNRv5` $(\Delta t_{\rm NR}, a_6, d_{\rm SO})$ model, as well as, to a version of `SEOBNRv5` calibrated only via $\Delta t_{\rm NR}$. Figure 2.15 shows the cumulative maximum mismatch against the NR simulations over the binary's total-mass range $10M_\odot \leq M \leq 300M_\odot$, for the $(\ell, m) = (2, 2)$ mode.

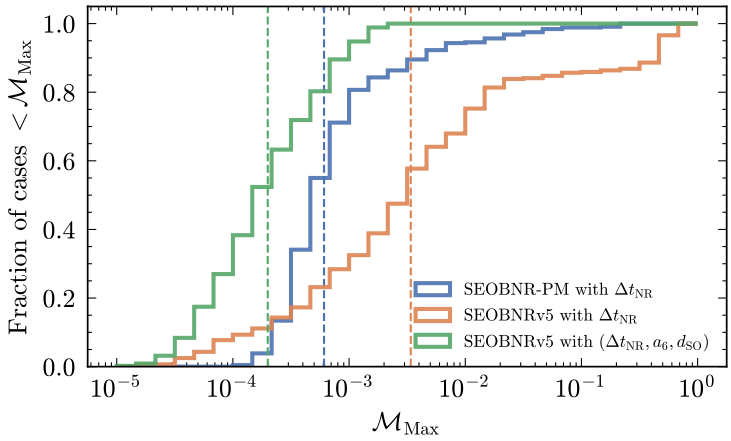

Figure 2.15: Cumulative maximum mismatch over the binary's total-mass range $10M_\odot \leq M \leq 300M_\odot$ for the (calibrated) SEOBNR-PM and SEOBNRv5 models. The study uses 441 SXS NR waveforms, and focuses on the $(\ell, m) = (2, 2)$ mode. The vertical dashed lines indicate the medians of the mismatch distributions.

The performance of SEOBNR-PM lies between the two SEOBNRv5 variations, with a median value $\mathcal{M}_{\rm median} \sim 6.1 \times 10^{-4}$, indicating a remarkably good agreement. For configurations with large positive spins, we observe an increase in mismatch for both SEOBNR-PM and the $\Delta t_{\rm NR}$-only SEOBNRv5, though the effect is more pronounced in the latter. This is likely due to SEOBNRv5 including spin-orbit (3.5PN), spin-squared (4PN), and spin-cubic (3.5PN) terms at lower PN order, whereas SEOBNR-PM includes spin terms up to 5PM.

These results are promising, especially given that SEOBNR-PM is the first complete waveform model informed by PM theory, but they mark only the beginning. Resumming the PM potentials and introducing additional calibration parameters in the EOB Hamiltonian will be essential to further improve its accuracy, an avenue we leave for future work.

3 Parameter estimation of gravitational waves from binary black hole mergers

3.1 Parameter estimation of gravitational-wave sources

As introduced in Sec. 1.2, the goal of Bayesian PE is to infer the posterior probability distribution $p(\boldsymbol{\lambda}|d)$ for the parameters $\boldsymbol{\lambda}$ given the observed data d, using Bayes theorem

$$p(\boldsymbol{\lambda} \mid d) = \frac{\mathcal{L}(d \mid \boldsymbol{\lambda})\pi(\boldsymbol{\lambda})}{Z}, \tag{3.1}$$

where $\mathcal{L}(d|\boldsymbol{\lambda})$ is the likelihood of observing the data d given the parameters $\boldsymbol{\lambda}$, $\pi(\boldsymbol{\lambda})$ is the prior on $\boldsymbol{\lambda}$, and $Z = \int \mathrm{d}\boldsymbol{\lambda}\mathcal{L}(d \mid \boldsymbol{\lambda})\pi(\boldsymbol{\lambda})$ is the evidence [174]. To determine whether a model A is preferred over a model B, one can look at the Bayes factor, defined as the ratio of the evidence for the two different models $\mathcal{B}^A_B = Z_A/Z_B$. The Bayes factor naturally accounts for model complexity: models with more parameters tend to fit the data better and achieve a higher likelihood, but they are penalized due to the larger prior volume. However, caution is warranted in the interpretation of Bayes factors. A larger value does not necessarily indicate that a model offers a more faithful representation of the underlying signal; in certain cases, misrepresented correlations can lead to artificially narrow posteriors and spuriously strong model preferences [550, 551].

The GW likelihood function, $\mathcal{L}(d|\boldsymbol{\lambda})$, quantifies how well the data d are described by a given set of parameters $\boldsymbol{\lambda}$, given a model for the signal. Under the assumption of stationary, Gaussian detector noise, the likelihood takes the form [552]

$$\mathcal{L}(d|\boldsymbol{\lambda}) \propto \exp\left[-\frac{1}{2}\left(d - h(\boldsymbol{\lambda})|d - h(\boldsymbol{\lambda})\right)\right], \tag{3.2}$$

where $h(\boldsymbol{\lambda})$ is a model for the gravitational strain waveform, as measured by the interferometer, given the parameters $\boldsymbol{\lambda}$. The noise-weighted inner product $(.|.)$ is

defined in Eq. (1.37). The integration limits $f_{\rm low}$ and $f_{\rm high}$ are set according to the bandwidth of the detector. In typical LVK analyses, one sets $f_{\rm low} = 20$ Hz, while $f_{\rm high} = \alpha(f_s/2)$ where f_s is the sampling frequency ($f_s/2$ is the Nyquist frequency). The roll-off factor $\alpha = 0.875$ is included to avoid power loss due to the application of a window function to the time-domain data, and the sampling rate f_s is chosen to fully resolve the $\ell = 3$ modes in the ringdown [49].

The prior distribution, $\pi(\boldsymbol{\lambda})$, encodes our knowledge or assumptions about the parameters before observing the data. In GW analyses, uninformative or uniform priors are typically used for most parameters [49, 179]. In the following analyses, we sample the binary component masses using the chirp mass ($\mathcal{M}_c$) and inverse mass ratio ($1/q$), with priors uniform in component masses. For precessing-spin binaries, the priors on the dimensionless spin vectors are uniform in magnitude $a_i \in [0, 0.99]$, and isotropically distributed in the unit sphere for the spin directions. For aligned-spin analyses, the individual spin components follow the marginal distribution implied by the isotropic spin prior. For the luminosity distance, we employ a prior uniform in the comoving-frame of the source. For events observed by multiple detectors, we adopt a detector-based sky parameterization, which samples the sky location in terms of azimuth and zenith angles, relative to the vector connecting the vertices of the two interferometers with the highest SNR. These are then converted to right ascension and declination in post-processing.

In most cases, the posterior distribution cannot be handled analytically, requiring stochastic sampling techniques. Markov Chain Monte Carlo [177] or nested sampling [178] algorithms are commonly used to generate posterior samples that approximate the target distribution. These posterior samples are typically visualized as *corner plots*, which show the marginalized one- and two-dimensional posterior probability distributions for each parameter (see, e.g., Fig. 3.1).

In this work, we primarily use nested sampling [178], a method originally developed to compute the Bayesian evidence Z, but which also produces posterior samples as a by-product. The algorithm maintains a set of *live points* drawn from the prior. At each iteration, the point with the lowest likelihood is removed and replaced by a new point sampled from the prior, constrained to have a higher likelihood – typically using MCMC or similar methods. Each discarded point is assigned a prior volume, and the evidence is approximated by summing the product of likelihood and prior volume across all samples. As the algorithm progresses toward higher-likelihood regions, it estimates an upper bound on the remaining contribution to the evidence. This can be used to define a termination condition based on when the estimated contribution of the remaining prior volume falls below a predefined threshold (for example, $\delta \log Z < 0.1$ [553]).

To reduce the dimensionality of the parameter space and improve sampler convergence, it is sometimes possible to define a likelihood that explicitly marginalizes over certain parameters, such as the coalescence time, phase at coalescence, and/or luminosity distance [174]. The posterior distributions for the marginalized parameters can then be reconstructed in postprocessing. In the analyses that follow, we apply distance marginalization by default.

To perform PE, we use the `bilby` package [486] together with the nested sampler `dynesty` [553], which constitute the standard tools adopted in recent LVK analyses [49]. In some cases, we employ `parallel bilby` [470], a highly parallelized implementation designed to accelerate inference on multiple computing nodes. For the sampler settings, we generally adopt the `acceptance-walk` stepping method, average number of accepted steps per MCMC chain naccept = 60 and a total number of live points nlive = 1000, keeping the remaining sampler settings to their default values. These choices are consistent with those used in the latest LVK analyses [183].

3.2 Parameter estimation using SEOBNRv5HM

In this section, we demonstrate the performance of the `SEOBNRv5HM` waveform model presented in Sec. 2.2 through Bayesian PE, validating its accuracy using a high-mass-ratio NR injection and reanalyzing previously observed GW events, with comparisons to results obtained using the `IMRPhenomXHM` model.

3.2.1 Parameter estimation of a numerical-relativity synthetic signal

We begin by examining a parameter recovery on a synthetic signal injected in a network of three detectors (LIGO Hanford, LIGO Livingston, and Virgo) using a zero-noise configuration. The injected waveform is `SXS:BBH:2464` from the `SXS` Collaboration, with intrinsic parameters $1/q = m_2/m_1 = 0.067$, $\chi_1 = 0.5$ and $\chi_2 = 0$. We choose a detector-frame total mass of $162M_\odot$, an inclination of $\iota = \pi/3$ to enhance the contribution of higher harmonics, and a luminosity distance of 700 Mpc, resulting in a network SNR of approximately ~ 16.6. The full set of injected parameters is listed in the left column of Table 3.1. We perform two PE runs on this injection, one using the `SEOBNRv5HM` model, and another using the phenomenological model `IMRPhenomXHM` [297].

The median recovered values and corresponding 90% credible intervals for both models are summarized in Table 3.1, with selected marginalized posteriors shown in Fig. 3.1. The results show that `SEOBNRv5HM` recovers the injected signal more

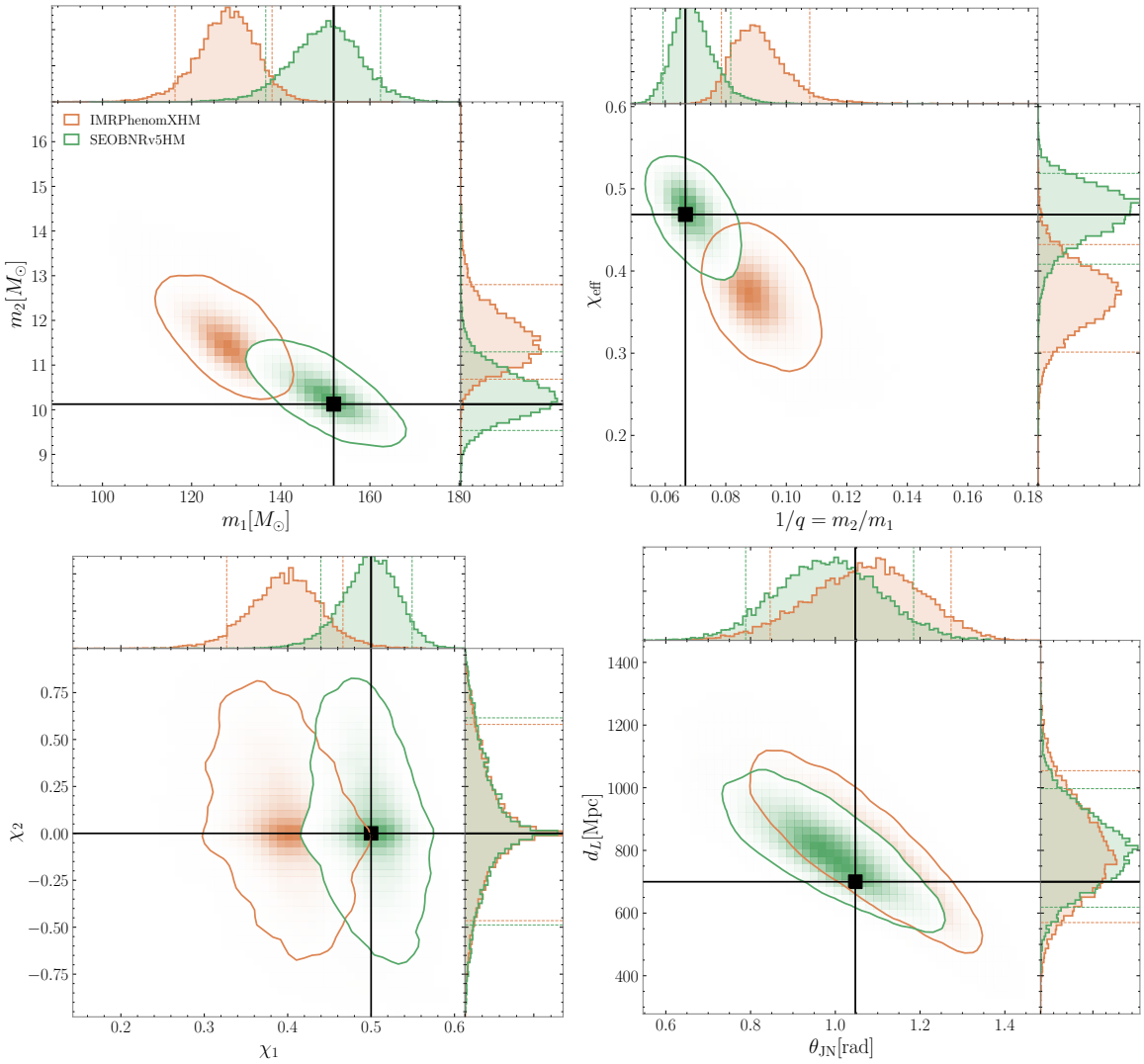

Figure 3.1: One- and two-dimensional marginalized posterior distributions for selected parameters measured from the synthetic BBH signal based on the `SXS` NR waveform `SXS:BBH:2464`, with inverse mass ratio $1/q = 0.067$, total detector-frame mass of $162M_\odot$, dimensionless spins $\chi_{1z} = 0.5$ and $\chi_{2z} = 0.0$. The other injected parameters are given in Table 3.1. The contours mark the 90% credible regions, while the dashed lines on the one-dimensional marginalized distributions mark the 90% credible intervals. The black vertical and horizontal lines mark the injected values. Parameter estimation is performed with the `SEOBNRv5HM` model (green) and the `IMRPhenomXHM` model (orange).

Parameter	Injected value	IMRPhenomXHM recovery	SEOBNRv5HM recovery
$M/M_\odot$	162.0	$139.6^{+9.55}_{-10.93}$	$160.58^{+11.57}_{-12.91}$
$\mathcal{M}_c/M_\odot$	29.53	$29.65^{+1.46}_{-0.94}$	$29.7^{+1.07}_{-0.9}$
$m_1/M_\odot$	151.88	$128.09^{+9.95}_{-11.81}$	$150.27^{+12.12}_{-13.64}$
$m_2/M_\odot$	10.13	$11.54^{+1.26}_{-0.86}$	$10.32^{+0.98}_{-0.78}$
$1/q$	0.067	$0.09^{+0.02}_{-0.01}$	$0.07^{+0.01}_{-0.01}$
$\chi_{\rm eff}$	0.469	$0.37^{+0.06}_{-0.07}$	$0.47^{+0.05}_{-0.06}$
χ_{1z}	0.50	$0.4^{+0.07}_{-0.07}$	$0.5^{+0.05}_{-0.06}$
χ_{2z}	0.0	$0.02^{+0.56}_{-0.49}$	$0.03^{+0.59}_{-0.51}$
ι/rad	1.047	$1.08^{+0.2}_{-0.23}$	$0.98^{+0.2}_{-0.2}$
d_L/Mpc	700.0	$792.04^{+262.38}_{-222.3}$	$798.97^{+198.04}_{-180.23}$
$\varphi_{\rm ref}$/rad	0.80	$3.57^{+1.98}_{-2.1}$	$3.05^{+2.92}_{-2.73}$
ψ/rad	2.17	$2.29^{+0.3}_{-0.28}$	$2.33^{+0.22}_{-0.23}$
α/rad	3.81	$3.84^{+0.09}_{-0.09}$	$3.84^{+0.07}_{-0.07}$
δ/rad	0.63	$0.6^{+0.09}_{-0.11}$	$0.59^{+0.06}_{-0.09}$
$\rho^{\rm H1}_{\rm mf}$	8.42	$8.05^{+0.08}_{-0.15}$	$8.26^{+0.07}_{-0.14}$
$\rho^{\rm L1}_{\rm mf}$	9.98	$9.54^{+0.09}_{-0.17}$	$9.79^{+0.08}_{-0.17}$
$\rho^{\rm V1}_{\rm mf}$	10.18	$9.67^{+0.08}_{-0.16}$	$9.98^{+0.08}_{-0.16}$
$\log \mathcal{BF}$		91.26 ± 0.20	97.53 ± 0.21

Table 3.1: Injected and median posterior values for a synthetic NR injection based on the SXS simulation SXS:BBH:2464, recovered using IMRPhenomXHM and SEOBNRv5HM. The binary parameters include to the total mass M, chirp mass $\mathcal{M}_c$, individual masses $m_{1,2}$, inverse mass ratio $1/q$, effective spin $\chi_{\rm eff}$, individual spin components $\chi_{1z,2z}$, inclination angle ι, luminosity distance d_L, reference phase $\varphi_{\rm ref}$, polarization angle ψ, right ascension α, declination δ, matched-filtered SNR in the LIGO-Hanford, LIGO-Livingston, and Virgo detectors $\rho^{\rm H1,L1,V1}_{\rm mf}$ and signal-versus-noise log Bayes factor $\log \mathcal{BF}$.

accurately, particularly for the intrinsic parameters: all injected values lie within the 90% intervals, with minimal deviations between posterior medians and true values. The only notable exception is the reference phase, which is prior-dominated. In contrast, the IMRPhenomXHM model exhibits significant biases in several intrinsic parameters, with the injected values lying outside the 90% credible intervals for component masses,

total mass, mass ratio, and effective spin $\chi_{\rm eff}$. For extrinsic parameters, both models recover the injected values within the 90% intervals, showing comparable performance. The improved accuracy of `SEOBNRv5HM` in this challenging regime, characterized by a highly asymmetric mass ratio and a spinning primary BH, is further reflected in its higher matched-filter SNRs across all detectors and a larger Bayes factor compared to `IMRPhenomXHM`. These results are consistent with the unfaithfulness between the models and the NR injection: 0.5% for `SEOBNRv5HM` and 6.7% for `IMRPhenomXHM`, for the injected value of the total mass.

3.2.2 Parameter estimation on real data

We next perform PE for three real GW events: GW150914 [45], the first detection and a standard benchmark for waveform validation; GW170729 [554], a high-mass event from O2 analyzed with multimode waveform models; and GW190412 [555], the first confidently identified asymmetric-mass binary. For each event, we use the strain data, calibration uncertainties, and PSDs provided by the Gravitational Wave Open Science Center (GWOSC) [556]. Parameter estimation is performed with `bilby` [179, 486] with the `dynesty` sampler [553], employing standard priors and settings as described in Sec. 3.1.

As in the case of the NR injection, we compare results obtained with `SEOBNRv5HM` to those from the phenomenological model `IMRPhenomXHM`. Figure 3.2 shows representative marginalized posterior distributions. We observe good agreement between the two waveform models, consistent with published results for these events. Minor differences are expected, as LVK catalog analyses use precessing-spin models, while both `SEOBNRv5HM` and `IMRPhenomXHM` are aligned-spin models. The agreement is also expected given that the recovered parameters lie within the NR calibration region of both models. As with the NR injection in the previous section, we find a slight improvement in the matched-filter SNR and Bayes factor when using `SEOBNRv5HM`, particularly for the two more massive events. While the improvements are modest, they suggest that `SEOBNRv5HM` more accurately describes the data, consistent with the lower unfaithfulness values discussed in Sec. 2.2.4. Finally, we note that PE runs using `bilby` on a single node (64 cores) complete in under one day for GW150914 and GW170729, and in less than two days for GW190412. This confirms that `SEOBNRv5HM` is computationally efficient and compatible with standard LVK PE pipelines.

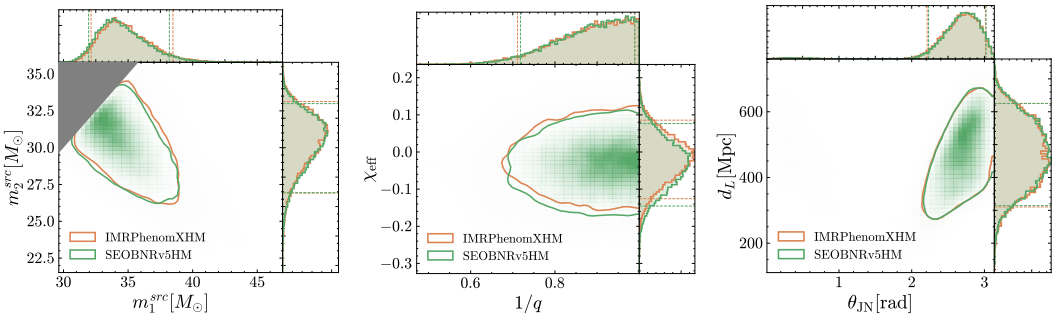

(a) GW150914.

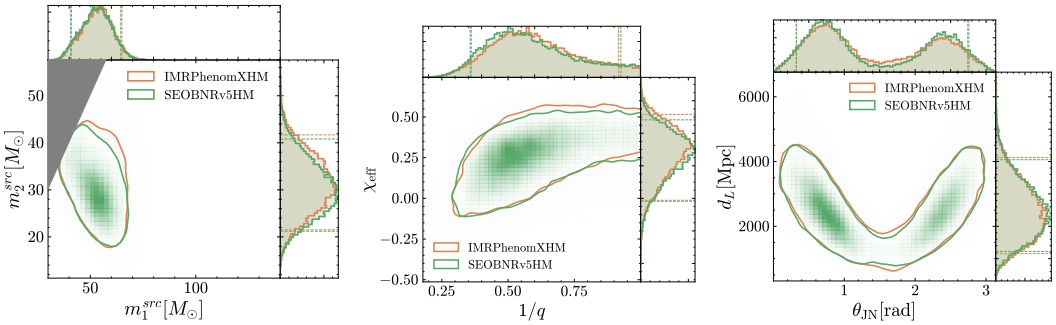

(b) GW170729.

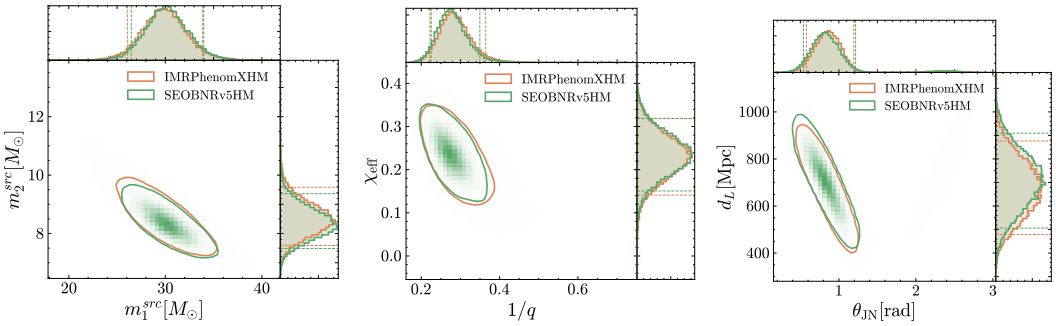

(c) GW190412.

Figure 3.2: One- and two-dimensional marginalized posterior distributions for selected parameters from the GW events GW150914, GW170729 and GW190412, analyzed with the SEOBNRv5HM model (green) and the IMRPhenomXHM model (orange).

3.3 Incorporating numerical-relativity calibration uncertainty in parameter estimation

Current waveform models have been sufficiently accurate to analyze most GW signals detected to date [428,429], with only a few exceptions where different models recovered noticeably different parameters [49, 430, 431]. Next-generation GW detectors [396, 397, 401], will offer unprecedented sensitivity, with SNR up to two orders of magnitude higher than current instruments [405]. This increased sensitivity makes waveform accuracy increasingly critical, as statistical uncertainties approach the systematic biases of the GW approximant models. Several studies predict severe biases in PE due to mismodeling errors with the upcoming fifth LVK observational run (O5) and XG detectors [429, 435], and the risk of false GR deviations [444].

A possible way to improve waveform accuracy is to include higher-order analytical information, while pushing calibration parameters to even higher orders. However, this requires careful studies on how to incorporate and resum this information, and improvements in the strong-field regime are not always guaranteed. As discussed in Sec. 2.3, leveraging novel perturbative methods, such as the GSF and PM approximations, offers another promising avenue. Finally, as shown in Sec. 2.2, improving the NR calibration of waveform models by employing longer, higher-resolution simulations covering more of the parameter space is crucial.

A common strategy for mitigating waveform systematics is to combine predictions from different waveform models. This can be done either by mixing posterior samples from various approximants [49, 428, 557, 558], or by sampling over a set of models treated as hyperparameters in the analysis [559–561]. However, if none of the models used is sufficiently accurate, these methods may still yield biased results. A complementary approach to avoid biased inference involves integrating error estimates directly into waveform models. Proposed methods include using Gaussian process regression to interpolate either waveform residuals or directly NR waveforms [277, 562–566], using frequency-dependent amplitude and phase corrections, as in the case of detector-calibration uncertainty [567], or introducing additional higher-order parameters designed to capture currently unknown PN terms [434]. In these approaches, waveform modeling uncertainties are accounted for by marginalizing over these additional degrees of freedom during the inference process. While this may lead to less precise parameter estimates (e.g., wider posterior distributions), it should improve their robustness, ensuring they remain reliable even in the presence of systematic modeling errors.

Nonetheless, most studies attempting to incorporate error estimates into waveform models often involved simplified physical descriptions (e.g., nonspinning binaries [434,

566]), and did not assess the impact of this approach on the analysis of realistic signals that could be observed with upcoming runs and XG detectors. In this section, we present recent work towards addressing this gap. As proof of principle, we employ the quasi-circular aligned-spin multipolar EOB model `SEOBNRv5HM` presented in Sec. 2.2, and analyze synthetic signals from NR surrogate waveforms, hybridized to PN-EOB ones (`NRHybSur3dq8` [276]), for loud *golden* BBH systems at SNRs consistent with current and future observations, using full Bayesian inference.

Similarly to Refs. [565, 566], we propose a semi-parametric probabilistic model for the GW signal from a BBH, which not only provides a best-fit point estimate but also allows for drawing waveform samples. We do so by modeling posterior probability distributions of the model's NR-calibration parameters, obtained from 441 NR simulations of aligned-spin BBHs produced with the `SpEC` code of the SXS Collaboration [256], and one produced with the `Einstein Toolkit` [508] (see Fig. 2.4). We interpolate the probability distributions across parameter space using mixture density networks (MDNs) [568], a neural-network architecture suited for modeling and predicting probability distributions over continuous variables. Using these probability distributions as priors, we sample the NR-calibration parameters together with the standard source parameters during inference, effectively marginalizing over the NR-calibration uncertainty in the model.

3.3.1 Probabilistic waveform model

As described in Sec. 2.2.3, the `SEOBNRv5HM` model includes three calibration parameters $\boldsymbol{\theta} = (\Delta t_{\rm NR}, a_6, d_{\rm SO})$. Here, we focus on the spin sector, where modeling errors are more significant, and consider only two of these parameters $\boldsymbol{\theta} = (\Delta t_{\rm NR}, d_{\rm SO})$. The parameter $\Delta t_{\rm NR}$ is a time shift between the Kerr ISCO and the peak of the $(2,2)$-mode amplitude (2.18), while $d_{\rm SO}$ is a 4.5PN spin-orbit coefficient in $H_{\rm EOB}$ (2.5).

The Bayesian calibration of the `SEOBNRv5HM` model results in a set of posterior distributions $p\left(\boldsymbol{\theta} \mid \boldsymbol{\Lambda_i}\right)$ for the calibration parameters, for each NR configuration with intrinsic parameters $\boldsymbol{\Lambda_i}$. These posteriors correspond to values of $\boldsymbol{\theta}$ that minimize a likelihood (2.32) based on the mismatch $\mathcal{M}$ and the difference in merger time $\delta t_{\rm merger}$ between EOB and NR waveforms with the same physical parameters $\boldsymbol{\Lambda} = (q, \chi_1, \chi_2)$. The mismatch and difference in merger time are required to lie below conservative NR error thresholds, $\sigma_{\mathcal{M}} = 10^{-3}$ and $\sigma_t = 5M$, respectively.

In Sec. 2.2.3, we described how in the `SEOBNRv5HM` model one fits a point measure $\boldsymbol{\theta}(\boldsymbol{\Lambda})$ for each NR simulation, like the median of the distribution, over the $\boldsymbol{\Lambda}$ parameter space, using least-square hierarchical fits. Here, we extend that approach by modeling the *full* posterior distributions of the calibration parameters $p\left(\boldsymbol{\theta} \mid \boldsymbol{\Lambda}\right)$, rather than just point estimates $\boldsymbol{\theta}(\boldsymbol{\Lambda})$. This provides a *best-fit* point measure from, e.g., the mean of

the posterior, while also giving access to parameter uncertainty. It can be interpreted as a probabilistic waveform model [277, 565, 566] by drawing samples of the calibration parameters.

Details of the mixture-density-network model

We model the calibration posteriors $p(\boldsymbol{\theta} \mid \boldsymbol{\Lambda})$ using a MDN, which expresses the posterior as a mixture of Gaussians conditioned on the physical parameters $\boldsymbol{\Lambda}$. We define

$$p(\boldsymbol{\theta} \mid \boldsymbol{\Lambda}) \approx \sum_{k=1}^{K} \pi_k(\boldsymbol{\Lambda}) \mathcal{N}\left(\boldsymbol{\theta} \mid \mu_k(\boldsymbol{\Lambda}), \Sigma_k(\boldsymbol{\Lambda})\right), \tag{3.3}$$

where $\mathcal{N}(\boldsymbol{\theta} \mid \mu, \Sigma)$ is a multivariate Gaussian distributions with mean μ and covariance matrix Σ,

$$\mathcal{N}(\boldsymbol{\theta} \mid \mu, \Sigma) \propto \exp\left[-\frac{1}{2}(\boldsymbol{\theta} - \mu)^T \Sigma^{-1} (\boldsymbol{\theta} - \mu)\right], \tag{3.4}$$

and $\pi_k(\boldsymbol{\Lambda})$ are the weights of the K Gaussian components in the mixture.

The MDN is implemented using the `PyTorch` framework [569]. Specifically, we construct the network using a `Sequential` container comprising multiple `Linear` layers. To introduce non-linearity within the network layers, we apply a Leaky ReLU (`LReLU`) activation function. The training process involves minimizing the following loss function with respect to the network weights w,

$$L(w) = -\frac{1}{N} \sum_{n=1}^{N} \ln\left[\sum_{k=1}^{K} \pi_k\left(\boldsymbol{\Lambda}^{(n)}, w\right) \times \mathcal{N}\left(\boldsymbol{\theta}^{(n)} \mid \mu_k\left(\boldsymbol{\Lambda}^{(n)}, w\right), \Sigma_k\left(\boldsymbol{\Lambda}^{(n)}, w\right)\right)\right], \tag{3.5}$$

where N is the number of NR-calibration posteriors used for training. This loss function represents the mean of the negative log-posterior of the MDN [570]. We model full covariance matrices, which we parametrize by their Cholesky decomposition. We use the `Adam` optimization algorithm for training the network. Model hyper-parameters (number of Gaussians in the mixture, number of network layers, `n_layers`, number of neurons per layer, `n_neurons`, and number of training epochs, `n_epochs`) are initially chosen with an 80-20 training-test split, and further refined by performing waveform sanity checks against `NRHybSur3dq8` waveforms not included in the training set. Our final settings are `n_layers` $= 6$, `n_neurons` $= 96$, `n_epochs` $= 5000$ and a single Gaussian component.

We transform the variables $\boldsymbol{\Lambda}$ from (q, χ_1, χ_2) to (ν, a_+, a_-). To improve the extrapolation behavior of the model, we fit the residuals of the calibration parameters $\boldsymbol{\theta}$ after subtracting the least-square fits of Ref. [2] (with the superscript v5), which we denote $(\delta\Delta t_{\rm NR}, \delta d_{\rm SO}) = \boldsymbol{\delta\theta}$. Test-particle ($\nu \to 0$) information is already enforced by

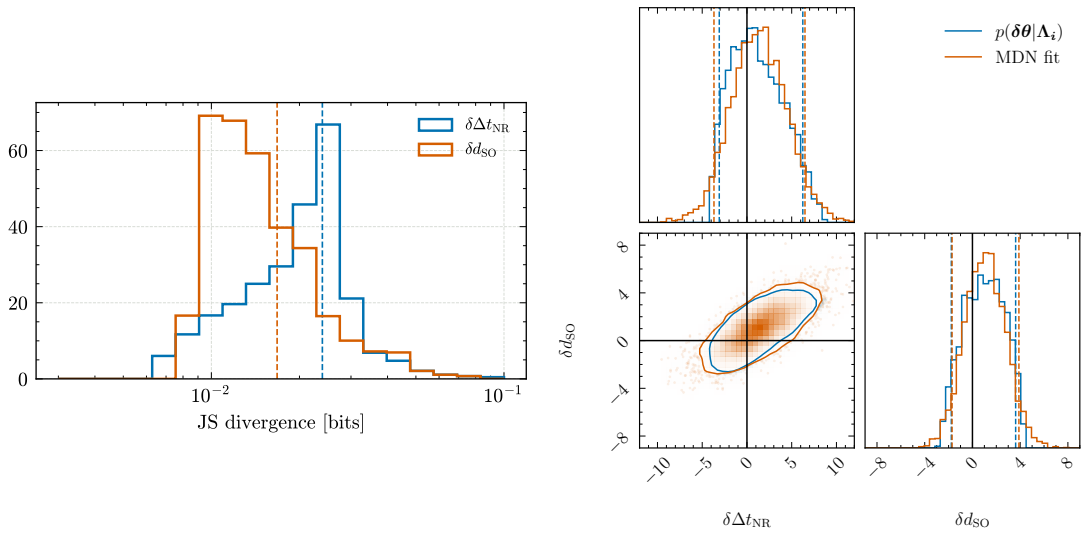

Figure 3.3: *Left panel:* Jensen-Shannon divergence (JSD) between the one-dimensional marginalized distributions of $(\delta\Delta t_{\rm NR}, \delta d_{\rm SO})$ for NR-calibration posterior residuals, $p(\boldsymbol{\delta\theta} \mid \boldsymbol{\Lambda})$, and our MDN fit, across the 400 spinning NR simulations used to build the model. The vertical dashed lines indicate the medians of the distributions. *Right panel:* Comparison of the NR-calibration posterior residual $p(\boldsymbol{\delta\theta} \mid \boldsymbol{\Lambda})$ and the corresponding MDN fit, for the NR simulation `SXS:BBH:2158` with parameters $\boldsymbol{\Lambda_i} = (q, \chi_1, \chi_2) \simeq (3.0, 0.5, 0.5)$. This case has JSD $\simeq 0.022$ for $\delta\Delta t_{\rm NR}$ and JSD $\simeq 0.017$ for $\delta d_{\rm SO}$. The posterior encompasses zero, indicated by the black lines, corresponding to the default `SEOBNRv5HM` fit.

the least-square fits, so we rescale the residual posteriors by ν to have the correction go to zero in that limit. In the small-spin limit, the posteriors are uninformative because the model is already well-calibrated, and the term containing $d_{\rm SO}$ in $H_{\rm EOB}$ is scaled by an a_+ factor (2.5). To recover the nonspinning limit of the model, and improve its robustness for small-spin configurations, we taper the corrections with a tanh function

$$\begin{aligned}\Delta t_{\rm NR} &= \Delta t^{\rm v5}_{\rm NR}\left(\nu, a_+, a_-\right) + \nu \tanh\left[\alpha\left(a_+^2 + a_-^2\right)\right] \Delta t^{\rm MDN}_{\rm NR}\left(\nu, a_+, a_-\right) \\ &= \Delta t^{\rm v5}_{\rm NR}\left(\nu, a_+, a_-\right) + \delta\Delta t_{\rm NR}\,, \qquad (3.6a)\\ d_{\rm SO} &= d^{\rm v5}_{\rm SO}\left(\nu, a_+, a_-\right) + \nu \tanh\left[\alpha\left(a_+^2 + a_-^2\right)\right] d^{\rm MDN}_{\rm SO}\left(\nu, a_+, a_-\right) \\ &= d^{\rm v5}_{\rm SO}\left(\nu, a_+, a_-\right) + \delta d_{\rm SO}. \qquad (3.6b)\end{aligned}$$

We choose $\alpha = 10$ based on sanity checks against NR and `NRHybSur3dq8` waveforms not used in the training. Before performing the fit, we finally apply a `StandardScaler` transformation with `scikit-learn` [571], such that the data have a mean of zero and a standard deviation of one.

To quantify the similarity between the NR-calibration posteriors residuals, $p(\boldsymbol{\delta\theta} \mid$

$\mathbf{\Lambda}$), and our MDN fit, we show in the left panel of Fig. 3.3 the Jensen-Shannon divergence (JSD) between one-dimensional marginalized distributions of $\boldsymbol{\delta\theta} = (\delta\Delta t_{\rm NR}, \delta d_{\rm SO})$, for the 400 spinning NR simulations employed to build the model. The JSD ranges between 0 and 1 bits, with the similarity between the distributions being greater when the JSD is closer to zero. The JSD between two distributions $p(\vartheta)$ and $q(\vartheta)$ is defined as a symmetrized version of the Kullback-Leibler divergence:

$$\mathrm{JSD} = \frac{D_{\rm KL}(p|q) + D_{\rm KL}(q|p)}{2}, \tag{3.7}$$

where the Kullback-Leibler divergence is defined as

$$D_{\rm KL}(p|q) = \int d\vartheta\, p(\vartheta) \log_2 \left(\frac{p(\vartheta)}{q(\vartheta)}\right). \tag{3.8}$$

For both $(\delta\Delta t_{\rm NR}, \delta d_{\rm SO})$ the median JSD, indicated by the vertical dashed lines, is around 0.02 bits. As an illustrative example, we compare in the right panel of Fig. 3.3 the NR-calibration posterior residual $p(\boldsymbol{\delta\theta} \mid \mathbf{\Lambda})$ and the corresponding MDN fit, for the NR simulation `SXS:BBH:2158` with parameters $\mathbf{\Lambda} = (q, \chi_1, \chi_2) \simeq (3.0, 0.5, 0.5)$. This is a representative case with JSD $\simeq 0.022$ for $\delta\Delta t_{\rm NR}$ and JSD $\simeq 0.017$ for $\delta d_{\rm SO}$. Note that the posterior encompasses zero, indicated by the black lines, which corresponds to the default `SEOBNRv5HM` fit. The largest JSD values correspond to broader, more uninformative posteriors, which are harder to fit accurately. These occur particularly near nonspinning or negative-spin configurations. However, this is not a significant issue since uninformative posteriors indicate that the default `SEOBNRv5HM` model is already accurate.

We now turn to waveform sanity checks, computing the maximum (2,2)-mode mismatch over a range of total masses between 10 and 300 $M_\odot$ using the zero-detuned high-power aLIGO PSD [525] for different `SEOBNRv5` variations. We compare the default `SEOBNRv5` model, a version of `SEOBNRv5` using the mean of the MDN fit of $p(\boldsymbol{\delta\theta} \mid \mathbf{\Lambda})$ for $\boldsymbol{\delta\theta}$, and one in which we take median mismatch over 100 samples for $\boldsymbol{\delta\theta}$ from the MDN model.

In the left panel of Fig. 3.4, we compare the three `SEOBNRv5` variations against the 442 NR simulations used in this study, showing the cumulative distribution of the maximum mismatch. We also include 42 nonspinning simulations, not used to build the MDN model, to allow a direct comparison with the results of Sec. 2.2.4. Using the mean of the MDN fit for $\boldsymbol{\delta\theta}$ leads to a more NR-faithful model than the default `SEOBNRv5`. The median of the distribution, indicated by the vertical dashed lines, decreases by almost a factor of 2 from $\sim 2 \times 10^{-4}$ to 1.1×10^{-4}. Additionally, the fraction of cases with maximum mismatch $\lesssim 1 \times 10^{-3}$ increases from 90% to 96%.

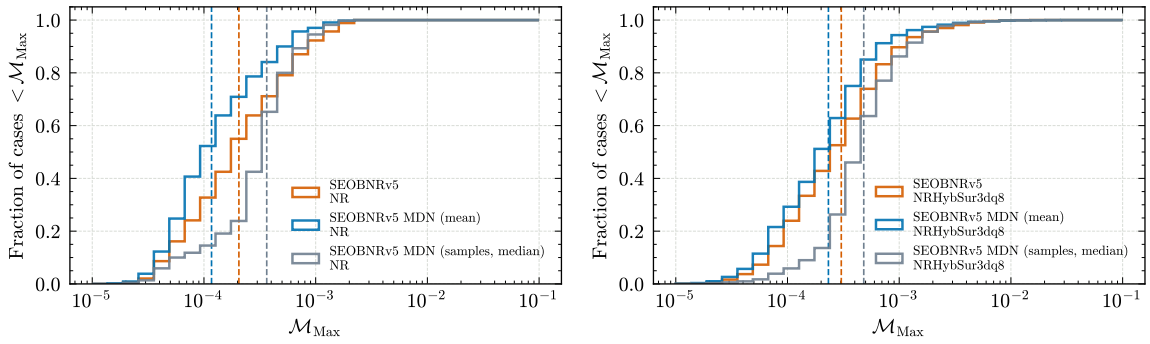

Figure 3.4: *Left panel:* cumulative distribution of the maximum (2,2)-mode mismatch over 10 and 300 $M_\odot$, against the 442 NR simulations used in this work. *Right panel:* cumulative distribution of the maximum (2,2)-mode mismatch over 10 and 300 $M_\odot$, against `NRHybSur3dq8`, for 5000 random configurations with $q \in [1, 8], |\chi_i| \leq 0.9$. The vertical dashed lines show the medians. In both panels, we compare the results of the default `SEOBNRv5` model, a version of `SEOBNRv5` using the mean of the MDN fit of $p(\boldsymbol{\delta\theta} \mid \boldsymbol{\Lambda})$ for $\boldsymbol{\delta\theta}$, and one in which we take median mismatch over 100 samples for $\boldsymbol{\delta\theta}$ from the MDN model.

Using different samples for $\boldsymbol{\delta\theta}$ from the MDN fit also provides comparable accuracy, mostly below the $\sim 1 \times 10^{-3}$ level, consistent with the likelihood function used in the calibration. The median mismatch is 3.6×10^{-4}, with about 92% of cases having a mismatch $\lesssim 1 \times 10^{-3}$.

The right panel of Fig. 3.4 presents a similar comparison against `NRHybSur3dq8` waveforms not used in the training. We use 5000 random configurations with $q \in [1, 8], |\chi_i| \leq 0.9$ and a dimensionless orbital frequency $M\Omega_0 = 0.015$, allowing some extrapolation outside the surrogate's training region ($|\chi_i| \leq 0.8$) to test the extrapolation of the MDN fit. The mismatch values are comparable to the ones against NR, albeit slightly higher because of the larger number of challenging cases with high q and high spin in this comparison. The `SEOBNRv5` version using the mean of the MDN fit for $\boldsymbol{\delta\theta}$ outperforms the default `SEOBNRv5` model, with the median mismatch decreasing from 3.0×10^{-4} to 2.3×10^{-4} and fraction of cases with mismatch $\lesssim 1 \times 10^{-3}$ increasing from 87% to 93%. This confirms that, regardless of the uncertainty estimate, the MDN fit is a more flexible method compared to the hierarchical least-square fits used in the default `SEOBNRv5` model. It captures subdominant features present in the NR data without overfitting. Also in this case, taking different samples for $\boldsymbol{\delta\theta}$ from the MDN provides comparable performance and confirms that the uncertainty estimate leads to well-behaved waveforms overall. The median mismatch in this case is 4.8×10^{-4}, with about 83% of cases having a mismatch $\lesssim 1 \times 10^{-3}$.

As a concrete example, the upper panel of Fig. 3.5 shows an `SEOBNRv5HM` waveform

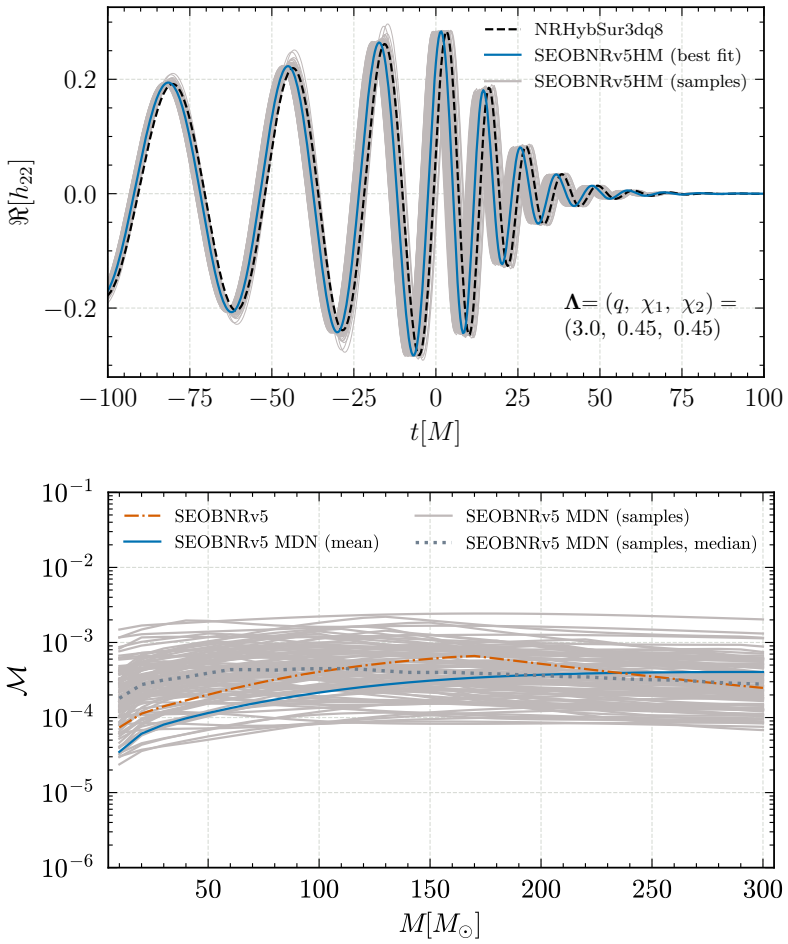

Figure 3.5: *Upper panel:* An `SEOBNRv5HM` waveform with its uncertainty estimate, compared against the `NRHybSur3dq8` model after a low-frequency alignment. The waveforms start at a frequency of 20 Hz for a binary with total mass $M = 60\ M_\odot$. The best-fit `SEOBNRv5HM` waveform uses as NR-calibration parameters $\boldsymbol{\theta}$ the mean of the MDN fit of the calibration posterior $p\left(\boldsymbol{\theta} \mid \mathbf{\Lambda}\right)$, while the uncertainty corresponds to 100 samples from the same distribution. The time $t = 0$ corresponds to the peak of the $(2, 2)$ mode of the NR waveform. *Lower panel:* Mismatch distribution as a function of the total mass between `NRHybSur3dq8` and different variations of `SEOBNRv5`, for $\mathbf{\Lambda} = (q, \chi_1, \chi_2) = (3.0, 0.45, 0.45)$. We show the default `SEOBNRv5` model and variations which use the mean or different samples of the MDN fit for $\boldsymbol{\delta\theta}$.

with its uncertainty estimate, from different calibration posterior samples, for $\mathbf{\Lambda} = (q, \chi_1, \chi_2) = (3.0, 0.45, 0.45)$, compared against the `NRHybSur3dq8` model. The lower panel shows the mismatch distribution as a function of the total mass for 100 samples from the MDN model, for the same configuration. The darker dotted line indicates the median mismatch across the 100 samples, while the default `SEOBNRv5` model and the version using the mean of the MDN fit for $\boldsymbol{\delta\theta}$ are represented by the orange and blue lines, respectively. The mean of the posterior for the calibration parameters generally provides better agreement than most samples, depending on the binary's total mass. However, it does not always correspond to the *best-fit* (i.e., maximum likelihood) waveform, as the posterior is not strictly Gaussian.

3.3.2 Parameter estimation results

We now evaluate the impact of marginalizing over the NR-calibration uncertainty in the parameter inference of loud *golden* BBH systems. To marginalize over modeling uncertainties in PE, we sample both the source parameters and corrections to the NR-calibration parameters $\boldsymbol{\delta\theta}$, using $p(\boldsymbol{\delta\theta} \mid \mathbf{\Lambda})$ as conditional priors. As in Ref. [434] we also compare these results to those obtained using uniform priors on $\boldsymbol{\delta\theta}$. We choose a range within $[-50, 50]$ for both $\delta\Delta t_{\rm NR}$ and $\delta d_{\rm SO}$, slightly wider than the typical support of the NR-calibration posteriors.

To simulate and analyze the GW signals we use the `parallel bilby` package [179, 470, 486] and the nested sampler `dynesty` [553], using standard settings and priors as described in Sec. 3.1. We consider four GW ground-based detector networks, consisting of current detectors at their design and upgraded sensitivities, and a configuration where upgraded current detectors work in conjunction with an XG detector. These are listed below:

- O4 network: This network includes the advanced LIGO detectors at Hanford and Livingston operating at O4 sensitivity, and the advanced Virgo detector operating at design sensitivity. We use the noise curves available in `bilby`, specifically `aLIGO O4 high` [398] and `AdV` [395]. The minimum frequency is set to $f_{\rm low} = 20$ Hz.
- O5 network: This network consists of the advanced LIGO detectors at Hanford and Livingston operating at design (A+) sensitivity, using the same noise curve as in [435], along with the advanced Virgo detector at design sensitivity. The minimum frequency is set to $f_{\rm low} = 15$ Hz.
- A# network: This network includes the advanced LIGO detectors at Hanford and Livingston operating at A# sensitivity, using the same noise curve as in [435], and the advanced Virgo detector at design sensitivity. The minimum frequency

is set to $f_{\rm low} = 10$ Hz.

- ET-A# network: This network features a 10 km ET in Europe, at the Virgo location, using the same noise curve as in [435], combined with LIGO detectors at Hanford and Livingston operating at A# sensitivity. While the ET is proposed to have a triangular configuration, the `bilby pipe` wrapper is limited to L-shaped interferometers, and we assume the ET to be L-shaped as in Ref. [435]. The likelihood integration begins at $f_{\rm low} = 10$ Hz. Although a lower frequency of $\sim 3-5$ Hz would be more realistic for ET, the accuracy of long NR simulations and of hybridized NR surrogate waveforms, which we use to simulate signals, is not guaranteed to be sufficient for such long durations [276].

For all configurations, we use a maximum frequency $f_{\rm high} = 1024$ Hz, which is above the ringdown frequency of the higher-order modes for all the systems considered in this study. The sampling frequency is then chosen to be $f_{\rm s} = 2048$ Hz. While proposed XG detector networks often include the ET operating in conjunction with one or more CE detectors, we do not explore these configurations here. The sources we consider would have an SNR around 1500 in such a network. For such high SNRs, the accuracy of current NR waveforms may not be adequate [429], potentially complicating efforts to identify the origins of any biases.

For each detector network, we simulate two BBH signals in zero-noise using the `NRHybSur3dq8` model, selecting configurations with unequal masses ($q = 3$) and either positive ($\chi_1 = \chi_2 = 0.45$) or negative ($\chi_1 = \chi_2 = -0.45$) spins. While these configurations lie within the NR-calibration region of the model, they are still relatively challenging and may exhibit non-negligible modeling errors at high SNR. We fix the detector-frame total mass of the binary to $M = 60M_{\odot}$, which gives $\mathcal{M}_c \simeq 21.976$ for $q = 3$. Common parameters for both systems include: inclination angle $\iota = 0.438$, azimuthal angle $\varphi = 0$, sky location $\alpha = 1.827$, $\delta = -1.252$ (radians), luminosity distance $d_L = 600.0$Mpc, polarization angle $\psi = 2.562$ and GPS time at the geocenter 1126259462.409 s. For the negative (positive)-spin configuration, the network optimal SNR ranges from 39.3 (51.8) in the O4 network, to 366.7 (439.2) in the ET-A# network.

For each of the eight configurations, we perform three inference runs. In the first, we use the default `SEOBNRv5HM` model and sample only the standard source parameters. In the other two, we account for NR-calibration uncertainty by sampling over corrections to the NR-calibration parameters $\boldsymbol{\delta\theta}$ with either $p\left(\boldsymbol{\delta\theta} \mid \boldsymbol{\Lambda}\right)$ or uniform priors, as previously described.

Figure 3.6 presents marginalized posterior distributions for the chirp mass, inverse mass ratio, and effective spin, for the negative-spin configuration in the ET-A# detector network (SNR= 366.7). The `SEOBNRv5HM` recovery shows biases in $\mathcal{M}_{\rm c}$, $1/q$,

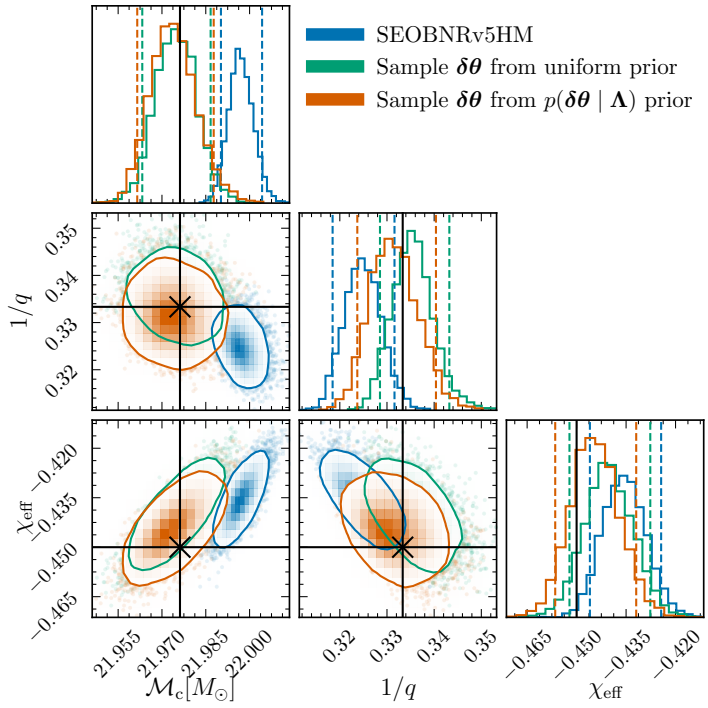

Figure 3.6: Marginalized posterior distributions for the chirp mass, inverse mass ratio, and effective spin in the ET-A# detector network. Parameter estimation is performed by injecting a `NRHybSur3dq8` signal, with an SNR of 366.72, and recovering it using three versions of `SEOBNRv5HM`: one sampling only the standard source parameters, and the others including corrections to the NR-calibration parameters $\boldsymbol{\delta\theta}$. For $\boldsymbol{\delta\theta}$, both uniform priors and $p\left(\boldsymbol{\delta\theta} \mid \boldsymbol{\Lambda}\right)$ priors, reflecting NR-calibration uncertainty, are used. In the latter case, we accurately recover the injected values within the 90% credible region, indicated by dashed vertical lines in the one-dimensional marginalized posteriors and contours in the two-dimensional marginalized posteriors.

$\chi_{\rm eff}$, with the injected value falling outside the 90% credible intervals, indicated by dashed vertical lines in the one-dimensional marginalized posteriors and contours in the two-dimensional marginalized posteriors. Sampling over $\boldsymbol{\delta\theta}$ with uniform priors reduces these biases, bringing the injected parameters at the edge of the 90% contours. This improvement is partially due to the increase in statistical uncertainty, though all parameters also peak closer to the injected values. Using $p\left(\boldsymbol{\delta\theta} \mid \boldsymbol{\Lambda}\right)$ priors for $\boldsymbol{\delta\theta}$ further improves the recovery of $1/q$ and $\chi_{\rm eff}$, with the injected values now falling well within the two-dimensional contours. The increase in statistical error and decrease in systematic error when accounting for waveform uncertainties is qualitatively consistent with the earlier results of Refs. [562–564] and with the PN model of Ref. [434]. Biases arise because the template model can provide a better fit to the signal when the parameters are not the true ones. By improving the match through adjustments in *nuisance* parameters like $\boldsymbol{\delta\theta}$, the need for shifts in the physical parameters is reduced. The increase in statistical error is due to additional correlations introduced by the

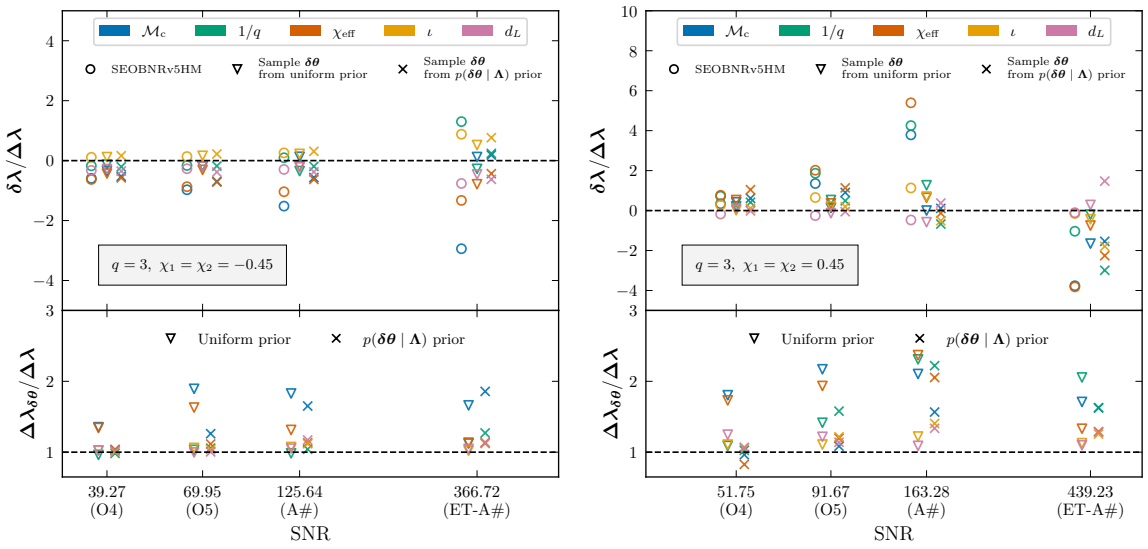

Figure 3.7: *Upper panels*: Ratio of systematic bias to statistical errors ($\boldsymbol{\delta\lambda/\Delta\lambda}$) for the chirp mass, inverse mass ratio, effective spin, inclination, and luminosity distance, as a function of the network SNR, for upcoming runs, O4, O5, A#, and next-generation ground-based detector networks (ET-A#). Parameter estimation is performed by injecting a `NRHybSur3dq8` signal, and recovering it with three versions of `SEOBNRv5HM`: one sampling only the standard parameters, and the others including corrections to the NR-calibration parameters $\boldsymbol{\delta\theta}$. For $\boldsymbol{\delta\theta}$, both uniform priors and $p\,(\boldsymbol{\delta\theta} \mid \boldsymbol{\Lambda})$ priors, reflecting NR-calibration uncertainty, are used. *Bottom panels*: Ratio of statistical errors ($\boldsymbol{\Delta\lambda}$) with and without corrections to the NR-calibration parameters $\boldsymbol{\delta\theta}$, using different priors.

nuisance parameters.

Figure 3.7 presents the ratio of systematic bias to statistical errors ($\boldsymbol{\delta\lambda/\Delta\lambda}$) for the same set of parameters, as well as inclination and luminosity distance, as a function of the SNR across the four detector networks. The left panel corresponds to the negative-spin configuration; the right panel shows the positive-spin case. We take $\boldsymbol{\delta\lambda}$ to be the difference between the injected parameters and the median of the one-dimensional marginalized posteriors, and $\boldsymbol{\Delta\lambda}$ to be half of the width of the 90% one-dimensional credible interval.

In the negative-spin case (left panel), the original model exhibits biases in masses and spins (e.g., $|\boldsymbol{\delta\lambda/\Delta\lambda}| > 1$) at SNRs of ~ 100 and above. These biases are substantially mitigated when accounting for NR-calibration uncertainties, with all cases having $|\boldsymbol{\delta\lambda/\Delta\lambda}| \lesssim 1$ when including corrections to the NR-calibration parameters $\boldsymbol{\delta\theta}$. To assess whether this improvement results from an actual reduction in bias or simply reflects an increase in statistical uncertainty, the bottom panel shows the ratio of $\boldsymbol{\Delta\lambda}$ with and without $\boldsymbol{\delta\theta}$ corrections. For both prior choices, there is an increase of a factor

of a few in statistical errors, mainly for masses and spins, with a marginal increase for distance and inclination. The use of MDN-informed priors lead to a smaller increase in statistical errors, especially at lower SNRs where the default `SEOBNRv5HM` model is unbiased. The increase in statistical error can be below the $\boldsymbol{\delta\lambda}/\boldsymbol{\Delta\lambda}$ ratio of the default `SEOBNRv5HM` model, even when models with uncertainty corrections achieve $\boldsymbol{\delta\lambda}/\boldsymbol{\Delta\lambda} \lesssim 1$, indicating a shift of the recovered parameters toward the injected values.

For the positive-spin configuration (right panel), similar improvements are seen at SNR ~ 100 (O5 and A# networks), where sampling over $\boldsymbol{\delta\theta}$ parameters significantly mitigates biases. This is not true in the ET-A# network, in which the injected signal has SNR $= 439.2$, although biases are still slightly reduced, especially when looking at two-dimensional marginalized posterior distributions. The presence of a bias suggests that the $\boldsymbol{\delta\theta}$ parameters do not provide sufficient flexibility to match `NRHybSur3dq8` with the required precision, for the same values of the physical parameters $\boldsymbol{\lambda}$. This could be due to the ineffectiveness of the parameters being varied, missing physics in the `SEOBNRv5HM` model (e.g., some higher-order modes), or potential inaccuracies in the `NRHybSur3dq8` model (either due to NR resolution or to the hybridization procedure), which may become significant at such high SNRs [429]. This is expected, as the chosen $\boldsymbol{\delta\theta}$ may not fully account for all sources of error, and mismodeling in other parts of the waveform construction could become relevant at sufficiently high SNR.

One possible explanation for the residual biases is the absence or mismodeling of higher-order modes. To quantify the impact of neglecting certain higher-order modes, we first perform a test where we include the same set of modes in both the injected and recovered waveforms. Specifically, `NRHybSur3dq8` includes the $(\ell, m) = (2, 0)$,-$(3, 1), (3, 0), (4, 2), (5, 5)$ modes, which are not incorporated by default in `SEOBNRv5HM`. We find that this change reduces the biases only slightly, and does not qualitatively affect the results, indicating that the lack of higher-order modes is not the primary source of error. In `SEOBNRv5HM`, higher-order modes are calibrated to NR in the merger-ringdown phase, but they are less accurate than the dominant $(2, 2)$ mode. This is due to both the lower NR quality for these modes and the increased difficulty of fitting subdominant modes, which often exhibit complex morphologies. The $\boldsymbol{\delta\theta}$ parameters we focus on do not account for these inaccuracies.

To assess the impact of higher-mode mismodeling, we repeat the analysis using only the dominant $(2, 2)$ mode in both the signal and template. We show in Fig. 3.8 the marginalized posterior distributions for the chirp mass, inverse mass ratio, and effective spin. In this case, we observe that biases are still present in `SEOBNRv5HM`, but are mitigated when sampling on $\boldsymbol{\delta\theta}$. This indicates that mismodeling of higher-order modes is a significant source of error. The NR-calibration parameters $\boldsymbol{\theta}$ we consider

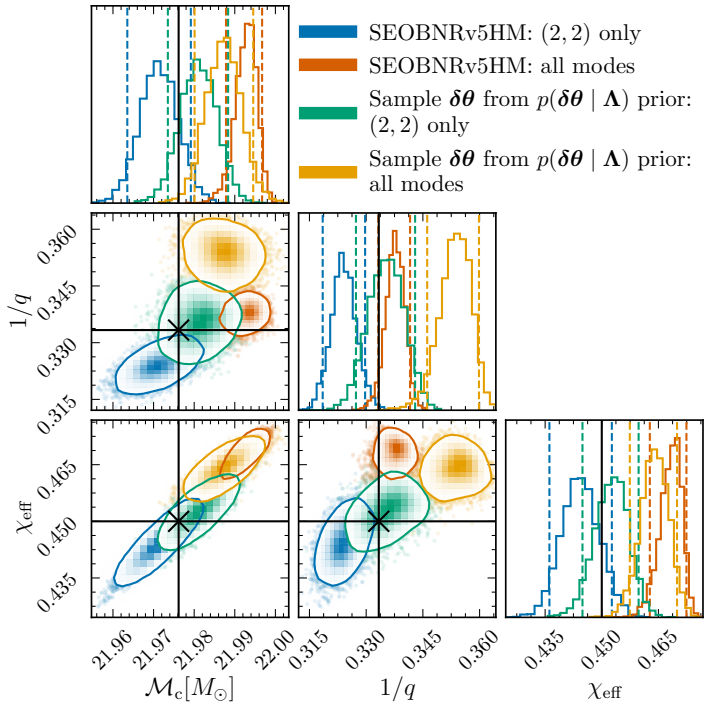

Figure 3.8: Marginalized posterior distributions for the chirp mass, inverse mass ratio, and effective spin in the ET-A# detector network. Parameter estimation is performed by injecting a `NRHybSur3dq8` signal and recovering it using `SEOBNRv5HM`, either sampling only the standard source parameters, or including corrections to the NR-calibration parameters $\boldsymbol{\delta\theta}$. For $\boldsymbol{\delta\theta}$, both uniform priors and $p\left(\boldsymbol{\delta\theta} \mid \boldsymbol{\Lambda}\right)$ priors, reflecting NR-calibration uncertainty, are used. We compare results using all available modes in both the signal and template, and using only the dominant $(2, 2)$ mode. In the latter case, biases are mitigated when sampling on $\boldsymbol{\delta\theta}$.

only shape the waveform model in specific directions; it appears that the waveform space that these parameters allow to explore that does not allow us to approach the NR waveform closely enough without also modifying the standard binary parameters $\boldsymbol{\lambda}$. To address this, additional $\boldsymbol{\delta\theta}$ parameters should be considered to account for mismodeling specific to higher-order modes. This could be achieved by introducing parametrized deviations in the amplitude and frequency at the merger, similar to what is done in tests of GR [369], after determining appropriate priors across the parameter space.

To assess the effectiveness of our method across parameter space, we extend the analysis to a larger set of 12 configurations with mass ratios $q \in [1.5, 3.0, 6.0]$ and equal spins $\chi_i \in [-0.75, -0.45, 0.45, 0.75]$, fixing the chirp mass to $\mathcal{M}_c \simeq 21.976$. For simplicity, we restrict this study to the A# detector network. At a fixed luminosity distance, the SNR of the injected signal decreases with increasing mass ratio and increases with higher spins, ranging from 88.0 for the configuration with $q = 6$ and

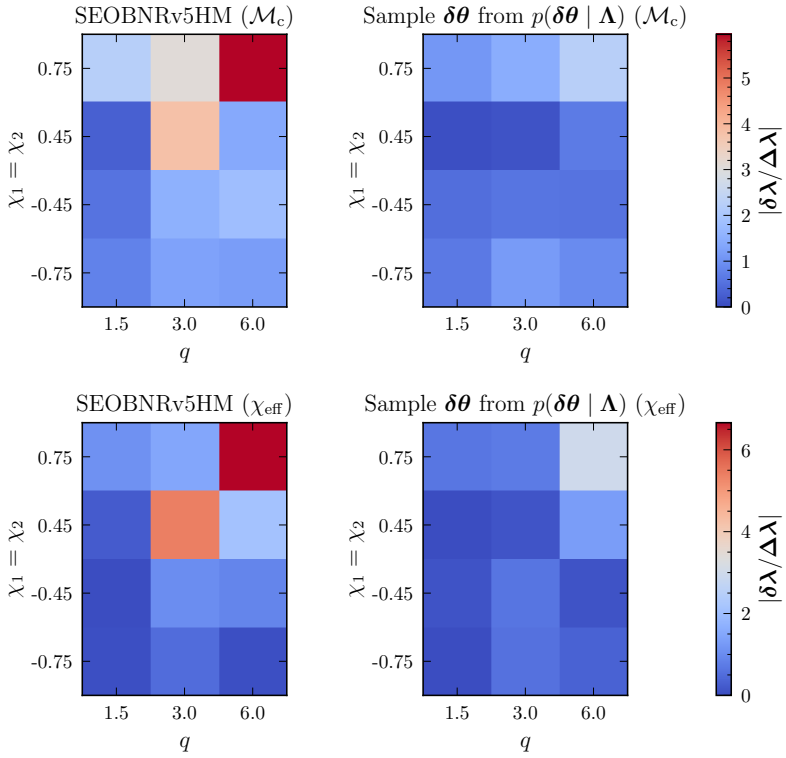

Figure 3.9: Ratio of systematic bias to statistical error ($|\boldsymbol{\delta\lambda}/\boldsymbol{\Delta\lambda}|$) for the chirp mass and effective spin across 12 configurations with varying mass ratios ($q \in 1.5, 3.0, 6.0$) and equal spins ($\chi_i \in -0.75, -0.45, 0.45, 0.75$) in the A# detector network. Left columns display results using the default `SEOBNRv5HM` model; right columns incorporate corrections to the NR-calibration parameters $\boldsymbol{\delta\theta}$ using MDN-informed priors $p(\boldsymbol{\delta\theta} \mid \boldsymbol{\Lambda})$. Including calibration uncertainty systematically reduces biases, particularly for configurations with large positive spins and unequal mass ratios.

$\chi_i = -0.75$, to 187.8 for $q = 1.5$ and $\chi_i = 0.75$. In this case, we recover `NRHybSur3dq8` signals using `SEOBNRv5HM`, either sampling only the standard source parameters, or including corrections to the NR-calibration parameters $\boldsymbol{\delta\theta}$ with $p(\boldsymbol{\delta\theta} \mid \boldsymbol{\Lambda})$ priors. Figure 3.9 shows the ratio of systematic bias to statistical errors ($|\boldsymbol{\delta\lambda}/\boldsymbol{\Delta\lambda}|$) across the parameter space, for the chirp mass and $\chi_{\rm eff}$. The left columns present the default `SEOBNRv5HM` recovery, while the right columns show results sampling on corrections to the NR-calibration parameters $\boldsymbol{\delta\theta}$ with $p(\boldsymbol{\delta\theta} \mid \boldsymbol{\Lambda})$ priors. Including corrections to the NR-calibration parameters generally reduces biases across the parameter space, especially for the most challenging configurations with large positive spins and unequal mass ratios.

While the inclusion of $\boldsymbol{\delta\theta}$ corrections generally reduces biases, it does not always eliminate them entirely – for example, in the case with $q = 6$ and $\chi_i = 0.75$. When considering an approximate model $H(\boldsymbol{\Lambda})$ and the "true" waveform $h_{\rm true}(\boldsymbol{\Lambda})$, we only

have an approximate relation $h_{\rm true}(\boldsymbol{\Lambda}) \simeq H(\boldsymbol{\Lambda}, \boldsymbol{\theta}(\boldsymbol{\Lambda}) + \boldsymbol{\delta\theta}(\boldsymbol{\Lambda}))$. The effectiveness of the $\boldsymbol{\delta\theta}$ correction in reducing the difference between the approximate and "true" waveforms depends crucially on the choice of the calibration parameters $\boldsymbol{\theta}$. Additional corrections, such as higher-order terms in the EOB Hamiltonian and energy flux, or corrections to higher modes, may be relevant depending on the source's properties and SNR.

The $\boldsymbol{\delta\theta}$ corrections we focus on account for the inevitable errors in the fits to NR, as well as the fact that NR is only an approximation of the "true" signal. While this may represent only a partial source of error, it is inherently linked to the construction of all IMR models calibrated to NR, and must be accounted for. Specifically, our results indicate that this source of error would be significant in the near future, potentially as early as O5. For events from previous LVK observing runs, we expect that our uncertainty estimates would not yield significant differences, given the relatively low SNR. Reanalyses of the events GW150914 and GW190412 using the publicly released strain data [556, 572] show a maximum JSD across different parameters of 0.004 bits between recoveries with and without uncertainty estimates, comparable to the statistical uncertainty of stochastic sampling algorithms [179].

On the other hand, the method we introduced does not account, e.g., for missing physical effects. Therefore, incorporating all relevant physical effects into waveform models remains essential. Additionally, while our method addresses uncertainties within the NR-calibration region of the model, it does not necessarily lead to increasing error estimates in regions of the parameter space lacking training data. However, model differences can be large outside their NR-calibration region [435]. To account for these extrapolation uncertainties, one could introduce error estimates based on model-to-model differences rather than relying solely on NR data.

An advantage of our method is that, by using the native time-domain `SEOBNRv5HM` model, it can already be applied to its spin-precessing and eccentric BBH extensions, as well as systems containing NSs, to account for NR-calibration uncertainties in the quasi-circular aligned-spin BBH sector common to all the models. Once EOB models are calibrated to eccentric and spin-precessing NR simulations, our method can be extended to handle specific uncertainties related to these features. Our results with uniform priors on $\boldsymbol{\delta\theta}$ also suggest that PE for spin-precessing and eccentric BBHs could be improved even without detailed calibration to NR, provided that reasonable priors can be set on appropriate calibration parameters. Our method could also enhance the robustness of tests of GR based on EOB waveforms [367–370, 418], and may help mitigate false GR deviation caused by waveform systematics [369, 418].

Despite adding extra parameters, the computational cost of recoveries including $\boldsymbol{\delta\theta}$ is lower than for the default model, due to fewer likelihood evaluations needed for

convergence. This is especially true with MDN-based priors on $\boldsymbol{\delta\theta}$, with $\sim 30\%$ fewer likelihood evaluations required.

4 Tests of general relativity with gravitational waves from binary black hole mergers

4.1 Tests of general relativity with gravitational-wave sources

In addition to providing insight into BH and NS populations and their astrophysical formation channels, GWs also offer a unique probe of fundamental physics. They have already led to improved constraints on the NS equation of state [573] and enabled independent measurements of the Hubble-Lemaître parameter [574, 575].

The binary dynamics and waveforms described throughout the previous chapters are derived assuming GR, which continues to be supported by all precision tests conducted to date, from weak-field regimes to relativistic systems [15]. Despite its successes, GR is expected to be an effective low-energy approximation of a more fundamental, and as yet unknown, quantum theory of gravity. Such a theory would reconcile GR with quantum mechanics and is expected to introduce deviations from classical GR predictions at small but finite energy or length scales [576].

Modified theories of gravity, developed as potential extensions or alternatives to GR, predict both qualitative and quantitative changes in the dynamics of compact binaries and the resulting GW signals. These deviations can manifest as modifications to the orbital evolution, waveform phase and amplitude, polarization content, or propagation speed of GWs [576]. Importantly, many of these effects are either enhanced or exclusively present in the strong-field, highly dynamical regimes characteristic of BH and NS mergers, regimes that are otherwise inaccessible to traditional tests of gravity such as Solar System experiments [577] or binary pulsar observations [578]. Gravitational-wave astronomy thus offers a unique and powerful probe of gravity in the strong-field, nonlinear regime.

So far, GW observations have shown remarkable agreement with GR, placing

increasingly stringent bounds on deviations from its predictions [250, 251, 439–441]. However, the current constraints are limited by the sensitivity of existing detectors and the relatively modest SNR of most events. Next-generation observatories such as ET, CE, and LISA will bring substantial improvements both in sensitivity and frequency coverage. These detectors are expected to observe thousands of GW events per year, some with significantly higher SNR, offering exceptional opportunities for high-precision tests of GR in the strong-field regime [579, 580].

Parametrized and theory-specific tests of general relativity

General relativity has a long and rich history of progress in solving the relativistic two-body problem, which has led to increasingly accurate models for the dynamics and gravitational radiation of compact binaries across all stages of their evolution. In contrast, the modeling of compact binaries in modified gravity theories is still in its infancy. In the absence of waveform predictions within most alternative theories of gravity, the majority of tests of GR with GWs have been carried out so far following theory-independent approaches.

Theory-independent tests, while often motivated by specific beyond-GR phenomena, are designed to be agnostic to specific alternative theories and allow for a broad range of possible departures from GR predictions. These tests may modify GR waveform models by introducing some generic, parametrized deviations, which are constrained by comparing the waveform templates with an observed GW signal [367,368,370,581–590]. Alternatively, they may look for consistency between the signal and the data, or between different portions of the signal, without invoking any parametrization of the deviations [591–595]. Any statistically significant departure from the null hypothesis would hint at the existence of a class of exotic compact objects, or at a potential deviation from GR. While theory-independent tests can, in principle, constrain a wide range of alternative theories, parametrized deviations are not unique, and degeneracies among different deviation parameters complicate constraining multiple of them at the same time unless specific combinations are selected [596]. Moreover, there is no guarantee that parametrized deviations can represent the potentially infinite landscape of beyond-GR theories (see Ref. [597] for an attempt to address this issue). Furthermore, although such tests are valuable in identifying possible deviations from GR, they do not necessarily inform us about the new physics at play; without reference to specific alternatives, it is difficult to assess the ability of these methods to detect actual GR violations [598].

In some cases, it has been possible to carry out theory-specific tests of GR (see, e.g., Refs. [15, 440, 599–604]). These rely on waveform predictions derived directly within a particular alternative theory of gravity and aim to estimate its underlying physical

parameters. Unlike theory-independent approaches, theory-specific tests allow for a more direct and robust interpretation of any deviations from GR, but they require well-developed analytical and numerical predictions within each theory. Developing accurate waveform predictions for use in theory-specific tests is an active area of research, pursued both analytically (see, e.g., Refs. [33,40,41,371–375,605–626]) and numerically (see, e.g., Refs. [627–658]). Nevertheless, no alternative theory of gravity has yet reached the level of maturity and precision achieved in GR. In Sec. 4.2, we present recent work in this direction by describing the first example of a full IMR waveform model incorporating analytical beyond-GR corrections, focusing on Einstein-scalar-Gauss-Bonnet (ESGB) gravity, a class of theories which supplement GR with a massless scalar field coupled to the Gauss-Bonnet scalar $\mathcal{G} = R^{\mu\nu\rho\sigma}R_{\mu\nu\rho\sigma} - 4R^{\mu\nu}R_{\mu\nu} + R^2$. These theories have attracted particular attention in recent years, thanks to their rich phenomenology for BHs with scalar *hair*.

Classification of tests of general relativity with gravitational waves

In modified gravity theories, GWs may show deviations from GR predictions in three main aspects: generation, propagation, and polarization. Generation effects refer to modifications to the source dynamics and GW emission. Propagation effects are related to how GWs travel through spacetime to the detectors. For example, some alternative theories of gravity – such as massive graviton or Lorentz-violating theories – predict GW dispersion, where different frequency components travel at different speeds [659]. This leads to a characteristic dephasing in the waveform, which can be modeled using a parametrized dispersion relation [660]. Constraints on such deviations can be translated into bounds on the graviton mass m_g [251]. Polarization effects involve the number and nature of GW polarizations. While GR permits only two tensor polarizations (plus and cross), generic metric theories can allow up to six polarizations, including scalar and vector modes [661]. However, not all alternative theories predict additional polarizations—some modify only the generation or propagation of GWs [15, 599].

Another useful distinction – related to generation effects – classifies tests of GR based on the stage of the binary coalescence they target, namely, the inspiral, merger, or ringdown phase. Inspiral tests primarily constrain parametrized deviations in the PN coefficients governing the frequency-domain GW phase evolution [370, 581–587, 590], as observations are generally more sensitive to changes in the phase than in the amplitude. These constraints can often be translated into bounds on specific modified gravity theories [440, 601, 662]. Another class of inspiral tests targets the spin-induced quadrupole moment of the binary components to assess the BBH nature of the system [663, 664]. The spin-induced quadrupole moment arises from the rotational

deformation of compact objects and enters the GW phase evolution starting at 2PN order [665]. In GR, a Kerr BH's quadrupole moment is uniquely determined by its mass and spin [666–668]; any deviation from this relation would signal the presence of exotic compact objects rather than BHs. The merger phase is not analytically tractable and must be modeled using NR. Deviations from GR are typically probed by introducing parametrized deviations in phenomenological coefficients that are used to calibrate the waveform models against NR simulations [369, 587, 590].

The ringdown phase, characterized by the emission of QNMs as the perturbed remnant BH transitions to a stationary Kerr state, offers a particularly promising avenue for testing GR. The QNMs are characterized by discrete frequencies and decay times determined solely by the remnant's mass and spin [236–240]. According to the *no-hair* conjecture [22–25], an astrophysical, electrically neutral BH in GR is fully described by only two parameters: its mass and spin. Consequently, these two quantities uniquely determine its QNM spectrum. Measuring at least two QNMs enables a self-consistency test of the remnant's properties - an idea known as BH spectroscopy [247–251, 367, 368, 417, 669–673]. Any inconsistency between these estimates would suggest a non-BH nature of the remnant object, or the incompleteness of GR as the underlying theory of gravity.

While the QNM frequencies and damping times depend solely on the remnant's properties, the amplitude of each mode and the relative phases between them encode information about the progenitor binary and the merger dynamics. These quantities cannot generally be predicted from first principles, but can be accurately extracted from numerical simulations [674–680]. Leveraging NR-informed amplitude parametrizations, while introducing additional assumptions about the nature of the coalescence, breaks degeneracies between remnant mass, spin, and GR-deviations in the QNM frequencies, that are otherwise present for a single QNM. This approach opens the possibility of measuring deviations from GR even when only one mode is resolvable [251,367,368,681].

Consistent modeling of the merger-ringdown together with the inspiral eliminates ambiguities associated with the choice of the ringdown start time. It also leverages the full signal power and improves sensitivity to deviations from GR during the ringdown. This is the strategy adopted by the parametrized `SEOBNR` (`pSEOBNR`) framework, one of the flagship tests of GR performed within the LVK Collaboration [250, 251]. Initially developed in Refs. [367,368], this approach introduced GR deviations into the ringdown as part of a full EOB IMR model [112,113], calibrated to NR simulations for aligned-spin BBHs. The model was later extended to parametrize deviations in the plunge-merger stages [369] and to perform theory-specific tests of GR [602]. The `pSEOBNR` model has been applied to 12 BBH signals from the LVK third Gravitational-Wave Transient Catalog (GWTC-3), showing consistency with GR, and constraining deviations to the

frequency and decay time of the dominant QNM at the level of approximately 10% and 20%, respectively, through a hierarchical combination of multiple events [250, 251]. In Sec. 4.3, we present `pSEOBNRv5PHM`, the latest iteration of the `pSEOBNR` framework, which extends the analysis to spin-precessing binaries by incorporating parametrized deviations into the `SEOBNRv5PHM` model [139].

Combining information from multiple events

Combining information from multiple events allows placing stronger constraints on the deviation parameters. We will apply this approach in our analyses of real data, employing both theory-specific and theory-independent frameworks.

Assuming that the deviations parameters are constant across events, joint constraints can be obtained by multiplying the individual-event posteriors (given a flat prior on the deviation parameters) [441, 682, 683]. For N events, let us consider the posterior distribution $p(\delta x \mid d^{(j)})$ for a generic deviation parameter δx, obtained from the analysis of the j-th event $d^{(j)}$, where $j = 1, ..., N$. The joint posterior probability is given as,

$$p\left(\delta x \mid \{d^{(j)}\}\right) \propto \prod_{j=1}^{N} p\left(\delta x \mid d^{(j)}\right) \propto \prod_{j=1}^{N} p\left(d^{(j)} \mid \delta x\right)\ p\left(\delta x\right), \tag{4.1}$$

where $p\big(d^{(j)} \mid \delta x\big)$ is the likelihood and $p(\delta x)$ is prior. One generally considers uniform priors for δx, and in that case, the joint posterior is proportional to the product of the individual likelihoods and a single instance of the prior. This method is well-suited for theory-specific tests, where the deviation parameter corresponds to a fundamental coupling expected to be universal across sources. However, in many beyond-GR theories, deviations in the PN coefficients in the GW phase or the QNM spectrum are expected to vary depending on the source's properties. In such cases, this assumption is not valid, and the method is less appropriate for theory-independent, parametrized tests.

Relaxing the assumption of constant deviations across all events requires a hierarchical inference framework, as originally proposed in Refs. [683, 684]. This technique assumes that the non-GR parameters are drawn from a common underlying distribution, whose properties are inferred from the population of events. Following Refs. [250, 251, 683, 684] we model the population distribution with a Gaussian $\delta x \sim \mathcal{N}(\mu, \sigma)$ of unknown mean μ and standard deviation σ (the *hyperparameters*). Setting $\sigma = 0$ amounts to assuming that all systems share the same beyond-GR parameter δx. The goal is then to infer a posterior distribution $p(\mu, \sigma|\{d^{(j)}\})$ for μ and σ from a joint analysis of a set of events $\{d^j\}$, $j = 1, ..., N$. From Bayes' theorem,

the joint posterior on μ and σ is given by,

$$p\left(\mu,\sigma \mid \{d^{(j)}\}\right) \propto \prod_{j=1}^{N} p\left(d^{(j)} \mid \mu,\sigma\right)\ p(\mu,\sigma) \propto p(\mu,\sigma) \prod_{j=1}^{N} p\left(d^{(j)} \mid \mu,\sigma\right), \tag{4.2}$$

where $p(\mu,\sigma)$ is the prior on hyperparameters (μ,σ), usually assumed to be uniform. The quantity $p\big(d^{(j)} \mid \mu,\sigma\big)$ can be written as a function of the individual-event likelihood for the deviation parameter δx,

$$p\big(d^{(j)} \mid \mu,\sigma\big) = \int p\left(d^{(j)} \mid \delta x\right)\ p\big(\delta x \mid \mu,\sigma\big)\ d\big[\delta x\big], \tag{4.3}$$

where $p\big(\delta x \mid \mu,\sigma\big) = \mathcal{N}(\mu,\sigma)$ by construction. The quantity $p\big(d^{(j)} \mid \delta x\big)$ is the standard likelihood obtained from individual-event PE analyses. From a posterior on the hyperparameters $p\big(\mu,\sigma \mid \{d^{(j)}\}\big)$, we infer population distributions of δx by marginalizing over μ and σ,

$$p\left(\delta x \mid \{d^{(j)}\}\right) = \int p\big(\delta x \mid \mu,\sigma\big) p\left(\mu,\sigma \mid \{d^{(j)}\}\right)\ d\mu\, d\sigma. \tag{4.4}$$

If GR is correct, the hyperparameter posterior should be consistent with $\mu = 0$ and $\sigma = 0$.

A recent extension of this method incorporates information about the underlying astrophysical population in the hierarchical analysis, by jointly modeling the distribution of source parameters, such as component masses and spins [685]. This is important for mitigating the impact of unphysical prior assumptions on astrophysical parameters, which can impact non-GR deviations due to parameter correlations. However, we leave such an extension for future work, and use the same setup as in Refs. [250, 251, 368].

We also do not account for selection effects in our analyses (e.g., the fact that the loudest sources are most likely to be detected) [686]; as such, this procedure constrains the *detected population* of deviations, rather than the *intrinsic* underlying distribution. To properly incorporate selection effects in a hierarchical inference framework, one should perform injections of simulated beyond-GR signals and assess their detectability. Preliminary analyses suggest that selection biases have a minimal impact on inspiral tests [687], but more detailed studies are required to assess their influence across a broader range of tests of GR.

4.2 Effective-one-body waveforms in Einstein-scalar--Gauss-Bonnet gravity

One promising avenue for theory-specific tests of gravity is the development of accurate IMR waveform models in alternative theories, combining analytical and NR results, as done in GR. In this section, we present the first example of a full IMR waveform model that incorporates analytical beyond-GR corrections. We focus on ESGB theories, a well-motivated class of modifications to GR which introduce a massless scalar field φ coupled to the Gauss-Bonnet scalar,

$$\mathcal{G} = R^{\mu\nu\rho\sigma}R_{\mu\nu\rho\sigma} - 4R^{\mu\nu}R_{\mu\nu} + R^2, \tag{4.5}$$

with a coupling of the form $\ell_{\rm GB}^2 f(\varphi)\mathcal{G}$ in the action. Einstein-scalar-Gauss-Bonnet theories are a subclass of Horndeski gravity [688], and can emerge in the low-energy limit of string theory [689] or from an effective field theory perspective [690, 691].

Due to the coupling between the scalar field and the Gauss-Bonnet scalar, BHs in these theories can evade traditional no-hair theorems [26–41], leading to BH solutions endowed with a monopolar scalar *hair*. In binary systems, this scalar hair can source dipolar scalar radiation [607], leading to a rich phenomenology in the orbital dynamics and GW signal. In particular, for specific coupling functions $f(\varphi)$, BHs can undergo spontaneous [692–697] or dynamical [626, 640, 648] (de)scalarization phenomena analogous to those predicted for NSs in scalar-tensor (ST) theories of gravity [606, 628, 630, 631]. Several methods have been proposed to include dynamical scalarization effects into waveform models [698–701]. These features make ESGB gravity a particularly compelling candidate for theory-specific tests using BBH mergers, both with current [600, 601, 702, 703] and future GW observatories [579].

The rich phenomenology of ESGB theories has sparked growing interest in the literature. Recent advances in ESGB gravity include the derivation of inspiral waveforms within the PN and EOB formalisms [40, 41, 373, 620, 704], the computation of QNM frequencies of rotating BHs at second order in a small-spin expansion [611, 621, 623] and recently for large spins [705, 706], and numerical simulations of BBHs [634, 637, 641, 642, 645, 653, 656, 657, 707].

In this section, we describe the extension of the state-of-the-art EOB waveform model `SEOBNRv5PHM` [139] to ESGB gravity. `SEOBNRv5PHM` generalizes the `SEOBNRv5HM` model discussed in Sec. 2.2 to spin-precessing BBHs. We describe how ESGB corrections are incorporated in the EOB Hamiltonian, the GW and scalar-energy fluxes, the spherical-harmonic GW modes, the QNM spectrum, and the mass and spin of the remnant BH. To account for the uncertainty in merger features that may only

be determined when further NR simulations are available in ESGB gravity, we use parametrized deviations inspired by the `pSEOBNR` analysis [367–369], interpreted as nuisance parameters. We implement the waveform model within the `pySEOBNR` package [1] described in Sec. 2.1.

In a second step, we use our `SEOBNRv5PHM_ESGB` model to constrain the coupling length $\ell_{\rm GB}$ of the dilatonic theory $f(\varphi) = \exp(2\varphi)/4$ by analyzing the GW events GW190412, GW190814 and GW230529. Unlike previous analyses [600, 601, 702, 703], which considered only the inspiral phase, our model incorporates ESGB corrections across the full IMR waveform. Our waveform model also allows us to perform Bayesian model-selection to assess whether the GR hypothesis is favored over a specific modified gravity theory [682]. We compute Bayes factors between the GR and ESGB hypotheses and find that, for all three events, the data are consistent with GR.

4.2.1 Einstein-scalar-Gauss-Bonnet gravity

We study a class of theories defined by the Einstein-frame action [40, 605]

$$S = \frac{1}{16\pi}\int d^4x\sqrt{-g}\big(R - 2g^{\mu\nu}\partial_\mu\varphi\partial_\nu\varphi + \ell_{\rm GB}^2 f(\varphi)\mathcal{G}\big) + S_{\rm m}[\Psi, \mathcal{A}^2(\varphi)g_{\mu\nu}]\,, \tag{4.6}$$

where the Gauss-Bonnet scalar $\mathcal{G}$ is given in Eq. (4.5). Matter fields Ψ couple minimally to the Jordan metric $\tilde{g}_{\mu\nu} = \mathcal{A}^2(\varphi)g_{\mu\nu}$. The theory is specified by the coupling length $\ell_{\rm GB}$ and the dimensionless functions $\mathcal{A}(\varphi)$ and $f(\varphi)$. In the limit $\ell_{\rm GB} = 0$ or for constant $f(\varphi)$, the theory reduces to ST gravity. If $\mathcal{A}$ (and φ) is also constant, we recover GR. We will refer to the theory described by the action (4.6) as ESGB gravity, noting that ST theories are included as a special case.

To model compact objects, we adopt the phenomenological approach introduced in Refs. [605, 708] in ST theories, and treat them as point particles:

$$S_{\rm m} \to S_{\rm m}^{\rm pp}[g_{\mu\nu}, \varphi, \{x_i^\mu\}] = -\sum_i \int m_i(\varphi)\, ds_i\,, \tag{4.7}$$

where $ds_i = \sqrt{-g_{\mu\nu}dx_i^\mu dx_i^\nu}$ and $x_i^\mu[s_i]$ is the worldline of particle i. In this formulation, the constant GR mass is replaced by a function $m_i(\varphi)$ that depends on the internal structure of body i and on the value of the scalar field at its location, to account for the coupling of the compact object to its scalar field environment

Post-Newtonian framework

When the relative orbital velocity is small and the gravitational field is weak, the dynamics of compact binaries can be studied in the PN framework. To this end,

the field equations derived from the action (4.6) with the substitution (4.7) are solved perturbatively around a flat metric $g_{\mu\nu} = \eta_{\mu\nu} + \delta g_{\mu\nu}$, and a constant scalar field background $\varphi = \varphi_0 + \delta\varphi$, where φ_0 is imposed by the binary's cosmological environment.

From now on, a superscript 0 denotes a quantity evaluated at $\varphi = \varphi_0$. For a binary system with component masses $m_1^0 \geq m_2^0$, we define its total mass, reduced mass, and the dimensionless ratios

$$M = m_1^0 + m_2^0, \qquad \mu = \frac{m_1^0 m_2^0}{M}, \qquad q = \frac{m_1^0}{m_2^0}, \qquad \hat{\ell}_{\rm GB} = \frac{\ell_{\rm GB}}{\mu}. \tag{4.8}$$

The functions $m_1(\varphi)$ and $m_2(\varphi)$, describing bodies 1 and 2, can be expanded at 3PN order by introducing the following quantities:

$$\alpha_1^0 = \frac{d\ln m_1}{d\varphi}(\varphi_0), \tag{4.9a}$$

$$\beta_1^0 = \frac{d\alpha_1}{d\varphi}(\varphi_0), \tag{4.9b}$$

$$\beta'^0_1 = \frac{d\beta_1}{d\varphi}(\varphi_0), \tag{4.9c}$$

$$\beta''^0_1 = \frac{d\beta'_1}{d\varphi}(\varphi_0), \tag{4.9d}$$

and their counterparts for body 2. We also introduce the notation $f'(\varphi_0) = (df/d\varphi)_{\varphi_0}$. The quantities defined in Eq. (4.9), often referred to as *sensitivities*, characterize a BH's adiabatic response to the slowly varying scalar field sourced by its binary companion. In particular, α_1^0 can be interpreted as the ratio of the scalar charge to the mass of body 1 [41].

The ESGB corrections included in this work depend only on the theory-dependent product $\ell_{\rm GB}^2 f'(\varphi_0)$ and on ten body-dependent parameters: the masses of bodies 1 and 2, along with their scalar-field sensitivities defined in Eqs. (4.9). For instance, at leading (0PN) order, ESGB corrections appear as a modified gravitational coupling:

$$G_{12} = 1 + \alpha_1^0 \alpha_2^0. \tag{4.10}$$

Higher-order PN corrections involve additional combinations of the sensitivities; these expressions are summarized in Table I of Ref. [4]. We recover ST theories in the limit $\ell_{\rm GB}^2 f'(\varphi_0) = 0$, and GR when, in addition, $m_1(\varphi)$ and $m_2(\varphi)$ are constants. In this case, all sensitivities in Eqs. (4.9) are zero, so that $G_{12} = 1$ and all other corrections vanish.

The example of dilatonic Einstein-scalar-Gauss-Bonnet gravity

The sensitivities (4.9) can be computed once the theory and the compact objects are specified. They have been derived for BHs in ESGB gravity – including spontaneously and dynamically scalarized ones – in Refs. [40, 41, 626].

For illustration, we focus on the dilatonic ESGB theory, defined by

$$f(\varphi) = \frac{1}{4}\exp(2\varphi), \quad \mathcal{A}(\varphi) = 1, \tag{4.11}$$

for which the action (4.6) is invariant under the simultaneous redefinitions $\varphi \to \varphi + \Delta\varphi$ and $\ell_{\rm GB} \to \ell_{\rm GB}\exp(-\Delta\varphi)$, where $\Delta\varphi$ is constant. In this theory, the sensitivities (4.9) for nonspinning BHs have been obtained both analytically and numerically in Refs. [40, 41]. For a given a BH 1, they depend on two parameters: φ_0, which we set to zero without loss of generality using the symmetry of the theory, and the dimensionless coupling $\ell_{\rm GB}/m_1^0 \lesssim 0.831$, where the bound ensures the regularity of the horizon [41].

In this work, we model BBHs and NSBH binaries as follows. For BBHs, we use the analytical, nonperturbative $(5,5)$-Padé approximant of α_1^0 (and α_2^0) from Sec. III.B of Ref. [41], which accurately reproduces numerical results. We then compute β_1^0, ${\beta'}_1^0$ and ${\beta''}_1^0$ (and their counterparts for BH 2) using Eqs. (4.9b)–(4.9d). Since $m_1^0 \geq m_2^0$, it is sufficient to impose the horizon regularity bound on BH 2.

In contrast, Eqs. (4.9) have not yet been computed for NSs in the dilatonic ESGB theory. However, we can describe NSBH binaries at leading order in a small-$\ell_{\rm GB}$ expansion. In this limit, we have for a BH 1 [40, 41],

$$\alpha_1^0\big|_{\rm BH} = -\frac{1}{4}\left(\frac{\ell_{\rm GB}}{m_1^0}\right)^2 + \mathcal{O}\left(\frac{\ell_{\rm GB}}{m_1^0}\right)^4. \tag{4.12}$$

At this order, the theory reduces to the shift-symmetric ESGB model [40], in which NSs carry no scalar monopole [607, 690]. Since Eq. (4.9a) is proportional to the latter [605], we conclude that for a NS 2 [703],

$$\alpha_2^0\big|_{\rm NS} = \mathcal{O}\left(\frac{\ell_{\rm GB}}{m_2^0}\right)^4. \tag{4.13}$$

In the small-$\ell_{\rm GB}$ approximation, the contributions from β_1^0, ${\beta'}_1^0$ and ${\beta''}_1^0$ (and their counterparts for NS 2) are subleading and can be neglected.

4.2.2 Corrections to the effective-one-body Hamiltonian and equations of motion

The effective-one-body Hamiltonian

The ESGB corrections to the two-body Hamiltonian for non-spinning binaries have been derived up to 3PN order in several previous works. The ST two-body Lagrangian was derived at 1PN by Damour and Esposito-Farèse [605], extended to 2PN by Mirshekari and Will [608], and to 3PN by Bernard [617]. It was later generalized to include ESGB corrections by Julié and Berti [40]. The resulting conservative dynamics was included within an EOB Hamiltonian at 2PN by Julié and Deruelle [371–373], and at 3PN by Julié et al. [373]; see also Jain et al. [374, 375] in the ST limit.

To include ESGB corrections up to 3PN order in the `SEOBNRv5PHM` Hamiltonian, we follow the prescription of Ref. [373]:

1. We augment the metric potentials, which are for now Taylor-expanded (Tay) with respect to u, with the corrections derived in Refs. [371, 373]:

$$A^{\rm Tay}_{\rm noS}(u) = A^{\rm GR}_{\rm noS}(u) + 2(\langle\bar{\beta}\rangle - \bar{\gamma}_{12})u^2 + \delta\bar{a}_3 u^3 + [\delta\bar{a}_4 + \bar{a}_{4,\ln}\ln u]u^4, \quad (4.14a)$$

$$\bar{D}^{\rm Tay}_{\rm noS}(u) = \bar{D}^{\rm GR}_{\rm noS}(u) - 2\bar{\gamma}_{12}u + \delta\bar{d}_2 u^2 + \delta\bar{d}_3 u^3, \quad (4.14b)$$

$$Q^{\rm Tay}_{\rm noS}(u, p_{r_*}) = Q^{\rm GR}_{\rm noS}(u, p_{r_*}) + \delta\bar{q}_1 p^4_{r_*} u^2 + \bar{q}_2 p^6_{r_*} u, \quad (4.14c)$$

   where $\langle\bar{\beta}\rangle$ and $\bar{\gamma}_{12}$ are defined in Table I of Ref. [4], and the explicit expressions of $(\delta\bar{a}_3,\, \delta\bar{a}_4,\, \bar{a}_{4,\ln})$, $(\delta\bar{d}_2,\, \delta\bar{d}_3)$ and $(\delta\bar{q}_1,\, \bar{q}_2)$ are given in Appendix B of Ref. [4]. We highlight the presence of the logarithmic correction $\bar{a}_{4,\ln}\ln u$, which originates from nonlocal-in-time *tail* effects. In ESGB gravity, tail effects appear already at 3PN, due to dipolar scalar radiation – unlike in GR, where such effects only arise at 4PN. The corrections in Eq. (4.14c) also include tail effects, up to sixth order in eccentricity, i.e., $\mathcal{O}(p^6_{r_*})$. The ESGB corrections to the EOB potentials are valid for arbitrary choices of the functions $f(\varphi)$ and $\mathcal{A}(\varphi)$ appearing in the action (4.6). They can be specified to a particular theory and compact binary once the corresponding values of the quantities (4.9) are given.

2. We redefine the variable u as

$$u = \frac{G_{12}M}{r}, \quad (4.15)$$

   at all PN orders in the potentials $A^{\rm Tay}_{\rm noS}$, $\bar{D}^{\rm Tay}_{\rm noS}$ and $Q^{\rm Tay}_{\rm noS}$, including the GR terms, where G_{12} is defined in Eq. (4.10).

To improve the accuracy of the model against NR waveforms in the GR limit, we resum $A^{\rm Tay}_{\rm noS}(u)$ using a (1,5)-Padé approximant with respect to u (see Sec. 2.2.3)

$$A_{\rm noS}(u) = P^1_5[A^{\rm Tay}_{\rm noS}(u)], \tag{4.16}$$

and resum $\bar{D}_{\rm noS}(u)$ as a (2,3)-Padé approximant

$$\bar{D}_{\rm noS}(u) = P^2_3[\bar{D}^{\rm Tay}_{\rm noS}(u)]. \tag{4.17}$$

Note that the ESGB corrections in the $A_{\rm noS}$ and $\bar{D}_{\rm noS}$ potentials are added before performing the Padé resummations (which are the same as in GR) so that the potentials remain qualitatively consistent with their GR counterparts as $\ell_{\rm GB}$ is increased.

For generic spins, the `SEOBNRv5PHM` Hamiltonian takes inspiration from that of a test mass in a deformed Kerr background [144,311,333,334]. It includes SO information up to NNLO, SS information to NNLO, as well as cubic- and quartic-in-spin terms at LO, corresponding to the 4PN order for generic, precessing spins. For efficiency, in-plane spin contributions are analytically orbit-averaged for circular orbits [144]. More details and full expressions can be found in Refs. [139, 144]. We do not add any ESGB correction in the spin contributions to the Hamiltonian, because they are currently unknown.

The effective-one-body equations of motion and radiation-reaction force

For aligned-spin binaries, the equations of motion used by the `SEOBNRv5HM` model are given by Eqs. (2.7). On quasi-circular orbits, the RR force is computed as [312]

$$\mathcal{F}_\phi = -\frac{\mathcal{F}}{\Omega}, \quad \mathcal{F}_r = \mathcal{F}_\phi \frac{p_{r_*}}{p_\phi}, \tag{4.18}$$

where $\mathcal{F}$ is the energy flux radiated by the binary. In ESGB theories, this flux includes contributions from both the metric and scalar field:

$$\mathcal{F} = \mathcal{F}^{\rm metric} + \mathcal{F}^{\rm scalar}. \tag{4.19}$$

The metric flux is obtained by summing over the contributions of the factorized metric modes $h^{\rm F}_{\ell m}$ [316–319] (see Eq. (2.8)). For spin-precessing binaries, the `SEOBNRv5PHM` model adopts the same equations of motion as Eqs.(2.7) in the co-precessing frame, where the gravitational radiation resembles that of aligned-spin binaries [126–130]. The spin and angular momentum evolution equations are separately provided as PN-expanded equations inferred from $\hat{H}_{\rm EOB}$ [139, 144]. We follow the spin-precession

description employed in `SEOBNRv5PHM` and refer to Ref. [144] and Sec.II of Ref. [139] for further details.

The scalar flux is currently known up to 2.5PN order relative to the leading-order dipolar term. In ST theories, the scalar waveform for nonspinning binaries was derived at 2PN order by Lang [610] and extended to 2.5PN order by Bernard et al. [622]. The latter also provided a spherical harmonic decomposition of the scalar waveform $\delta\varphi$, but only up to 1.5PN. In this work, we directly use the scalar flux at 2.5PN order from Ref. [622]. Beyond the ST case, corrections to the scalar flux arising from the Gauss-Bonnet coupling $\ell_{\rm GB}$ were computed at leading PN order (3PN) by Shiralilou et al. [620, 709]. However, the corresponding ST contribution at this order is unknown. Thus, the scalar flux is complete only up to 2.5PN in both ST and ESGB theories, differing only by specific values of the parameters (4.9). As a result, the scalar flux is complete only up to 2.5PN order in both ST and ESGB theories, with differences between the two encoded through the values of the parameters (4.9).

The results in Refs. [610, 622] were presented in a Jordan-frame formulation of the theory. Details about the conversion of these expressions to our Einstein-frame definition, and their expressions in terms of the quantities in Eqs. (4.9), are provided in Sec. IVB of Ref. [4]. For circular orbits, the ESGB scalar flux takes the form:

$$\mathcal{F}^{\rm scalar} = \frac{\nu^2 x^5}{(1+\alpha_1^0\alpha_2^0)^2}\Big[x^{-1}f_{-1\rm PN} + f_{0\rm PN} + x^{1/2}f_{0.5\rm PN} + x f_{1\rm PN} + x^{3/2}f_{1.5\rm PN} + \cdots\Big], \quad (4.20)$$

where x is redefined as

$$x = (G_{12}M\Omega)^{2/3}, \quad (4.21)$$

and the explicit expressions of the PN coefficients $f_{i\rm PN}$ are given in Appendix D of Ref. [4]. To facilitate comparison with the metric flux, the PN orders iPN here are defined relative to the quadrupolar order. We note that the coefficient $f_{-1\rm PN}$ is proportional to $(\alpha_1 - \alpha_2)^2$, meaning that at dipolar order, the scalar flux vanishes for symmetric binaries.

Figure 4.1 illustrates the scalar flux (4.20), truncated at successive PN orders, as a function of x. We consider as an example a BBH with mass ratio $q = 4$ and dimensionless coupling $\hat{\ell}_{\rm GB} = 1$ in the dilatonic ESGB theory (4.11). The curves terminate at merger, defined as the peak amplitude of the $(2, 2)$ GW mode computed with the full PN scalar flux contribution. The corresponding number of GW cycles is also indicated in the top axis. Comparing the scalar flux truncated at various PN orders to the leading-order (-1PN) term reveals poor convergence during late inspiral stages at lower PN orders. However, convergence appears improved upon including higher-order corrections. A detailed exploration of potential resummation methods for the scalar flux will be addressed in future work when additional NR waveforms in

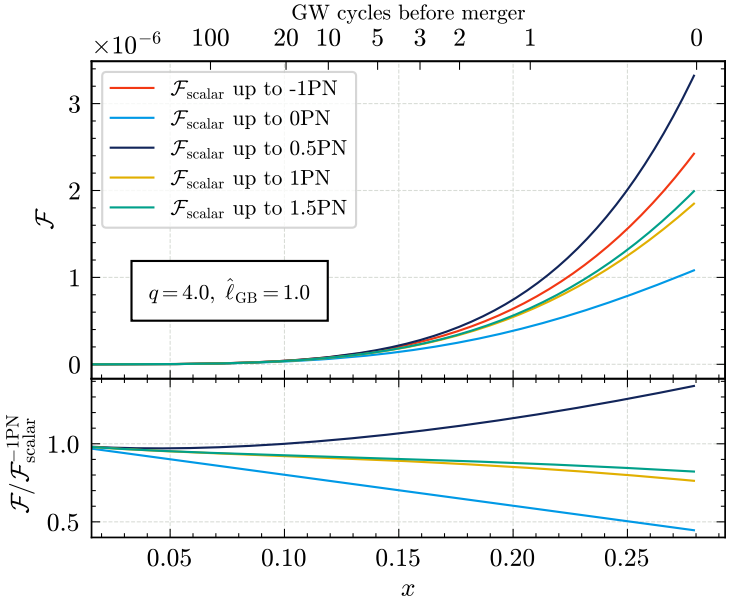

Figure 4.1: *Top panel:* The PN-expanded scalar flux (4.20), truncated at successive PN orders. We consider a BBH with $q = 4$ and $\hat{\ell}_{\rm GB} = 1$ in the dilatonic theory $f(\varphi) = \exp(2\varphi)/4$ and $\mathcal{A}(\varphi) = 1$. The curves terminate at merger, taken as the peak of the $(2, 2)$ mode when all PN orders of the scalar flux contribute to the binary's evolution. *Bottom panel:* Ratio between the scalar flux truncated at different PN orders and the leading -1PN term.

ESGB gravity become available.

4.2.3 Corrections to the inspiral-merger-ringdown waveform modes

In the EOB framework, the metric modes are decomposed into inspiral-plunge and merger-ringdown contributions (2.11). These modes are matched at a time $t^{22}_{\rm peak}$ suitably chosen to agree with the corresponding time in NR simulations. Specifically, in the `SEOBNRv5PHM` model, one defines

$$t^{22}_{\rm peak} = t_{\rm ISCO} + \Delta t_{\rm NR} \tag{4.22}$$

where $t_{\rm ISCO}$ is the time at which u reaches $u_{\rm ISCO}$, the inverse radius of the Kerr ISCO [710] with the mass and spin of the remnant BH, as predicted by NR fitting formulas [517, 518]. The calibration parameter $\Delta t_{\rm NR}$ is determined via comparison to NR simulations. Here, we also use Eq. (4.22), formally replacing u by its ESGB expression (4.15), to determine the merger-ringdown attachment time. While ESGB corrections affect $t_{\rm ISCO}$ due to modifications to the orbital dynamics, we do not change

$\Delta t_{\rm NR}$, as such corrections would require calibration to NR simulations in ESGB gravity.

Inspiral-plunge $h_{\ell m}$ modes

The inspiral-plunge EOB modes (2.13) are expressed as a product of the factorized, resummed metric modes $h^{\rm F}_{\ell m}$ for aligned-spin binaries on circular orbits [316, 318, 319], and a NQC correction $N_{\ell m}$ [320] (see Sec. 2.2.2).

The metric modes in ESGB gravity are fully known up to 2PN order, for nonspinning binaries. In ST theories, the metric waveform was derived at leading (0PN) order by Damour and Esposito-Farèse [605] and extended to 2PN by Lang [609, 610], relative to the quadrupolar order. The corresponding metric modes for circular orbits $h_{\ell m}$ were inferred by Sennett et al. [612]. Leading-order corrections due to the Gauss-Bonnet coupling $\ell_{\rm GB}$, entering at 3PN, were computed by Shiralilou et al. [620, 709]. As the ST contribution at 3PN is unknown, the metric modes are complete only up to 2PN in both ST and ESGB theories, differing only by specific values of the parameters (4.9).

As with the scalar flux, the results in Ref. [612] were given in a Jordan-frame formulation of ST theories based on a set of Brans-Dicke-inspired parameters. The translation to our Einstein-frame convention, including the conversion of the parameters of Ref. [612] to those defined in Eq. (4.9), is detailed in Sec. IVA of Ref. [4].

The factorized form of the waveform modes described in Sec. 2.2.2 can be generalized to ESGB theories, starting from the 2PN metric modes. Specifically, we include the ESGB corrections to the metric modes as follows:

1. In the first three factors $h^{\rm N,GR}_{\ell m}$, $\hat{S}^{\rm GR}_{\rm eff}$ and $T^{\rm GR}_{\ell m}$ of Eq. (2.14), we formally replace the effective and EOB energies by their ESGB counterparts $\hat{H}_{\rm eff}$ and $\hat{H}_{\rm EOB}$ (see Sec. 4.2.2), and $x_{\rm GR} = (M\Omega)^{2/3}$ by x (4.21).

2. For $\ell + m$ odd, we normalize $\hat{S}^{\rm GR}_{\rm eff}(x, \hat{p}_\phi)$ by its Newtonian value on circular orbits in ESGB gravity, that is

$$\hat{S}_{\rm eff} = \frac{\sqrt{x}\hat{p}_\phi}{1 + \alpha^0_1\alpha^0_2}, \qquad \ell + m \text{ odd}. \tag{4.23}$$

3. In the nonspinning parts of $\rho^{\rm GR}_{\ell m}$ and $\delta^{\rm GR}_{\ell m}$, we formally replace $x_{\rm GR}$ by x (4.21), and $y_{\rm GR} = H^{\rm GR}_{\rm EOB}\Omega^{2/3}$ by

$$y = \left(H_{\rm EOB}\Omega\right)^{2/3}. \tag{4.24}$$

4. We add ESGB corrections to the factorized amplitudes and phases:

$$f_{\ell m} = \begin{cases} (\rho^{\rm GR}_{\ell m} + \delta\rho_{\ell m})^\ell, & m \text{ even}, \\ (\rho^{\rm noS,GR}_{\ell m})^\ell + f^{\rm S,GR}_{\ell m} + \delta f_{\ell m}, & m \text{ odd}, \end{cases} \tag{4.25}$$

$$\delta_{\ell m} = \begin{cases} \delta^{\rm GR}_{\ell m} + \delta\delta_{\ell m}, & m \text{ even}, \\ \delta^{\rm noS,GR}_{\ell m}, & m \text{ odd}. \end{cases} \tag{4.26}$$

The different treatment for odd m is related to the fact that the $h_{\ell m}$ modes are imaginary and proportional to δ at Newtonian order. However, some real ESGB corrections, entering at subleading PN orders, are not. The scenario is similar to that of spin effects (see Sec. 2.2.2), and thus we incorporate ESGB corrections in a similar fashion. The nonzero ESGB corrections for $\delta\rho_{\ell m}$, $\delta f_{\ell m}$, and $\delta\delta_{\ell m}$ are given in Sec. V of Ref. [4].

The remaining $N_{\ell m}$ factor in the inspiral-plunge modes (2.13) is the NQC correction, which ensures that the modes' amplitude and frequency agree with NR input values, given by NR fits, at the matching point. By default we impose that the inspiral-plunge waveform (2.13) still matches the NR predictions in GR. In Sec. 4.2.3, we will discuss how to relax this assumption.

In Fig. 4.2, we show the GR and ESGB fluxes normalized by the leading order GR contribution

$$\bar{\mathcal{F}} = \frac{\mathcal{F}}{\frac{32}{5}\nu^2 x^5_{\rm GR}}, \tag{4.27}$$

considering only the ESGB corrections to the metric flux, or also adding the scalar flux. As in Fig. 4.1, we consider a binary with $q = 4$ and $\hat{\ell}_{\rm GB} = 1$ in the dilatonic theory (4.11). The bottom panel shows the fractional difference between the ESGB and GR fluxes. At low frequencies, the difference in the metric flux at low frequencies is constant with x (e.g., at leading PN order), and is due to the replacement of $x_{\rm GR}$ with x as in Eq. (4.21), while the difference when including the scalar flux increases at low frequencies as x^{-1}, due to the dipolar -1PN term.

Merger-ringdown $h_{\ell m}$ modes

To model the merger-ringdown waveform in ESGB gravity, we adopt the same phenomenological ansatz as in GR (see Sec. 2.2.2), but introduce an appropriate parametrization for the modes' amplitude and frequency [367–369]. We also use the QNMs derived recently in ESGB gravity [705].

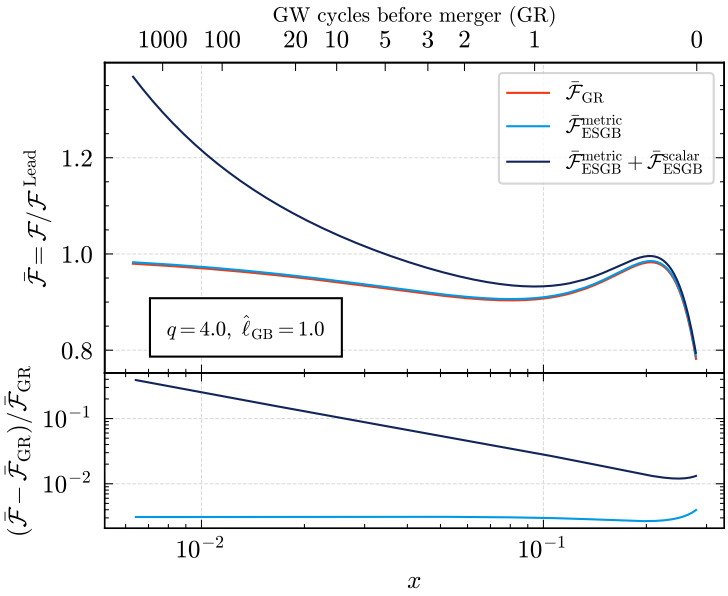

Figure 4.2: *Top panel*: Fluxes in GR and ESGB gravity normalized by the leading order GR contribution, considering only the ESGB corrections to the metric, or also adding the scalar flux. We consider a BBH with $q = 4$ and $\hat{\ell}_{\rm GB} = 1$ in the dilatonic theory $f(\varphi) = \exp(2\varphi)/4$ and $\mathcal{A}(\varphi) = 1$. *Bottom panel*: Fractional difference between the ESGB fluxes and the GR flux. We note that the difference in the metric flux at low frequencies is constant with x (e.g., at leading PN order), and is due to the redefinition of x as in Eq. (4.21), while the difference when including the scalar flux increases at low frequencies as x^{-1}, due to the dipolar -1PN term.

For the merger, the NQC corrections impose that the modes' amplitude and frequency agree with fits to NR waveforms in GR. Recently, considerable efforts have produced NR simulations of BBHs in ESGB gravity [634, 637, 639, 645, 648, 653]. For example, Ref. [645] found a negligible effect on the GW amplitude at merger with varying ESGB coupling, in contrast with the large effect found in the order-reduced simulation of Ref. [637], possibly due to the presence of secularly growing errors present in the latter perturbative approach [657].

Given limited NR data, full parameter-space calibrations as in GR are not yet feasible. Inspired by the parametrized `SEOBNR` approach [367–369], we introduce fractional deviations from the NR predictions in GR for the amplitude and frequency at the matching time (2.12)

$$|h^{\rm NR,GR}_{\ell m}| \to |h^{\rm NR,GR}_{\ell m}| \left(1 + \hat{\ell}_{\rm GB}{}^4 \delta A_{\ell m}\right), \tag{4.28a}$$

$$\omega^{\rm NR,GR}_{\ell m} \to \omega^{\rm NR,GR}_{\ell m} \left(1 + \hat{\ell}_{\rm GB}{}^4 \delta \omega_{\ell m}\right), \tag{4.28b}$$

where the $\hat{\ell}_{\rm GB}{}^4$ dependence is inspired by the scaling of the PN corrections in the

inspiral modes in the small-$\hat{\ell}_{\rm GB}$ regime, and ensures they vanish in the GR limit. These deviations parametrize our ignorance of the merger morphology with extra nuisance parameters, to be marginalized over in PE. In Sec. 4.2.5, we quantify the impact of marginalizing over these corrections, applied for simplicity only to the dominant $(2,2)$ mode, on the analysis of GW signals, and find it to be small. The $\hat{\ell}_{\rm GB}$-dependence in Eqs. (4.28), and how the merger morphology is modified for different modes, could be further studied using NR waveforms in ESGB gravity. Still, current NR simulations [645, 653] suggest that corrections at merger are small, for values of the coupling allowed by current observations.

Corrections to the quasi-normal-mode frequencies

To incorporate beyond-GR corrections in the merger-ringdown waveform using the ansatz of Sec. 2.2.2, several effects should be considered:

1. The complex frequency of the least-damped QNM for each (ℓ, m) harmonic $\sigma_{\ell m 0}$ is modified, given the BH's final mass and spin.

2. In several modified gravity theories, the BH metric perturbations with even and odd parity have different QNM frequencies, breaking the isospectrality of GR [241].

3. The final mass and spin of the remnant BH should deviate from the GR predictions due to differences in both the conservative and dissipative binary dynamics. For example, the NR simulations of Ref. [653] show smaller final mass and spin compared to GR.

4. The $c^{\ell m}_{i,f}$ and $d^{\ell m}_{i,f}$ coefficients, which model the early ringdown, are obtained through fits of NR waveforms in GR and should also be corrected. Since these could only be obtained through fits of beyond-GR NR waveforms, we neglect this last correction.

Quasinormal mode frequencies of nonspinning ESGB BHs were first computed in Refs. [33, 611], and later extended up to second order in a spin expansion in Refs. [621,623], focusing on the polar sector. Binary coalescences typically lead to BHs with final spin $\chi_f \sim 0.7$, making the accuracy of an expansion to second order in the spin limited. More recent methods – including Teukolsky formalisms [711–715] and perturbative spectral expansions [716, 717] – offer a way to calculate QNM frequencies in a wide class of modified gravity theories for BHs with generic spins.

In this work, we implement corrections to the dominant $(\ell, m, n) = (2, 2, 0)$ QNM derived by Ref. [705] for ESGB gravity at leading order in $\ell_{\rm GB}/M_f$, valid up to spins $\chi_f \sim 0.8$. While Ref. [705] provided corrections in both polar and axial sectors, following Ref. [602], we only consider the corrections to the polar sector, which are typically less damped and exhibit larger frequency shifts for spins around $\chi_f \sim 0.7$. Although Ref. [705] considered a shift-symmetric theory, our analysis involves the dilatonic theory (4.11). However, since constraints from real GW events remain in the small-coupling regime, the dilatonic and shift-symmetric theories coincide at leading order in $\hat{\ell}_{\rm GB}$ (see Sec. 4.2.1), justifying our use of these results.

Corrections to the final mass and spin

We now discuss ESGB corrections to the remnant BH's mass and spin of the as a function of the coupling, for a BBH in the dilatonic ESGB theory (4.11). While accurate estimates require NR simulations, EOB models can provide useful approximations based on the binary's dynamics. We restrict to spin-aligned binaries and focus on the remnant's mass and spin magnitude.

The final mass and spin of a BBH coalescence can be related to its energy and angular momentum at the ISCO [313, 718]. We estimate corrections to the remnant mass and orbital angular momentum from the values of $\nu\hat{H}_{\rm EOB} = H_{\rm EOB}/M$ and $\nu\hat{p}_\phi = p_\phi/M^2$ at the merger time, associated in the model with the peak of the (2,2)-mode waveform (4.22). We compute these quantities in both ESGB and GR, and apply the difference as a correction to the GR remnant estimates from NR fits [517,518]. This amounts to neglecting the effects of ESGB corrections to the post-merger radiation. In practice, we proceed iteratively: we first evaluate the ESGB corrections to the remnant mass and spin by inserting their GR values in Eq. (4.22). In a second step, we build waveforms by evaluating $\hat{t}_{\rm ISCO}$ in Eq. (4.22) using the corrected remnant mass and spin. A limitation of this estimates is that the merger time uses the $\Delta\hat{t}_{\rm NR}$ parameter (4.22), which is calibrated from NR simulations in GR, and should eventually be updated using ESGB NR data.

To avoid generating an additional GR waveform each time we wish to include this correction, we construct fits as a function of the intrinsic parameters and of the coupling $\hat{\ell}_{\rm GB}$. For simplicity, we consider equal-spin binaries with $\chi \in [-0.9, 0.9]$, for several mass ratios $q \in \{1, 2, 4, 10\}$, and coupling $\hat{\ell}_{\rm GB} \in [0, 0.5]$. We use a polynomial ansatz in (ν, χ) (with χ being promoted to $\chi_+ = (m_1^0/M)\chi_1 + (m_2^0/M)\chi_2$ for unequal spins), while the dependence on $\hat{\ell}_{\rm GB}$ is well approximated by a simple $\hat{\ell}_{\rm GB}^4$ scaling. We define:

$$\hat{M}_f = \hat{M}_f^{\rm GR} + \Delta\hat{M}_f^{\rm ESGB}, \tag{4.29a}$$

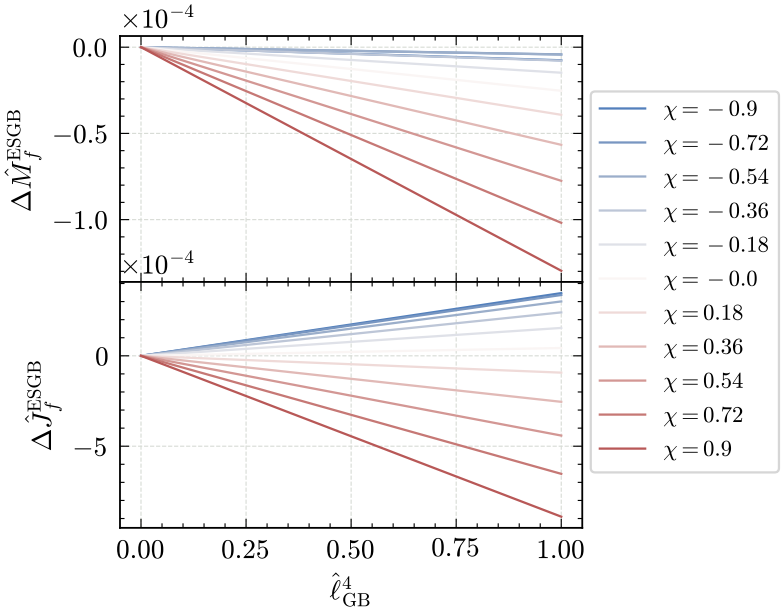

Figure 4.3: ESGB corrections to the (dimensionless) final mass (top panel) and angular momentum (bottom panel), for BBHs with equal-spin magnitude χ and mass ratio $q = 4$, in the dilatonic theory $f(\varphi) = \exp(2\varphi)/4$ and $\mathcal{A}(\varphi) = 1$.

$$\hat{J}_f = \hat{J}_f^{\rm GR} + \Delta\hat{J}_f^{\rm ESGB}, \tag{4.29b}$$

$$\chi_f = \frac{\hat{J}_f}{\hat{M}_f^2} = \chi_f^{\rm GR} + \Delta\chi_f^{\rm ESGB}, \tag{4.29c}$$

where $\hat{M}_f = M_f/M$ and $\hat{J}_f = J_f/M^2$ are the dimensionless final mass and total angular momentum, and $\hat{M}_f^{\rm GR}$, $\chi_f^{\rm GR}$ are given by the NR fitting formulas in GR [517, 518]. Fitting formulas for the ESGB corrections $\Delta\hat{M}_f^{\rm ESGB}$ and $\Delta\hat{J}_f^{\rm ESGB}$ are given in Sec. VD of Ref. [4]. By combining Eqs. (4.29), we can compute the linear correction to the final spin as

$$\Delta\chi_f^{\rm ESGB} = \frac{\Delta\hat{J}_f^{\rm ESGB}}{(\hat{M}_f^{\rm GR})^2} - 2\chi_f^{\rm GR}\frac{\Delta\hat{M}_f^{\rm ESGB}}{\hat{M}_f^{\rm GR}}. \tag{4.30}$$

Figure 4.3 shows the values of the ESGB corrections to the final mass and angular momentum for a set of BBHs with equal-spin magnitude χ and mass ratio $q = 4$, as a function of the ESGB coupling $\hat{\ell}^4_{\rm GB}$ in the dilatonic theory (4.11). These corrections are modest compared to those affecting the inspiral dynamics, being $\mathcal{O}(10^{-4})$ for $\hat{\ell}^4_{\rm GB} \sim 1$. We find that the corrections to the final mass are always negative, while the final angular momentum corrections can take both signs depending on the mass ratio and spins. Note that the value of $\hat{p}_\phi$ at the ISCO can be larger when adding ESGB corrections to the EOB Hamiltonian (see Fig. 4.5).

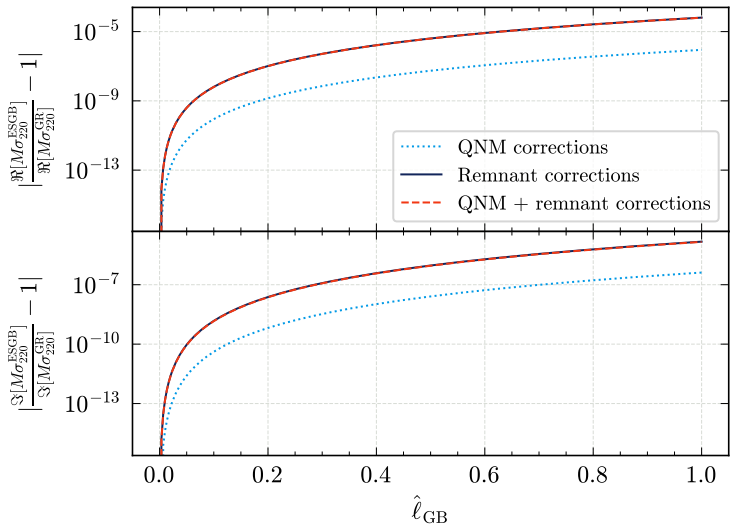

Figure 4.4: Fractional change between ESGB and GR in the real and imaginary part of the $(2,2)$-mode's ringdown frequency, as a function of $\hat{\ell}_{\rm GB}$, for a $q=4$ nonspinning BBH ($\chi_f \simeq 0.47$) in the dilatonic theory $f(\varphi)=\exp(2\varphi)/4$ and $\mathcal{A}(\varphi)=1$. We show the change only including corrections to the QNM spectrum, but fixing the final mass and spin to the GR values, only changing the final mass and spin using Eqs. (4.29), as well as combining both corrections.

Figure 4.4 shows the fractional difference between ESGB and GR in the real and imaginary part of the $(2,2)$ mode ringdown frequency, as a function of $\hat{\ell}_{\rm GB}$, for a $q=4$ nonspinning BBH ($\chi_f \simeq 0.47$). We either include corrections to the QNM spectrum only, change the final mass and spin using Eqs. (4.29), and both combined. As noted in Refs. [603, 623], corrections to the QNM spectrum are very small. While corrections to the remnant mass and spin are also modest, they can cause changes in the frequency of the ringdown waveform from one to two orders of magnitude larger than the ESGB corrections to the QNM spectrum. Accurately estimating these corrections would be useful for high-precision tests of GR with next-generation detectors, as they may significantly improve prospects for BH spectroscopy in ESGB gravity. Indeed, Ref. [603] showed that, when accounting only for corrections to the QNM spectrum, constraints on ESGB gravity from ringdown observations, even with next-generation GW detectors, are weaker than current bounds from LVK inspiral analyses. Our results suggest that incorporating information about changes to the remnant's mass and spin could significantly improve these prospects.

4.2.4 Waveform morphology

In this section, we describe the impact of the ESGB corrections on the dynamics and waveforms of BBH systems, modeled with `SEOBNRv5PHM_ESGB`. As a representative

case, we consider a nonspinning binary with mass ratio of $q = 4$, and $\hat{\ell}_{\rm GB} \in \{0, 0.7, 1.0\}$. The qualitative conclusions hold for other mass ratios and for binaries with nonzero spin. However, in the equal-mass limit, the deviations from the GR flux are smaller, as the leading-order -1PN dipolar term in the scalar flux (4.20) vanishes.

We begin by examining the orbital separation $\hat{r}$ and angular momentum $\hat{p}_\phi$ as a function of time in Fig. 4.5. The insets highlight the differences in the dynamics at the start of the evolution, which for all cases is taken at a dimensionless orbital frequency $M\Omega_i = 0.015$, and close to the ISCO, indicated by the dots. The values of $\hat{r}$ and $\hat{p}_\phi$ at the ISCO are determined by setting both the first and second derivatives of the Hamiltonian with respect to $\hat{r}$ to zero, taking $\hat{p}_{r_*} = 0$ (circular orbits) (i.e., $\partial H_{\rm EOB}(\hat{p}_{r_*} = 0)/\partial\hat{r} = 0 = \partial^2 H_{\rm EOB}(\hat{p}_{r_*} = 0)/\partial\hat{r}^2$). Each curve ends at merger, taken as the peak of the (2,2) mode waveform (4.22). We observe the following trends:

1. The binary merges at earlier times for larger values of the ESGB coupling, since more energy is radiated away due to the additional scalar field.

2. For a fixed initial dimensionless frequency, binaries start at a larger radius and angular momentum for larger values of the ESGB coupling. This is due to the replacement $1/\hat{r} \to G_{12}/\hat{r}$ in the EOB potentials, with $G_{12} \geq 1$. Note that the model uses quasi-circular, adiabatic, initial conditions [312], also used in the `SEOBNRv5PHM` model.

3. The ISCO is at a smaller separation [373] and slightly larger angular momentum compared to GR. This is a non-trivial effect due to higher-order PN corrections in the EOB Hamiltonian.

In Fig. 4.6 we show, for the same set of binaries, the amplitude of the (2,2) mode waveform, to highlight how a non-zero value of the coupling changes the time-to-merger when including different beyond-GR corrections. The dash-dotted vertical lines indicate the merger, defined as the peak of the (2,2) mode, and the dotted vertical lines correspond to the time at which $\hat{r} = \hat{r}_{\rm ISCO}$. We set $\hat{t} = 0$ at the GR merger time. In the top panel, we incorporate ESGB corrections in the Hamiltonian, while using the GR flux, and mostly observe that modifications to the conservative dynamics tend to delay the merger. In the middle panel, we include instead ESGB corrections in the dissipative sector and use the GR Hamiltonian. As expected, these corrections accelerate the inspiral, mostly due to the additional energy dissipation via the scalar field. In the bottom panel, we combine both contributions. Changes to the dissipative dynamics are dominant, and the binary merges earlier than GR for a

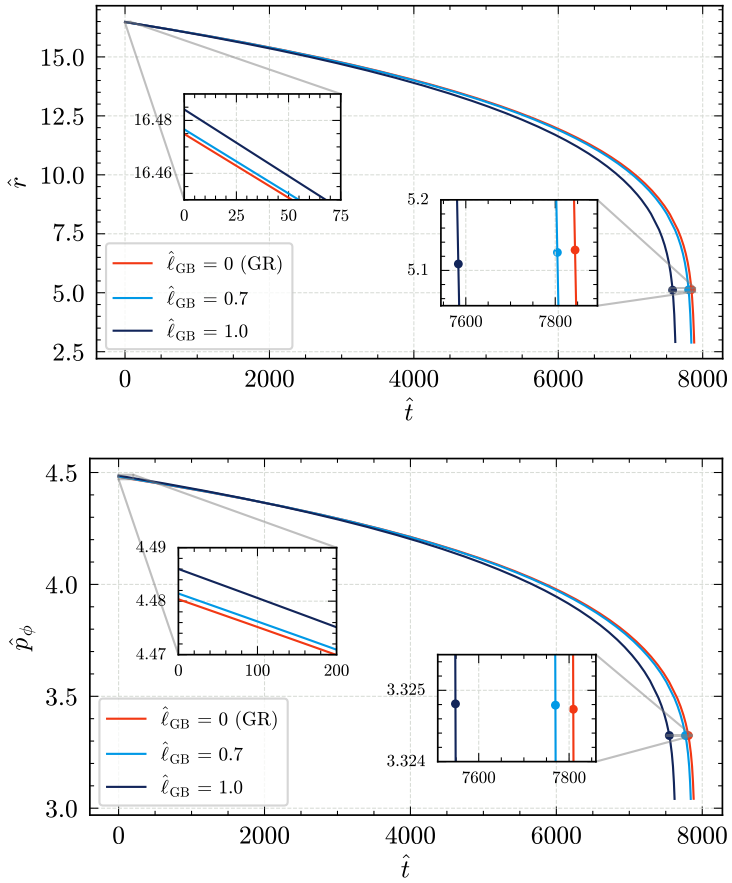

Figure 4.5: Orbital separation $\hat{r}$ (upper panel) and angular momentum $\hat{p}_\phi$ (lower panel) as a function of time for a nonspinning BBH with $q = 4$, starting at the same dimensionless orbital frequency $M\Omega_i = 0.015$, for different values of the ESGB coupling $\hat{\ell}_{\rm GB} \in \{0, 0.7, 1.0\}$ in the dilatonic theory $f(\varphi) = \exp(2\varphi)/4$ and $\mathcal{A}(\varphi) = 1$. The insets highlight the differences in the dynamics at the start of the evolution, and close to the ISCO, indicated by the dots. Each curve ends at merger, taken as the peak of the (2,2) mode. We note that: (i) The binary merges at earlier times for larger values of the ESGB coupling, as more energy is radiated away through the additional scalar field, (ii) ESGB binaries at the same initial dimensionless frequency start at a larger radius and angular momentum. This is due to the leading-order correction $1/\hat{r} \to G_{12}/\hat{r}$ in the EOB potentials, with $G_{12} \geq 1$ (iii) The ISCO is at a smaller separation and slightly larger angular momentum compared to GR. This is a non-trivial effect due to higher-order PN corrections in the EOB Hamiltonian.

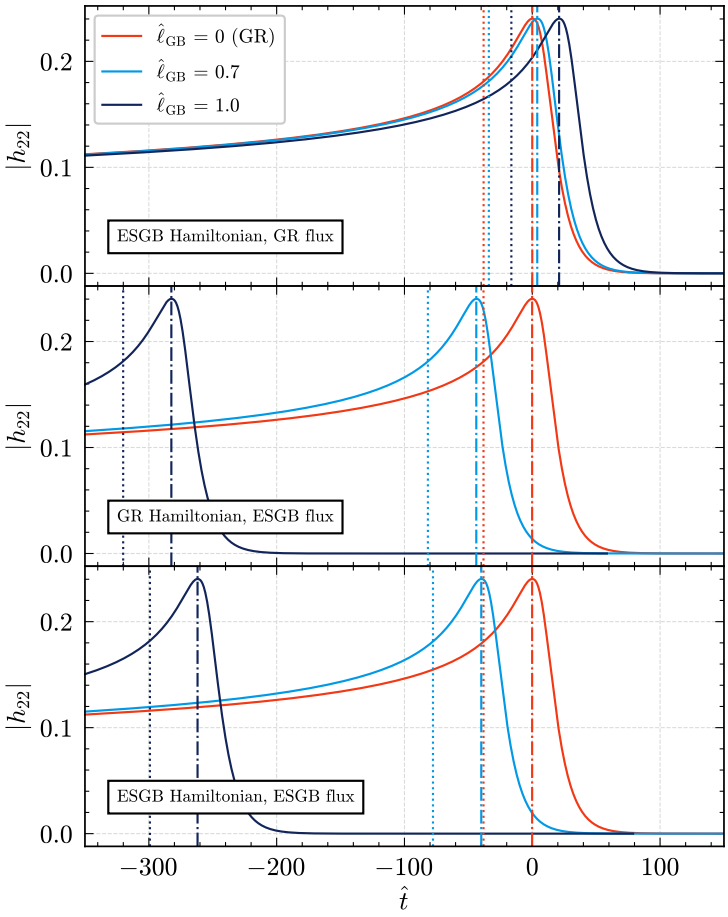

Figure 4.6: Amplitude of the (2,2) mode of a nonspinning BBH with $q = 4$, starting at a dimensionless frequency $M\Omega_i = 0.015$, for $\hat{\ell}_{\rm GB} \in \{0, 0.7, 1.0\}$ in the dilatonic theory $f(\varphi) = \exp(2\varphi)/4$ and $\mathcal{A}(\varphi) = 1$. The dash-dotted vertical lines indicate the merger, defined as the peak of the (2,2) mode, and the dotted vertical lines correspond to the time at which $\hat{r} = \hat{r}_{\rm ISCO}$. We set $\hat{t} = 0$ at the GR merger time. *Top panel*: we include ESGB corrections in the Hamiltonian, and use the GR flux. *Middle panel*: we include ESGB corrections in the flux, and use the GR Hamiltonian. *Bottom panel*: we include ESGB corrections in both the Hamiltonian and the flux. We see that corrections to the conservative dynamics delay the merger, while corrections to the dissipative sector accelerate the inspiral. The trend seen here is consistent with other cases we considered: when combining all contributions, the changes to the dissipative dynamics are dominant, and the binary merges earlier than in GR for a non-zero value of the coupling.

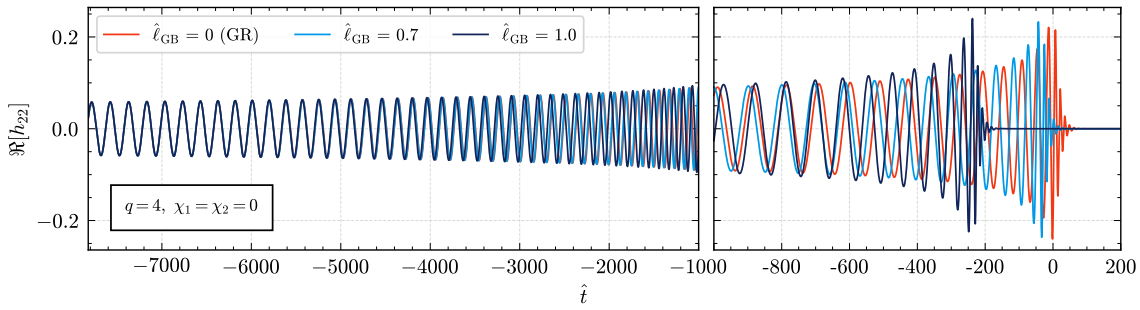

Figure 4.7: (2,2) mode of the `SEOBNRv5PHM_ESGB` waveform of a nonspinning BBH with $q = 4$, starting at a dimensionless orbital frequency $\Omega_i = 0.015$, for different values of the ESGB coupling $\hat{\ell}_{\rm GB} \in \{0, 0.7, 1.0\}$ in the dilatonic theory $f(\varphi) = \exp(2\varphi)/4$ and $\mathcal{A}(\varphi) = 1$. We set $\hat{t} = 0$ at the peak of the (2,2) mode of the GR waveform.

non-zero value of the ESGB coupling. The trend seen in this example is consistent with other cases we considered, and agrees qualitatively with NR simulations [645, 653]. Finally, Fig. 4.7 shows the real part of the (2,2) mode for the same set of binaries. The waveforms are aligned over a low-frequency interval, and display a difference in the time-to-merger and a noticeable dephasing as they approach the merger. Note that the ESGB corrections to the remnant mass and spin (entering the merger time and ringdown frequency, see Sec. 4.2.3) and to the QNM spectrum (see Sec. 4.2.3) are included in our waveforms. However, their impact is subdominant compared to the effects above.

Quantifying measurability of deviations from general relativity

We now quantify the magnitude of deviations from GR which could be detectable by GW detectors, and estimate the SNR required for such measurements using the mismatch (1.45) and the indistinguishability criterion (1.46). We consider the advanced LIGO (aLIGO) detector with the zero-detuned high-power noise PSD [525] and $f_{\rm low} = 20$Hz, and the ET detector, using the `EinsteinTelescopeP1600143` PSD implemented in `pyCBC` [484] and $f_{\rm low} = 5$Hz. For simplicity, we include only the dominant (2,2) mode when computing mismatches.

Figure 4.8 we show the mismatch of `SEOBNRv5PHM_ESGB` against its GR limit as a function of $\hat{\ell}_{\rm GB}$, for the aLIGO and ET detectors. We consider a nonspinning binary with total mass $20M_\odot$ and mass ratios $q \in \{2, 4, 8\}$ as a signal. Horizontal lines correspond to the indistinguishability thresholds (1.46) obtained by taking $D = 9$ (our waveform depends on two masses, 6 spin components and $\hat{\ell}_{\rm GB}$) for some realistic SNRs $(10, 30$ for aLIGO, $100, 300$ for ET). As expected, the mismatch increases with mass ratio due to enhanced dipolar scalar radiation, leading to stronger potential

constraints on $\hat{\ell}_{\rm GB}$ for asymmetric binaries.

The smallest value of $\hat{\ell}_{\rm GB}$ that could be distinguished from GR ranges from around 0.8 ($q = 2$, SNR $= 10$) to 0.3 ($q = 8$, SNR $= 30$) for aLIGO, and from 0.3 ($q = 2$, SNR $= 100$) to 0.1 ($q = 8$, SNR $= 300$) for ET. The main improvement for ET is its enhanced low-frequency sensitivity, where the scalar radiation dominates (see Fig. 4.2). Mismatch values $\lesssim 10^{-5}$ are not to be attributed to a non-zero coupling value, as differences of this order can be simply due to errors in the numerical integration of Hamilton's equations with finite tolerance. Comparing our results to existing constraints on ESGB gravity with LVK observations, the bound on GW190814 from Refs. [702, 703] (assuming the event is from a BBH), is given as a function of the coupling $\sqrt{\alpha_{\rm GB}} = \ell_{\rm GB}/(4\pi^{1/4})$ with $\ell_{\rm GB}/M = \nu\hat{\ell}_{\rm GB}$ by $\sqrt{\alpha_{\rm GB}} \lesssim 0.4$km. Taking a total mass of $\sim 26M_\odot$ and a mass ratio $q = 10$, this corresponds to $\hat{\ell}_{\rm GB} \lesssim 0.67$. Our prospective bound $\hat{\ell}_{\rm GB} \lesssim 0.1$ for an ET source with $q = 8$, $M = 20M_\odot$ translates instead to $\sqrt{\alpha_{\rm GB}} \lesssim 0.055$km. Low-mass NSBHs may also serve as *golden* sources for testing ESGB gravity, as we illustrate with GW230529 below. These results indicate that stellar-mass binaries observed with next-generation ground-based detectors will be ideal candidates to test ESGB gravity, likely outperforming constraints from extreme-mass-ratio inspirals detected by LISA [719].

The potential constraints on $\hat{\ell}_{\rm GB}$ presented here should be interpreted as order--of-magnitude estimates. The indistinguishability criterion provides a necessary, but not sufficient, condition for detectability; that is, a mismatch above the threshold does not guarantee that deviations are measurable [454]. Furthermore, only varying $\hat{\ell}_{\rm GB}$ neglects possible correlations between the ESGB coupling and GR parameters. For example, since a nonzero ESGB coupling primarily shortens the waveform, one could expect it to be anti-correlated with the chirp mass $\mathcal{M}_c$ of the binary, which affects the GW phase at leading PN order. As a result, these constraints represent optimistic single-event estimates. On the other hand, combining information from multiple events can significantly improve constraints, as the coupling $\ell_{\rm GB}$ is common across all sources. As discussed in Sec. 4.1, in such cases combined constraints can be obtained by multiplying the marginalized likelihoods from individual observations.

More refined predictions for the measurability of the ESGB coupling could be based on the Fisher matrix formalism (1.47) or employ full Bayesian inference. For example, Ref. [579] used a Fisher analysis based on corrections to the inspiral waveform within the parametrized post-Einsteinian (ppE) framework [583], mapping the ppE results to theory-specific constraints, and incorporating the effect of stacking multiple events. A similar study focused on the ringdown stage was recently presented in Ref. [603], using the parametrized spin-expansion coefficients (`ParSpec`) framework [589].

These analyses could be refined and extended using the `SEOBNRv5PHM_ESGB` wave-

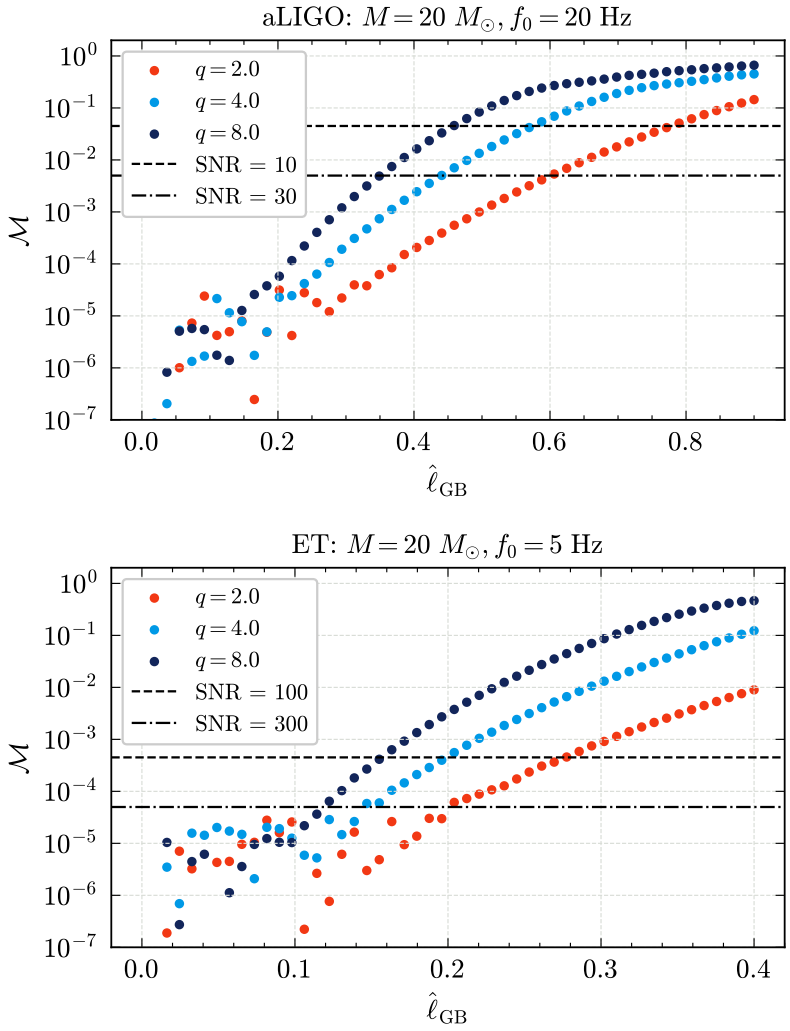

Figure 4.8: Mismatch of the (2,2) mode waveform of `SEOBNRv5PHM_ESGB` against its GR limit, as a function of the ESGB coupling $\hat{\ell}_{\rm GB}$ for the aLIGO (upper panel) and ET (lower panel) detectors. We consider a nonspinning BBH with total mass $20M_\odot$ and mass ratios $q \in \{2, 4, 8\}$ in the dilatonic theory $f(\varphi) = \exp(2\varphi)/4$ and $\mathcal{A}(\varphi) = 1$. The horizontal lines show the indistinguishability thresholds given by Eq. (1.46) for different SNRs.

form model. Notably, Ref. [579] employed `IMRPhenomPv2` [305] as the baseline GR waveform, which lacks higher modes and includes a simplified treatment of spin precession, making it less accurate than `SEOBNRv5PHM`. Furthermore, it tested modifications at a single PN order at a time, while our model incorporates modifications at each PN order as a function of the ESGB coupling. `SEOBNRv5PHM_ESGB` also includes beyond-GR effects in both the inspiral and ringdown stages. One could also employ Bayesian PE to provide forecasts for the next-generation GW detectors such as ET and CE, examining correlations between different parameters. While we leave such an in-depth analysis to future studies, we conclude this section with a practical application of `SEOBNRv5PHM_ESGB` to real GW data by performing Bayesian inference on selected events reported by the LVK Collaboration.

4.2.5 Constraining the Einstein-scalar-Gauss-Bonnet coupling

As an application of `SEOBNRv5PHM_ESGB` to GW data analysis, we perform Bayesian PE on selected events reported by the LVK Collaboration, including the ESGB coupling constant $\ell_{\rm GB}$ as a free parameter in the analysis. We consider three signals, GW190814 [555], GW190412 [120] and GW230529 [183], which have been analyzed in Refs. [601, 662, 702, 703, 720] to provide constraints on the coupling of the dilatonic ESGB theory (4.11), using waveform models that incorporate ESGB corrections only in the inspiral phase. To facilitate comparison with previous analyses, we translate between our conventions and those of Refs. [702, 703] by setting $\varphi = \sqrt{4\pi}\phi$ and $\ell_{\rm GB} = \sqrt{\alpha_{\rm GB}}\, 4\pi^{1/4}$.

The magnitude of ESGB corrections to the waveform is expected to be larger for low-mass systems, as the leading ESGB corrections to the phase are proportional to $\hat{\ell}^4_{\rm GB}$ [40, 373, 662, 703], and for asymmetric binaries, due to the increased scalar dipole radiation. As the sources of GW190412 and GW190814 are relatively low-mass binaries with asymmetric masses, these events are expected to offer better constraints on this theory. The source of GW190814, having a secondary with a mass around $2.6M_\odot$, is consistent with being either a BBH or a NSBH. Under the BBH interpretation, it imposes stringent bounds on ESGB gravity around $\sqrt{\alpha_{\rm GB}} \lesssim 0.4$ km [702, 703]. However, this bound is not necessarily robust, as the constraint weakens significantly if the secondary is a neutron star. In shift-symmetric ESGB gravity, neutron stars do not carry scalar monopolar charge, so the correction can be much larger for a BBH than for a NSBH, whose hair is carried by the more massive BH [601, 703].

The most likely interpretation of the source of GW230529 is that of a NSBH, with the primary being a BH with mass 2.5–4.5 $M_\odot$. Under this hypothesis, it currently places the best constraint on ESGB gravity [662, 720], with a 90% bound on $\sqrt{\alpha_{\rm GB}}$ ranging from 0.26 km to 0.35 km depending on the waveform approximant employed,

Event	GW230529	GW190814	GW190412	Combined
IMR	0.31 km	0.50 km	1.81 km	0.32 km
IMR with merger deviations	–	0.48 km	1.77 km	0.31 km
Inspiral only	–	0.41 km	2.15 km	0.30 km

Table 4.1: Summary of the 90% confidence bound on $\sqrt{\alpha_{\rm GB}}$ from the analysis of GW230529, GW190814 and GW190412, using the `SEOBNRv5PHM_ESGB` model in the dilatonic case $f(\varphi) = \exp(2\varphi)/4$ and $\mathcal{A}(\varphi) = 1$. We list the bounds from the full IMR analyses, without adding deviations to the merger and marginalized over parametrized merger deviations, and for inspiral-only analyses. We perform a single analysis for GW230529, since it has negligible SNR in the merger-ringdown stage.

when including ESGB corrections in the inspiral phase. We note that for GW230529 one cannot determine from GW data alone if either component of the source is a NS or a BH, and the primary analysis from the LVK Collaboration [183] employed BBH waveforms, including the `SEOBNRv5PHM` model used here as a baseline GR approximant. Furthermore, Ref. [662] finds that, when considering parametrized deviations to the inspiral phase, NSBH and BNS results with the tides constrained to realistic values are very similar to the BBH results. Therefore, in our analysis, we also neglect tidal effects, but we take the sensitivities for the secondary to be 0, as is the case for NSs in shift-symmetric ESGB theories and in the dilatonic ESGB theory at leading order in the coupling (see Sec 4.2.1). For simplicity, we analyze GW190814 and GW190412 under the BBH assumption, and GW230529 under the NSBH assumption.

We carry out the analysis using `parallel bilby` [470], and the nested sampler `dynesty` [553], using standard settings and priors for the GR parameters, as described in Sec. 3.1. We use uniform priors on $\ell_{\rm GB}$, with the constraint $\ell_{\rm GB}/m_2^0 \lesssim 0.831$ in the BBH case (see Sec. 4.2.1). In the NSBH case, we rather impose $\ell_{\rm GB}/m_1^0 \lesssim 0.831$. To facilitate comparison with other results in the literature, we also perform inspiral-only analyses, taking a maximum frequency for the likelihood of 137 Hz for GW190814 and 83 Hz for GW190412, following Ref. [702]. These cutoff frequencies correspond with the ISCO frequency in GR. We do not perform an inspiral-only analysis for GW230529 as the cutoff frequency for the inspiral stage would be around 600 Hz, and while the default analysis extends up to 1792 Hz, we do not expect significant differences due to the reduced sensitivity of the LIGO detectors in this high-frequency range.

As discussed in Sec. 4.2.3, our model incorporates parametrized deviations in the merger waveform amplitude and frequency (4.28), which can be varied during sampling. We perform analyses both assuming that they take GR values, as well as

allowing them to vary for the $(2,2)$ mode. We use uniform priors in the range $[-1,1]$ for both δA_{22} and $\delta\omega_{22}$. We introduce additional merger parameters only in the IMR analysis, as the merger deviations do not significantly impact the results when only analyzing the inspiral. For the same reason, we do not include these corrections in the analysis of GW230529, which has negligible SNR in the merger-ringdown stage.

Figure 4.9 presents the one-dimensional marginalized posteriors of $\ell_{\rm GB}$ (or, equivalently, $\sqrt{\alpha_{\rm GB}}$) obtained from the analysis of GW230529, GW190814 and GW190412. The vertical dashed lines indicate the 90% confidence bounds, also summarized in Table 4.1. We show the posteriors for the full IMR analyses, without adding corrections to the merger amplitude and frequency (light blue) and marginalized over parametrized merger deviations (yellow), and for inspiral-only analyses (dark blue). In all cases, the posteriors are compatible with $\ell_{\rm GB}=0$.

For the NSBH event GW230529, we find a 90% upper bound on $\sqrt{\alpha_{\rm GB}}$ of 0.31 km. This contraint is slightly less stringent than those of Refs. [662, 720] when relying on a BBH baseline model in GR, as they found $\sqrt{\alpha_{\rm GB}}\lesssim 0.28$ km and $\sqrt{\alpha_{\rm GB}}\lesssim 0.26$ km, respectively. However, our analysis differs in three ways: (i) our model includes ESGB corrections at higher PN orders. The works above include corrections to the conservative sector at 2PN, and to the dissipative sector at 1.5PN and 1PN relatively to the quadrupolar order, respectively; (ii) our model resums these ESGB corrections within the EOB framework; (iii) the waveform models of these works differ in the GR limit, i.e. `SEOBNRv4HM_ROM` [387] and `IMRPhenomXPHM` [137] respectively. This last factor alone leads to comparable discrepancies in the bounds between these works.

For GW190814, our results are consistent with previous analyses [702, 703], with a 90% constraints on $\sqrt{\alpha_{\rm GB}}$ ranging from 0.41 km to 0.48 km. We notice that, for this event, the inspiral-only analysis provides a slightly tighter constraint compared to the IMR analyses. Figure 4.10 shows the posterior distribution of $\ell_{\rm GB}$, inverse mass ratio $1/q$ and chirp mass $\mathcal{M}_c$ inferred from GW190814, along with the mass values recovered assuming GR. We observe: (i) a slight anti-correlation between $\ell_{\rm GB}$ and the chirp mass, whether the plunge-merger-ringdown is included or not, as expected for inspiral-dominated signals (see Sec. 4.2.4); and (ii) that neglecting the plunge-merger-ringdown signal results in a wider chirp mass posterior shifted towards larger values. These two points might contribute to the slightly tighter constraint from the inspiral-only analysis. Another factor could be that the merger-ringdown waveform is practically indistinguishable from GR for this event; its inclusion reduces the mismatch of the waveform with its GR counterpart at fixed $\ell_{\rm GB}$.

For the BBH event GW190412, we obtain $\sqrt{\alpha_{\rm GB}}=2.15$ km from the inspiral-only analysis and a slightly stronger bound $\sqrt{\alpha_{\rm GB}}=1.77$ km when including the plunge-merger-ringdown portions of the signal, owing to the additional SNR. This represents

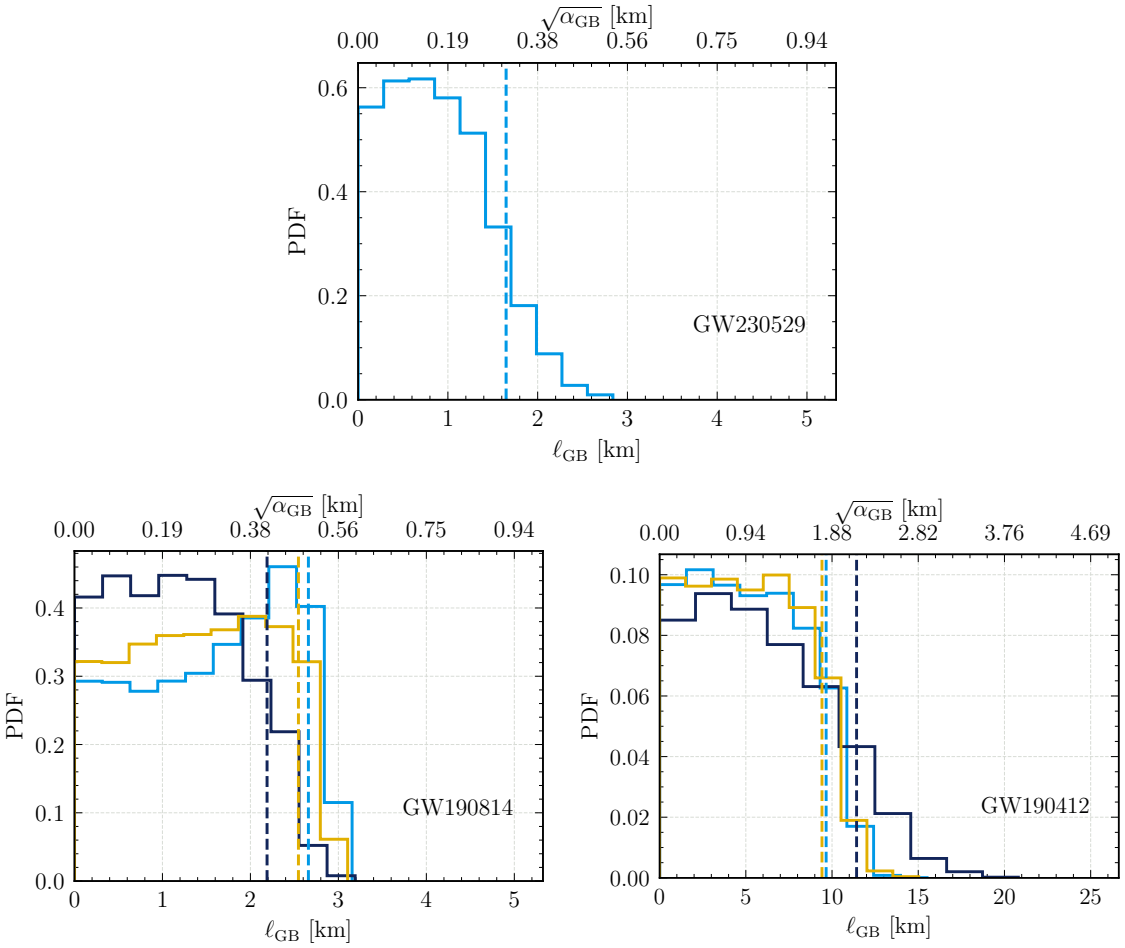

Figure 4.9: One-dimensional marginalized posterior of $\ell_{\rm GB}$ ($\sqrt{\alpha_{\rm GB}}$) obtained from the analysis of GW230529, GW190814 and GW190412, using the `SEOBNRv5PHM_ESGB` model in the dilatonic case $f(\varphi) = \exp(2\varphi)/4$ and $\mathcal{A}(\varphi) = 1$. The vertical dashed lines indicate the 90% confidence bound. We show the posteriors for the full IMR analyses, without adding the merger corrections (4.28) (light blue) or marginalizing over them (yellow), and for inspiral-only analyses (dark blue). We perform a single analysis for GW230529, since it has negligible SNR in the merger-ringdown stage.

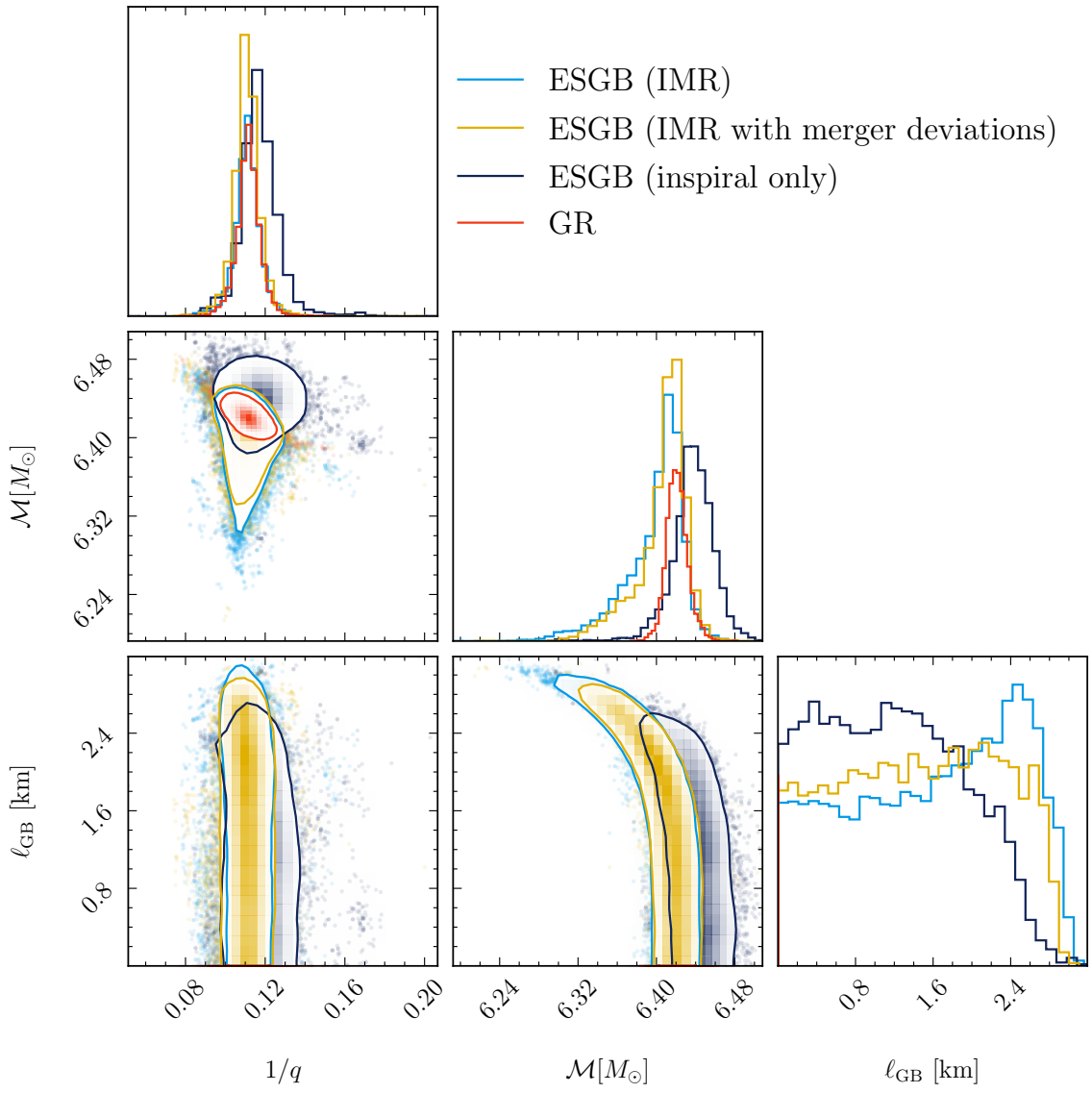

Figure 4.10: Posterior distribution of $\ell_{\rm GB}$, inverse mass ratio $1/q$ and chirp mass $\mathcal{M}_c$ obtained from the analysis of GW190814 using the `SEOBNRv5PHM_ESGB` model in the dilatonic case $f(\varphi) = \exp(2\varphi)/4$ and $\mathcal{A}(\varphi) = 1$. For the masses, we also show the values recovered assuming GR using the `SEOBNRv5PHM` model. We notice a slight anti-correlation between $\ell_{\rm GB}$ and the chirp mass, as well as a wider chirp mass posterior shifted to larger values for the inspiral-only analysis. This might contribute to a marginally better constraint on $\ell_{\rm GB}$ for the inspiral-only analysis, despite the lower recovered SNR.

Event	GW230529	GW190814	GW190412
IMR	-0.94	-0.02	-0.52
IMR with merger deviations	—	-3.0	-4.1

Table 4.2: Natural log Bayes factors between the dilatonic ESGB and GR hypotheses from the analysis of GW230529, GW190814 and GW190412, using the `SEOBNRv5PHM_ESGB` model. We consider the IMR analyses in ESGB, both with and without parametrized deviations to the waveform amplitude and frequency at merger.

roughly a factor two improvement over previous analyses [702]. The larger chirp mass of the source ($\mathcal{M}_c \sim 15\ M_\odot$, compared to $\mathcal{M}_c \sim 6\ M_\odot$ for GW190814 and $\mathcal{M}_c \sim 2\ M_\odot$ for GW230529) results in a higher relative SNR in the late-inspiral stage, increasing the impact of higher order PN corrections and the EOB resummation. For GW190412 and GW190814, the bounds on $\sqrt{\alpha_{\rm GB}}$ are robust with respect to uncertainties in the merger morphology, with a slight decrease when marginalized over parametrized merger deviations.

Combining constraints from all three events by multiplying the marginalized posteriors yields a joint bound on $\sqrt{\alpha_{\rm GB}}$ ranging from 0.30 km (for the inspiral-only analyses) to $0.31-0.32$ km (for the IMR analyses, with and without merger deviations respectively). The combined constraint is very similar to the one obtained by analyzing GW230529 alone, and if anything slightly worsened in the IMR analyses by the fact that the $\sqrt{\alpha_{\rm GB}}$ posterior for GW190814 peaks slightly away from 0.

We find, a posteriori, that our bounds are within the small-coupling limit. This justifies using the QNM expressions from Ref. [705], as well as employing the leading-order expressions (4.12) and (4.13) for the quantities in Eqs. (4.9) when analyzing GW230529 (see Sec. 4.2.1). For GW230529, we find $\ell_{\rm GB}/m_1^0 \lesssim 0.28$ at 90% confidence. For GW190412 we obtain $\ell_{\rm GB}/M_f \lesssim 0.15$, while for GW190814 $\ell_{\rm GB}/M_f \lesssim 0.065$.

Table 4.2 summarizes the natural log-Bayes factors between the ESGB and GR hypotheses, derived from the full IMR analyses of the signals. Without adding deviations to the merger amplitude and frequency, we find a log Bayes factor of -0.94 for GW230529, of -0.02 for GW190814 and of -0.52 GW190412, indicating no substantial preference for either hypothesis [721]. When parametrized merger deviations are included, we obtain lower Bayes factors, of -3.0 for GW190814 and of -4.1 GW190412. This indicates that allowing additional freedom in the merger signal does not improve the model's fit to the data, which is consistent with GW190412 and GW190814 being inspiral-dominated signals with low SNR in the merger-ringdown. The lower Bayes factors thus reflect the Occam penalty for introducing additional

parameters. Accurate modeling of the merger phase with NR simulations in ESGB gravity would be valuable to improve this analysis.

The combined constraint presented here could be further strengthened by incorporating additional events – particularly the NSBH events GW200105, GW200115, which have previously placed competitive bounds on this theory [703]. Because these systems are low-mass binaries, leading to inspiral-dominated signals, the constraints on ESGB gravity would likely be similar to those obtained by Ref. [703], which found the result to be robust with respect to the inclusion of higher-order PN corrections. On the other hand, slightly improved bounds could be obtained for heavier binaries when using `SEOBNRv5PHM_ESGB`. However, the result obtained by combining several events would likely improve marginally, as GW230529 provides a significantly more stringent bound compared to other events. Another way to improve the combined constraint would be to incorporate information about the underlying astrophysical population following Ref. [685]. This would involve jointly inferring the distribution of astrophysical parameters to correctly account for correlations between intrinsic parameters and the ESGB coupling.

4.3 A parametrized effective-one-body waveform model for tests of general relativity

Anticipated upgrades to the LVK interferometers [395] and the deployment of future detectors [396, 397, 401] will greatly increase the number of detected GW sources. At the same time, events will be observed with higher SNRs, enabling more stringent tests of GR. However, this improved sensitivity presents a major challenge for waveform accuracy, as statistical uncertainties become comparable to systematic biases in GW models [429, 435].

For tests of GR using the full IMR signal, such as the `pSEOBNR` approach, waveform systematics could lead to false indications of deviations from GR [369, 418, 443, 444]. For instance, Ref. [418] showed that applying the `pSEOBNR` analysis to massive BH binaries with LISA could incorrectly indicate deviations from GR at SNRs of ~ 100, because of waveform mismodeling. The severity of such biases depends strongly on binary parameters. Merger-dominated signals, where the higher-order modes play a significant role, are especially sensitive to systematic errors (see Sec. 2.2.4). For a simulated stellar-mass BBH signal, detectable in O5 with an SNR of 75 and a large fraction of the SNR accumulated during the inspiral phase, the analysis found results consistent with GR [368].

Currently, the `pSEOBNR` analysis, as well as ringdown-only analyses based on similar templates [681], are limited to BBHs with spins aligned or anti-aligned with the orbital angular momentum of the binary. An analysis of the event GW200129_065458 in Ref. [369] reported an apparent deviation from GR in the merger amplitude of the waveform, while the QNM-deviation parameters remained consistent with GR predictions. This result was interpreted as a false violation of GR, originating either from waveform systematics [722] – the absence of spin precession in the GR baseline model – or from data-quality issues [723]. Similar concerns about systematic biases in tests of GR from neglecting or mismodeling spin precession have been raised in other studies [445, 724], highlighting the need of improving waveform models and incorporating all relevant physical effect to perform robust tests of gravity.

In this section, we present the extension of the `pSEOBNR` framework to spin-precessing binaries, by introducing parametrized deviations in the `SEOBNRv5PHM` model [139], which generalizes the `SEOBNRv5HM` model discussed in Sec. 2.2 to spin-precessing BBHs. We focus here on modifications to the ringdown stage, where fractional deviations are introduced in the frequency and damping time of the fundamental QNMs. The model also includes parametrized deviations in the plunge-merger stage, following Ref. [369], and – for the first time – in the inspiral stage, by modifying the NR-calibration parameters in the EOB Hamiltonian. This increased flexibility

enables the model to capture more generic deviations from GR, which are generally expected to affect all stages of the coalescence. The parametrization of inspiral and plunge-merger deviations is described in detail in Ref. [6].

The new parametrized waveform model `pSEOBNRv5PHM` is implemented in the `pySEOBNR` package [1] described in Sec. 2.1. We validate our model through Bayesian PE, focusing on the ringdown of the $(\ell, m, n) = (2, 2, 0)$ mode, as it is the primary test currently performed in LVK analyses with `pSEOBNR` models [250, 251]. By recovering synthetic signals from NR simulations of highly precessing BH mergers [256], we demonstrate that `pSEOBNRv5PHM` correctly recovers consistency with GR. In contrast, neglecting spin-precession effects leads to false indications of deviations from GR, even at current detector sensitivity. Conversely, when analyzing a synthetic signal from a NR simulation of a binary boson-star merger [725], the model successfully identifies a deviation from a GR BBH signal. Finally, we reanalyze 12 events from GWTC-3 that were previously analyzed using an earlier version of the `pSEOBNR` model for aligned-spin binaries, `pSEOBNRv4HM` [368], by the LVK Collaboration [250, 251].

4.3.1 The parametrized waveform model

We start this section with a reminder of the construction of the multipolar spin-precessing `SEOBNRv5PHM` model [139], and then we describe, in Sec. 4.3.1, how we deform this baseline model to introduce modifications to the QNM spectrum.

Effective-one-body dynamics for precessing-spin binary black holes

As mentioned in Sec. 1.1.2, a common strategy for constructing precessing-spin waveforms is to start from aligned-spin waveforms in the so-called *co-precessing frame*, in which the z-axis remains perpendicular to the instantaneous orbital plane, and then applying a suitable rotation to the inertial frame of the observer [126–130]. More specifically, `SEOBNRv5PHM` builds on previous studies that used aligned-spin orbital dynamics in the co-precessing frame coupled to PN-expanded spin-precessing equations [136, 138, 337] to mitigate the cost of solving the equations of motion using the full precessing-spin EOB Hamiltonian (1.43) [132–134]. To model precessional effects more accurately, `SEOBNRv5PHM` extends beyond this approach by using an EOB Hamiltonian with partial precessional effects, $H_{\rm EOB}^{\rm pprec}$, in the co-precessing frame. This Hamiltonian includes orbit-averaged in-plane spin contributions for circular orbits [144], and reduces to the aligned-spin Hamiltonian used in `SEOBNRv5HM` in the appropriate limit (see Sec. (2.2.1)).

The equations of motion in the co-precessing frame have the same form as those for aligned-spin binaries (2.7) except for employing $H_{\rm EOB}^{\rm pprec}$, and for using, into the

Hamiltonian and aligned-spin modes, suitable projections of the spins onto the angular momentum at every timestep of the evolution [139]. The spins and angular momentum are evolved using PN-expanded equations with higher-order PN terms and spin-supplementary conditions consistent $H_{\rm EOB}^{\rm pprec}$ [144]. These evolution equations are used both to compute frame rotations during the inspiral, as summarized below, and for augmenting the co-precessing frame orbital dynamics.

Inspiral-plunge waveforms

In the co-precessing frame, the GW modes are decomposed into inspiral-plunge ($h_{\ell m}^{\rm insp-plunge}$) and merger-ringdown ($h_{\ell m}^{\rm merger-RD}$) waveforms, matched at the peak of the $(2,2)$ mode amplitude, as in the aligned-spin `SEOBNRv5HM` model (2.12). `SEOBNRv5PHM` includes in the co-precessing frame the same set of modes as its aligned-spin counterpart: $(\ell,|m|) = \{(2,2),(2,1),(3,3),(3,2),(4,4),(4,3),(5,5)\}$. Negative-$m$ modes are derived from the positive-m ones using the reflection symmetry $h_{\ell m} = (-1)^\ell h^*_{\ell -m}$, which is exact for aligned-spin binaries but not in the spin-precessing case [146], even in the co-precessing frame.

The inspiral-plunge modes in the co-precessing frame use the construction described in Sec. 2.2.2 for the `SEOBNRv5HM` model. In particular, they use factorized, resummed expressions of the PN GW modes (2.14) [316–319] evaluated along the EOB dynamics. Their accuracy during the plunge is improved by applying the numerically-tuned NQC corrections $N_{\ell m}$ (2.17), which also allow for a smooth connection between the inspiral-plunge and merger-ringdown waveforms. The main difference in the spin-precessing case is that the modes are evaluated using time-dependent spin projections along the orbital angular momentum.

The GW polarizations in the inertial frame of the observer are those required for data-analysis applications. The `SEOBNRv5PHM` model uses three reference frames (see Fig. 1 of Ref. [139]):

1. The inertial frame of the observer (*source frame*). Quantities in this frame are denoted with the superscript I.
2. An inertial frame where the z-axis is aligned with the final angular momentum of the system ($\boldsymbol{J}_{\rm f}$*-frame*). Quantities in this frame are denoted with the superscript J. This frame facilitates the construction of the merger-ringdown modes. The QNMs are defined with respect to the direction of the final spin, and thus, the description of the ringdown signal as a linear combination of QNMs, is formally valid in this frame.
3. A non-inertial frame which tracks the instantaneous motion of the orbital plane (the *co-precessing frame*). Quantities in this frame are denoted with the superscript CP.

The inertial-frame modes are related to the co-precessing-frame modes by a time-dependent rotation from the co-precessing frame to the $\boldsymbol{J}_{\rm f}$-frame, followed by a time-independent rotation from the $\boldsymbol{J}_{\rm f}$-frame to the final inertial frame

$$h^{\rm I}_{\ell m}(t) = \sum_{m',m''} \left(\mathbf{R}^{\rm J\to I}\right)_{m,m'} \left(\mathbf{R}^{\rm CP\to J}\right)_{m',m''} h^{\rm CP}_{\ell m''}(t), \tag{4.31}$$

where $\mathbf{R}^{\rm X\to Y}$ denotes the rotation operator from the frame X to the frame Y, and m', m'' are summation indices over the modes available in the co-precessing frame. These rotations are implemented in `pySEOBNR` using quaternions, but can also be expressed in terms of Euler angles $\{\alpha(t), \beta(t), \gamma(t)\}$ [128]. Notably, spin precession induces mixing of modes with the same ℓ but different m, potentially altering the mode hierarchy compared to the non-precessing scenario [127, 679, 726–728].

Merger-ringdown waveforms

After the merger, the EOB formalism models the transition to the ringdown stage using a phenomenological model [326] based on the QNMs of the remnant BH. In `SEOBNRv5PHM`, the merger-ringdown waveform is attached in the co-precessing frame, using the multipolar model developed for aligned-spin binaries in `SEOBNRv5HM`, as described in Sec. 2.2.2. For clarity, we reproduce the ansatz here with explicit reference to the frames involved:

$$h^{\text{merger-RD}}_{\ell m}(t) = \nu\ \tilde{A}_{\ell m}(t)\ e^{i\tilde{\phi}_{\ell m}(t)}\ e^{-i\sigma^{\rm CP}_{\ell m0}(t-t^{\ell m}_{\rm match})}, \tag{4.32}$$

where $\sigma^{\rm CP}_{\ell m0} = \sigma^{\rm R,\,CP}_{\ell m} - i\sigma^{\rm I,\,CP}_{\ell m}$ denotes the complex frequency of the least-damped QNM of the remnant BH, in the co-precessing frame. The final mass and spin of the remnant are estimated using NR fits [517, 518]. The functions $\tilde{A}_{\ell m}$ and $\tilde{\phi}_{\ell m}$ in Eq. (4.32) are time-dependent amplitude and phase functions (see Eqs. (2.22) and (2.23)).

The real and imaginary parts of $\sigma_{\ell m0}$, whether in the co-precessing or $\boldsymbol{J}_{\rm f}$-frame, are related to QNM oscillation frequency and damping time:

$$f_{\ell m0} = \frac{1}{2\pi}\mathrm{Re}(\sigma_{\ell m0}) = \frac{1}{2\pi}\omega^{\rm QNM}_{\ell m0}\,, \tag{4.33a}$$

$$\tau_{\ell m0} = -\frac{1}{\mathrm{Im}(\sigma_{\ell m0})}\,. \tag{4.33b}$$

To compute the waveform in the inertial frame, a prescription is needed for the co-precessing frame Euler angles $\{\alpha(t), \beta(t), \gamma(t)\}$ which extends beyond merger. `SEOBNRv5PHM` adopts a phenomenological model based on insights from NR simulations [729]. Specifically, it has been shown that the co-precessing frame continues to

precess approximately around the direction of the final angular momentum with a precession frequency, $\omega_{\rm prec}$, proportional to the difference between the lowest overtone of the $(2,2,0)$ and $(2,1,0)$ QNM frequencies. This leads to the following expressions for the merger-ringdown angles relating the $\boldsymbol{J}_{\rm f}$-frame and the co-precessing frame used in `SEOBNRv5PHM`,

$$\begin{aligned}
\alpha^{\rm merger-RD} &= \alpha(t_{\rm match}) + \omega_{\rm prec}(t - t_{\rm match}),\\
\beta^{\rm merger-RD} &= \beta(t_{\rm match}),\\
\gamma^{\rm merger-RD} &= \gamma(t_{\rm match}) - \omega_{\rm prec}(t - t_{\rm match})\cos\beta(t_{\rm match}),
\end{aligned} \tag{4.34}$$

where $t_{\rm match} = t^{22}_{\rm peak}$ is the peak of the (2,2) mode amplitude (2.18) in the co-precessing frame.

The behavior studied in Ref. [729] describes prograde-spin configurations, where the remnant spin is positively aligned with the orbital angular momentum at merger. Following Ref. [134], `SEOBNRv5PHM` extends the prescription to retrograde-spin cases by imposing simple precession around the final spin at a rate $\omega_{\rm prec} \geq 0$

$$\omega_{\rm prec} = \begin{cases} \omega_{220}^{\rm QNM,\,J}(\chi_f) - \omega_{210}^{\rm QNM,\,J}(\chi_f) & \boldsymbol{\chi}_f \cdot \boldsymbol{L}_f > 0 \\ \omega_{210}^{\rm QNM,\,J}(\chi_f) - \omega_{220}^{\rm QNM,\,J}(\chi_f) & \boldsymbol{\chi}_f \cdot \boldsymbol{L}_f < 0 \end{cases}, \tag{4.35}$$

that depends on whether the total angular momentum at merger $\boldsymbol{\chi}_f \propto \boldsymbol{J}_f$ is aligned or not with the orbital angular momentum at merger $\boldsymbol{L}_f$. Here χ_f is a *signed* final spin with magnitude $|\boldsymbol{\chi}_f|$, and the same sign of $\boldsymbol{\chi}_f \cdot \boldsymbol{L}_f$. This prescription of the post-merger extension of the Euler angles in the retrograde case ($\boldsymbol{\chi}_f \cdot \boldsymbol{L}_f < 0$) is significantly less tested than in the prograde case due to the limited availability of NR simulations covering the relevant region of parameter space – most notably high mass-ratio binaries – which also includes systems with transitional precession [122].

As mentioned earlier, the QNM frequencies obtained from BH perturbation theory are formally valid in the $\boldsymbol{J}_{\rm f}$-frame. Following recent insights from NR [730], `SEOBNRv5PHM` computes the co-precessing frame QNM frequencies from the ones in the $\boldsymbol{J}_{\rm f}$-frame as (see Ref. [139], Eq. (22) and Ref. [730], Eq. (35)),

$$\omega_{\ell m0}^{\rm QNM,\,CP} = \omega_{\ell m0}^{\rm QNM,\,J} - m\,(1 - |\cos\beta(t_{\rm match})|)\,\omega_{\rm prec}. \tag{4.36}$$

Parametrized ringdown deviations

We introduce non-GR deformations to the QNMs, following the same strategy used in Refs. [367–369], applying the substitutions:

$$f^{\rm J}_{\ell m 0} \to f^{\rm J}_{\ell m 0}\,(1+\delta f_{\ell m 0}), \tag{4.37a}$$

$$\tau^{\rm J}_{\ell m 0} \to \tau^{\rm J}_{\ell m 0}\,(1+\delta \tau_{\ell m 0}), \tag{4.37b}$$

with $\delta\tau_{\ell m 0} > -1$ to ensure that the remnant BH is stable; it rings downs, instead of "ringing-up" exponentially. Hereafter, we will always refer to frequencies in the $\boldsymbol{J}_{\rm f}$-frame, and drop the superscript J to lighten the notation.

For spin-precessing binaries, care must be taken due to the multiple reference frames involved. In `pSEOBNRv5PHM`, QNM deviations affect both the co-precessing frame waveform modes (4.32) and the Euler angles governing the rotation from $\boldsymbol{J}_{\rm f}$-frame to co-precessing frame after merger (4.34). Since BH perturbation theory defines QNM frequencies in the $\boldsymbol{J}_{\rm f}$-frame, it is natural to introduce deviations there. This directly modifies the effective precession rate $\omega_{\rm prec}$ (4.35), which propagates both into the co-precessing frame QNM frequencies (4.36) and the post-merger Euler angles (4.34).

At the transition between prograde-spin and retrograde-spin configurations ($\boldsymbol{\chi}_f \cdot \boldsymbol{L}_f = 0$), a small discontinuity present in the rotations in the GR limit of the model is amplified by non-zero QNM deviations: the same deviation in δf_{220}, or in δf_{210}, changes $\omega_{\rm prec}$ in opposite directions depending on the sign of $\boldsymbol{\chi}_f \cdot \boldsymbol{L}_f$ (see Eq. (4.35)). This highlights the need to revisit the prescription for retrograde-spin configurations as more NR simulations in this regime become available [258]. Here, to safely avoid this problem, we introduce a boolean parameter `omega_prec_deviation` which controls whether QNM deviations are propagated to $\omega_{\rm prec}$. For PE applications, we enable this only if all posterior samples from a corresponding GR run are in a prograde-spin configuration. For posteriors that are entirely in a negative-spin configuration, no discontinuity arises; however, we still prefer not to include QNM deviations in the rotations since the prescription has not been extensively validated against NR simulations. We also note that such configurations, characterized by high mass ratios and negative spins, are uncommon among the observed events.

To illustrate how parametrized deviations $\delta f_{\ell m 0}$ and $\delta\tau_{\ell m 0}$ modify the gravitational-wave (GW) signal, we consider a spin-precessing binary system with the following mass ratio and spins:

$$q = 2.0, \quad \text{and} \quad \boldsymbol{\chi}_1 = \boldsymbol{\chi}_2 = [0.5, 0, 0.5]\,, \tag{4.38}$$

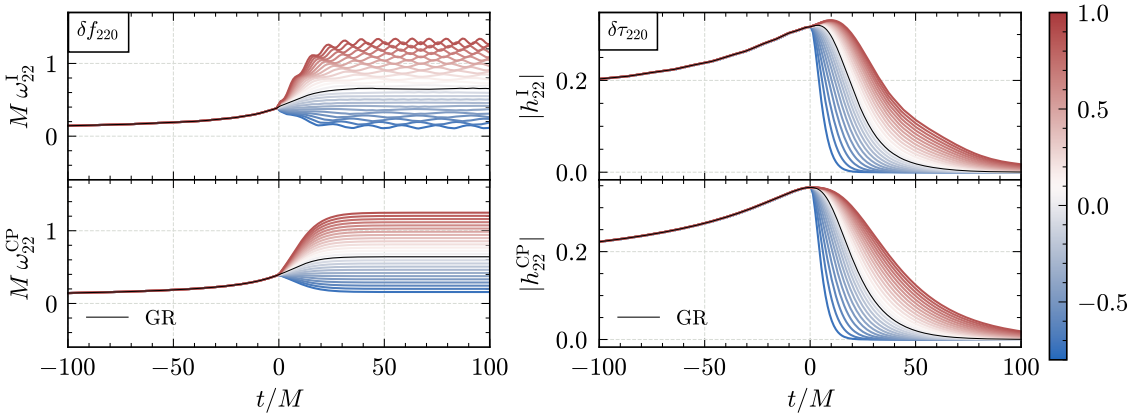

Figure 4.11: Impact of QNM deviations on the waveform morphology. The left panel shows the effect of frequency deviations δf_{220} on the instantaneous GW frequency in the inertial frame ($M\omega_{22}^{\rm I}$) and the co-precessing frame ($M\omega_{22}^{\rm CP}$). The right panel illustrates the effect of damping time deviations $\delta\tau_{220}$ on the waveform amplitude in both frames ($|h_{22}^{\rm I}|$ and $|h_{22}^{\rm CP}|$). The time $t = 0$ is defined as the peak amplitude of the co-precessing $(2, 2)$ mode. For precessing binaries, mode mixing is evident in the inertial frame, while the co-precessing frame exhibits a morphology consistent with aligned-spin binaries.

where the spins are defined at a dimensionless orbital frequency $M\Omega = 0.015$, corresponding to a frequency of 20 Hz for a binary with total mass of approximately 50 $M_\odot$. We examine the impact of the deviations on the waveform in both co-precessing and inertial frames, focusing on the $(2, 2)$ mode for clarity.

Figure 4.11 shows the effects of varying δf_{220} (left panel) and $\delta\tau_{220}$ (right panel). For the frequency deviations δf_{220}, the top row shows the instantaneous GW frequency in the inertial frame ($M\omega_{22}^{\rm I}$), and the bottom row shows the frequency in the co-precessing frame ($M\omega_{22}^{\rm CP}$). For the damping time deviations, we plot the waveform amplitude in both inertial ($|h_{22}^{\rm I}|$) and co-precessing ($|h_{22}^{\rm CP}|$) frames. The colored envelopes span the range $(\delta f_{220},\ \delta\tau_{220}) \in [-0.8, 1.0]$, and the black curves correspond to the GR predictions. The time $t = 0$ is defined as the peak amplitude of the co-precessing $(2, 2)$ mode. For precessing binaries, modulations due to mode-mixing between modes with the same ℓ in the co-precessing frame are evident in the inertial frame, particularly in the frequency. In the co-precessing frame, however, the morphology is analogous to that observed for aligned-spin binaries in previous studies [368]. Overall, the parametrized model provides smooth deviations from GR, even in the inertial frame. As with aligned-spin binaries, QNM corrections affect the waveform only after merger, which corresponds to the peak of the co-precessing $(2, 2)$ mode.

4.3.2 Parameter estimation of synthetic signals

We validate `pSEOBNRv5PHM` through Bayesian PE, focusing on the ringdown of the $(\ell, m, n) = (2, 2, 0)$ mode. We simulate and analyze signals using the `bilby` package [179,486], and the nested sampler `dynesty` [553], using standard priors and settings as described in Sec. 3.1. For the QNM deviation parameters, we use uniform priors in the ranges

$$\delta f_{220} \in [-0.8, 2.0] \quad \text{and} \quad \delta\tau_{220} \in [-0.8, 2.0]. \tag{4.39}$$

In cases exhibiting railing, we extend the prior range to $[-0.8, 4.0]$. When analyzing simulated signals, we consider a three-detector (LIGO Hanford, LIGO Livingston and Virgo) network, using the LIGO PSD at O4 sensitivity [398] and Virgo PSD at advanced Virgo sensitivity [395]. The noise curves are named `aLIGO_O4_high` and `AdV` in `bilby`.

Injection of a binary black hole signal in general relativity

In this section, we assess the importance of including spin-precession effects when performing tests of GR, by analyzing a synthetic NR signal from the public SXS catalog [256]: `SXS:BBH:0165`. This BBH system has mass ratio $q = 6$, detector-frame total mass $M = 95\,M_\odot$ and BH's dimensionless spin vectors defined at 20 Hz of $\boldsymbol{\chi}_1 = [-0.06, 0.78, -0.4]$ and $\boldsymbol{\chi}_2 = [0.08, -0.17, -0.23]$. Notably, this BBH system exhibits strong spin precession, with a high mass ratio and a significant effective precessing-spin of $\chi_{\rm p} \sim 0.78$. It stands out as one of the most challenging systems to model in the public SXS catalog [256]. The source is placed at an inclination $\iota = \pi/2$ rad with respect to the line of sight. The coalescence and polarization phases are $\phi = 1.2$ rad and $\psi = 0.7$ rad, respectively. The sky-position is defined by its right ascension of 0.33 rad and declination of -0.6 rad at a geocentric time of 1249852257 s. The luminosity distance to the source is chosen to be 1200 Mpc, producing a network SNR of 18.1.

For this configuration, PE under the assumption of GR, using the `SEOBNRv5PHM` waveform model, yields posterior samples in both prograde-spin and retrograde-spin configurations. As discussed in Sec. 4.3.1, at the transition between these configurations, corrections to δf_{220} introduce a discontinuity in $\omega_{\rm prec}$. To address this, we exclude corrections to the $\omega_{\rm prec}$ term in such cases. Nevertheless, we analyze the signal under both approaches to evaluate the impact of this choice.

Figure 4.12 shows the posterior probability distributions for the fractional deviations in the frequency and damping time of the $(2, 2, 0)$ QNM (δf_{220} and $\delta\tau_{220}$) for this synthetic signal. We compare three parameter recoveries: with the `pSEOBNRv4HM_PA` model [369, 383] (blue), and with the `pSEOBNRv5PHM` model, with (orange) and

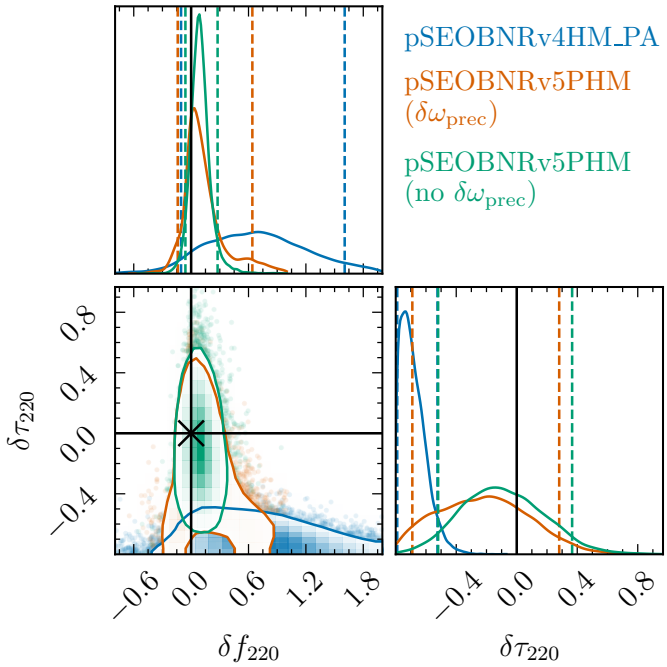

Figure 4.12: Posterior probability distributions for the fractional deviations in the frequency and damping time of the $(2, 2, 0)$ QNM (δf_{220} and $\delta\tau_{220}$), for a synthetic signal of a highly-precessing BBH NR waveform from the public SXS catalog `SXS:BBH:0165`. The PE is performed with the `pSEOBNRv4HM_PA` model (blue) and with the `pSEOBNRv5PHM` model, including (orange) or excluding (green) the QNM corrections in the computation of the precession rate $\omega_{\rm prec}$ (4.35). The contours mark the 90% credible regions, while the dashed lines on the one-dimensional marginalized distributions mark the 90% credible intervals. The black vertical and horizontal lines indicate the GR predictions ($\delta f_{220} = \delta\tau_{220} = 0$).

without (green) including QNM corrections in the computation of the precession rate $\omega_{\rm prec}$ (4.35). The contours mark the 90% credible regions, while the dashed lines on the one-dimensional marginals mark the 90% credible intervals. The black vertical and horizontal lines indicate the GR predictions ($\delta f_{220} = \delta\tau_{220} = 0$).

First, we observe that the `pSEOBNRv4HM_PA` model, which does not include precession effects, recovers a significant bias in the damping time away from the GR prediction. Although some GR parameters (e.g., the component masses) are accurately recovered, others – such as the binary's inclination – are significantly biased. As shown in previous studies [369, 445], waveform systematics, due to the absence of spin-precession effects, can mimic apparent deviations from GR. In contrast, the `pSEOBNRv5PHM` model is sufficiently accurate to recover GR predictions reliably even for challenging binary configurations, at current detector sensitivity. This holds both with and without including QNM corrections in $\omega_{\rm prec}$, although posterior distributions in the latter case appear more sensible, consistently with the avoidance of a discontinuous

limit. This choice has no significant impact on other parameters, which are accurately recovered in both configurations of `pSEOBNRv5PHM`.

The natural log Bayes factor between `pSEOBNRv5PHM` without and with QNM corrections in $\omega_{\rm prec}$ is $\ln \mathcal{B} \simeq 0.2$, comparable to the estimated error in the Bayes factor. This indicates no significant preference over either model. On the other hand, the natural log Bayes factor between `pSEOBNRv5PHM` without QNM corrections in $\omega_{\rm prec}$ and `pSEOBNRv4HM` is $\ln \mathcal{B} \simeq 5.7$ indicating a significant preference for the former. Finally, the natural log Bayes factor between `pSEOBNRv5PHM` without QNM corrections in $\omega_{\rm prec}$ and `SEOBNRv5PHM` in GR is $\ln \mathcal{B} \simeq -1.5$, indicating overall preference for the GR hypothesis.

Injection of a binary boson-star signal

In this section, we assess whether our model can distinguish a signal that does not originate from a BBH merger in GR. To do so, we analyze a synthetic signal from a publicly available NR simulation of a scalar-field solitonic boson star (BS) [731] merger. The simulation was produced with the `GRChombo` code [732,733] and described in Ref. [725], which presented several high-precision, IMR waveforms spanning approximately 20 orbits for equal-mass, quasicircular, nonspinning BS binaries of different compactness.

Boson stars are modeled by a complex scalar field, which can be decomposed into amplitude A and frequency ω, as $\varphi(t,r) = A(r)e^{\mathrm{i}(\epsilon\omega t+\delta\phi)}$. Following Ref. [725] we introduce the parameter $\epsilon = \pm 1$ determining the rotation of the scalar field in the complex plane, and a phase offset $\delta\phi$. The primary BS always has $\epsilon = 1$, $\delta\phi = 0$, and we consider the configuration with secondary parameters $\epsilon = 1$ and $\delta\phi = \pi$ (*antiphase*). The simulation we consider has central amplitude $A(0) = 0.17$, which gives rise to highly compact BSs with compactness $\mathcal{C} = 0.2$ and dimensionless tidal deformability $\Lambda \sim 10$. The coalescence results in the formation of a BH with final spin $\chi_f \simeq 0.7$, similar to the remnant of a nonspinning equal-mass BBH merger.

The injection setup matches that of the BBH NR injections, but we include only the $\ell = 2$ modes in both injection and recovery, since they are the only ones contained in the NR data. We take the same total mass and extrinsic parameters as for the `SXS:BBH:0165` NR injection, except for the inclination angle which we take $\iota = \pi/3$ rad to give an optimal SNR of 31.5.

The left panel of Fig. 4.13 shows the posterior probability distributions for the fractional deviations in the frequency and damping time of the $(2,2,0)$ QNM (δf_{220}, $\delta\tau_{220}$) for the synthetic binary BS signal recovered with `pSEOBNRv5PHM`. The prediction for a BBH in GR ($\delta f_{220} = \delta\tau_{220} = 0$) is excluded at the 90% credible level, demonstrating that `pSEOBNRv5PHM` successfully identifies a deviation from the signal of a BBH in GR.

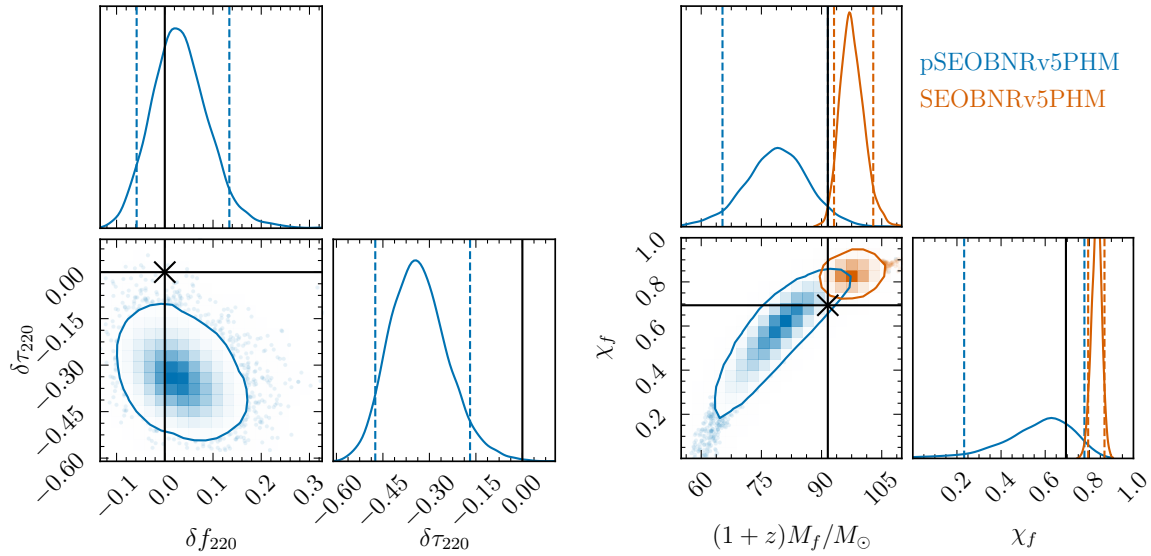

Figure 4.13: *Left panel*: Posterior probability distributions for the fractional deviations in the frequency and damping time of the $(2, 2, 0)$ QNM (δf_{220} and $\delta\tau_{220}$), for a synthetic signal of a binary BS merger recovered with `pSEOBNRv5PHM`. The contours mark the 90% credible regions, while the dashed lines on the one-dimensional marginalized distributions mark the 90% credible intervals. The black vertical and horizontal lines mark the predictions for a BBH in GR ($\delta f_{220} = \delta\tau_{220} = 0$). *Right panel*: Posterior probability distributions for the detector-frame mass and spin of the remnant BH, estimated with the `pSEOBNRv5PHM` and `SEOBNRv5PHM` models. For `pSEOBNRv5PHM`, the remnant properties are estimated from the complex QNM frequencies by inverting the fitting formula provided in Ref. [417]. The black vertical and horizontal lines mark the true values.

Specifically, while δf_{220} remains consistent with zero, the posterior for $\delta\tau_{220}$ shows a preference for negative values, indicating a more strongly damped ringdown signal compared to what would be predicted from the component masses and spins of a BBH merger remnant that matches the inspiral signal.

Analyzing the BS signal under the GR BBH assumption can lead to biased reconstructions of the ringdown, because the inferred component masses and spins are themselves biased, and the final mass and spin are computed assuming a remnant from a BBH merger. For the simulation considered, the bias in the component masses and spins is the larger source of error, as the mass and spin of the remnant BH are nearly identical to those of a BBH merger remnant. The biases in the final mass and spin lead to incorrect predictions of the ringdown frequency and damping time. By allowing for deviations in the QNM frequencies, the `pSEOBNR` model is partially able to mitigate these biases and provide a better fit to the BS simulation. This is confirmed by the right panel of Fig. 4.13, which shows the detector-frame mass and

spin of the remnant BH, estimated with the `pSEOBNRv5PHM` and `SEOBNRv5PHM` models. For `pSEOBNRv5PHM`, the remnant properties are estimated from the complex QNM frequencies by inverting the fitting formula provided in Ref. [417]. The `SEOBNRv5PHM` estimate is not compatible with the true values, indicated by the black vertical and horizontal lines. The inclusion of a damping time deviation in the `pSEOBNRv5PHM` model shifts the posterior towards the true values, particularly for the final spin, which are now recovered within the 90% credible region.

Notably, the `pSEOBNR` model is capable of detecting that the signal does not originate from a BBH coalescence, even if the remnant is a Kerr BH in GR. In contrast, ringdown analyses limited to the post-merger stage might not reveal such discrepancies unless the ringdown results are compared to those from a complete IMR analysis based on the BBH assumption. In that scenario, the deviation could manifest either as a discrepancy between the recovered frequency and damping time and those predicted by the IMR analysis (when using an agnostic damped-sinusoid model) or as a mismatch between the IMR-inferred remnant mass and spin and those obtained from the ringdown stage (when employing a ringdown model that assumes a Kerr remnant).

Consistent with the findings in Ref. [725], we also observe significant biases in standard GR parameters. In particular, the posterior shows significant support away from equal masses, where the true value $q = 1$ is excluded at the 90% credible level, leading to an overestimation of the primary mass. The spin magnitudes are biased toward higher values ($a_1, a_2 > 0.5$), with moderate alignment to the orbital angular momentum ($\chi_{\rm eff} \simeq 0.5$). The biases in the mass ratio and effective spin help the BBH model better replicate the shallower chirp observed in the BS inspiral. Additionally, the luminosity distance is overestimated.

4.3.3 Parameter estimation on real data

In this section, we apply our model to real data by re-analyzing 12 events from GWTC-3, which were originally analyzed using the `pSEOBNRv4HM` model [368] in Ref. [251].

A known degeneracy in the `pSEOBNR` framework exists between the fundamental QNM frequency deviation parameter and the remnant mass [368], particularly for low-SNR events dominated by the postmerger phase and lacking significant higher-mode content. To mitigate this issue, a selection criterion is applied, requiring that both the inspiral and post-inspiral regimes achieve SNR > 8, a criterion met by 12 binary systems from GWTC-3 that also satisfy the other selection criteria for tests of GR (detection in multiple interferometers and false-alarm rates $< 10^{-3}$ yr^{-1}). The final list of selected events is provided in Table 4.3. We use strain data from GWOSC [556]

and the publicly released PSDs and calibration envelopes.

As in previous studies [250,251,441], we combine information from multiple events to place tighter constraints on the deviation parameters. As in Refs. [251,368], we present joint posteriors obtained by multiplying the individual-event posteriors (equivalent to assuming that the fractional deviations $(\delta f_{220}, \delta\tau_{220})$ are constant across events). In addition, we present hierarchically combined results, assuming that the non-GR parameters $(\delta f_{220}, \delta\tau_{220})$ are drawn from a common underlying Gaussian distribution $\mathcal{N}(\mu, \sigma)$ of unknown mean μ and standard deviation σ (the *hyperparameters*). The events GW191109_010717 and GW200208_130117 were excluded from the combined bounds (hierarchical or joint posterior) in Ref. [251], as the posteriors on δf_{220} show multimodal features likely due to possibility of noise systematics not accounted for. We performed single-event analyses also for these events, finding consistent results with Ref. [251]. Accordingly, we also exclude them from the combined results.

Figure 4.14 summarizes the results of our reanalysis. The left panel shows the two-dimensional posteriors for the frequency and damping time deviations (along with the one-dimensional marginalized posteriors) for all the events listed in Table 4.3. The contours are colored by the median detector-frame total mass $(1+z)M$ of the corresponding binary. We highlight the posteriors from two events, GW150914 and GW200129_065458, which are among the loudest detected so far and provide strongest single-event bounds. The combined constraints are reported both by multiplying individual posteriors and by hierarchically combining events. In the right panel of Fig. 4.14 we also provide a summary of the 90% credible intervals on the one-dimensional marginalized posteriors, color coded by the median detector-frame mass of the binary.

Our results for GW150914 are broadly consistent with Ref. [251], with a Bayes factor between `pSEOBNRv5PHM` and `pSEOBNRv4HM` $\ln\mathcal{B} \simeq 0.6$. This is expected, as GW150914 is consistent with originating from a nonspinning binary, making the impact of waveform systematics subdominant [428]. In contrast, the posterior for GW200129_065458 differs more noticeably from the one in Ref. [251]. This event exhibits evidence of spin precession under the assumption of a binary in a quasicircular orbit [722]. However, uncertainties in glitch subtraction could affect the evidence for spin precession [723,734], and an alternative interpretation as an aligned-spin eccentric binary has been proposed [448].

Compared to the result of Ref. [251] for GW200129_065458, we note that the posterior of $\delta\tau_{220}$ exhibits a larger tail towards positive values. This shift in $\delta\tau_{220}$ is driven by a slightly different recovery of the binary's luminosity distance and inclination angle when spin precession is included in the analysis. When analyzing the event with `pSEOBNRv5HM` under the aligned-spin assumption, we find results consistent

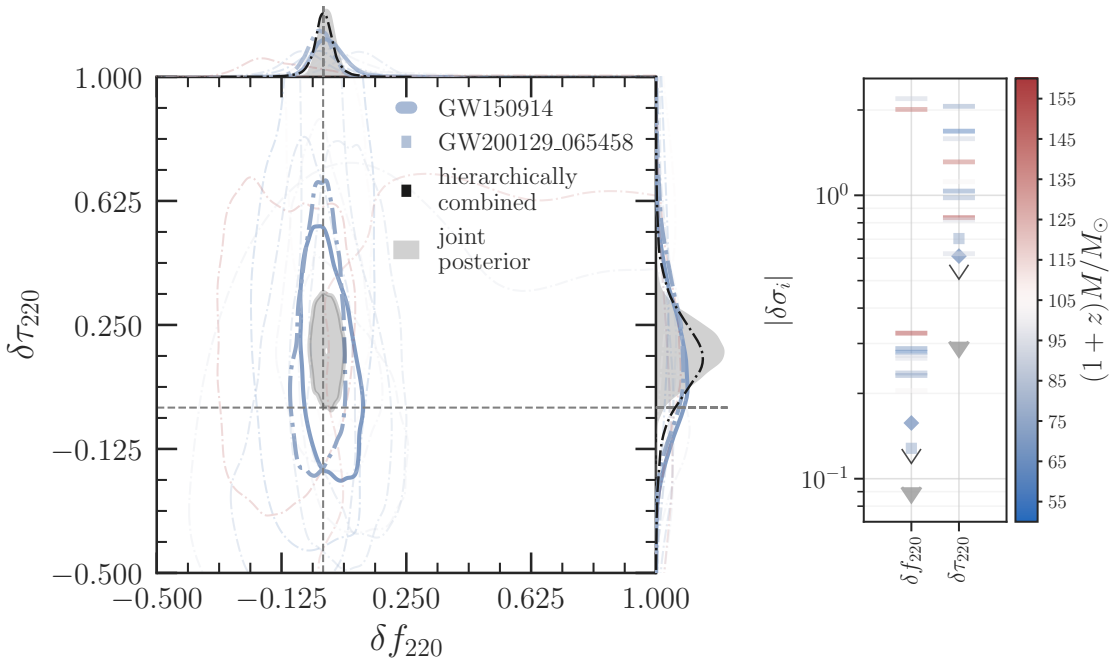

Figure 4.14: *Left panel*: The 90% credible regions of the posterior probability distribution of the fractional deviations in the frequency and damping time of the $(2, 2, 0)$ QNM, δf_{220} and $\delta\tau_{220}$, and their corresponding one-dimensional marginalized posterior distributions, for events from GWTC-3 passing a SNR threshold of 8 in both the inspiral and post-inspiral signal. Posteriors for GW150914 and GW200129_065458 are separately shown. The filled gray contours denote the 90% credible regions on the joint constraints for $(\delta f_{220}, \delta\tau_{220})$ obtained by multiplying the individual event posteriors (given a flat prior), while the hierarchical method of combination yields the black dot dashed curves only shown in the one-dimensional marginalized posteriors. The dashed gray lines mark the GR prediction $(\delta f_{220}, \delta\tau_{220}) = (0, 0)$. *Right panel*: 90% credible interval on the one-dimensional marginalized posteriors on $\delta\sigma_i = (\delta f_{220}, \delta\tau_{220})$, colored by the median detector-frame total mass $(1 + z)M$, inferred assuming GR. Filled gray (unfilled black) triangles mark the constraints obtained when all the events are combined by multiplying likelihoods (hierarchically). The bounds from GW200129_065458 (square) and GW150914 (diamond) are indicated by the separate markers.

Event	δf_{220}	$\delta\tau_{220}$	f_{220} (Hz)	τ_{220} (ms)	$(1+z)M_f/M_\odot$	χ_f
GW150914	$0.02^{+0.09}_{-0.07}$	$0.12^{+0.33}_{-0.27}$	$240.5^{+25.1}_{-25.6}$	$4.48^{+1.29}_{-1.06}$	$72.9^{+12.3}_{-12.8}$	$0.72^{+0.13}_{-0.28}$
GW170104	$-0.02^{+0.14}_{-0.13}$	$0.43^{+1.01}_{-0.66}$	$296.6^{+58.9}_{-54.5}$	$5.04^{+3.76}_{-2.37}$	$69.9^{+16.2}_{-20.6}$	$0.87^{+0.09}_{-0.42}$
GW190519_153544	$-0.14^{+0.20}_{-0.13}$	$0.17^{+0.48}_{-0.35}$	$120.4^{+17.2}_{-18.4}$	$8.36^{+3.96}_{-2.65}$	$140.7^{+34.8}_{-31.2}$	$0.67^{+0.20}_{-0.45}$
GW190521_074359	$0.06^{+0.17}_{-0.10}$	$-0.03^{+0.35}_{-0.26}$	$198.5^{+30.6}_{-28.9}$	$5.41^{+1.82}_{-1.41}$	$88.4^{+14.9}_{-16.6}$	$0.72^{+0.16}_{-0.37}$
GW190630_185205	$-0.06^{+0.12}_{-0.16}$	$0.00^{+0.56}_{-0.45}$	$247.6^{+34.9}_{-44.2}$	$3.96^{+2.32}_{-1.76}$	$69.4^{+16.5}_{-17.9}$	$0.70^{+0.20}_{-0.54}$
GW190828_063405	$0.11^{+0.11}_{-0.12}$	$0.18^{+0.52}_{-0.45}$	$226.7^{+40.1}_{-41.3}$	$6.18^{+2.67}_{-2.40}$	$88.4^{+15.6}_{-20.1}$	$0.85^{+0.09}_{-0.37}$
GW190910_112807	$0.01^{+0.11}_{-0.09}$	$0.60^{+0.63}_{-0.47}$	$175.0^{+23.7}_{-20.1}$	$9.45^{+3.48}_{-2.67}$	$122.6^{+18.1}_{-18.6}$	$0.90^{+0.05}_{-0.12}$
GW191109_010717	$1.31^{+0.65}_{-1.26}$	$-0.06^{+0.82}_{-0.53}$	$162.7^{+97.5}_{-80.3}$	$13.67^{+16.67}_{-10.46}$	$147.0^{+118.6}_{-72.3}$	$0.94^{+0.04}_{-0.39}$
GW200129_065458	$-0.01^{+0.06}_{-0.07}$	$0.18^{+0.42}_{-0.29}$	$259.4^{+30.0}_{-23.0}$	$5.30^{+1.97}_{-1.35}$	$76.5^{+11.0}_{-10.9}$	$0.85^{+0.08}_{-0.19}$
GW200208_130117	$0.25^{+1.65}_{-0.35}$	$-0.07^{+1.10}_{-0.43}$	$215.0^{+131.8}_{-56.9}$	$5.06^{+10.90}_{-2.33}$	$80.9^{+32.8}_{-25.6}$	$0.76^{+0.23}_{-0.56}$
GW200224_222234	$0.01^{+0.15}_{-0.11}$	$0.22^{+0.46}_{-0.33}$	$206.2^{+25.4}_{-18.4}$	$7.07^{+2.76}_{-1.94}$	$98.9^{+13.0}_{-15.2}$	$0.87^{+0.08}_{-0.17}$
GW200311_115853	$0.01^{+0.15}_{-0.07}$	$0.29^{+1.57}_{-0.54}$	$256.2^{+32.3}_{-24.3}$	$5.99^{+6.78}_{-2.55}$	$81.6^{+21.9}_{-21.4}$	$0.88^{+0.09}_{-0.35}$

Table 4.3: The median and symmetric 90% credible intervals of the one-dimensional marginalized posteriors of the fractional deviations in the frequency and damping time of the $(2,2,0)$ QNM, $(\delta f_{220}, \delta\tau_{220})$, and of the remnant properties. The third and fourth columns list the frequency and damping time of the $(2,2,0)$ QNM, as measured using the `pSEOBNRv5PHM` model. The last two columns report the mass and spin of the remnant object, estimated from the complex QNM frequencies by inverting the fitting formula provided in Ref. [417].

with Ref. [251], indicating that the difference arises solely from the inclusion of spin precession. Overall, the pSEOBNRv5PHM model provides a significantly better fit to the data compared to pSEOBNRv4HM, with a natural log Bayes factor of $\ln \mathcal{B} \simeq 5.1$, favoring a spin-precessing quasicircular hypothesis over an aligned-spin quasicircular one. Under the assumption of a spin-precessing quasicircular binary, the impact of waveform systematics for this event remains non-negligible. A notable feature absent in pSEOBNRv5PHM is the inclusion of multipole asymmetries in the co-precessing frame, which are important for capturing evidence of spin precession in this event [735].

Overall, the pSEOBNRv5PHM and pSEOBNRv4HM models produce qualitatively consistent results across all events. For several events, the pSEOBNRv5PHM model achieves tighter constraints on δf_{220}. Results for $\delta\tau_{220}$ are also largely consistent, but a tail toward large $\delta\tau_{220}$ values is seen for GW200129_065458, as previously noted, and is even more pronounced for GW200311_115853. For GW200311_115853, this tail is again driven by a different recovery of the binary's distance and inclination angle when spin precession is included in the analysis, while using pSEOBNRv5HM under the aligned-spin assumption gives results consistent with Ref. [251]. The posteriors for the distance and inclination recovered using pSEOBNRv5HM are also in agreement with those obtained using SEOBNRv5PHM assuming GR. The maximum likelihood point recovered by pSEOBNRv5PHM corresponds to a positive $\delta\tau_{220}$, indicating a genuine correlation that provides a good fit to the data. This is confirmed not to be a sampling issue, as additional runs with more stringent sampler settings (nlive = 2000, maxmcmc = 10000) yield consistent results. Furthermore, the natural log Bayes factor of $\ln \mathcal{B} \simeq 1.7$ favors pSEOBNRv5PHM under the spin-precessing hypothesis over the aligned-spin scenario.

The combined bounds on the fractional deviations in the frequency and damping time of the $(2, 2, 0)$ QNM using the pSEOBNRv5PHM model read

$$\delta f_{220} = 0.01^{+0.04}_{-0.04} \quad \text{and} \quad \delta\tau_{220} = 0.17^{+0.14}_{-0.13}, \tag{4.40}$$

by multiplying the posteriors and

$$\begin{aligned} \delta f_{220} &= 0.00^{+0.06}_{-0.06} \quad \left[\mu = 0.00^{+0.03}_{-0.03},\ \sigma < 0.05\right] \\ \delta\tau_{220} &= 0.15^{+0.26}_{-0.24} \quad \left[\mu = 0.15^{+0.15}_{-0.15},\ \sigma < 0.22\right] \end{aligned} \tag{4.41}$$

by combining hierarchically. The numbers in the square brackets are the hyperparameter estimates. These results are broadly consistent with those reported by the LVK Collaboration from the analysis of the same 10 GW events from GWTC-3 [251], which used the pSEOBNRv4HM model without accounting for spin-precession effects.

In Fig. 4.15, we compare the combined constraints on δf_{220} and $\delta\tau_{220}$ derived from GWTC-3 events, using the pSEOBNRv5PHM model (dark, unfilled curves) and

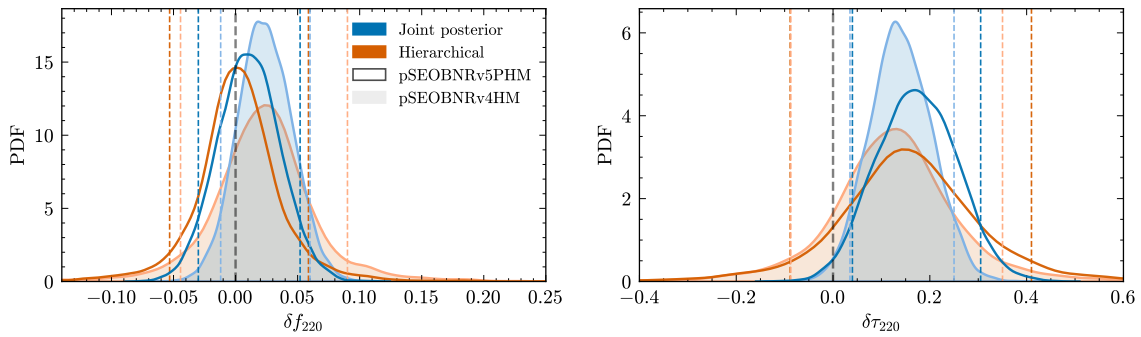

Figure 4.15: The one-dimensional combined constraints on δf_{220} and $\delta\tau_{220}$, obtained by multiplying the posteriors from individual events (in blue), and using hierarchical combination (in orange), from GWTC-3 events. We compare results using the `pSEOBNRv5PHM` model (dark, unfilled curves) and the `pSEOBNRv4HM` model (light, filled curves). Vertical dashed lines represent the 90% credible intervals.

the `pSEOBNRv4HM` model (light, filled curves). Results obtained by multiplying the posteriors from individual events are shown in blue, while constraints using hierarchical combination are shown in orange. The vertical dashed lines indicate the 90% credible intervals, and the GR predictions $(\delta f_{220}, \delta\tau_{220}) = (0, 0)$ are marked by gray dashed lines.

The updated analysis using `pSEOBNRv5PHM` yields slightly tighter constraints on δf_{220} compared to previous results, particularly when combining events hierarchically. This improvement is consistent with narrower posteriors obtained for several single-event results. Additionally, the peak of the posterior for δf_{220} is closer to zero in both the joint and hierarchically combined analyses. For $\delta\tau_{220}$, both the joint and hierarchically combined posteriors are broader and slightly shifted towards positive values. This is consistent with the presence of tails in single-event posteriors for specific events such as GW200311_115853 and GW200129_065458.

Similar to the results from GWTC-3, the joint posterior distribution for $\delta\tau_{220}$ places the GR prediction near the edge of the 90% credible level. This discrepancy could arise from a variety of factors, including noise fluctuations [250, 368], parameter correlations [251], or intrinsic variance due to the limited number of events in the catalog [736]. Incorporating additional events from ongoing observing runs may help clarify this tension. To further explore the potential influence of waveform systematics or noise fluctuations on the inferred deviation parameters, it would be important to perform large-scale injection studies using NR or NR surrogate waveforms, along with incorporating Gaussian noise realizations or real-noise injections. These effects should be thoroughly investigated and quantified in order to be able to claim a GR violation in GW observations [444].

To quantify consistency with GR, we also compute the GR quantile of a two-dimensional posterior distribution $p(x, y)$ defined as:

$$Q_0 = \int_{\substack{\{x,y\} \text{ where} \\ p(x,y) \geq p(0,0)}} p(x, y)\, dx\, dy. \tag{4.42}$$

The GR quantile corresponds to the fraction of the posterior enclosed by the isoprobability contour that passes through the GR value $(0, 0)$ [593], and is defined such that $Q_0 = 0$ ($Q_0 = 1$) indicates full consistency (full inconsistency) with the null hypothesis. For the joint posteriors, we consider $\{x, y\} = \{\delta f_{220}, \delta\tau_{220}\}$, while for the hierarchically results we have $\{x, y\} = \{\mu, \sigma^2\}$. Using the `pSEOBNRv5PHM` model, we find $Q_0 = 0.93$ when multiplying the posteriors, while the hierarchical combination yields $Q_0 = 0.003$ for δf_{220} and $Q_0 = 0.74$ for $\delta\tau_{220}$. For the `pSEOBNRv4HM` model, the GR quantile when multiplying the posteriors is $Q_0 = 0.97$, whereas the hierarchical combination gives $Q_0 = 0.32$ for δf_{220} and $Q_0 = 0.81$ for $\delta\tau_{220}$. Overall, the `pSEOBNRv5PHM` model shows slightly better consistency with GR in all cases.

The `pSEOBNRv5PHM` model can also be used to estimate the properties of the remnant BH. We compute effective values for the QNM frequency and damping time as follows:

$$f_{\ell m 0} = f^{\rm GR}_{\ell m 0}\,(1 + \delta f_{\ell m 0})\,, \tag{4.43a}$$

$$\tau_{\ell m 0} = \tau^{\rm GR}_{\ell m 0}\,(1 + \delta\tau_{\ell m 0})\,, \tag{4.43b}$$

where $f^{\rm GR}_{\ell m 0}$ and $\tau^{\rm GR}_{\ell m 0}$ are derived as functions of the component masses and spins using NR fits. The mass and spin of the remnant object can then be estimated from the complex QNM frequencies by inverting the fitting formula provided in Ref. [417]. These results are summarized in Table 4.3.

5 Conclusions

This thesis presented the development of accurate and efficient models for the gravitational radiation emitted by coalescing compact binaries, with a focus on advancing the SEOBNR family of waveform models. In Chapter 2, we detailed the development of improved gravitational waveform models for BBH mergers, SEOBNRv5HM and SEOBNR-PM, and the supporting pySEOBNR infrastructure. Chapter 3 focused on the application of these waveform models to the PE of GW signals from BBH mergers and introduced a novel probabilistic approach that marginalizes over waveform uncertainties arising from NR calibration. Chapter 4 presented extensions of the SEOBNRv5 models to explore potential deviations from GR. In the theory-specific direction, we constructed IMR waveforms in ESGB gravity, an extension of GR predicting distinctive signatures in BH coalescences. In the theory-agnostic direction, we extend the parametrized pSEOBNR framework to the spin-precessing binaries, focusing on BH spectroscopy tests.

The variety of models introduced in this thesis, as well as those presented in other publications, highlights the flexibility and the modularity of the pySEOBNR code infrastructure presented in Sec. 2.1. The rapid and diverse developments achieved in recent years underscore the successful realization of pySEOBNR's primary goal: facilitating the development of future SEOBNR waveform models.

Central to this thesis is the SEOBNRv5HM model presented in Sec.2.2, which offers improved accuracy and computational efficiency compared to previous generations. This model has become the cornerstone of the SEOBNRv5 waveform family, serving as a foundation for several extensions addressing more complex physical scenarios, including spin-precessing BBHs in quasi-circular orbits (SEOBNRv5PHM) [139, 479], aligned-spin eccentric BBHs (SEOBNRv5EHM) [345], aligned-spin BNSs in quasi-circular orbits (SEOBNRv5THM and SEOBNRv5_ROM_NRTidalv3) [356,509], as well as parametrized models for tests of GR (pSEOBNRv5PHM) [6], and an extension to ESGB gravity (SEOBNRv5PHM_ESGB) [4].

The SEOBNRv5HM model described in this thesis, along with its subsequent generalizations, has already seen widespread application by the LVK Collaboration during its fourth observing run, including use in matched-filter searches, PE, and tests of GR. I have actively contributed to several of these analyses, applying and validating the

models on real GW data. Beyond current detectors, the models are also being used in studies targeting next-generation observatories and have been adopted within the LISA Distributed Data Processing Center in preparation for the upcoming LISA Data Challenge (`Mojito`).

Upcoming work in the `SEOBNRv5` family will naturally revolve around incorporating additional physical effects. Short-term developments will particularly target eccentric spin-precessing BBHs, likely employing variations of the twisting-up technique. Due to degeneracies between eccentricity and spin precession, especially in short-duration signals [737, 738], a robust eccentric, spin-precessing IMR waveform model would be crucial for robustly interpreting some GW signals detected to date that show signs of eccentricity [448, 449, 739–742]. Additional development efforts should focus on binaries containing NSs, including modeling quasi-circular spin-precessing and eccentric aligned-spin BNS systems, as well as extending the models to NSBH binaries.

In addition to incorporating further physical effects, improving the accuracy of waveform models against NR simulations will be crucial. As shown in Sec. 2.2.4, the current accuracy of the `SEOBNRv5HM` model is roughly an order of magnitude above NR errors. This issue is even more pronounced for its spin-precessing counterpart, `SEOBNRv5PHM`, which currently lacks detailed NR calibration. The accuracy of current models will not be sufficient for analyzing signals from future LVK observing runs and next-generation detectors.

Results from Sec. 2.2.4 highlight that a primary accuracy limitation for aligned-spin models lies in modeling higher-order modes during the merger-ringdown phase. Addressing this will require the development of improved merger-ringdown ansätze specifically suited to higher modes, as well as alternatives to the current NQC corrections. A successful calibration relies critically on accurate analytic information as a starting point. Therefore, incorporating additional PN corrections – all terms up to 3.5PN into the waveform modes and RR force [497, 537], the recently derived 4PN terms in the dominant (2,2) mode [196, 197], and higher-order test-particle information [743, 744] – will be essential for achieving a reliable NR calibration. Including additional waveform modes, particularly the $m = 0$ modes which also feature null memory contributions [745], is also important [746].

Extending the calibration pipeline presented in this thesis to calibrate `SEOBNRv5PHM` to spin-precessing NR simulations and `SEOBNRv5EHM` to eccentric NR data will further improve their accuracy. Exploring more efficient calibration strategies, potentially leveraging modern computational tools such as machine learning [747] and automatic differentiation [748, 749], is also promising. Eventually, as NR surrogate models expand their coverage of the parameter space, it may become beneficial to hybridize EOB waveforms with NR surrogate models. However, further development of hybridization

techniques for spin-precessing and eccentric binaries is still required [263, 750, 751].

Leveraging recent progress from the PM and GSF approximations also represents an exciting frontier for waveform modeling. Notably, progress in PM theory has opened a promising direction for waveform development. The `SEOBNR-PM` model introduced in Sec. 2.3 marks the first astrophysically relevant implementation of these PM advancements. However, significant work remains to be done to reach fully mature PM-based waveform models. To further improve accuracy, it will be essential to resum PM potentials and introduce additional calibration parameters into the EOB Hamiltonian, similarly to the strategy adopted in the `SEOBNRv5` model. Preliminary studies suggest that alternative resummation techniques, tailored to the structure of the PM potentials, may be necessary to match the precision of PN-based models. Ultimately, a primary motivation for developing `SEOBNR-PM` lies in its potential application to highly eccentric binaries. This extension could build on the eccentric waveform and RR force from the `SEOBNRv5EHM` model to construct a PM-informed eccentric, aligned-spin model. Moreover, PM corrections could also be fed into the EOB RR forces and gravitational modes; this would be important for highly eccentric systems, where PN-based fluxes are expected to be inadequate.

In parallel, strategies for mitigating waveform systematics by marginalizing over waveform uncertainties should be further developed. In Sec. 3.3, we presented initial work in this direction. While the results are promising, further refinement is necessary before these methods can be employed in production-level analyses, including extending the framework to spin-precessing binaries and identifying optimal parametrizations for encoding waveform uncertainties. Additionally, it would be valuable to explore how this methodology could be adapted to tests of GR. For instance, it would be interesting to investigate whether such techniques can mitigate false deviations from GR in the analysis of massive BH binary signals detected by LISA. These systems, due to their high SNR ratio – often dominated by the merger-ringdown phase – are especially sensitive to waveform systematics [418].

In Sec. 4.2, we presented `SEOBNRv5PHM_ESGB`, an extension of `SEOBNRv5PHM` to ESGB gravity. A key assumption in this waveform model is that ESGB effects are small deformations of the GR-EOB potentials, fluxes, and waveform modes, such that the EOB resummation of PN-ESGB results in the strong-field regime follows the same strategy as in GR. Comparisons with NR simulations in ESGB gravity will test the validity of this assumption and inform alternative resummation approaches. Our study focused on BHs that have already scalarized; however, ESGB gravity also allows for dynamical scalarization [626, 698–701]. We plan to extend `SEOBNRv5PHM_ESGB` to include these nonperturbative effects, which can significantly affect the waveforms near merger, producing distinctive signatures that are absent in GR. Another extension of

our model would involve describing waveforms for BNSs and NSBHs in both ST and ESGB theories. The EOB Hamiltonian, modes, and fluxes implemented in `pySEOBNR` can be already applied to BNSs and NSBHs in any ESGB or ST theory, and the only additional input that would be required is the specification of the body-dependent sensitivities (4.9). On the data-analysis side, the simple forecast we presented in Sec. 4.2.4 can be refined by analyzing synthetic injections with Bayesian inference. It will be valuable to analyze both the projected constraints assuming GR is correct, and the ability to distinguish realistic deviations from GR, properly accounting for parameter degeneracies. In this context, our model can also serve as a useful tool to validate results from parametrized tests of GR and to test their effectiveness in different regimes.

In Sec. 4.3, we presented `pSEOBNRv5PHM`, an extension of the `pSEOBNR` framework to spin-precessing binaries. In that section, we validated our model through Bayesian PE for the ringdown of the dominant $(\ell, m, n) = (2, 2, 0)$ mode, as it is the primary test currently performed in LVK analyses. At current SNR, higher modes in the ringdown are not detectable with high statistical significance, but are expected to become confidently detectable with the improved SNR achievable through upcoming LVK upgrades [367, 681]. In future work, we plan to explore higher modes in the ringdown, as well as the measurability of deviations in the inspiral and plunge-merger stages.

Besides waveform accuracy, computational efficiency remains a critical limitation for GW data analysis, particularly in preparation for next-generation ground-based detectors and the LISA mission. One of the primary computational costs for time-domain models stems from the need to interpolate waveforms onto a constant time grid to perform FFTs and convert them to the frequency domain. Exploring techniques to mitigate this bottleneck, such as improved interpolation schemes, non-uniform FFTs, or time-frequency parametrizations [752, 753], could offer significant performance gains. GPU acceleration is another promising avenue, as demonstrated in the case of extreme mass ratio inspiral waveforms, which are typically long and complex but can be generated efficiently using hardware acceleration [754,755]. Further work is also needed to develop more efficient ROMs and surrogates for spin-precessing and eccentric systems. Machine learning-based surrogates offer additional benefits, including simplifying GPU deployment and the potential for automatic waveform differentiation [457]. In parallel, advances in PE methods – such as gradient-based samplers and neural posterior estimation frameworks – can further complement waveform acceleration strategies. Addressing these challenges is a key future direction for the continued development of the `pySEOBNR` infrastructure, which provides the ideal platform for implementing and testing such computational improvements.

As we enter an exciting era of high-precision GW astronomy – driven by next-generation ground-based detectors and the upcoming LISA mission – waveform models will play an increasingly central role in enabling precision astrophysics and fundamental tests of gravity. We hope that the results and tools presented in this thesis will contribute meaningfully to the continued development of waveform models and data analysis techniques, and support the broader community in meeting the challenges and embracing the opportunities of this bright new era in GW astronomy.

Acknowledgements

First and foremost, I would like to express my deepest gratitude to my supervisor, Alessandra Buonanno, for her continuous guidance and support throughout my PhD. Her confidence in me and the many opportunities she provided were instrumental to my growth as a researcher. She leads by example in her dedication to science, showing the importance of commitment, initiative, and active engagement in the research community. From her, I learned to think broadly and long-term about the questions we work on, and to value clarity, precision, and rigor in both thought and writing.

I am sincerely thankful to all members of the AEI. Doing my PhD here has played a huge role in shaping my research, and I feel truly lucky to have been part of such a stimulating and supportive community. I would like to especially thank Aldo Gamboa, Alex Toubiana, Arnab Dhani, Deyan Mihaylov, Elisa Maggio, Elise Sänger, Félix Julié, Gustav Mogull, Harald Pfieffer, Héctor Estellés, Hector Silva, Jonathan Gair, Maarten van de Meent, Michael Pürrer, Mohammed Khalil, P.J. Nee, Raj Patil, Raffi Enficiaud, Sebastian Völkel, and Toni Ramos-Buades, whose collaboration, stimulating conversations, and continued support were essential to the research presented in this thesis. A special thanks goes to Serguei Ossokine for his kindness and dedication as a mentor during the first half of my PhD. I owe much of my understanding of waveform modeling, coding, and data analysis to him. I would like to thank all fellow AEI PhD students for the many discussions, moka coffee breaks, and good company over the years – it was always fun to come to the office. My work has benefited from many interactions with members of the LVK Collaboration. I am grateful for the many discussions during regular calls and in-person meetings, it's been a privilege to exchange ideas with so many brilliant scientists. I also wish to thank Sascha Husa and Geraint Pratten for kindly agreeing to serve on my committee and review this thesis.

I am very grateful to my friends in Italy, especially Matteo, Alessio, Giorgia, Giulio P., and Giulio C., who stayed close no matter the distance. A special thanks to Andrea, Robert, Danny, Sarta, and Stiopa for encouraging my music and finding ways to keep it out in the world.

Finally, I am eternally grateful to my family for their unwavering support, love, and belief in me. Your presence, advice, and example have been invaluable.

Computing acknowledgements

The computational work for this research was carried out on the `Hypatia` computer cluster at the Max Planck Institute for Gravitational Physics. The material presented in this work is based upon work supported by National Science Foundation's (NSF) LIGO Laboratory, which is a major facility fully funded by the NSF. This research has made use of data or software obtained from the Gravitational Wave Open Science Center (gwosc.org), a service of LIGO Laboratory, the LIGO Scientific Collaboration, the Virgo Collaboration, and KAGRA. LIGO Laboratory and Advanced LIGO are funded by the United States National Science Foundation (NSF) as well as the Science and Technology Facilities Council (STFC) of the United Kingdom, the Max-Planck-Society (MPS), and the State of Niedersachsen/Germany for support of the construction of Advanced LIGO and construction and operation of the GEO600 detector. Additional support for Advanced LIGO was provided by the Australian Research Council. Virgo is funded, through the European Gravitational Observatory (EGO), by the French Centre National de Recherche Scientifique (CNRS), the Italian Istituto Nazionale di Fisica Nucleare (INFN) and the Dutch Nikhef, with contributions by institutions from Belgium, Germany, Greece, Hungary, Ireland, Japan, Monaco, Poland, Portugal, Spain. KAGRA is supported by Ministry of Education, Culture, Sports, Science and Technology (MEXT), Japan Society for the Promotion of Science (JSPS) in Japan; National Research Foundation (NRF) and Ministry of Science and ICT (MSIT) in Korea; Academia Sinica (AS) and National Science and Technology Council (NSTC) in Taiwan.

Bibliography

[1] Mihaylov D P, Ossokine S, Buonanno A, Estelles H, Pompili L, Pürrer M and Ramos-Buades A 2025 *SoftwareX* **30** 102080 [arXiv:2303.18203]

[2] Pompili L *et al.* 2023 *Phys. Rev. D* **108** 124035 [arXiv:2303.18039]

[3] Buonanno A, Mogull G, Patil R and Pompili L 2024 *Phys. Rev. Lett.* **133** 211402 [arXiv:2405.19181]

[4] Julié F L, Pompili L and Buonanno A 2025 *Phys. Rev. D* **111** 024016 [arXiv:2406.13654]

[5] Pompili L, Buonanno A and Pürrer M 2025 *Phys. Rev. D* **112** 044062 [arXiv:2410.16859]

[6] Pompili L, Maggio E, Silva H O and Buonanno A 2025 *Phys. Rev. D* **111** 124040 [arXiv:2504.10130]

[7] Racine E 2008 *Phys. Rev. D* **78** 044021 [arXiv:0803.1820]

[8] Santamaria L *et al.* 2010 *Phys. Rev. D* **82** 064016 [arXiv:1005.3306]

[9] Schmidt P, Ohme F and Hannam M 2015 *Phys. Rev. D* **91** 024043 [arXiv:1408.1810]

[10] Einstein A 1915 *Sitzungsber. Preuss. Akad. Wiss. Berlin (Math. Phys.)* **1915** 778–786 [Addendum: Sitzungsber.Preuss.Akad.Wiss.Berlin (Math.Phys.) 1915, 799–801 (1915)]

[11] Einstein A 1915 *Sitzungsber. Preuss. Akad. Wiss. Berlin (Math. Phys.)* **1915** 844–847

[12] Wheeler J A and Ford K 1998 *Geons, black holes, and quantum foam: A life in physics*

[13] Dyson F W, Eddington A S and Davidson C 1920 *Phil. Trans. Roy. Soc. Lond. A* **220** 291–333

[14] Einstein A 1915 *Sitzungsber. Preuss. Akad. Wiss. Berlin (Math. Phys.)* **1915** 831–839

[15] Will C M 2014 *Living Rev. Rel.* **17** 4 [arXiv:1403.7377]

[16] Michell J 1784 *Phil. Trans. Roy. Soc. Lond.* **74** 35–57

[17] Schwarzschild K 1916 *Sitzungsber. Preuss. Akad. Wiss. Berlin (Math. Phys.)* **1916** 189–196 [arXiv:physics/9905030]

[18] Reissner H 1916 *Annalen Phys.* **355** 106–120

[19] Nordström G 1918 *Koninklijke Nederlandse Akademie van Wetenschappen Proceedings Series B Physical Sciences* **20** 1238–1245

[20] Kerr R P 1963 *Phys. Rev. Lett.* **11** 237–238

[21] Newman E T, Couch R, Chinnapared K, Exton A, Prakash A and Torrence R 1965 *J. Math. Phys.* **6** 918–919

[22] Israel W 1967 *Phys. Rev.* **164** 1776–1779

[23] Hawking S W 1972 *Commun. Math. Phys.* **25** 152–166

[24] Carter B 1971 *Phys. Rev. Lett.* **26** 331–333

[25] Robinson D C 1975 *Phys. Rev. Lett.* **34** 905–906

[26] Mignemi S and Stewart N R 1993 *Phys. Rev. D* **47** 5259–5269 [arXiv:hep-th/9212146]

[27] Kanti P, Mavromatos N E, Rizos J, Tamvakis K and Winstanley E 1996 *Phys. Rev. D* **54** 5049–5058 [arXiv:hep-th/9511071]

[28] Torii T, Yajima H and Maeda K i 1997 *Phys. Rev. D* **55** 739–753 [arXiv:gr-qc/9606034]

[29] Yunes N and Stein L C 2011 *Phys. Rev. D* **83** 104002 [arXiv:1101.2921]

[30] Sotiriou T P and Zhou S Y 2014 *Phys. Rev. Lett.* **112** 251102 [arXiv:1312.3622]

[31] Sotiriou T P and Zhou S Y 2014 *Phys. Rev. D* **90** 124063 [arXiv:1408.1698]

[32] Herdeiro C A R and Radu E 2014 *Phys. Rev. Lett.* **112** 221101 [arXiv:1403.2757]

[33] Pani P and Cardoso V 2009 *Phys. Rev. D* **79** 084031 [arXiv:0902.1569]

[34] Pani P, Macedo C F B, Crispino L C B and Cardoso V 2011 *Phys. Rev. D* **84** 087501 [arXiv:1109.3996]

[35] Ayzenberg D and Yunes N 2014 *Phys. Rev. D* **90** 044066 [Erratum: Phys.Rev.D 91, 069905 (2015)] [arXiv:1405.2133]

[36] Maselli A, Pani P, Gualtieri L and Ferrari V 2015 *Phys. Rev. D* **92** 083014 [arXiv:1507.00680]

[37] Kleihaus B, Kunz J, Mojica S and Radu E 2016 *Phys. Rev. D* **93** 044047 [arXiv:1511.05513]

[38] Antoniou G, Bakopoulos A and Kanti P 2018 *Phys. Rev. Lett.* **120** 131102 [arXiv:1711.03390]

[39] Cunha P V P, Herdeiro C A R and Radu E 2019 *Phys. Rev. Lett.* **123** 011101 [arXiv:1904.09997]

[40] Julié F L and Berti E 2019 *Phys. Rev. D* **100** 104061 [arXiv:1909.05258]

[41] Julié F L, Silva H O, Berti E and Yunes N 2022 *Phys. Rev. D* **105** 124031 [arXiv:2202.01329]

[42] Bolton C T 1972 *Nature* **235** 271–273 URL `https://api.semanticscholar.org/CorpusID:4222070`

[43] Webster B L and Murdin P 1972 *Nature* **235** 37–38

[44] Remillard R A and McClintock J E 2006 *Ann. Rev. Astron. Astrophys.* **44** 49–92 [arXiv:astro-ph/0606352]

[45] Abbott B P *et al.* (LIGO Scientific, Virgo) 2016 *Phys. Rev. Lett.* **116** 061102 [arXiv:1602.03837]

[46] Abbott B P *et al.* (LIGO Scientific, Virgo) 2019 *Phys. Rev. X* **9** 031040 [arXiv:1811.12907]

[47] Abbott R *et al.* (LIGO Scientific, Virgo) 2021 *Phys. Rev. X* **11** 021053 [arXiv:2010.14527]

[48] Abbott R *et al.* (LIGO Scientific, VIRGO) 2024 *Phys. Rev. D* **109** 022001 [arXiv:2108.01045]

[49] Abbott R *et al.* (KAGRA, VIRGO, LIGO Scientific) 2023 *Phys. Rev. X* **13** 041039 [arXiv:2111.03606]

[50] Miller M C and Colbert E J M 2004 *Int. J. Mod. Phys. D* **13** 1–64 [arXiv:astro-ph/0308402]

[51] Mezcua M 2017 *International Journal of Modern Physics D* **26** 1730021 ISSN 1793-6594 URL http://dx.doi.org/10.1142/S021827181730021X

[52] Schodel R *et al.* 2002 *Nature* **419** 694–696 [arXiv:astro-ph/0210426]

[53] Ghez A M, Salim S, Hornstein S D, Tanner A, Morris M, Becklin E E and Duchene G 2005 *Astrophys. J.* **620** 744–757 [arXiv:astro-ph/0306130]

[54] Gillessen S, Eisenhauer F, Trippe S, Alexander T, Genzel R, Martins F and Ott T 2009 *Astrophys. J.* **692** 1075–1109 [arXiv:0810.4674]

[55] Ghez A M *et al.* 2008 *Astrophys. J.* **689** 1044–1062 [arXiv:0808.2870]

[56] Akiyama K *et al.* (Event Horizon Telescope) 2019 *Astrophys. J. Lett.* **875** L1 [arXiv:1906.11238]

[57] Akiyama K *et al.* (Event Horizon Telescope) 2022 *Astrophys. J. Lett.* **930** L12 [arXiv:2311.08680]

[58] Oppenheimer J R and Snyder H 1939 *Phys. Rev.* **56** 455–459

[59] Penrose R 1969 *Riv. Nuovo Cim.* **1** 252–276

[60] Woosley S E, Heger A and Weaver T A 2002 *Rev. Mod. Phys.* **74** 1015–1071

[61] Volonteri M 2010 *Astron. Astrophys. Rev.* **18** 279–315 [arXiv:1003.4404]

[62] Inayoshi K, Visbal E and Haiman Z 2020 *Ann. Rev. Astron. Astrophys.* **58** 27–97 [arXiv:1911.05791]

[63] Zel'dovich Y B and Novikov I D 1967 *Sov. Astron.* **10** 602

[64] Hawking S 1971 *Mon. Not. Roy. Astron. Soc.* **152** 75

[65] Carr B J 1975 *Astrophys. J.* **201** 1–19

[66] Carr B, Kuhnel F and Sandstad M 2016 *Phys. Rev. D* **94** 083504 [arXiv:1607.06077]

[67] Bennett D P *et al.* 2002 *Astrophys. J.* **579** 639–659 [arXiv:astro-ph/0109467]

[68] Nitz A H, Kumar S, Wang Y F, Kastha S, Wu S, Schäfer M, Dhurkunde R and Capano C D 2023 *Astrophys. J.* **946** 59 [arXiv:2112.06878]

[69] Olsen S, Venumadhav T, Mushkin J, Roulet J, Zackay B and Zaldarriaga M 2022 *Phys. Rev. D* **106** 043009 [arXiv:2201.02252]

[70] Mehta A K, Olsen S, Wadekar D, Roulet J, Venumadhav T, Mushkin J, Zackay B and Zaldarriaga M 2023 [arXiv:2311.06061]

[71] Wadekar D, Roulet J, Venumadhav T, Mehta A K, Zackay B, Mushkin J, Olsen S and Zaldarriaga M 2023 [arXiv:2312.06631]

[72] Aasi J *et al.* (LIGO Scientific) 2015 *Class. Quant. Grav.* **32** 074001 [arXiv:1411.4547]

[73] Acernese F *et al.* (VIRGO) 2015 *Class. Quant. Grav.* **32** 024001 [arXiv:1408.3978]

[74] Abbott R *et al.* (KAGRA, VIRGO, LIGO Scientific) 2023 *Phys. Rev. X* **13** 011048 [arXiv:2111.03634]

[75] Barkat Z, Rakavy G and Sack N 1967 *Phys. Rev. Lett.* **18** 379–381

[76] Belczynski K *et al.* 2016 *Astron. Astrophys.* **594** A97 [arXiv:1607.03116]

[77] https://media.ligo.northwestern.edu/gallery/mass-plot/ accessed: 2025-03-10

[78] Bethe H A and Brown G E 1998 *Astrophys. J.* **506** 780–789 [arXiv:astro-ph/9802084]

[79] Belczynski K, Kalogera V and Bulik T 2002 *The Astrophysical Journal* **572** 407 URL https://dx.doi.org/10.1086/340304

[80] Dominik M, Belczynski K, Fryer C, Holz D, Berti E, Bulik T, Mandel I and O'Shaughnessy R 2012 *Astrophys. J.* **759** 52 [arXiv:1202.4901]

[81] Belczynski K, Holz D E, Bulik T and O'Shaughnessy R 2016 *Nature* **534** 512 [arXiv:1602.04531]

[82] Stevenson S, Vigna-Gómez A, Mandel I, Barrett J W, Neijssel C J, Perkins D and de Mink S E 2017 *Nature Commun.* **8** 14906 [arXiv:1704.01352]

[83] Portegies Zwart S F and McMillan S 2000 *Astrophys. J. Lett.* **528** L17 [arXiv:astro-ph/9910061]

[84] O'Leary R M, Rasio F A, Fregeau J M, Ivanova N and O'Shaughnessy R W 2006 *Astrophys. J.* **637** 937–951 [arXiv:astro-ph/0508224]

[85] Rodriguez C L, Morscher M, Pattabiraman B, Chatterjee S, Haster C J and Rasio F A 2015 *Phys. Rev. Lett.* **115** 051101 [Erratum: Phys.Rev.Lett. 116, 029901 (2016)] [arXiv:1505.00792]

[86] Antonini F and Rasio F A 2016 *Astrophys. J.* **831** 187 [arXiv:1606.04889]

[87] Samsing J 2018 *Phys. Rev. D* **97** 103014 [arXiv:1711.07452]

[88] Farr W M, Gair J R, Mandel I and Cutler C 2015 *Phys. Rev. D* **91** 023005 [arXiv:1302.5341]

[89] Stevenson S, Ohme F and Fairhurst S 2015 *Astrophys. J.* **810** 58 [arXiv:1504.07802]

[90] Rodriguez C L, Zevin M, Pankow C, Kalogera V and Rasio F A 2016 *Astrophys. J. Lett.* **832** L2 [arXiv:1609.05916]

[91] Gerosa D and Berti E 2017 *Phys. Rev. D* **95** 124046 [arXiv:1703.06223]

[92] Zevin M, Bavera S S, Berry C P L, Kalogera V, Fragos T, Marchant P, Rodriguez C L, Antonini F, Holz D E and Pankow C 2021 *Astrophys. J.* **910** 152 [arXiv:2011.10057]

[93] Kimball C, Talbot C, L Berry C P, Carney M, Zevin M, Thrane E and Kalogera V 2020 *Astrophys. J.* **900** 177 [arXiv:2005.00023]

[94] Einstein A 1916 *Sitzungsber. Preuss. Akad. Wiss. Berlin (Math. Phys.)* **1916** 688–696

[95] Einstein A 1918 *Sitzungsber. Preuss. Akad. Wiss. Berlin (Math. Phys.)* **1918** 154–167

[96] Kennefick D 1997 [arXiv:gr-qc/9704002]

[97] Buonanno A and Sathyaprakash B S 2014 *Sources of Gravitational Waves: Theory and Observations* [arXiv:1410.7832]

[98] Bondi H, Pirani F A E and Robinson I 1959 *Proc. Roy. Soc. Lond. A* **251** 519–533

[99] Weber J 1960 *Phys. Rev.* **117** 306–313

[100] Hulse R A and Taylor J H 1975 *Astrophys. J. Lett.* **195** L51–L53

[101] Maggiore M 2007 *Gravitational Waves. Vol. 1: Theory and Experiments* (Oxford University Press) ISBN 978-0-19-171766-6, 978-0-19-852074-0

[102] Le Tiec A and Novak J 2017 *Theory of Gravitational Waves* pp 1–41 [arXiv:1607.04202]

[103] Lasky P D 2015 *Publ. Astron. Soc. Austral.* **32** e034 [arXiv:1508.06643]

[104] Kotake K, Sato K and Takahashi K 2006 *Rept. Prog. Phys.* **69** 971–1144 [arXiv:astro-ph/0509456]

[105] Futamase T and Itoh Y 2007 *Living Rev. Rel.* **10** 2

[106] Blanchet L 2014 *Living Rev. Rel.* **17** 2 [arXiv:1310.1528]

[107] Schäfer G and Jaranowski P 2018 *Living Rev. Rel.* **21** 7 [arXiv:1805.07240]

[108] Thorne K S 1980 *Rev. Mod. Phys.* **52** 299–339

[109] Kidder L E 2008 *Phys. Rev. D* **77** 044016 [arXiv:0710.0614]

[110] Schmidt P, Harry I W and Pfeiffer H P 2017 [arXiv:1703.01076]

[111] Berti E, Cardoso V, Gonzalez J A, Sperhake U, Hannam M, Husa S and Bruegmann B 2007 *Phys. Rev. D* **76** 064034 [arXiv:gr-qc/0703053]

[112] Pan Y, Buonanno A, Boyle M, Buchman L T, Kidder L E, Pfeiffer H P and Scheel M A 2011 *Phys. Rev. D* **84** 124052 [arXiv:1106.1021]

[113] Cotesta R, Buonanno A, Bohé A, Taracchini A, Hinder I and Ossokine S 2018 *Phys. Rev. D* **98** 084028 [arXiv:1803.10701]

[114] Barausse E, Buonanno A, Hughes S A, Khanna G, O'Sullivan S and Pan Y 2012 *Phys. Rev. D* **85** 024046 [arXiv:1110.3081]

[115] Taracchini A, Buonanno A, Khanna G and Hughes S A 2014 *Phys. Rev. D* **90** 084025 [arXiv:1404.1819]

[116] Varma V, Ajith P, Husa S, Bustillo J C, Hannam M and Pürrer M 2014 *Phys. Rev. D* **90** 124004 [arXiv:1409.2349]

[117] Graff P B, Buonanno A and Sathyaprakash B S 2015 *Phys. Rev. D* **92** 022002 [arXiv:1504.04766]

[118] Usman S A, Mills J C and Fairhurst S 2019 *Astrophys. J.* **877** 82 [arXiv:1809.10727]

[119] Kalaghatgi C, Hannam M and Raymond V 2020 *Phys. Rev. D* **101** 103004 [arXiv:1909.10010]

[120] Abbott R *et al.* (LIGO Scientific, Virgo) 2020 *Phys. Rev. D* **102** 043015 [arXiv:2004.08342]

[121] Campanelli M, Lousto C O and Zlochower Y 2006 *Phys. Rev. D* **74** 041501 [arXiv:gr-qc/0604012]

[122] Apostolatos T A, Cutler C, Sussman G J and Thorne K S 1994 *Phys. Rev. D* **49** 6274–6297

[123] Kidder L E 1995 *Phys. Rev. D* **52** 821–847 [arXiv:gr-qc/9506022]

[124] Kesden M, Gerosa D, O'Shaughnessy R, Berti E and Sperhake U 2015 *Phys. Rev. Lett.* **114** 081103 [arXiv:1411.0674]

[125] Gerosa D, Kesden M, Sperhake U, Berti E and O'Shaughnessy R 2015 *Phys. Rev. D* **92** 064016 [arXiv:1506.03492]

[126] Buonanno A, Chen Y b and Vallisneri M 2003 *Phys. Rev. D* **67** 104025 [Erratum: Phys.Rev.D 74, 029904 (2006)] [arXiv:gr-qc/0211087]

[127] Schmidt P, Hannam M, Husa S and Ajith P 2011 *Phys. Rev. D* **84** 024046 [arXiv:1012.2879]

[128] Boyle M, Owen R and Pfeiffer H P 2011 *Phys. Rev. D* **84** 124011 [arXiv:1110.2965]

[129] O'Shaughnessy R, Vaishnav B, Healy J, Meeks Z and Shoemaker D 2011 *Phys. Rev. D* **84** 124002 [arXiv:1109.5224]

[130] Schmidt P, Hannam M and Husa S 2012 *Phys. Rev. D* **86** 104063 [arXiv:1207.3088]

[131] Hannam M, Schmidt P, Bohé A, Haegel L, Husa S, Ohme F, Pratten G and Pürrer M 2014 *Phys. Rev. Lett.* **113** 151101 [arXiv:1308.3271]

[132] Pan Y, Buonanno A, Taracchini A, Kidder L E, Mroué A H, Pfeiffer H P, Scheel M A and Szilágyi B 2014 *Phys. Rev. D* **89** 084006 [arXiv:1307.6232]

[133] Babak S, Taracchini A and Buonanno A 2017 *Phys. Rev. D* **95** 024010 [arXiv:1607.05661]

[134] Ossokine S *et al.* 2020 *Phys. Rev. D* **102** 044055 [arXiv:2004.09442]

[135] Varma V, Field S E, Scheel M A, Blackman J, Gerosa D, Stein L C, Kidder L E and Pfeiffer H P 2019 *Phys. Rev. Research.* **1** 033015 [arXiv:1905.09300]

[136] Estellés H, Husa S, Colleoni M, Keitel D, Mateu-Lucena M, García-Quirós C, Ramos-Buades A and Borchers A 2022 *Phys. Rev. D* **105** 084039 [arXiv:2012.11923]

[137] Pratten G *et al.* 2021 *Phys. Rev. D* **103** 104056 [arXiv:2004.06503]

[138] Gamba R, Akçay S, Bernuzzi S and Williams J 2022 *Phys. Rev. D* **106** 024020 [arXiv:2111.03675]

[139] Ramos-Buades A, Buonanno A, Estellés H, Khalil M, Mihaylov D P, Ossokine S, Pompili L and Shiferaw M 2023 *Phys. Rev. D* **108** 124037 [arXiv:2303.18046]

[140] Sturani R Note on the derivation of the angular momentum and spin precessing equations in spintaylor codes `https://dcc.ligo.org/public/0122/T1500554/023/dLdS.pdf`

[141] Bohe A, Marsat S, Faye G and Blanchet L 2013 *Class. Quant. Grav.* **30** 075017 [arXiv:1212.5520]

[142] Klein A, Cornish N and Yunes N 2013 *Phys. Rev. D* **88** 124015 [arXiv:1305.1932]

[143] Chatziioannou K, Klein A, Yunes N and Cornish N 2013 *Phys. Rev. D* **88** 063011 [arXiv:1307.4418]

[144] Khalil M, Buonanno A, Estelles H, Mihaylov D P, Ossokine S, Pompili L and Ramos-Buades A 2023 *Phys. Rev. D* **108** 124036 [arXiv:2303.18143]

[145] Arun K G, Buonanno A, Faye G and Ochsner E 2009 *Phys. Rev. D* **79** 104023 [Erratum: Phys.Rev.D 84, 049901 (2011)] [arXiv:0810.5336]

[146] Boyle M, Kidder L E, Ossokine S and Pfeiffer H P 2014 [arXiv:1409.4431]

[147] Bruegmann B, Gonzalez J A, Hannam M, Husa S and Sperhake U 2008 *Phys. Rev. D* **77** 124047 [arXiv:0707.0135]

[148] Ma S, Giesler M, Varma V, Scheel M A and Chen Y 2021 *Phys. Rev. D* **104** 084003 [arXiv:2107.04890]

[149] Mielke J, Ghosh S, Borchers A and Ohme F 2025 *Phys. Rev. D* **111** 064009 [arXiv:2412.06913]

[150] Ramos-Buades A, van de Meent M, Pfeiffer H P, Rüter H R, Scheel M A, Boyle M and Kidder L E 2022 *Phys. Rev. D* **106** 124040 [arXiv:2209.03390]

[151] Shaikh M A, Varma V, Pfeiffer H P, Ramos-Buades A and van de Meent M 2023 *Phys. Rev. D* **108** 104007 [arXiv:2302.11257]

[152] Peters P and Mathews J 1963 *Phys.Rev.* **131** 435–439

[153] Rodriguez C L, Amaro-Seoane P, Chatterjee S, Kremer K, Rasio F A, Samsing J, Ye C S and Zevin M 2018 *Phys. Rev. D* **98** 123005 [arXiv:1811.04926]

[154] Zevin M, Romero-Shaw I M, Kremer K, Thrane E and Lasky P D 2021 *Astrophys. J. Lett.* **921** L43 [arXiv:2106.09042]

[155] Dandapat S, Ebersold M, Susobhanan A, Rana P, Gopakumar A, Tiwari S, Haney M, Lee H M and Kolhe N 2023 *Phys. Rev. D* **108** 024013 [arXiv:2305.19318]

[156] Abbott B P *et al.* (LIGO Scientific, Virgo) 2020 *Class. Quant. Grav.* **37** 055002 [arXiv:1908.11170]

[157] Aasi J *et al.* (LIGO Scientific) 2013 *Nature Photon.* **7** 613–619 [arXiv:1310.0383]

[158] Ganapathy D *et al.* (LIGO O4 Detector) 2023 *Phys. Rev. X* **13** 041021

[159] Abbott B P *et al.* (LIGO Scientific) 2017 *Phys. Rev. D* **95** 062003 [arXiv:1602.03845]

[160] Sun L *et al.* 2020 *Class. Quant. Grav.* **37** 225008 [arXiv:2005.02531]

[161] Farr W, Farr B and Littenberg T 2014 Modelling calibration errors in cbc waveforms Tech. Rep. LIGO-T1400682 `https://dcc.ligo.org/LIGO-T1400682/public`

[162] Finn L S and Chernoff D F 1993 *Phys. Rev. D* **47** 2198–2219 [arXiv:gr-qc/9301003]

[163] Essick R, Vitale S and Evans M 2017 *Phys. Rev. D* **96** 084004 [arXiv:1708.06843]

[164] Allen B, Anderson W G, Brady P R, Brown D A and Creighton J D E 2012 *Phys. Rev.* **D85** 122006 [arXiv:gr-qc/0509116]

[165] Welch P 1967 *IEEE Transactions on Audio and Electroacoustics* **15** 70–73

[166] Littenberg T B and Cornish N J 2015 *Phys. Rev. D* **91** 084034 [arXiv:1410.3852]

[167] Sathyaprakash B S and Dhurandhar S V 1991 *Phys. Rev. D* **44** 3819–3834

[168] Owen B J 1996 *Phys. Rev. D* **53** 6749–6761 [arXiv:gr-qc/9511032]

[169] Owen B J and Sathyaprakash B S 1999 *Phys. Rev. D* **60** 022002 [arXiv:gr-qc/9808076]

[170] Allen B 2005 *Phys. Rev. D* **71** 062001 [arXiv:gr-qc/0405045]

[171] Klimenko S, Yakushin I, Mercer A and Mitselmakher G 2008 *Class. Quant. Grav.* **25** 114029 [arXiv:0802.3232]

[172] Cornish N J and Littenberg T B 2015 *Class. Quant. Grav.* **32** 135012 [arXiv:1410.3835]

[173] Veitch J *et al.* 2015 *Phys. Rev. D* **91** 042003 [arXiv:1409.7215]

[174] Thrane E and Talbot C 2019 *Publ. Astron. Soc. Austral.* **36** e010 [Erratum: Publ.Astron.Soc.Austral. 37, e036 (2020)] [arXiv:1809.02293]

[175] Flanagan E E and Hughes S A 1998 *Phys. Rev. D* **57** 4566–4587 [arXiv:gr-qc/9710129]

[176] Cutler C and Vallisneri M 2007 *Phys. Rev. D* **76** 104018 [arXiv:0707.2982]

[177] Foreman-Mackey D, Hogg D W, Lang D and Goodman J 2013 *Publ. Astron. Soc. Pac.* **125** 306–312 [arXiv:1202.3665]

[178] Skilling J 2006 *Bayesian Analysis* **1** 833–859

[179] Romero-Shaw I M *et al.* 2020 *Mon. Not. Roy. Astron. Soc.* **499** 3295–3319 [arXiv:2006.00714]

[180] Abbott B P *et al.* (LIGO Scientific, Virgo) 2017 *Phys. Rev. Lett.* **119** 161101 [arXiv:1710.05832]

[181] Abbott B P *et al.* (LIGO Scientific, Virgo) 2020 *Astrophys. J. Lett.* **892** L3 [arXiv:2001.01761]

[182] Abbott R *et al.* (LIGO Scientific, KAGRA, VIRGO) 2021 *Astrophys. J. Lett.* **915** L5 [arXiv:2106.15163]

[183] Abac A G *et al.* (LIGO Scientific, Virgo,, KAGRA, VIRGO) 2024 *Astrophys. J. Lett.* **970** L34 [arXiv:2404.04248]

[184] Abbott B P *et al.* (LIGO Scientific, Virgo, Fermi GBM, INTEGRAL, IceCube, AstroSat Cadmium Zinc Telluride Imager Team, IPN, Insight-Hxmt, ANTARES, Swift, AGILE Team, 1M2H Team, Dark Energy Camera GW-EM, DES, DLT40, GRAWITA, Fermi-LAT, ATCA, ASKAP, Las Cumbres Observatory Group, OzGrav, DWF (Deeper Wider Faster Program), AST3, CAASTRO, VINROUGE, MASTER, J-GEM, GROWTH, JAGWAR, CaltechNRAO, TTU-NRAO, NuSTAR, Pan-STARRS, MAXI Team, TZAC Consortium, KU, Nordic Optical Telescope, ePESSTO, GROND, Texas Tech University, SALT Group, TOROS, BOOTES, MWA, CALET, IKI-GW Follow-up, H.E.S.S., LOFAR, LWA, HAWC, Pierre Auger, ALMA, Euro VLBI Team, Pi of Sky, Chandra Team at McGill University, DFN, ATLAS Telescopes, High Time Resolution Universe Survey, RIMAS, RATIR, SKA South Africa/MeerKAT) 2017 *Astrophys. J. Lett.* **848** L12 [arXiv:1710.05833]

[185] GraceDB (gracedb.ligo.org)

[186] Price R H 1972 *Phys. Rev. D* **5** 2419–2438

[187] Price R H 1972 *Phys. Rev. D* **5** 2439–2454

[188] Damour T, Jaranowski P and Schäfer G 2014 *Phys. Rev. D* **89** 064058 [arXiv:1401.4548]

[189] Jaranowski P and Schäfer G 2015 *Phys. Rev. D* **92** 124043 [arXiv:1508.01016]

[190] Bernard L, Blanchet L, Bohé A, Faye G and Marsat S 2016 *Phys. Rev. D* **93** 084037 [arXiv:1512.02876]

[191] Bernard L, Blanchet L, Bohé A, Faye G and Marsat S 2017 *Phys. Rev.* **D95** 044026 [arXiv:1610.07934]

[192] Damour T, Jaranowski P and Schäfer G 2016 *Phys. Rev. D* **93** 084014 [arXiv:1601.01283]

[193] Bini D, Damour T and Geralico A 2019 *Phys. Rev. Lett.* **123** 231104 [arXiv:1909.02375]

[194] Bini D, Damour T and Geralico A 2020 *Phys. Rev. D* **102** 024062 [arXiv:2003.11891]

[195] Bini D, Damour T and Geralico A 2020 *Phys. Rev. D* **102** 084047 [arXiv:2007.11239]

[196] Blanchet L, Faye G, Henry Q, Larrouturou F and Trestini D 2023 *Phys. Rev. D* **108** 064041 [arXiv:2304.11186]

[197] Blanchet L, Faye G, Henry Q, Larrouturou F and Trestini D 2023 *Phys. Rev. Lett.* **131** 121402 [arXiv:2304.11185]

[198] Bertotti B 1956 *Nuovo Cim.* **4** 898–906

[199] Westpfahl K and Goller M 1979 *Lett. Nuovo Cim.* **26** 573–576

[200] Bel L, Damour T, Deruelle N, Ibanez J and Martin J 1981 *Gen. Rel. Grav.* **13** 963–1004

[201] Westpfahl K 1985 *Fortsch. Phys.* **33** 417–493

[202] Schäfer G 1986 *Gen. Rel. Grav.* **18** 255–270

[203] Buonanno A, Khalil M, O'Connell D, Roiban R, Solon M P and Zeng M 2022 Snowmass White Paper: Gravitational Waves and Scattering Amplitudes *2022 Snowmass Summer Study* [arXiv:2204.05194]

[204] Bjerrum-Bohr N E J, Damgaard P H, Plante L and Vanhove P 2022 *J. Phys. A* **55** 443014 [arXiv:2203.13024]

[205] Kosower D A, Monteiro R and O'Connell D 2022 *J. Phys. A* **55** 443015 [arXiv:2203.13025]

[206] Khalil M, Buonanno A, Steinhoff J and Vines J 2022 *Phys. Rev. D* **106** 024042 [arXiv:2204.05047]

[207] Bern Z, Parra-Martinez J, Roiban R, Ruf M S, Shen C H, Solon M P and Zeng M 2021 *Phys. Rev. Lett.* **126** 171601 [arXiv:2101.07254]

[208] Bern Z, Parra-Martinez J, Roiban R, Ruf M S, Shen C H, Solon M P and Zeng M 2022 *Phys. Rev. Lett.* **128** 161103 [arXiv:2112.10750]

[209] Damgaard P H, Hansen E R, Planté L and Vanhove P 2023 *JHEP* **09** 183 [arXiv:2307.04746]

[210] Dlapa C, Kälin G, Liu Z and Porto R A 2022 *Phys. Rev. Lett.* **128** 161104 [arXiv:2112.11296]

[211] Dlapa C, Kälin G, Liu Z and Porto R A 2023 *JHEP* **08** 109 [arXiv:2304.01275]

[212] Jakobsen G U, Mogull G, Plefka J, Sauer B and Xu Y 2023 *Phys. Rev. Lett.* **131** 151401 [arXiv:2306.01714]

[213] Jakobsen G U, Mogull G, Plefka J and Sauer B 2024 *Phys. Rev. D* **109** L041504 [arXiv:2312.00719]

[214] Driesse M, Jakobsen G U, Klemm A, Mogull G, Nega C, Plefka J, Sauer B and Usovitsch J 2024 [arXiv:2411.11846]

[215] Driesse M, Jakobsen G U, Mogull G, Plefka J, Sauer B and Usovitsch J 2024 [arXiv:2403.07781]

[216] Guevara A, Ochirov A and Vines J 2019 *JHEP* **09** 056 [arXiv:1812.06895]

[217] Bern Z, Luna A, Roiban R, Shen C H and Zeng M 2021 *Phys. Rev. D* **104** 065014 [arXiv:2005.03071]

[218] Kosmopoulos D and Luna A 2021 *JHEP* **07** 037 [arXiv:2102.10137]

[219] Chen W M, Chung M Z, Huang Y t and Kim J W 2022 *JHEP* **08** 148 [arXiv:2111.13639]

[220] Jakobsen G U and Mogull G 2022 *Phys. Rev. Lett.* **128** 141102 [arXiv:2201.07778]

[221] Jakobsen G U and Mogull G 2023 *Phys. Rev. D* **107** 044033 [arXiv:2210.06451]

[222] Febres Cordero F, Kraus M, Lin G, Ruf M S and Zeng M 2023 *Phys. Rev. Lett.* **130** 021601 [arXiv:2205.07357]

[223] Damour T, Nagar A, Placidi A and Rettegno P 2025 [arXiv:2503.05487]

[224] Mino Y, Sasaki M and Tanaka T 1997 *Phys. Rev. D* **55** 3457–3476 [arXiv:gr-qc/9606018]

[225] Quinn T C and Wald R M 1997 *Phys. Rev. D* **56** 3381–3394 [arXiv:gr-qc/9610053]

[226] Barack L, Mino Y, Nakano H, Ori A and Sasaki M 2002 *Phys. Rev. Lett.* **88** 091101 [arXiv:gr-qc/0111001]

[227] Barack L and Ori A 2003 *Phys. Rev. Lett.* **90** 111101 [arXiv:gr-qc/0212103]

[228] Gralla S E and Wald R M 2008 *Class. Quant. Grav.* **25** 205009 [Erratum: Class.Quant.Grav. 28, 159501 (2011)] [arXiv:0806.3293]

[229] Detweiler S L 2008 *Phys. Rev.* **D77** 124026 [arXiv:0804.3529]

[230] Pound A 2012 *Phys. Rev. Lett.* **109** 051101 [arXiv:1201.5089]

[231] van de Meent M 2018 *Phys. Rev. D* **97** 104033 [arXiv:1711.09607]

[232] Pound A, Wardell B, Warburton N and Miller J 2020 *Phys. Rev. Lett.* **124** 021101 [arXiv:1908.07419]

[233] Warburton N, Pound A, Wardell B, Miller J and Durkan L 2021 *Phys. Rev. Lett.* **127** 151102 [arXiv:2107.01298]

[234] Wardell B, Pound A, Warburton N, Miller J, Durkan L and Le Tiec A 2021 [arXiv:2112.12265]

[235] Antonelli A, Kavanagh C, Khalil M, Steinhoff J and Vines J 2020 *Phys. Rev. Lett.* **125** 011103 [arXiv:2003.11391]

[236] Vishveshwara C V 1970 *Nature* **227** 936–938

[237] Teukolsky S A 1973 *Astrophys. J.* **185** 635–647

[238] Chandrasekhar S and Detweiler S L 1975 *Proc. Roy. Soc. Lond. A* **344** 441–452

[239] Kokkotas K D and Schmidt B G 1999 *Living Rev. Rel.* **2** 2 [arXiv:gr-qc/9909058]

[240] Berti E, Cardoso V and Starinets A O 2009 *Class. Quant. Grav.* **26** 163001 [arXiv:0905.2975]

[241] Chandrasekhar S 1985 *The mathematical theory of black holes* ISBN 978-0-19-850370-5

[242] Regge T and Wheeler J A 1957 *Phys. Rev.* **108** 1063–1069

[243] Zerilli F J 1970 *Phys. Rev. Lett.* **24** 737–738

[244] Berti E and Klein A 2014 *Phys. Rev. D* **90** 064012 [arXiv:1408.1860]

[245] Gibbons G W 1975 *Commun. Math. Phys.* **44** 245–264

[246] Blandford R D and Znajek R L 1977 **179** 433–456

[247] Detweiler S L 1980 *Astrophys. J.* **239** 292–295

[248] Dreyer O, Kelly B J, Krishnan B, Finn L S, Garrison D and Lopez-Aleman R 2004 *Class. Quant. Grav.* **21** 787–804 [arXiv:gr-qc/0309007]

[249] Berti E *et al.* 2025 [arXiv:2505.23895]

[250] Abbott R *et al.* (LIGO Scientific, Virgo) 2021 *Phys. Rev. D* **103** 122002 [arXiv:2010.14529]

[251] Abbott R *et al.* (LIGO Scientific, VIRGO, KAGRA) 2021 [arXiv:2112.06861]

[252] Pretorius F 2005 *Phys. Rev. Lett.* **95** 121101 [arXiv:gr-qc/0507014]

[253] Campanelli M, Lousto C O, Marronetti P and Zlochower Y 2006 *Phys. Rev. Lett.* **96** 111101 [arXiv:gr-qc/0511048]

[254] Baker J G, Centrella J, Choi D I, Koppitz M and van Meter J 2006 *Phys. Rev. Lett.* **96** 111102 [arXiv:gr-qc/0511103]

[255] Jani K, Healy J, Clark J A, London L, Laguna P and Shoemaker D 2016 *Class. Quant. Grav.* **33** 204001 [arXiv:1605.03204]

[256] Boyle M *et al.* 2019 *Class. Quant. Grav.* **36** 195006 [arXiv:1904.04831]

[257] Healy J and Lousto C O 2022 *Phys. Rev. D* **105** 124010 [arXiv:2202.00018]

[258] Hamilton E *et al.* 2023 [arXiv:2303.05419]

[259] Scheel M A *et al.* 2025 [arXiv:2505.13378]

[260] Hinder I, Herrmann F, Laguna P and Shoemaker D 2010 *Phys. Rev. D* **82** 024033 [arXiv:0806.1037]

[261] Mroue A H, Pfeiffer H P, Kidder L E and Teukolsky S A 2010 *Phys. Rev. D* **82** 124016 [arXiv:1004.4697]

[262] Hinder I, Kidder L E and Pfeiffer H P 2018 *Phys. Rev. D* **98** 044015 [arXiv:1709.02007]

[263] Ramos-Buades A, Husa S, Pratten G, Estellés H, García-Quirós C, Mateu-Lucena M, Colleoni M and Jaume R 2020 *Phys. Rev. D* **101** 083015 [arXiv:1909.11011]

[264] Nee P J *et al.* 2025 [arXiv:2503.05422]

[265] Damour T, Guercilena F, Hinder I, Hopper S, Nagar A and Rezzolla L 2014 *Phys. Rev. D* **89** 081503 [arXiv:1402.7307]

[266] Damour T and Rettegno P 2022 [arXiv:2211.01399]

[267] Hopper S, Nagar A and Rettegno P 2023 *Phys. Rev. D* **107** 124034 [arXiv:2204.10299]

[268] Rettegno P, Pratten G, Thomas L M, Schmidt P and Damour T 2023 *Phys. Rev. D* **108** 124016 [arXiv:2307.06999]

[269] Swain S, Pratten G and Schmidt P 2025 *Phys. Rev. D* **111** 064048 [arXiv:2411.09652]

[270] Albanesi S, Rashti A, Zappa F, Gamba R, Cook W, Daszuta B, Bernuzzi S, Nagar A and Radice D 2025 *Phys. Rev. D* **111** 024069 [arXiv:2405.20398]

[271] Wittek N A, Barack L, Pfeiffer H P, Pound A, Deppe N, Kidder L E, Macedo A, Nelli K C, Throwe W and Vu N L 2024 [arXiv:2410.22290]

[272] Abbott B P *et al.* (LIGO Scientific, Virgo) 2016 *Phys. Rev. Lett.* **116** 241102 [arXiv:1602.03840]

[273] Blackman J, Field S E, Galley C R, Szilágyi B, Scheel M A, Tiglio M and Hemberger D A 2015 *Phys. Rev. Lett.* **115** 121102 [arXiv:1502.07758]

[274] Blackman J, Field S E, Scheel M A, Galley C R, Hemberger D A, Schmidt P and Smith R 2017 *Phys. Rev. D* **95** 104023 [arXiv:1701.00550]

[275] Blackman J, Field S E, Scheel M A, Galley C R, Ott C D, Boyle M, Kidder L E, Pfeiffer H P and Szilágyi B 2017 *Phys. Rev. D* **96** 024058 [arXiv:1705.07089]

[276] Varma V, Field S E, Scheel M A, Blackman J, Kidder L E and Pfeiffer H P 2019 *Phys. Rev. D* **99** 064045 [arXiv:1812.07865]

[277] Williams D, Heng I S, Gair J, Clark J A and Khamesra B 2020 *Phys. Rev. D* **101** 063011 [arXiv:1903.09204]

[278] Rifat N E M, Field S E, Khanna G and Varma V 2020 *Phys. Rev. D* **101** 081502 [arXiv:1910.10473]

[279] Islam T, Varma V, Lodman J, Field S E, Khanna G, Scheel M A, Pfeiffer H P, Gerosa D and Kidder L E 2021 *Phys. Rev. D* **103** 064022 [arXiv:2101.11798]

[280] Islam T, Field S E, Hughes S A, Khanna G, Varma V, Giesler M, Scheel M A, Kidder L E and Pfeiffer H P 2022 *Phys. Rev. D* **106** 104025 [arXiv:2204.01972]

[281] Yoo J, Varma V, Giesler M, Scheel M A, Haster C J, Pfeiffer H P, Kidder L E and Boyle M 2022 *Phys. Rev. D* **106** 044001 [arXiv:2203.10109]

[282] Yoo J *et al.* 2023 *Phys. Rev. D* **108** 064027 [arXiv:2306.03148]

[283] Varma V, Gerosa D, Stein L C, Hébert F and Zhang H 2019 *Phys. Rev. Lett.* **122** 011101 [arXiv:1809.09125]

[284] Magaña Zertuche L *et al.* 2024 [arXiv:2408.05300]

[285] Pacilio C, Bhagwat S, Nobili F and Gerosa D 2024 *Phys. Rev. D* **110** 103037 [arXiv:2408.05276]

[286] Nobili F, Bhagwat S, Pacilio C and Gerosa D 2025 [arXiv:2504.17021]

[287] Pan Y, Buonanno A, Baker J G, Centrella J, Kelly B J, McWilliams S T, Pretorius F and van Meter J R 2008 *Phys. Rev. D* **77** 024014 [arXiv:0704.1964]

[288] Ajith P *et al.* 2007 *Class. Quant. Grav.* **24** S689–S700 [arXiv:0704.3764]

[289] Ajith P *et al.* 2011 *Phys. Rev. Lett.* **106** 241101 [arXiv:0909.2867]

[290] Husa S, Khan S, Hannam M, Pürrer M, Ohme F, Jiménez Forteza X and Bohé A 2016 *Phys. Rev. D* **93** 044006 [arXiv:1508.07250]

[291] Khan S, Husa S, Hannam M, Ohme F, Pürrer M, Jiménez Forteza X and Bohé A 2016 *Phys. Rev. D* **93** 044007 [arXiv:1508.07253]

[292] London L, Khan S, Fauchon-Jones E, García C, Hannam M, Husa S, Jiménez-Forteza X, Kalaghatgi C, Ohme F and Pannarale F 2018 *Phys. Rev. Lett.* **120** 161102 [arXiv:1708.00404]

[293] Khan S, Chatziioannou K, Hannam M and Ohme F 2019 *Phys. Rev. D* **100** 024059 [arXiv:1809.10113]

[294] Khan S, Ohme F, Chatziioannou K and Hannam M 2020 *Phys. Rev. D* **101** 024056 [arXiv:1911.06050]

[295] Dietrich T, Samajdar A, Khan S, Johnson-McDaniel N K, Dudi R and Tichy W 2019 *Phys. Rev. D* **100** 044003 [arXiv:1905.06011]

[296] Pratten G, Husa S, Garcia-Quiros C, Colleoni M, Ramos-Buades A, Estelles H and Jaume R 2020 *Phys. Rev. D* **102** 064001 [arXiv:2001.11412]

[297] García-Quirós C, Colleoni M, Husa S, Estellés H, Pratten G, Ramos-Buades A, Mateu-Lucena M and Jaume R 2020 *Phys. Rev. D* **102** 064002 [arXiv:2001.10914]

[298] Estellés H, Ramos-Buades A, Husa S, García-Quirós C, Colleoni M, Haegel L and Jaume R 2021 *Phys. Rev. D* **103** 124060 [arXiv:2004.08302]

[299] Estellés H, Colleoni M, García-Quirós C, Husa S, Keitel D, Mateu-Lucena M, Planas M d L and Ramos-Buades A 2022 *Phys. Rev. D* **105** 084040 [arXiv:2105.05872]

[300] Hamilton E, London L, Thompson J E, Fauchon-Jones E, Hannam M, Kalaghatgi C, Khan S, Pannarale F and Vano-Vinuales A 2021 *Phys. Rev. D* **104** 124027 [arXiv:2107.08876]

[301] Thompson J E, Hamilton E, London L, Ghosh S, Kolitsidou P, Hoy C and Hannam M 2024 *Phys. Rev. D* **109** 063012 [arXiv:2312.10025]

[302] Colleoni M, Vidal F A R, García-Quirós C, Akçay S and Bera S 2024 [arXiv:2412.16721]

[303] Planas M d L, Ramos-Buades A, García-Quirós C, Estellés H, Husa S and Haney M 2025 [arXiv:2503.13062]

[304] Ajith P *et al.* 2008 *Phys. Rev. D* **77** 104017 [Erratum: Phys.Rev.D 79, 129901 (2009)] [arXiv:0710.2335]

[305] Bohé A, Hannam M, Husa S, Ohme F, Pürrer M and Schmidt P 2016 PhenomPv2 – technical notes for the LAL implementation Tech. Rep. LIGO-T1500602 `https://dcc.ligo.org/LIGO-T1500602/public`

[306] Ghosh S, Kolitsidou P and Hannam M 2024 *Phys. Rev. D* **109** 024061 [arXiv:2310.16980]

[307] Rosselló-Sastre M, Husa S and Bera S 2024 *Phys. Rev. D* **110** 084074 [arXiv:2405.17302]

[308] Buonanno A and Damour T 1999 *Phys. Rev. D* **59** 084006 [arXiv:gr-qc/9811091]

[309] Buonanno A and Damour T 2000 *Phys. Rev. D* **62** 064015 [arXiv:gr-qc/0001013]

[310] Damour T, Jaranowski P and Schaefer G 2000 *Phys. Rev. D* **62** 084011 [arXiv:gr-qc/0005034]

[311] Damour T 2001 *Phys. Rev. D* **64** 124013 [arXiv:gr-qc/0103018]

[312] Buonanno A, Chen Y and Damour T 2006 *Phys. Rev. D* **74** 104005 [arXiv:gr-qc/0508067]

[313] Buonanno A, Cook G B and Pretorius F 2007 *Phys. Rev. D* **75** 124018 [arXiv:gr-qc/0610122]

[314] Damour T, Jaranowski P and Schäfer G 2015 *Phys. Rev. D* **91** 084024 [arXiv:1502.07245]

[315] Damour T, Iyer B R and Sathyaprakash B S 1998 *Phys. Rev. D* **57** 885–907 [arXiv:gr-qc/9708034]

[316] Damour T and Nagar A 2007 *Phys. Rev. D* **76** 064028 [arXiv:0705.2519]

[317] Damour T and Nagar A 2008 *Phys. Rev. D* **77** 024043 [arXiv:0711.2628]

[318] Damour T, Iyer B R and Nagar A 2009 *Phys. Rev. D* **79** 064004 [arXiv:0811.2069]

[319] Pan Y, Buonanno A, Fujita R, Racine E and Tagoshi H 2011 *Phys. Rev. D* **83** 064003 [Erratum: Phys.Rev.D 87, 109901 (2013)] [arXiv:1006.0431]

[320] Damour T, Iyer B R, Jaranowski P and Sathyaprakash B S 2003 *Phys. Rev. D* **67** 064028 [arXiv:gr-qc/0211041]

[321] Buonanno A, Pan Y, Baker J G, Centrella J, Kelly B J, McWilliams S T and van Meter J R 2007 *Phys. Rev. D* **76** 104049 [arXiv:0706.3732]

[322] Damour T and Nagar A 2009 *Phys. Rev.* **D79** 081503 [arXiv:0902.0136]

[323] Taracchini A, Pan Y, Buonanno A, Barausse E, Boyle M, Chu T, Lovelace G, Pfeiffer H P and Scheel M A 2012 *Phys. Rev. D* **86** 024011 [arXiv:1202.0790]

[324] Damour T, Nagar A and Bernuzzi S 2013 *Phys. Rev. D* **87** 084035 [arXiv:1212.4357]

[325] Taracchini A *et al.* 2014 *Phys. Rev. D* **89** 061502 [arXiv:1311.2544]

[326] Damour T and Nagar A 2014 *Phys. Rev. D* **90** 024054 [arXiv:1406.0401]

[327] Damour T, Jaranowski P and Schaefer G 2008 *Phys. Rev. D* **78** 024009 [arXiv:0803.0915]

[328] Pan Y, Buonanno A, Buchman L T, Chu T, Kidder L E, Pfeiffer H P and Scheel M A 2010 *Phys. Rev. D* **81** 084041 [arXiv:0912.3466]

[329] Barausse E and Buonanno A 2010 *Phys. Rev. D* **81** 084024 [arXiv:0912.3517]

[330] Barausse E and Buonanno A 2011 *Phys. Rev. D* **84** 104027 [arXiv:1107.2904]

[331] Nagar A 2011 *Phys. Rev. D* **84** 084028 [Erratum: Phys.Rev.D 88, 089901 (2013)] [arXiv:1106.4349]

[332] Damour T and Nagar A 2014 *Phys. Rev. D* **90** 044018 [arXiv:1406.6913]

[333] Balmelli S and Damour T 2015 *Phys. Rev. D* **92** 124022 [arXiv:1509.08135]

[334] Khalil M, Steinhoff J, Vines J and Buonanno A 2020 *Phys. Rev. D* **101** 104034 [arXiv:2003.04469]

[335] Bohé A *et al.* 2017 *Phys. Rev. D* **95** 044028 [arXiv:1611.03703]

[336] Nagar A *et al.* 2018 *Phys. Rev. D* **98** 104052 [arXiv:1806.01772]

[337] Akcay S, Gamba R and Bernuzzi S 2021 *Phys. Rev. D* **103** 024014 [arXiv:2005.05338]

[338] Nagar A, Rettegno P, Gamba R, Albanesi S, Albertini A and Bernuzzi S 2023 *Phys. Rev. D* **108** 124018 [arXiv:2304.09662]

[339] Nagar A, Pratten G, Riemenschneider G and Gamba R 2020 *Phys. Rev. D* **101** 024041 [arXiv:1904.09550]

[340] Nagar A, Riemenschneider G, Pratten G, Rettegno P and Messina F 2020 *Phys. Rev. D* **102** 024077 [arXiv:2001.09082]

[341] Hinderer T and Babak S 2017 *Phys. Rev. D* **96** 104048 [arXiv:1707.08426]

[342] Chiaramello D and Nagar A 2020 *Phys. Rev. D* **101** 101501 [arXiv:2001.11736]

[343] Nagar A, Bonino A and Rettegno P 2021 *Phys. Rev. D* **103** 104021 [arXiv:2101.08624]

[344] Ramos-Buades A, Buonanno A, Khalil M and Ossokine S 2022 *Phys. Rev. D* **105** 044035 [arXiv:2112.06952]

[345] Gamboa A *et al.* 2024 [arXiv:2412.12823]

[346] Nagar A, Gamba R, Rettegno P, Fantini V and Bernuzzi S 2024 [arXiv:2404.05288]

[347] Albanesi S, Gamba R, Bernuzzi S, Fontbuté J, Gonzalez A and Nagar A 2025 [arXiv:2503.14580]

[348] Bernuzzi S, Nagar A, Dietrich T and Damour T 2015 *Phys. Rev. Lett.* **114** 161103 [arXiv:1412.4553]

[349] Hinderer T *et al.* 2016 *Phys. Rev. Lett.* **116** 181101 [arXiv:1602.00599]

[350] Steinhoff J, Hinderer T, Buonanno A and Taracchini A 2016 *Phys. Rev. D* **94** 104028 [arXiv:1608.01907]

[351] Akcay S, Bernuzzi S, Messina F, Nagar A, Ortiz N and Rettegno P 2019 *Phys. Rev. D* **99** 044051 [arXiv:1812.02744]

[352] Steinhoff J, Hinderer T, Dietrich T and Foucart F 2021 *Phys. Rev. Res.* **3** 033129 [arXiv:2103.06100]

[353] Matas A *et al.* 2020 *Phys. Rev. D* **102** 043023 [arXiv:2004.10001]

[354] Gonzalez A, Gamba R, Breschi M, Zappa F, Carullo G, Bernuzzi S and Nagar A 2023 *Phys. Rev. D* **107** 084026 [arXiv:2212.03909]

[355] Gamba R *et al.* 2023 [arXiv:2307.15125]

[356] Haberland M, Buonanno A and Steinhoff J 2025 [arXiv:2503.18934]

[357] Damour T 2010 *Phys. Rev. D* **81** 024017 [arXiv:0910.5533]

[358] Le Tiec A, Barausse E and Buonanno A 2012 *Phys. Rev. Lett.* **108** 131103 [arXiv:1111.5609]

[359] Akcay S, Barack L, Damour T and Sago N 2012 *Phys. Rev. D* **86** 104041 [arXiv:1209.0964]

[360] Damour T 2016 *Phys. Rev. D* **94** 104015 [arXiv:1609.00354]

[361] Damour T 2018 *Phys. Rev. D* **97** 044038 [arXiv:1710.10599]

[362] Antonelli A, Buonanno A, Steinhoff J, van de Meent M and Vines J 2019 *Phys. Rev. D* **99** 104004 [arXiv:1901.07102]

[363] Antonelli A, van de Meent M, Buonanno A, Steinhoff J and Vines J 2020 *Phys. Rev. D* **101** 024024 [arXiv:1907.11597]

[364] van de Meent M, Buonanno A, Mihaylov D P, Ossokine S, Pompili L, Warburton N, Pound A, Wardell B, Durkan L and Miller J 2023 *Phys. Rev. D* **108** 124038 [arXiv:2303.18026]

[365] Buonanno A, Jakobsen G U and Mogull G 2024 [arXiv:2402.12342]

[366] Leather B, Buonanno A and van de Meent M 2025 [arXiv:2505.11242]

[367] Brito R, Buonanno A and Raymond V 2018 *Phys. Rev. D* **98** 084038 [arXiv:1805.00293]

[368] Ghosh A, Brito R and Buonanno A 2021 *Phys. Rev. D* **103** 124041 [arXiv:2104.01906]

[369] Maggio E, Silva H O, Buonanno A and Ghosh A 2022 [arXiv:2212.09655]

[370] Mehta A K, Buonanno A, Cotesta R, Ghosh A, Sennett N and Steinhoff J 2023 *Phys. Rev. D* **107** 044020 [arXiv:2203.13937]

[371] Julié F L and Deruelle N 2017 *Phys. Rev. D* **95** 124054 [arXiv:1703.05360]

[372] Julié F L 2018 *Phys. Rev. D* **97** 024047 [arXiv:1709.09742]

[373] Julié F L, Baibhav V, Berti E and Buonanno A 2023 *Phys. Rev. D* **107** 104044 [arXiv:2212.13802]

[374] Jain T, Rettegno P, Agathos M, Nagar A and Turco L 2023 *Phys. Rev. D* **107** 084017 [arXiv:2211.15580]

[375] Jain T 2023 *Phys. Rev. D* **107** 084018 [arXiv:2301.01070]

[376] Damour T, Nagar A, Pollney D and Reisswig C 2012 *Phys. Rev. Lett.* **108** 131101 [arXiv:1110.2938]

[377] Nagar A, Damour T, Reisswig C and Pollney D 2016 *Phys. Rev. D* **93** 044046 [arXiv:1506.08457]

[378] Ossokine S, Dietrich T, Foley E, Katebi R and Lovelace G 2018 *Phys. Rev. D* **98** 104057 [arXiv:1712.06533]

[379] Le Tiec A, Mroue A H, Barack L, Buonanno A, Pfeiffer H P, Sago N and Taracchini A 2011 *Phys. Rev. Lett.* **107** 141101 [arXiv:1106.3278]

[380] Hinderer T *et al.* 2013 *Phys. Rev. D* **88** 084005 [arXiv:1309.0544]

[381] Nagar A and Rettegno P 2019 *Phys. Rev. D* **99** 021501 [arXiv:1805.03891]

[382] Rettegno P, Martinetti F, Nagar A, Bini D, Riemenschneider G and Damour T 2020 *Phys. Rev. D* **101** 104027 [arXiv:1911.10818]

[383] Mihaylov D P, Ossokine S, Buonanno A and Ghosh A 2021 *Phys. Rev. D* **104** 124087 [arXiv:2105.06983]

[384] Field S E, Galley C R, Hesthaven J S, Kaye J and Tiglio M 2014 *Phys. Rev. X* **4** 031006 [arXiv:1308.3565]

[385] Pürrer M 2014 *Class. Quant. Grav.* **31** 195010 [arXiv:1402.4146]

[386] Pürrer M 2016 *Phys. Rev. D* **93** 064041 [arXiv:1512.02248]

[387] Cotesta R, Marsat S and Pürrer M 2020 *Phys. Rev. D* **101** 124040 [arXiv:2003.12079]

[388] Gadre B, Pürrer M, Field S E, Ossokine S and Varma V 2022 [arXiv:2203.00381]

[389] Thomas L M, Pratten G and Schmidt P 2022 *Phys. Rev. D* **106** 104029 [arXiv:2205.14066]

[390] Barausse E, Racine E and Buonanno A 2009 *Phys. Rev. D* **80** 104025 [Erratum: Phys.Rev.D 85, 069904 (2012)] [arXiv:0907.4745]

[391] Abadie J *et al.* (LIGO Scientific, VIRGO) 2011 *Phys. Rev. D* **83** 122005 [Erratum: Phys.Rev.D 86, 069903 (2012)] [arXiv:1102.3781]

[392] Abadie J *et al.* (LIGO Scientific, VIRGO) 2012 *Phys. Rev. D* **85** 082002 [arXiv:1111.7314]

[393] Aasi J *et al.* (LIGO Scientific, VIRGO) 2013 *Phys. Rev. D* **87** 022002 [arXiv:1209.6533]

[394] Akutsu T *et al.* (KAGRA) 2021 *PTEP* **2021** 05A101 [arXiv:2005.05574]

[395] Abbott B P *et al.* (KAGRA, LIGO Scientific, Virgo, VIRGO) 2018 *Living Rev. Rel.* **21** 3 [arXiv:1304.0670]

[396] Abac A *et al.* 2025 [arXiv:2503.12263]

[397] Evans M *et al.* 2021 [arXiv:2109.09882]

[398] 2022 Noise curves used for simulations in the update of the observing scenarios paper LIGO Document T2000012-v2 URL `https://dcc.ligo.org/LIGO-T2000012/public`

[399] Unofficial sensitivity curves (asd) for aligo, kagra, virgo, voyager, cosmic explorer, and einstein telescope Tech. Rep. LIGO-T1500293 `https://dcc.ligo.org/LIGO-T1500293/public`

[400] A# strain sensitivity Tech. Rep. LIGO-T2300041 `https://dcc.ligo.org/LIGO-T2300041/public`

[401] Colpi M *et al.* (LISA) 2024 [arXiv:2402.07571]

[402] Luo J *et al.* (TianQin) 2016 *Class. Quant. Grav.* **33** 035010 [arXiv:1512.02076]

[403] Wu Y L *et al.* (Taiji Scientific) 2021 *Commun. Phys.* **4** 34

[404] Broekgaarden F S, Banagiri S and Payne E 2024 *Astrophys. J.* **969** 108 [arXiv:2303.17628]

[405] Borhanian S and Sathyaprakash B S 2022 [arXiv:2202.11048]

[406] Gupta I *et al.* 2023 [arXiv:2307.10421]

[407] Branchesi M *et al.* 2023 *JCAP* **07** 068 [arXiv:2303.15923]

[408] Iacovelli F, Mancarella M, Foffa S and Maggiore M 2022 *Astrophys. J.* **941** 208 [arXiv:2207.02771]

[409] Ng K K Y, Vitale S, Farr W M and Rodriguez C L 2021 *Astrophys. J. Lett.* **913** L5 [arXiv:2012.09876]

[410] Ng K K Y, Franciolini G, Berti E, Pani P, Riotto A and Vitale S 2022 *Astrophys. J. Lett.* **933** L41 [arXiv:2204.11864]

[411] Reali L, Cotesta R, Antonelli A, Kritos K, Strokov V and Berti E 2024 *Phys. Rev. D* **110** 103002 [arXiv:2406.01687]

[412] Borhanian S, Dhani A, Gupta A, Arun K G and Sathyaprakash B S 2020 *Astrophys. J. Lett.* **905** L28 [arXiv:2007.02883]

[413] Chen H Y, Ezquiaga J M and Gupta I 2024 *Class. Quant. Grav.* **41** 125004 [arXiv:2402.03120]

[414] Pacilio C, Maselli A, Fasano M and Pani P 2022 *Phys. Rev. Lett.* **128** 101101 [arXiv:2104.10035]

[415] Breschi M, Bernuzzi S, Godzieba D, Perego A and Radice D 2022 *Phys. Rev. Lett.* **128** 161102 [arXiv:2110.06957]

[416] Gupta P K, Puecher A, Pang P T H, Janquart J, Koekoek G and Broeck Van Den C 2022 [arXiv:2205.01182]

[417] Berti E, Cardoso V and Will C M 2006 *Phys. Rev. D* **73** 064030 [arXiv:gr-qc/0512160]

[418] Toubiana A, Pompili L, Buonanno A, Gair J R and Katz M L 2024 *Phys. Rev. D* **109** 104019 [arXiv:2307.15086]

[419] Babak S, Gair J, Sesana A, Barausse E, Sopuerta C F, Berry C P L, Berti E, Amaro-Seoane P, Petiteau A and Klein A 2017 *Phys. Rev. D* **95** 103012 [arXiv:1703.09722]

[420] Toubiana A *et al.* 2021 *Phys. Rev. Lett.* **126** 101105 [arXiv:2010.06056]

[421] Speri L, Antonelli A, Sberna L, Babak S, Barausse E, Gair J R and Katz M L 2023 *Phys. Rev. X* **13** 021035 [arXiv:2207.10086]

[422] Cole P S, Bertone G, Coogan A, Gaggero D, Karydas T, Kavanagh B J, Spieksma T F M and Tomaselli G M 2023 *Nature Astron.* **7** 943–950 [arXiv:2211.01362]

[423] Sesana A 2016 *Phys. Rev. Lett.* **116** 231102 [arXiv:1602.06951]

[424] Jani K, Shoemaker D and Cutler C 2019 *Nature Astron.* **4** 260–265 [arXiv:1908.04985]

[425] Klein A *et al.* 2022 [arXiv:2204.03423]

[426] Barausse E, Yunes N and Chamberlain K 2016 *Phys. Rev. Lett.* **116** 241104 [arXiv:1603.04075]

[427] Toubiana A, Marsat S, Barausse E, Babak S and Baker J 2020 *Phys. Rev. D* **101** 104038 [arXiv:2004.03626]

[428] Abbott B P *et al.* (LIGO Scientific, Virgo) 2017 *Class. Quant. Grav.* **34** 104002 [arXiv:1611.07531]

[429] Pürrer M and Haster C J 2020 *Phys. Rev. Res.* **2** 023151 [arXiv:1912.10055]

[430] Hu Q and Veitch J 2022 *Phys. Rev. D* **106** 044042 [arXiv:2205.08448]

[431] Islam T, Vajpeyi A, Shaik F H, Haster C J, Varma V, Field S E, Lange J, O'Shaughnessy R and Smith R 2023 [arXiv:2309.14473]

[432] Gamba R, Breschi M, Bernuzzi S, Agathos M and Nagar A 2021 *Phys. Rev. D* **103** 124015 [arXiv:2009.08467]

[433] Kunert N, Pang P T H, Tews I, Coughlin M W and Dietrich T 2022 *Phys. Rev. D* **105** L061301 [arXiv:2110.11835]

[434] Owen C B, Haster C J, Perkins S, Cornish N J and Yunes N 2023 *Phys. Rev. D* **108** 044018 [arXiv:2301.11941]

[435] Dhani A, Völkel S, Buonanno A, Estelles H, Gair J, Pfeiffer H P, Pompili L and Toubiana A 2024 [arXiv:2404.05811]

[436] Kapil V, Reali L, Cotesta R and Berti E 2024 *Phys. Rev. D* **109** 104043 [arXiv:2404.00090]

[437] Ferguson D, Jani K, Laguna P and Shoemaker D 2021 *Phys. Rev. D* **104** 044037 [arXiv:2006.04272]

[438] Jan A, Ferguson D, Lange J, Shoemaker D and Zimmerman A 2023 [arXiv:2312.10241]

[439] Abbott B P *et al.* (LIGO Scientific, Virgo) 2016 *Phys. Rev. Lett.* **116** 221101 [Erratum: Phys.Rev.Lett. 121, 129902 (2018)] [arXiv:1602.03841]

[440] Yunes N, Yagi K and Pretorius F 2016 *Phys. Rev. D* **94** 084002 [arXiv:1603.08955]

[441] Abbott B P *et al.* (LIGO Scientific, Virgo) 2019 *Phys. Rev. D* **100** 104036 [arXiv:1903.04467]

[442] Pang P T H, Calderón Bustillo J, Wang Y and Li T G F 2018 *Phys. Rev. D* **98** 024019 [arXiv:1802.03306]

[443] Hu Q and Veitch J 2023 *Astrophys. J.* **945** 103 [arXiv:2210.04769]

[444] Gupta A *et al.* 2024 [arXiv:2405.02197]

[445] Chandramouli R S, Prokup K, Berti E and Yunes N 2025 *Phys. Rev. D* **111** 044026 [arXiv:2410.06254]

[446] Favata M 2014 *Phys. Rev. Lett.* **112** 101101 [arXiv:1310.8288]

[447] Divyajyoti, Kumar S, Tibrewal S, Romero-Shaw I M and Mishra C K 2024 *Phys. Rev. D* **109** 043037 [arXiv:2309.16638]

[448] Gupte N *et al.* 2024 Evidence for eccentricity in the population of binary black holes observed by LIGO-Virgo-KAGRA [arXiv:2404.14286]

[449] Morras G, Pratten G and Schmidt P 2025 [arXiv:2503.15393]

[450] Lindblom L, Owen B J and Brown D A 2008 *Phys. Rev. D* **78** 124020 [arXiv:0809.3844]

[451] McWilliams S T, Kelly B J and Baker J G 2010 *Phys. Rev. D* **82** 024014 [arXiv:1004.0961]

[452] Baird E, Fairhurst S, Hannam M and Murphy P 2013 *Phys. Rev. D* **87** 024035 [arXiv:1211.0546]

[453] Chatziioannou K, Klein A, Yunes N and Cornish N 2017 *Phys. Rev. D* **95** 104004 [arXiv:1703.03967]

[454] Toubiana A and Gair J R 2024 [arXiv:2401.06845]

[455] Cutler C and Flanagan E E 1994 *Phys. Rev. D* **49** 2658–2697 [arXiv:gr-qc/9402014]

[456] Vallisneri M 2008 *Phys. Rev. D* **77** 042001 [arXiv:gr-qc/0703086]

[457] Chua A J K, Galley C R and Vallisneri M 2019 *Phys. Rev. Lett.* **122** 211101 [arXiv:1811.05491]

[458] Khan S and Green R 2021 *Phys. Rev. D* **103** 064015 [arXiv:2008.12932]

[459] Thomas L M, Chatziioannou K, Varma V and Field S E 2025 *Phys. Rev. D* **111** 104029 [arXiv:2501.16462]

[460] Hu Q and Veitch J 2024 [arXiv:2412.02651]

[461] Cornish N J 2010 [arXiv:1007.4820]

[462] Zackay B, Dai L and Venumadhav T 2018 [arXiv:1806.08792]

[463] Cornish N J 2021 *Phys. Rev. D* **104** 104054 [arXiv:2109.02728]

[464] Leslie N, Dai L and Pratten G 2021 *Phys. Rev. D* **104** 123030 [arXiv:2109.09872]

[465] Vinciguerra S, Veitch J and Mandel I 2017 *Class. Quant. Grav.* **34** 115006 [arXiv:1703.02062]

[466] Morisaki S 2021 *Phys. Rev. D* **104** 044062 [arXiv:2104.07813]

[467] Canizares P, Field S E, Gair J R and Tiglio M 2013 *Phys. Rev. D* **87** 124005 [arXiv:1304.0462]

[468] Smith R, Field S E, Blackburn K, Haster C J, Pürrer M, Raymond V and Schmidt P 2016 *Phys. Rev. D* **94** 044031 [arXiv:1604.08253]

[469] Baker A M, Lasky P D, Thrane E and Golomb J 2025 [arXiv:2503.04073]

[470] Smith R J E, Ashton G, Vajpeyi A and Talbot C 2020 *Mon. Not. Roy. Astron. Soc.* **498** 4492–4502 [arXiv:1909.11873]

[471] Lange J, O'Shaughnessy R and Rizzo M 2018 [arXiv:1805.10457]

[472] Green S R and Gair J 2021 *Mach. Learn. Sci. Tech.* **2** 03LT01 [arXiv:2008.03312]

[473] Dax M, Green S R, Gair J, Macke J H, Buonanno A and Schölkopf B 2021 *Phys. Rev. Lett.* **127** 241103 [arXiv:2106.12594]

[474] Dax M, Green S R, Gair J, Pürrer M, Wildberger J, Macke J H, Buonanno A and Schölkopf B 2022 [arXiv:2210.05686]

[475] Wong K W K, Isi M and Edwards T D P 2023 *Astrophys. J.* **958** 129 [arXiv:2302.05333]

[476] Littenberg T B and Cornish N J 2023 *Phys. Rev. D* **107** 063004 [arXiv:2301.03673]

[477] Katz M L, Karnesis N, Korsakova N, Gair J R and Stergioulas N 2025 *Phys. Rev. D* **111** 024060 [arXiv:2405.04690]

[478] Deng S, Babak S, Le Jeune M, Marsat S, Plagnol E and Sartirana A 2025 *Phys. Rev. D* **111** 103014 [arXiv:2501.10277]

[479] Estellés H, Buonanno A, Enficiaud R, Foo C and Pompili L 2025 [arXiv:2506.19911]

[480] Afshordi N *et al.* (LISA Consortium Waveform Working Group) 2023 [arXiv:2311.01300]

[481] `https://waveforms.docs.ligo.org/software/pyseobnr/`

[482] LIGO Scientific Collaboration 2018 LIGO Algorithm Library - LALSuite free software (GPL)

[483] Van Rossum G and Drake F L 2009 *Python 3 Reference Manual* (Scotts Valley, CA: CreateSpace) ISBN 1441412697

[484] Nitz A, Harry I, Brown D, Biwer C M, Willis J, Canton T D, Capano C, Dent T, Pekowsky L, Davies G S C, De S, Cabero M, Wu S, Williamson A R, Macleod D, Machenschalk B, Pannarale F, Kumar P, Reyes S, dfinstad, Kumar S, Tápai M, Singer L, Kumar P, Gadre B U V, maxtrevor, veronica villa, Khan S, Fairhurst S and Chandra K 2023 gwastro/pycbc: v2.3.2 release of pycbc URL `https://doi.org/10.5281/zenodo.10137381`

[485] `https://git.ligo.org/lscsoft/pyring/`

[486] Ashton G *et al.* 2019 *Astrophys. J. Suppl.* **241** 27 [arXiv:1811.02042]

[487] Behnel S, Bradshaw R, Citro C, Dalcin L, Seljebotn D S and Smith K 2011 *Computing in Science & Engineering* **13** 31–39

[488] Inc W R Mathematica, Version 13.2 champaign, IL, 2022 URL `https://www.wolfram.com/mathematica`

[489] Harris C R, Millman K J, van der Walt S J, Gommers R, Virtanen P, Cournapeau D, Wieser E, Taylor J, Berg S, Smith N J, Kern R, Picus M, Hoyer S, van Kerkwijk M H, Brett M, Haldane A, del Río J F, Wiebe M, Peterson P, Gérard-Marchant P, Sheppard K, Reddy T, Weckesser W, Abbasi H, Gohlke C and Oliphant T E 2020 *Nature* **585** 357–362 URL `https://doi.org/10.1038/s41586-020-2649-2`

[490] Virtanen P, Gommers R, Oliphant T E, Haberland M, Reddy T, Cournapeau D, Burovski E, Peterson P, Weckesser W, Bright J, van der Walt S J, Brett M, Wilson J, Millman K J, Mayorov N, Nelson A R J, Jones E, Kern R, Larson E, Carey C J, Polat İ, Feng Y, Moore E W, VanderPlas J, Laxalde D, Perktold J, Cimrman R, Henriksen I, Quintero E A, Harris C R, Archibald A M, Ribeiro A H, Pedregosa F, van Mulbregt P and SciPy 10 Contributors 2020 *Nature Methods* **17** 261–272

[491] Galassi M and et al Gnu scientific library reference manual (3rd ed.) `http://www.gnu.org/software/gsl/`

[492] `https://github.com/pygsl/pygsl`

[493] Research W 2019 wolframclient for python `https://github.com/WolframResearch/WolframClientForPython`

[494] 2007 Gnu general public license, version 3 `http://www.gnu.org/licenses/gpl.html` last retrieved 2020-01-01

[495] `https://git-scm.com`

[496] Colleoni M, Mateu-Lucena M, Estellés H, García-Quirós C, Keitel D, Pratten G, Ramos-Buades A and Husa S 2021 *Phys. Rev. D* **103** 024029 [arXiv:2010.05830]

[497] Henry Q, Marsat S and Khalil M 2022 *Phys. Rev. D* **106** 124018 [arXiv:2209.00374]

[498] `http://www.black-holes.org/waveforms`

[499] Chu T, Fong H, Kumar P, Pfeiffer H P, Boyle M, Hemberger D A, Kidder L E, Scheel M A and Szilagyi B 2016 *Class. Quant. Grav.* **33** 165001 [arXiv:1512.06800]

[500] Hemberger D A, Lovelace G, Loredo T J, Kidder L E, Scheel M A, Szilagyi B, Taylor N W and Teukolsky S A 2013 *Phys. Rev.* **D88** 064014 [arXiv:1305.5991]

[501] Scheel M A, Giesler M, Hemberger D A, Lovelace G, Kuper K, Boyle M, Szilagyi B and Kidder L E 2015 *Class. Quant. Grav.* **32** 105009 [arXiv:1412.1803]

[502] Lovelace G *et al.* 2015 *Class. Quant. Grav.* **32** 065007 [arXiv:1411.7297]

[503] Abbott B P *et al.* (Virgo, LIGO Scientific) 2016 *Phys. Rev.* **D94** 064035 [arXiv:1606.01262]

[504] Lovelace G *et al.* 2016 *Class. Quant. Grav.* **33** 244002 [arXiv:1607.05377]

[505] Abbott B P *et al.* (Virgo, LIGO Scientific) 2016 *Phys. Rev. Lett.* **116** 241103 [arXiv:1606.04855]

[506] Kumar P, Barkett K, Bhagwat S, Afshari N, Brown D A, Lovelace G, Scheel M A and Szilagyi B 2015 *Phys. Rev.* **D92** 102001 [arXiv:1507.00103]

[507] Mroue A H *et al.* 2013 *Phys. Rev. Lett.* **111** 241104 [arXiv:1304.6077]

[508] Brandt S R *et al.* 2024 The einstein toolkit URL `https://doi.org/10.5281/zenodo.12588764`

[509] Abac A, Dietrich T, Buonanno A, Steinhoff J and Ujevic M 2024 *Phys. Rev. D* **109** 024062 [arXiv:2311.07456]

[510] Vines J, Kunst D, Steinhoff J and Hinderer T 2016 *Phys. Rev. D* **93** 103008 [Erratum: Phys.Rev.D 104, 029902 (2021)] [arXiv:1601.07529]

[511] Antonelli A, Kavanagh C, Khalil M, Steinhoff J and Vines J 2020 *Phys. Rev. D* **102** 124024 [arXiv:2010.02018]

[512] Mandal M K, Mastrolia P, Patil R and Steinhoff J 2022 [arXiv:2209.00611]

[513] Kim J W, Levi M and Yin Z 2022 [arXiv:2208.14949]

[514] Vines J and Steinhoff J 2018 *Phys. Rev. D* **97** 064010 [arXiv:1606.08832]

[515] Blanchet L 1998 *Class. Quant. Grav.* **15** 113–141 [Erratum: Class.Quant.Grav. 22, 3381 (2005)] [arXiv:gr-qc/9710038]

[516] Blanchet L, Faye G, Iyer B R and Sinha S 2008 *Class. Quant. Grav.* **25** 165003 [Erratum: Class.Quant.Grav. 29, 239501 (2012)] [arXiv:0802.1249]

[517] Jiménez-Forteza X, Keitel D, Husa S, Hannam M, Khan S and Pürrer M 2017 *Phys. Rev. D* **95** 064024 [arXiv:1611.00332]

[518] Hofmann F, Barausse E and Rezzolla L 2016 *Astrophys. J. Lett.* **825** L19 [arXiv:1605.01938]

[519] Stein L C 2019 *J. Open Source Softw.* **4** 1683 [arXiv:1908.10377]

[520] Guyon I, Weston J, Barnhill S and Vapnik V 2002 *Machine Learning* **46** 389–422

[521] Kelly B J and Baker J G 2013 *Phys. Rev. D* **87** 084004 [arXiv:1212.5553]

[522] Berti E, Cardoso V and Casals M 2006 *Phys. Rev. D* **73** 024013 [Erratum: Phys.Rev.D 73, 109902 (2006)] [arXiv:gr-qc/0511111]

[523] Kumar Mehta A, Tiwari P, Johnson-McDaniel N K, Mishra C K, Varma V and Ajith P 2019 *Phys. Rev. D* **100** 024032 [arXiv:1902.02731]

[524] Nagar A and Rettegno P 2021 *Phys. Rev. D* **104** 104004 [arXiv:2108.02043]

[525] Barsotti L, Fritschel P, Evans M and Gras S (LIGO Collaboration) 2018 Updated advanced ligo sensitivity design curve LIGO Document T1800044-v5 URL `https://dcc.ligo.org/LIGO-T1800044/public`

[526] Williams M J, Veitch J and Messenger C 2021 *Phys. Rev. D* **103** 103006 [arXiv:2102.11056]

[527] Barack L and Sago N 2010 *Phys. Rev. D* **81** 084021 [arXiv:1002.2386]

[528] Isoyama S, Barack L, Dolan S R, Le Tiec A, Nakano H, Shah A G, Tanaka T and Warburton N 2014 *Phys. Rev. Lett.* **113** 161101 [arXiv:1404.6133]

[529] Capano C, Pan Y and Buonanno A 2014 *Phys. Rev. D* **89** 102003 [arXiv:1311.1286]

[530] Riemenschneider G, Rettegno P, Breschi M, Albertini A, Gamba R, Bernuzzi S and Nagar A 2021 *Phys. Rev. D* **104** 104045 [arXiv:2104.07533]

[531] Mandal M K, Mastrolia P, Patil R and Steinhoff J 2022 [arXiv:2210.09176]

[532] Kim J W, Levi M and Yin Z 2022 [arXiv:2209.09235]

[533] Levi M, Morales R and Yin Z 2022 [arXiv:2210.17538]

[534] Levi M and Yin Z 2022 [arXiv:2211.14018]

[535] Levi M, Mougiakakos S and Vieira M 2021 *JHEP* **01** 036 [arXiv:1912.06276]

[536] Levi M and Teng F 2021 *JHEP* **01** 066 [arXiv:2008.12280]

[537] Henry Q 2022 [arXiv:2210.15602]

[538] Dietrich T, Bernuzzi S, Ujevic M and Tichy W 2017 *Phys. Rev. D* **95** 044045 [arXiv:1611.07367]

[539] Cheung C, Rothstein I Z and Solon M P 2018 *Phys. Rev. Lett.* **121** 251101 [arXiv:1808.02489]

[540] Bern Z, Cheung C, Roiban R, Shen C H, Solon M P and Zeng M 2019 *Phys. Rev. Lett.* **122** 201603 [arXiv:1901.04424]

[541] Bern Z, Kosmopoulos D, Luna A, Roiban R and Teng F 2023 *Phys. Rev. Lett.* **130** 201402 [arXiv:2203.06202]

[542] Kosower D A, Maybee B and O'Connell D 2019 *JHEP* **02** 137 [arXiv:1811.10950]

[543] Bjerrum-Bohr N J, Damgaard P H, Festuccia G, Planté L and Vanhove P 2018 *Phys. Rev. Lett.* **121** 171601 [arXiv:1806.04920]

[544] Brandhuber A, Chen G, Travaglini G and Wen C 2021 *JHEP* **10** 118 [arXiv:2108.04216]

[545] Vines J 2018 *Class. Quant. Grav.* **35** 084002 [arXiv:1709.06016]

[546] Kälin, Gregor and Porto, Rafael A 2020 *JHEP* **11** 106 [arXiv:2006.01184]

[547] Kälin, Gregor and Liu, Zhengwen and Porto, Rafael A 2020 *Phys. Rev. Lett.* **125** 261103 [arXiv:2007.04977]

[548] Mogull G, Plefka J and Steinhoff J 2021 *JHEP* **02** 048 [arXiv:2010.02865]

[549] Jakobsen G U, Mogull G, Plefka J and Steinhoff J 2022 *JHEP* **01** 027 [arXiv:2109.04465]

[550] Hoy C 2022 *Phys. Rev. D* **106** 083003 [arXiv:2208.00106]

[551] Romero-Shaw I M, Thrane E and Lasky P D 2022 *Publ. Astron. Soc. Austral.* **39** e025 [arXiv:2202.05479]

[552] Whittle P 1953 *Journal of the Royal Statistical Society: Series B (Methodological)* **15** 125–139

[553] Speagle J S 2020 *Mon. Not. Roy. Astron. Soc.* **493** 3132–3158 [arXiv:1904.02180]

[554] Chatziioannou K *et al.* 2019 *Phys. Rev. D* **100** 104015 [arXiv:1903.06742]

[555] Abbott R *et al.* (LIGO Scientific, Virgo) 2020 *Astrophys. J. Lett.* **896** L44 [arXiv:2006.12611]

[556] Abbott R *et al.* (LIGO Scientific, Virgo) 2021 *SoftwareX* **13** 100658 [arXiv:1912.11716]

[557] Ashton G and Khan S 2020 *Phys. Rev. D* **101** 064037 [arXiv:1910.09138]

[558] Jan A Z, Yelikar A B, Lange J and O'Shaughnessy R 2020 *Phys. Rev. D* **102** 124069 [arXiv:2011.03571]

[559] Ashton G and Dietrich T 2022 *Nature Astron.* **6** 961–967 [arXiv:2111.09214]

[560] Puecher A, Samajdar A, Ashton G, Van Den Broeck C and Dietrich T 2024 *Phys. Rev. D* **109** 023019 [arXiv:2310.03555]

[561] Hoy C, Akcay S, Mac Uilliam J and Thompson J E 2024 [arXiv:2409.19404]

[562] Moore C J and Gair J R 2014 *Phys. Rev. Lett.* **113** 251101 [arXiv:1412.3657]

[563] Gair J R and Moore C J 2015 *Phys. Rev. D* **91** 124062 [arXiv:1504.02767]

[564] Moore C J, Berry C P L, Chua A J K and Gair J R 2016 *Phys. Rev. D* **93** 064001 [arXiv:1509.04066]

[565] Doctor Z, Farr B, Holz D E and Pürrer M 2017 *Phys. Rev.* **D96** 123011 [arXiv:1706.05408]

[566] Khan S 2024 *Phys. Rev. D* **109** 104045 [arXiv:2403.11534]

[567] Read J S 2023 *Class. Quant. Grav.* **40** 135002 [arXiv:2301.06630]

[568] Bishop C M 1994 Mixture density networks URL `https://publications.aston.ac.uk/id/eprint/373/`

[569] Paszke A *et al.* 2019 [arXiv:1912.01703]

[570] Kruse J 2020 *CoRR* **abs/2003.05739** [arXiv:2003.05739] URL `https://arxiv.org/abs/2003.05739`

[571] Pedregosa F, Varoquaux G, Gramfort A, Michel V, Thirion B, Grisel O, Blondel M, Prettenhofer P, Weiss R, Dubourg V, Vanderplas J, Passos A, Cournapeau D, Brucher M, Perrot M and Duchesnay E 2011 *Journal of Machine Learning Research* **12** 2825–2830

[572] Abbott R *et al.* (KAGRA, VIRGO, LIGO Scientific) 2023 *Astrophys. J. Suppl.* **267** 29 [arXiv:2302.03676]

[573] Abbott B P *et al.* (LIGO Scientific, Virgo) 2018 *Phys. Rev. Lett.* **121** 161101 [arXiv:1805.11581]

[574] Abbott B P *et al.* (LIGO Scientific, Virgo, 1M2H, Dark Energy Camera GW-E, DES, DLT40, Las Cumbres Observatory, VINROUGE, MASTER) 2017 *Nature* **551** 85–88 [arXiv:1710.05835]

[575] Abbott R *et al.* (LIGO Scientific, VIRGO, KAGRA) 2021 [arXiv:2111.03604]

[576] Yunes N and Siemens X 2013 *Living Rev. Rel.* **16** 9 [arXiv:1304.3473]

[577] Bertotti B, Iess L and Tortora P 2003 *Nature* **425** 374–376

[578] Kramer M *et al.* 2006 *Science* **314** 97–102 [arXiv:astro-ph/0609417]

[579] Perkins S E, Yunes N and Berti E 2021 *Phys. Rev. D* **103** 044024 [arXiv:2010.09010]

[580] Arun K G *et al.* (LISA) 2022 *Living Rev. Rel.* **25** 4 [arXiv:2205.01597]

[581] Blanchet L and Sathyaprakash B S 1995 *Phys. Rev. Lett.* **74** 1067–1070

[582] Arun K G, Iyer B R, Qusailah M S S and Sathyaprakash B S 2006 *Phys. Rev. D* **74** 024006 [arXiv:gr-qc/0604067]

[583] Yunes N and Pretorius F 2009 *Phys. Rev. D* **80** 122003 [arXiv:0909.3328]

[584] Cornish N, Sampson L, Yunes N and Pretorius F 2011 *Phys. Rev. D* **84** 062003 [arXiv:1105.2088]

[585] Li T G F, Del Pozzo W, Vitale S, Van Den Broeck C, Agathos M, Veitch J, Grover K, Sidery T, Sturani R and Vecchio A 2012 *Phys. Rev. D* **85** 082003 [arXiv:1110.0530]

[586] Agathos M, Del Pozzo W, Li T G F, Van Den Broeck C, Veitch J and Vitale S 2014 *Phys. Rev. D* **89** 082001 [arXiv:1311.0420]

[587] Meidam J *et al.* 2018 *Phys. Rev. D* **97** 044033 [arXiv:1712.08772]

[588] Cardoso V, Kimura M, Maselli A, Berti E, Macedo C F B and McManus R 2019 *Phys. Rev. D* **99** 104077 [arXiv:1901.01265]

[589] Maselli A, Pani P, Gualtieri L and Berti E 2020 *Phys. Rev. D* **101** 024043 [arXiv:1910.12893]

[590] Roy S, Haney M, Pratten G, Pang P T H and Van Den Broeck C 2025 [arXiv:2504.21147]

[591] Hughes S A and Menou K 2005 *Astrophys. J.* **623** 689–699 [arXiv:astro-ph/0410148]

[592] Ghosh A *et al.* 2016 *Phys. Rev. D* **94** 021101 [arXiv:1602.02453]

[593] Ghosh A, Johnson-Mcdaniel N K, Ghosh A, Mishra C K, Ajith P, Del Pozzo W, Berry C P L, Nielsen A B and London L 2018 *Class. Quant. Grav.* **35** 014002 [arXiv:1704.06784]

[594] Ghonge S, Chatziioannou K, Clark J A, Littenberg T, Millhouse M, Cadonati L and Cornish N 2020 [arXiv:2003.09456]

[595] Isi M, Farr W M, Giesler M, Scheel M A and Teukolsky S A 2020 [arXiv:2012.04486]

[596] Datta S, Saleem M, Arun K G and Sathyaprakash B S 2022 [arXiv:2208.07757]

[597] Xie Y, Chatterjee D, Narayan G and Yunes N 2024 [arXiv:2403.18936]

[598] Chua A J K and Vallisneri M 2020 [arXiv:2006.08918]

[599] Berti E *et al.* 2015 *Class. Quant. Grav.* **32** 243001 [arXiv:1501.07274]

[600] Nair R, Perkins S, Silva H O and Yunes N 2019 *Phys. Rev. Lett.* **123** 191101 [arXiv:1905.00870]

[601] Perkins S E, Nair R, Silva H O and Yunes N 2021 *Phys. Rev. D* **104** 024060 [arXiv:2104.11189]

[602] Silva H O, Ghosh A and Buonanno A 2023 *Phys. Rev. D* **107** 044030 [arXiv:2205.05132]

[603] Maselli A, Yi S, Pierini L, Vellucci V, Reali L, Gualtieri L and Berti E 2023 [arXiv:2311.14803]

[604] Maenaut S, Carullo G, Cano P A, Liu A, Cardoso V, Hertog T and Li T G F 2024 [arXiv:2411.17893]

[605] Damour T and Esposito-Farese G 1992 *Class. Quant. Grav.* **9** 2093–2176

[606] Damour T and Esposito-Farese G 1993 *Phys. Rev. Lett.* **70** 2220–2223

[607] Yagi K, Stein L C, Yunes N and Tanaka T 2012 *Phys. Rev. D* **85** 064022 [Erratum: Phys.Rev.D 93, 029902 (2016)] [arXiv:1110.5950]

[608] Mirshekari S and Will C M 2013 *Phys. Rev. D* **87** 084070 [arXiv:1301.4680]

[609] Lang R N 2014 *Phys. Rev. D* **89** 084014 [arXiv:1310.3320]

[610] Lang R N 2015 *Phys. Rev. D* **91** 084027 [arXiv:1411.3073]

[611] Blázquez-Salcedo J L, Macedo C F B, Cardoso V, Ferrari V, Gualtieri L, Khoo F S, Kunz J and Pani P 2016 *Phys. Rev. D* **94** 104024 [arXiv:1609.01286]

[612] Sennett N, Marsat S and Buonanno A 2016 *Phys. Rev. D* **94** 084003 [arXiv:1607.01420]

[613] Julié F L 2018 *JCAP* **01** 026 [arXiv:1711.10769]

[614] Cárdenas M, Julié F L and Deruelle N 2018 *Phys. Rev. D* **97** 124021 [arXiv:1712.02672]

[615] Julié F L 2018 *JCAP* **10** 033 [arXiv:1809.05041]

[616] Bernard L 2018 *Phys. Rev. D* **98** 044004 [arXiv:1802.10201]

[617] Bernard L 2019 *Phys. Rev. D* **99** 044047 [arXiv:1812.04169]

[618] Bernard L 2020 *Phys. Rev. D* **101** 021501 [Erratum: Phys.Rev.D 107, 069901 (2023)] [arXiv:1906.10735]

[619] Khalil M, Sennett N, Steinhoff J, Vines J and Buonanno A 2018 *Phys. Rev. D* **98** 104010 [arXiv:1809.03109]

[620] Shiralilou B, Hinderer T, Nissanke S M, Ortiz N and Witek H 2022 *Class. Quant. Grav.* **39** 035002 [arXiv:2105.13972]

[621] Pierini L and Gualtieri L 2021 *Phys. Rev. D* **103** 124017 [arXiv:2103.09870]

[622] Bernard L, Blanchet L and Trestini D 2022 *JCAP* **08** 008 [arXiv:2201.10924]

[623] Pierini L and Gualtieri L 2022 *Phys. Rev. D* **106** 104009 [arXiv:2207.11267]

[624] Creci G, Hinderer T and Steinhoff J 2023 *Phys. Rev. D* **108** 124073 [arXiv:2308.11323]

[625] Bernard L, Dones E and Mougiakakos S 2024 *Phys. Rev. D* **109** 044006 [arXiv:2310.19679]

[626] Julié F L 2023 [arXiv:2312.16764]

[627] Healy J, Bode T, Haas R, Pazos E, Laguna P, Shoemaker D and Yunes N 2012 *Class. Quant. Grav.* **29** 232002 [arXiv:1112.3928]

[628] Barausse E, Palenzuela C, Ponce M and Lehner L 2013 *Phys. Rev. D* **87** 081506 [arXiv:1212.5053]

[629] Berti E, Cardoso V, Gualtieri L, Horbatsch M and Sperhake U 2013 *Phys. Rev. D* **87** 124020 [arXiv:1304.2836]

[630] Shibata M, Taniguchi K, Okawa H and Buonanno A 2014 *Phys. Rev. D* **89** 084005 [arXiv:1310.0627]

[631] Palenzuela C, Barausse E, Ponce M and Lehner L 2014 *Phys. Rev. D* **89** 044024 [arXiv:1310.4481]

[632] Okounkova M, Stein L C, Scheel M A and Hemberger D A 2017 *Phys. Rev. D* **96** 044020 [arXiv:1705.07924]

[633] Cayuso J, Ortiz N and Lehner L 2017 *Phys. Rev. D* **96** 084043 [arXiv:1706.07421]

[634] Witek H, Gualtieri L, Pani P and Sotiriou T P 2019 *Phys. Rev. D* **99** 064035 [arXiv:1810.05177]

[635] Okounkova M, Stein L C, Scheel M A and Teukolsky S A 2019 *Phys. Rev. D* **100** 104026 [arXiv:1906.08789]

[636] Okounkova M, Stein L C, Moxon J, Scheel M A and Teukolsky S A 2020 *Phys. Rev. D* **101** 104016 [arXiv:1911.02588]

[637] Okounkova M 2020 *Phys. Rev. D* **102** 084046 [arXiv:2001.03571]

[638] Julié F L and Berti E 2020 *Phys. Rev. D* **101** 124045 [arXiv:2004.00003]

[639] Witek H, Gualtieri L and Pani P 2020 *Phys. Rev. D* **101** 124055 [arXiv:2004.00009]

[640] Silva H O, Witek H, Elley M and Yunes N 2021 *Phys. Rev. Lett.* **127** 031101 [arXiv:2012.10436]

[641] East W E and Ripley J L 2021 *Phys. Rev. D* **103** 044040 [arXiv:2011.03547]

[642] East W E and Ripley J L 2021 *Phys. Rev. Lett.* **127** 101102 [arXiv:2105.08571]

[643] Figueras P and França T 2022 *Phys. Rev. D* **105** 124004 [arXiv:2112.15529]

[644] Lara G, Bezares M and Barausse E 2022 *Phys. Rev. D* **105** 064058 [arXiv:2112.09186]

[645] Corman M, Ripley J L and East W E 2023 *Phys. Rev. D* **107** 024014 [arXiv:2210.09235]

[646] Aresté Saló L, Clough K and Figueras P 2022 *Phys. Rev. Lett.* **129** 261104 [arXiv:2208.14470]

[647] Doneva D D, Vañó Viñuales A and Yazadjiev S S 2022 *Phys. Rev. D* **106** L061502 [arXiv:2204.05333]

[648] Elley M, Silva H O, Witek H and Yunes N 2022 *Phys. Rev. D* **106** 044018 [arXiv:2205.06240]

[649] Franchini N, Bezares M, Barausse E and Lehner L 2022 *Phys. Rev. D* **106** 064061 [arXiv:2206.00014]

[650] R A H K, Ripley J L and Yunes N 2023 *Phys. Rev. D* **107** 044044 [arXiv:2211.08477]

[651] Ma S, Varma V, Stein L C, Foucart F, Duez M D, Kidder L E, Pfeiffer H P and Scheel M A 2023 *Phys. Rev. D* **107** 124051 [arXiv:2304.11836]

[652] Cayuso R, Figueras P, França T and Lehner L 2023 *Phys. Rev. Lett.* **131** 111403

[653] Aresté Saló L, Clough K and Figueras P 2023 *Phys. Rev. D* **108** 084018 [arXiv:2306.14966]

[654] Doneva D D, Aresté Saló L, Clough K, Figueras P and Yazadjiev S S 2023 *Phys. Rev. D* **108** 084017 [arXiv:2307.06474]

[655] Brady S E, Aresté Saló L, Clough K, Figueras P and S A P 2023 *Phys. Rev. D* **108** 104022 [arXiv:2308.16791]

[656] Lara G, Pfeiffer H P, Wittek N A, Vu N L, Nelli K C, Carpenter A, Lovelace G, Scheel M A and Throwe W 2024 [arXiv:2403.08705]

[657] Corman M, Lehner L, East W E and Dideron G 2024 [arXiv:2405.15581]

[658] Corman M and East W E 2024 [arXiv:2405.18496]

[659] Will C M 1998 *Phys. Rev. D* **57** 2061–2068 [arXiv:gr-qc/9709011]

[660] Mirshekari S, Yunes N and Will C M 2012 *Phys. Rev. D* **85** 024041 [arXiv:1110.2720]

[661] Eardley D M, Lee D L, Lightman A P, Wagoner R V and Will C M 1973 *Phys. Rev. Lett.* **30** 884–886

[662] Sänger E M *et al.* 2024 [arXiv:2406.03568]

[663] Krishnendu N V, Arun K G and Mishra C K 2017 *Phys. Rev. Lett.* **119** 091101 [arXiv:1701.06318]

[664] Krishnendu N V, Mishra C K and Arun K G 2019 *Phys. Rev. D* **99** 064008 [arXiv:1811.00317]

[665] Poisson E 1998 *Phys. Rev.* **D57** 5287–5290 [arXiv:gr-qc/9709032]

[666] Geroch R P 1970 *J. Math. Phys.* **11** 2580–2588

[667] Hansen R O 1974 *J. Math. Phys.* **15** 46–52

[668] Beig R and Simon W 1981 *Proceedings of the Royal Society of London Series A* **376** 333–341

[669] Gossan S, Veitch J and Sathyaprakash B S 2012 *Phys. Rev. D* **85** 124056 [arXiv:1111.5819]

[670] Isi M, Giesler M, Farr W M, Scheel M A and Teukolsky S A 2019 *Phys. Rev. Lett.* **123** 111102 [arXiv:1905.00869]

[671] Carullo G, Del Pozzo W and Veitch J 2019 *Phys. Rev. D* **99** 123029 [Erratum: Phys.Rev.D 100, 089903 (2019)] [arXiv:1902.07527]

[672] Isi M and Farr W M 2021 [arXiv:2107.05609]

[673] Baibhav V, Cheung M H Y, Berti E, Cardoso V, Carullo G, Cotesta R, Del Pozzo W and Duque F 2023 *Phys. Rev. D* **108** 104020 [arXiv:2302.03050]

[674] Kamaretsos I, Hannam M, Husa S and Sathyaprakash B S 2012 *Phys. Rev. D* **85** 024018 [arXiv:1107.0854]

[675] Kamaretsos I, Hannam M and Sathyaprakash B 2012 *Phys. Rev. Lett.* **109** 141102 [arXiv:1207.0399]

[676] London L, Shoemaker D and Healy J 2014 *Phys. Rev. D* **90** 124032 [Erratum: Phys.Rev.D 94, 069902 (2016)] [arXiv:1404.3197]

[677] London L T 2020 *Phys. Rev. D* **102** 084052 [arXiv:1801.08208]

[678] Cheung M H Y, Berti E, Baibhav V and Cotesta R 2024 *Phys. Rev. D* **109** 044069 [Erratum: Phys.Rev.D 110, 049902 (2024)] [arXiv:2310.04489]

[679] Zhu H *et al.* 2025 *Phys. Rev. D* **111** 064052 [arXiv:2312.08588]

[680] Carullo G 2024 *JCAP* **10** 061 [arXiv:2406.19442]

[681] Gennari V, Carullo G and Del Pozzo W 2024 *Eur. Phys. J. C* **84** 233 [arXiv:2312.12515]

[682] Del Pozzo W, Veitch J and Vecchio A 2011 *Phys. Rev. D* **83** 082002 [arXiv:1101.1391]

[683] Zimmerman A, Haster C J and Chatziioannou K 2019 *Phys. Rev. D* **99** 124044 [arXiv:1903.11008]

[684] Isi M, Chatziioannou K and Farr W M 2019 *Phys. Rev. Lett.* **123** 121101 [arXiv:1904.08011]

[685] Payne E, Isi M, Chatziioannou K and Farr W M 2023 *Phys. Rev. D* **108** 124060 [arXiv:2309.04528]

[686] Mandel I, Farr W M and Gair J R 2019 *Mon. Not. Roy. Astron. Soc.* **486** 1086–1093 [arXiv:1809.02063]

[687] Magee R, Isi M, Payne E, Chatziioannou K, Farr W M, Pratten G and Vitale S 2024 *Phys. Rev. D* **109** 023014 [arXiv:2311.03656]

[688] Kobayashi T 2019 *Rept. Prog. Phys.* **82** 086901 [arXiv:1901.07183]

[689] Gross D J and Sloan J H 1987 *Nucl. Phys. B* **291** 41–89

[690] Yagi K, Stein L C and Yunes N 2016 *Phys. Rev. D* **93** 024010 [arXiv:1510.02152]

[691] Cano P A and Ruipérez A 2019 *JHEP* **05** 189 [Erratum: JHEP 03, 187 (2020)] [arXiv:1901.01315]

[692] Doneva D D and Yazadjiev S S 2018 *Phys. Rev. Lett.* **120** 131103 [arXiv:1711.01187]

[693] Silva H O, Sakstein J, Gualtieri L, Sotiriou T P and Berti E 2018 *Phys. Rev. Lett.* **120** 131104 [arXiv:1711.02080]

[694] Minamitsuji M and Ikeda T 2019 *Phys. Rev. D* **99** 044017 [arXiv:1812.03551]

[695] Silva H O, Macedo C F B, Sotiriou T P, Gualtieri L, Sakstein J and Berti E 2019 *Phys. Rev. D* **99** 064011 [arXiv:1812.05590]

[696] Macedo C F B, Sakstein J, Berti E, Gualtieri L, Silva H O and Sotiriou T P 2019 *Phys. Rev. D* **99** 104041 [arXiv:1903.06784]

[697] Dima A, Barausse E, Franchini N and Sotiriou T P 2020 *Phys. Rev. Lett.* **125** 231101 [arXiv:2006.03095]

[698] Sennett N and Buonanno A 2016 *Phys. Rev. D* **93** 124004 [arXiv:1603.03300]

[699] Sennett N, Shao L and Steinhoff J 2017 *Phys. Rev. D* **96** 084019 [arXiv:1708.08285]

[700] Khalil M, Sennett N, Steinhoff J and Buonanno A 2019 *Phys. Rev. D* **100** 124013 [arXiv:1906.08161]

[701] Khalil M, Mendes R F P, Ortiz N and Steinhoff J 2022 *Phys. Rev. D* **106** 104016 [arXiv:2206.13233]

[702] Wang H T, Tang S P, Li P C, Han M Z and Fan Y Z 2021 *Phys. Rev. D* **104** 024015 [arXiv:2104.07590]

[703] Lyu Z, Jiang N and Yagi K 2022 *Phys. Rev. D* **105** 064001 [Erratum: Phys.Rev.D 106, 069901 (2022), Erratum: Phys.Rev.D 106, 069901 (2022)] [arXiv:2201.02543]

[704] van Gemeren I, Shiralilou B and Hinderer T 2023 *Phys. Rev. D* **108** 024026 [arXiv:2302.08480]

[705] Chung A K W and Yunes N 2024 [arXiv:2405.12280]

[706] Chung A K W and Yunes N 2024 [arXiv:2406.11986]

[707] Lara G *et al.* 2025 [arXiv:2505.14785]

[708] Eardley D M 1975 *Astrophys. J. Lett*

[709] Shiralilou B, Hinderer T, Nissanke S, Ortiz N and Witek H 2021 *Phys. Rev. D* **103** L121503 [arXiv:2012.09162]

[710] Bardeen J M, Press W H and Teukolsky S A 1972 *Astrophys. J.* **178** 347

[711] Li D, Wagle P, Chen Y and Yunes N 2023 *Phys. Rev. X* **13** 021029 [arXiv:2206.10652]

[712] Hussain A and Zimmerman A 2022 *Phys. Rev. D* **106** 104018 [arXiv:2206.10653]

[713] Cano P A, Fransen K, Hertog T and Maenaut S 2023 *Phys. Rev. D* **108** 024040 [arXiv:2304.02663]

[714] Li D, Hussain A, Wagle P, Chen Y, Yunes N and Zimmerman A 2023 [arXiv:2310.06033]

[715] Wagle P, Li D, Chen Y and Yunes N 2023 [arXiv:2311.07706]

[716] Chung A K W, Wagle P and Yunes N 2024 *Phys. Rev. D* **109** 044072 [arXiv:2312.08435]

[717] Chung A K W, Wagle P and Yunes N 2023 *Phys. Rev. D* **107** 124032 [arXiv:2302.11624]

[718] Buonanno A, Kidder L E and Lehner L 2008 *Phys. Rev. D* **77** 026004 [arXiv:0709.3839]

[719] Speri L, Barsanti S, Maselli A, Sotiriou T P, Warburton N, van de Meent M, Chua A J K, Burke O and Gair J 2024 [arXiv:2406.07607]

[720] Gao B, Tang S P, Wang H T, Yan J and Fan Y Z 2024 [arXiv:2405.13279]

[721] Kass R E and Raftery A E 1995 *Journal of the American Statistical Association* **90** 773–795 [arXiv:https://www.tandfonline.com/doi/pdf/10.1080/01621459.1995.10476572]

[722] Hannam M *et al.* 2022 *Nature* **610** 652–655 [arXiv:2112.11300]

[723] Payne E, Hourihane S, Golomb J, Udall R, Udall R, Davis D and Chatziioannou K 2022 *Phys. Rev. D* **106** 104017 [arXiv:2206.11932]

[724] Foo C and Hamilton E 2024 *Phys. Rev. D* **110** 104024 [arXiv:2408.02671]

[725] Evstafyeva T, Sperhake U, Romero-Shaw I M and Agathos M 2024 *Phys. Rev. Lett.* **133** 131401 [arXiv:2406.02715]

[726] Boyle M 2013 *Phys. Rev. D* **87** 104006 [arXiv:1302.2919]

[727] Hughes S A, Apte A, Khanna G and Lim H 2019 *Phys. Rev. Lett.* **123** 161101 [arXiv:1901.05900]

[728] Siegel H, Isi M and Farr W M 2023 *Phys. Rev. D* **108** 064008 [arXiv:2307.11975]

[729] O'Shaughnessy R, London L, Healy J and Shoemaker D 2013 *Phys. Rev. D* **87** 044038 [arXiv:1209.3712]

[730] Hamilton E, London L and Hannam M 2023 [arXiv:2301.06558]

[731] Liebling S L and Palenzuela C 2023 *Living Rev. Rel.* **26** 1 [arXiv:1202.5809]

[732] Clough K, Figueras P, Finkel H, Kunesch M, Lim E A and Tunyasuvunakool S 2015 *Class. Quant. Grav.* **32** 245011 [arXiv:1503.03436]

[733] Andrade T *et al.* 2021 *J. Open Source Softw.* **6** 3703 [arXiv:2201.03458]

[734] Macas R, Lundgren A and Ashton G 2024 *Phys. Rev. D* **109** 062006 [arXiv:2311.09921]

[735] Kolitsidou P, Thompson J E and Hannam M 2025 *Phys. Rev. D* **111** 024050 [arXiv:2402.00813]

[736] Pacilio C, Gerosa D and Bhagwat S 2024 *Phys. Rev. D* **109** L081302 [arXiv:2310.03811]

[737] Calderón Bustillo J, Sanchis-Gual N, Torres-Forné A and Font J A 2021 *Phys. Rev. Lett.* **126** 201101 [arXiv:2009.01066]

[738] Romero-Shaw I M, Gerosa D and Loutrel N 2023 *Mon. Not. Roy. Astron. Soc.* **519** 5352–5357 [arXiv:2211.07528]

[739] Romero-Shaw I M, Lasky P D and Thrane E 2019 *Mon. Not. Roy. Astron. Soc.* **490** 5210–5216 [arXiv:1909.05466]

[740] Gayathri V, Healy J, Lange J, O'Brien B, Szczepanczyk M, Bartos I, Campanelli M, Klimenko S, Lousto C O and O'Shaughnessy R 2022 *Nature Astron.* **6** 344–349 [arXiv:2009.05461]

[741] Gamba R, Breschi M, Carullo G, Albanesi S, Rettegno P, Bernuzzi S and Nagar A 2023 *Nature Astron.* **7** 11–17 [arXiv:2106.05575]

[742] Romero-Shaw I M, Lasky P D and Thrane E 2022 *Astrophys. J.* **940** 171 [arXiv:2206.14695]

[743] Fujita R 2012 *Prog. Theor. Phys.* **128** 971–992 [arXiv:1211.5535]

[744] Fujita R 2015 *PTEP* **2015** 033E01 [arXiv:1412.5689]

[745] Mitman K *et al.* 2024 *Class. Quant. Grav.* **41** 223001 [arXiv:2405.08868]

[746] Yi S, Iacovelli F, Marsat S, Wadekar D and Berti E 2025 [arXiv:2502.12237]

[747] Keith B, Khadse A and Field S E 2021 *Phys. Rev. Res.* **3** 043101 [arXiv:2102.12695]

[748] Edwards T D P, Wong K W K, Lam K K H, Coogan A, Foreman-Mackey D, Isi M and Zimmerman A 2024 *Phys. Rev. D* **110** 064028 [arXiv:2302.05329]

[749] Mezzasoma S, Haster C J, Owen C B, Cornish N J and Yunes N 2025 [arXiv:2503.23304]

[750] Bonino A, Schmidt P and Pratten G 2024 *Phys. Rev. D* **110** 104002 [arXiv:2404.18875]

[751] Sun D, Boyle M, Mitman K, Scheel M A, Stein L C, Teukolsky S A and Varma V 2024 *Phys. Rev. D* **110** 104076 [arXiv:2403.10278]

[752] Digman M C and Cornish N J 2023 *Phys. Rev. D* **108** 023022 [arXiv:2212.04600]

[753] Tenorio R and Gerosa D 2025 *Phys. Rev. D* **111** 104044 [arXiv:2502.11823]

[754] Katz M L, Chua A J K, Speri L, Warburton N and Hughes S A 2021 *Phys. Rev. D* **104** 064047 [arXiv:2104.04582]

[755] Speri L, Katz M L, Chua A J K, Hughes S A, Warburton N, Thompson J E, Chapman-Bird C E A and Gair J R 2023 [arXiv:2307.12585]